

Alleviating the Adverse Haemodynamics of Arteries Treated with Drug-Eluting Stents without Compromising Drug Uptake

Pujith R. S. Vijayaratnam

A thesis in fulfilment of the requirements for the degree of
Doctor of Philosophy



UNSW
A U S T R A L I A

School of Mechanical and Manufacturing Engineering

Faculty of Engineering

September 2017

PLEASE TYPE**THE UNIVERSITY OF NEW SOUTH WALES
Thesis/Dissertation Sheet**

Surname or Family name: Vijayaratnam

First name: Pujith

Other name/s: Rajaguru Senapathy

Abbreviation for degree as given in the University calendar: PhD

School: Mechanical and Manufacturing Engineering

Faculty: Engineering

Title: Alleviating the Adverse Haemodynamics of Arteries Treated
with Drug-Eluting Stents without Compromising Drug Uptake**Abstract 350 words maximum: (PLEASE TYPE)**

Drug-eluting stents are small, metallic, wire-mesh tubes that are implanted into occluded arteries that have been restored to their original patency through the expansion of a balloon catheter. The stent acts as a mechanical scaffold that minimises the risk of arterial collapse, whilst a drug coating on the stent surfaces reduces smooth muscle cell proliferation at arterial injury sites. However, in-stent restenosis – defined as the reduction in diameter of a stented vessel by more than 50% – persists in up to 20% of drug-eluting stent patients. Furthermore, blood clots persist in up to 0.8% of patients after more than 30 days have passed since stent implantation. This condition, known as late stent thrombosis, is associated with a 45% mortality rate.

The primary aim of this thesis is to use computational fluid dynamics analyses to identify methods of attenuating the stent-induced haemodynamic disturbances that give rise to these diseases, without compromising drug transport into the arterial tissue. The haemodynamic and drug transport behaviour of stented arteries are also characterised in these numerical studies and the drug transport models used are validated using in-vitro experiments. The results obtained showed that the non-Newtonian properties of blood, its complex near-wall behaviour, and the pulsatility of its flow each have minimal impact on the drug transport behaviour from stents into arterial tissue. This is because the surfaces of the stents that are exposed to arterial blood flow are much more rapidly depleted of drug than the surfaces that directly contact arterial tissue.

Furthermore, the drug that is transported from these non-contacting surfaces is not significantly taken up by the arterial tissue but is instead lost to the surrounding blood flow. Hence, the overall drug uptake is driven primarily by this direct contact whilst flow-mediated drug transport is negligible. It is therefore concluded that drug transport can be enhanced in stented arteries by extending the region of contact between the drug coating and the arterial tissue. Finally, it is shown that this extended contact region can be used in conjunction with streamlined stent strut geometries to alleviate the adverse haemodynamics of stented vessels without compromising drug uptake.

Declaration relating to disposition of project thesis/dissertation

I hereby grant to the University of New South Wales or its agents the right to archive and to make available my thesis or dissertation in whole or in part in the University libraries in all forms of media, now or here after known, subject to the provisions of the Copyright Act 1968. I retain all property rights, such as patent rights. I also retain the right to use in future works (such as articles or books) all or part of this thesis or dissertation.

I also authorise University Microfilms to use the 350 word abstract of my thesis in Dissertation Abstracts International (this is applicable to doctoral theses only).

The University recognises that there may be exceptional circumstances requiring restrictions on copying or conditions on use. Requests for restriction for a period of up to 2 years must be made in writing. Requests for a longer period of restriction may be considered in exceptional circumstances and require the approval of the Dean of Graduate Research.

FOR OFFICE USE ONLY

Date of completion of requirements for Award:

COPYRIGHT STATEMENT

'I hereby grant the University of New South Wales or its agents the right to archive and to make available my thesis or dissertation in whole or part in the University libraries in all forms of media, now or here after known, subject to the provisions of the Copyright Act 1968. I retain all proprietary rights, such as patent rights. I also retain the right to use in future works (such as articles or books) all or part of this thesis or dissertation.

I also authorise University Microfilms to use the 350 word abstract of my thesis in Dissertation Abstract International (this is applicable to doctoral theses only).

I have either used no substantial portions of copyright material in my thesis or I have obtained permission to use copyright material; where permission has not been granted I have applied/will apply for a partial restriction of the digital copy of my thesis or dissertation.'

Signed

Date

AUTHENTICITY STATEMENT

'I certify that the Library deposit digital copy is a direct equivalent of the final officially approved version of my thesis. No emendation of content has occurred and if there are any minor variations in formatting, they are the result of the conversion to digital format.'

Signed

Date

Originality Statement

‘I hereby declare that this submission is my own work and to the best of my knowledge it contains no materials previously published or written by another person, or substantial proportions of material which have been accepted for the award of any other degree or diploma at UNSW or any other educational institution, except where due acknowledgement is made in the thesis. Any contribution made to the research by others, with whom I have worked at UNSW or elsewhere, is explicitly acknowledged in the thesis. I also declare that the intellectual content of this thesis is the product of my own work, except to the extent that assistance from others in the project's design and conception or in style, presentation and linguistic expression is acknowledged.’

Signed

Date

Abstract

Drug-eluting stents are small, metallic, wire-mesh tubes that are implanted into occluded arteries that have been restored to their original patency through the expansion of a balloon catheter. The stent acts as a mechanical scaffold that minimises the risk of arterial collapse, whilst a drug coating on the stent surfaces reduces smooth muscle cell proliferation at arterial injury sites. However, in-stent restenosis – defined as the reduction in diameter of a stented vessel by more than 50% – still persists in up to 20% of drug-eluting stent patients. Furthermore, blood clots persist on the surfaces of drug-eluting stents in up to 0.8% of patients even after more than 30 days have passed since stent implantation. This condition, known as late stent thrombosis, is associated with a 45% mortality rate.

The primary aim of this thesis is to use computational fluid dynamics analyses to identify methods of attenuating the stent-induced haemodynamic disturbances that give rise to these diseases, without compromising drug transport into the arterial tissue. The haemodynamic and drug transport behaviour of stented arteries are also characterised in these numerical studies and the drug transport models used are validated using in-vitro experiments.

The results obtained showed that the non-Newtonian properties of blood, its complex near-wall behaviour, and the pulsatility of its flow each have minimal impact on the drug transport behaviour from stents into arterial tissue. This is because the surfaces of the stents that are exposed to arterial blood flow are much more rapidly depleted of drug than the surfaces that directly contact arterial tissue. Furthermore, the drug that is transported from these non-contacting surfaces is not significantly taken up by the arterial tissue but is instead lost to the surrounding

blood flow. Hence, the overall drug uptake is driven primarily by this direct contact whilst flow-mediated drug transport is negligible. It is therefore concluded that drug transport can be enhanced in stented arteries by extending the region of contact between the drug coating and the arterial tissue. Finally, it is shown that this extended contact region can be used in conjunction with streamlined stent strut geometries to alleviate the adverse haemodynamics of stented vessels without compromising drug uptake. Ultimately, it is hoped that these results can be used by device designers to mitigate the risk of stent thrombosis and in-stent restenosis in the next generation of drug-eluting stents.

Acknowledgements

Firstly, I would like to acknowledge my supervisors, **Assoc. Prof. Tracie Barber** and **Prof. John Reizes** for all of their support and guidance over the past four years.

Tracie, it has been six years since you first inspired me to pursue a career in fluid dynamics (yes, it was your five minute simulation of a race truck with a questionable spoiler that did it for me) and I could not be more grateful for this decision and for choosing you as my supervisor. Thank you for granting me the freedom to explore the world of drug-eluting stents in my own way and for also ensuring that I never got too far off track. John, thank you for always taking the time to go through my work in Marianas Trench-levels of depth. Your suggestions are always welcome and I am a better writer and engineer for having received them. I hope that one day I will be able to reach your level of attention to detail and dad joke-telling ability; both goals seem equally unattainable at this stage but maybe one of the other stages will give me better luck. If you read that and you are not John, I apologise.

Secondly, I would like to extend my deepest gratitude to my predecessor, **Dr Caroline O'Brien**, for laying the groundwork on which this thesis is based. Caroline, this thesis could not have been completed without all the amazing work that you put into developing your in-vitro drug-eluting stent experiment. Thank you also for your advice during the early stages of my PhD and for showing me around your lab while I was in Boston.

Next, my gratitude to everyone who helped me out during my trips to the biomedical engineering laboratories. In particular, thanks to **Dr Penny Martens** for her supervision and for providing me with the resources that I needed to complete my experiments. I am also grateful for all the amazing work that she put into the

postgraduate research symposium and for coaxing me to participate in it while I was whinging about other deadlines. Penny, partaking in this symposium was the best decision that I ever unwillingly made. To **Dr Justine Roberts**, **Dr Josef Goding** and **Dr Khoon Lim**, thank you for teaching me the ways of hydrogel making. My regards also to **Dr Jeff Welch**, **Dr Vladimir Sytnyk** and **Ulises Aregueta Robles** for all their help with the microplate reader. Finally, a big thank you to **Lynn Ferris** for always being an uplifting presence in the labs and for always helping me find what I needed.

I would also like to acknowledge all the inhabitants of the microfluidics laboratory for their company and for letting me steal their PDMS. Many thanks to **Derek Chung** in particular for putting up with my distractions over the past two years and for the many cathartic discussions that followed my many failed experiments. Thanks also to **Dr Eldad Ben-Ishay** and **Dr Majid Ebrahimi Warkiani** for setting up and maintaining the labs, and letting me use its equipment. Finally, to **Yan Wang** and **Liyana Jawahir**, you were the best undergraduate students that I could have hoped for. I am super proud of you both for producing such excellent theses and I wish you both all the best in your respective careers.

My regards also to all the technical staff at the School of Mechanical and Manufacturing Engineering who made my simulations and experiments possible. To **John ‘Jay Z’ Zaitseff** and the rest of the staff in charge of the Leonardi and Trentino computing clusters, thanks for all the amazing work that you put into keeping these clusters running. To the workshop staff, **Ian Cassapi** and **Andy Higley**, thank you for all the wonderful acrylic bits and bobs that you made for me. Finally, I am grateful to **Joe Tscherry** for helping me through the long laboratory

induction process and for providing me with much of the equipment needed for my experiments.

I would also like to send my warmest regards to my neighbours in the CFD labs. To **Dr James Keogh** and **Dr David Fulker**, it has been a great journey and I cannot believe that four years have passed since we all started our PhDs together. Congratulations to both of you, as well as **Dr Reza Keshavarzi**, for reaching the finish line and I hope that I can finally join you guys soon. To **Azadeh Lotfi**, **Kyle Forster**, **John Carroll** and **Eamonn Colley**, I am looking forward to seeing all the amazing things that you guys come up with and I wish you all the best with your respective theses. My best regards also to **Julia Marlana-Moser** in all her future endeavours. Thank you all for making the CFD labs a fun place to work in and I'll see your sorry posteriors at the next nerf war!

I would also like to acknowledge everyone who has reminded me that there is more to life than stents over the past four years. In particular, thank you to the Sunswift team for being such a big part of my postgraduate life. Wishing you guys the best of luck with Violet – she looks amazing already and I cannot wait to see her in Adelaide. My warmest regards also to all the regulars and randoms that helped keep the sacred tradition of Wednesday evening football alive and well.

Finally, to **Mum** and **Dad**, thank you for your unending support and for being my two biggest sources of inspiration. I hope that this thesis is in some small way a testament to my gratitude to you for all the sacrifices that you made to ensure that I received a good education. Love you both. And yes, I will get a haircut.

List of Publications

Vijayaratnam, P.R.S., T.J. Barber, and J.A. Reizes, 2014, January. Using Magnetic Struts to Alleviate Adverse Haemodynamic Flow Effects around Drug-Eluting Stents. In *Cardiology*, 128, p. 340. Allschwilerstrasse 10, CH-4009 Basel, Switzerland: Karger.

Vijayaratnam, P.R.S., O'Brien, C.C., Reizes, J.A., Barber, T.J. and Edelman, E.R., 2015. The Impact of Blood Rheology on Drug Transport in Stented Arteries: Steady Simulations. *PloS one*, 10(6), p.e0128178.

Vijayaratnam, P.R.S., Barber, T.J. and Reizes, J.A., 2017. The Localized Hemodynamics of Drug-Eluting Stents Are Not Improved by the Presence of Magnetic Struts. *Journal of Biomechanical Engineering*, 139(1), p.014502.

Table of Contents

| | |
|---|-----|
| Abstract | i |
| Acknowledgements | iii |
| List of Publications | vi |
| Table of Contents | vii |
| Table of Figures..... | xiv |
| Nomenclature | xxi |
| Chapter 1 Introduction | 1 |
| 1.1 The Emergence of Drug-Eluting Stents | 2 |
| 1.1.1 Atherosclerosis..... | 2 |
| 1.1.2 Angioplasty | 3 |
| 1.1.3 Bare-Metal Stents | 6 |
| 1.1.4 Drug-Eluting Stents | 8 |
| 1.2 The Limitations of Drug-Eluting Stents | 10 |
| 1.3 The Adverse Haemodynamics of Drug-Eluting Stents..... | 13 |
| 1.3.1 Haemodynamics and In-Stent Restenosis | 15 |
| 1.3.2 Haemodynamics and Stent Thrombosis..... | 17 |
| 1.4 Modelling the Haemodynamics and Drug Transport of Stented Arteries | 20 |
| 1.4.1 Modelling the Non-Newtonian Properties of Blood..... | 21 |
| 1.4.2 Modelling the Individual Variations in Blood Behaviour | 23 |

| | | |
|---|---|----|
| 1.4.3 | Modelling the Near-Wall Behaviour of Blood..... | 25 |
| 1.4.4 | Modelling the Pulsatility of Blood Flow..... | 26 |
| 1.4.5 | The Significance of Flow-Mediated Drug Transport..... | 27 |
| 1.4.6 | Incomplete Stent Apposition..... | 28 |
| 1.5 | Alleviating the Adverse Haemodynamics of Arteries Treated with Drug- Eluting Stents..... | 31 |
| 1.6 | Aims and Scope | 34 |
| Chapter 2 The Impact of Blood Rheology on Drug Transport in Stented Arteries: Steady Analyses..... | | 35 |
| Chapter Aims | | 35 |
| 2.1 | Methods | 36 |
| 2.1.1 | Geometry..... | 36 |
| 2.1.2 | Mathematical Model | 37 |
| 2.1.3 | Boundary Conditions | 39 |
| 2.1.4 | Blood Rheological Models..... | 42 |
| 2.1.5 | Grid Description and Refinement | 45 |
| 2.2 | Results and Discussion..... | 47 |
| 2.2.1 | Rheological Effects on Blood Flow | 47 |
| 2.2.2 | Rheological Effects on Drug Transport..... | 53 |
| 2.3 | Outcomes | 64 |

| | | |
|-----------|---|-----|
| Chapter 3 | The Impact of Blood Rheology on Drug Transport in Stented Arteries: Pulsatile Analyses..... | 66 |
| | Chapter Aims | 66 |
| 3.1 | Methods | 67 |
| 3.1.1 | Geometry..... | 67 |
| 3.1.2 | Mathematical Model | 68 |
| 3.1.3 | Boundary Conditions | 71 |
| 3.1.4 | Spatial and Temporal Discretisation..... | 73 |
| 3.2 | Results and Discussion..... | 76 |
| 3.2.1 | Rheological Effects on Blood Flow | 76 |
| 3.2.2 | Rheological Effects on Drug Transport..... | 78 |
| 3.3 | Outcomes | 85 |
| Chapter 4 | The Impact of Blood Rheology on Drug Transport in Stented Arteries: Experimental Validation..... | 87 |
| | Chapter Aims | 87 |
| 4.1 | Methods | 88 |
| 4.1.1 | Experimental Framework | 88 |
| 4.1.2 | Diffusion Studies | 96 |
| 4.1.3 | Computational Framework..... | 105 |
| 4.2 | Results and Discussion..... | 110 |
| 4.2.1 | Experimental Results | 110 |

| | | |
|--|---|-----|
| 4.2.2 | Numerical Results | 115 |
| 4.3 | Outcomes | 116 |
| Chapter 5 The Haemodynamics and Drug Transport Behaviour Associated with Incomplete Stent Apposition | | |
| | | 117 |
| | Chapter Aims | 117 |
| 5.1 | Methods | 118 |
| 5.1.1 | Geometries | 118 |
| 5.1.2 | Mathematical Model | 121 |
| 5.1.3 | Boundary Conditions | 123 |
| 5.1.4 | Spatial and Temporal Discretisation..... | 124 |
| 5.2 | Results and Discussion..... | 127 |
| 5.2.1 | The Haemodynamics of Arteries with Malapposed Struts..... | 127 |
| 5.2.2 | The Drug Transport Behaviour of Malapposed Struts | 136 |
| 5.3 | Outcomes | 139 |
| Chapter 6 The Localised Haemodynamics of Drug-Eluting Stents are not Improved by the Presence of Magnetic Struts..... | | |
| | | 141 |
| | Chapter Aims | 141 |
| 6.1 | Methods | 142 |
| 6.1.1 | Geometry..... | 142 |
| 6.1.2 | Mathematical Model | 143 |
| 6.1.3 | Boundary Conditions | 145 |

| | | |
|-----------|---|-----|
| 6.1.4 | Grid Description..... | 148 |
| 6.2 | Results and Discussion..... | 148 |
| 6.3 | Outcomes | 152 |
| Chapter 7 | Streamlining Drug-Eluting Stents to Improve their Haemodynamic and Drug Transport Behaviour | 153 |
| | Chapter Aims | 153 |
| 7.1 | Methods | 154 |
| 7.1.1 | Geometry..... | 154 |
| 7.1.2 | Mathematical Model | 157 |
| 7.1.3 | Boundary Conditions | 159 |
| 7.1.4 | Grid Description and Refinement | 160 |
| 7.2 | Results and Discussion..... | 162 |
| 7.2.1 | Two-dimensional simulations | 162 |
| 7.2.2 | Three-dimensional simulations..... | 166 |
| 7.3 | Outcomes | 169 |
| Chapter 8 | Conclusions and Future Work..... | 170 |
| 8.1 | Thesis Significance | 171 |
| 8.2 | Arterial Blood Flow and its Impact on Stent-Based Drug Delivery..... | 171 |
| 8.3 | Alleviating the Adverse Haemodynamics of Arteries Treated with Drug-Eluting Stents without Compromising Drug Uptake | 175 |
| 8.4 | Limitations and Future Work | 178 |

| | |
|---|-----|
| References..... | 180 |
| Appendix A Grid Convergence Studies..... | A1 |
| Grid Convergence in Chapter 2..... | A2 |
| Grid Convergence in Chapter 3..... | A4 |
| Grid Convergence in Chapter 4..... | A7 |
| Grid Convergence in Chapter 5..... | A9 |
| Grid Convergence in Chapter 6..... | A16 |
| Grid Convergence in Chapter 7..... | A18 |
| Appendix B In-Vitro Experiment Setup..... | A27 |
| Equipment..... | A28 |
| Method..... | A28 |
| Appendix C Hydrogel Preparation..... | A35 |
| Equipment..... | A36 |
| Method..... | A36 |
| Appendix D Rhodamine B/PDMS Strut Preparation..... | A41 |
| Equipment..... | A42 |
| Method..... | A42 |
| Appendix E Diffusion Studies..... | A48 |
| Equipment..... | A49 |
| Diffusion Study of Rhodamine B in Glycerol-Water..... | A50 |
| Diffusion Study of Rhodamine B in PVA-MA..... | A52 |

| | |
|---|-----|
| Diffusion Study of Rhodamine B in a Rhodamine B/ PDMS film..... | A53 |
| Preparation of Standard Dilution Series | A55 |
| Plate Readings | A57 |

Table of Figures

| | |
|---|----|
| Figure 1-1. An artery with a stenosis. | 2 |
| Figure 1-2. Balloon angioplasty | 4 |
| Figure 1-3. Mechanisms of Restenosis. | 6 |
| Figure 1-4. Bare-metal stent implantation within an occluded artery..... | 7 |
| Figure 1-5. Photomicrograph representing the cross-sectional histology of an artery that has succumbed to in-stent restenosis caused by neointimal hyperplasia..... | 8 |
| Figure 1-6. First generation drug-eluting stents. | 9 |
| Figure 1-7. Histological section of an artery that has succumbed to stent thrombosis. | 10 |
| Figure 1-8. A diagram showing the two haemodynamic forces experienced in blood vessels. | 13 |
| Figure 1-9. The presence of drug-eluting stents establishes localised regions of recirculating flow adjacent to the stent struts..... | 14 |
| Figure 1-10. Endothelial dysfunction caused by low wall shear stresses promotes smooth muscle cell proliferation and migration. | 15 |
| Figure 1-11. Flow-mediated drug transport..... | 16 |
| Figure 1-12. Platelets that are activated in regions with high wall shear stress (WSS) may subsequently accumulate in recirculation zones downstream of the stent struts. | 18 |
| Figure 1-13. Locations of unactivated platelets (blue), activated platelets (black) and red blood cells (RBCs, red) after 1.58 seconds of simulating their transport, collision, activation, and adhesion and aggregation processes within coronary arteries featuring malapposed struts..... | 19 |

| | |
|--|----|
| Figure 1-14. Long chains of red blood cells, known as rouleaux, form in regions of low strain rate. | 21 |
| Figure 1-15. The viscosities predicted by the blood rheological models shown vary considerably at the same strain rates. | 23 |
| Figure 1-16. Burst release of Paclitaxel (PTx) from a poly(styrene-b-isobutylene-b-styrene) (SIBS) coating is believed to occur within two days of stent implantation. | 24 |
| Figure 1-17. In steady, fully developed flow, red blood cells (–) migrate towards the centre of the vessel whilst platelets (- -) are displaced towards the vessel wall. | 25 |
| Figure 1-18. Drug concentration profiles obtained within a two-dimensional artery model featuring a single drug-eluting stent strut. | 27 |
| Figure 1-19. Numerical studies of malapposed drug-eluting stents showed that appreciable quantities of drug can be delivered into arterial tissue even when there is no direct contact between tissue and strut. | 29 |
| Figure 1-20. The impact of malapposition distance on the flow in stented vessels. ... | 30 |
| Figure 1-21. A more haemodynamic stent profile has been established as a potential method of alleviating adverse haemodynamics of arteries treated with drug-eluting stents. | 33 |
| Figure 2-1. Geometry and boundary conditions. | 36 |
| Figure 2-2. Comparison of the velocity profile obtained with the Power Law rheological model 8 mm away from the inlet (Line 1) with the fully developed flow profile obtained with this rheological model (Line 2). | 41 |
| Figure 2-3. Experimental measurements of blood viscosity and non-Newtonian blood rheological models. | 45 |
| Figure 2-4. Drug concentration distribution and flow pathlines in the stented artery. | 47 |

| | |
|---|----|
| Figure 2-5. The effects of flow rate on the proximal and distal recirculation lengths. | 49 |
| Figure 2-6. The effects of blood rheology on the proximal and distal recirculation lengths. | 50 |
| Figure 2-7. Local non-Newtonian importance factors, I_L | 52 |
| Figure 2-8. Diffusive mass transport behaviour. | 55 |
| Figure 2-9. The effect of blood flow on the diffusive mass transport behaviour. | 56 |
| Figure 2-10. The effect of diffusion coefficient on the diffusive mass transport behaviour of stented arteries. | 57 |
| Figure 2-11. The effect of blood rheological model on the diffusive mass transport behaviour of stented arteries. The non-Newtonian blood rheological models produced similar $\partial c/\partial n$ patterns to the Newtonian model; however, their local maxima and minima were up to 59% smaller in magnitude. | 58 |
| Figure 2-12. The effect of blood rheological model and flow rate on the average tissue drug concentration. | 61 |
| Figure 2-13. Contour plots of the non-Newtonian drug concentration difference factor, I_D | 63 |
| Figure 3-1: Geometry and dimensions. Unlike the geometry used in the previous chapter, a 15 μm thick drug coating was modelled in the current geometry to simulate the depletion of drug within the coating..... | 67 |
| Figure 3-2: Pulsatile and steady inlet velocity profiles were used in this study. The mean flow rate of the Pulsatile waveform is identical to that of the steady waveform. A Poiseuille parabolic inlet velocity profile was used with the steady waveform whilst a plug-flow profile was used with the pulsatile waveform. | 72 |
| Figure 3-3: Wall shear stress distributions along the lumen-tissue interface..... | 77 |

| | |
|---|-----|
| Figure 3-4. The impact of blood rheological model selection and pulsatility on the area-weighted average concentration (AWAC) of drug in the arterial tissue. | 78 |
| Figure 3-5. Normalised drug concentration distribution at the culmination of 60 seconds..... | 80 |
| Figure 3-6. Normalised drug concentration at the outer surfaces of the strut coating after 60 seconds. | 81 |
| Figure 3-7. The normalised drug concentration at the strut coating obtained with two different drug transport models at the conclusion of 24 hours..... | 83 |
| Figure 3-8. Comparison of the normalised drug concentration contours obtained with various drug transport models..... | 84 |
| Figure 4-1. Schematic of the acrylic flow rig assembly (a) and the equipment used to monitor the drug uptake within the channel (b). Image copyright of O'Brien et al. [76] and modified with permission..... | 89 |
| Figure 4-2. Close-up of the hydrogel recess and the acrylic blocks that are used to clamp the strut onto the hydrogel..... | 90 |
| Figure 4-3. Hydrogel dimensions..... | 93 |
| Figure 4-4. Strut dimensions..... | 94 |
| Figure 4-5. 'Side-Bi-Side' diffusion cell schematic. | 96 |
| Figure 4-6. The plate readings of the standard dilutions revealed a linear relationship between the intensity of the emitted light and the concentration of Rhodamine B within each sample. | 100 |
| Figure 4-7. Relationship between the proportion of Rhodamine B released from the PDMS/Rhodamine B membrane and the square-root of the time of elution. | 101 |
| Figure 4-8. Relationship between the concentration of Rhodamine B in the receptor cell and the time of elution through a cell strainer membrane. | 102 |

| | |
|---|-----|
| Figure 4-9. Relationship between the concentration of Rhodamine B in the recipient cell and the time of elution through a cell strainer membrane. | 105 |
| Figure 4-10. Schematic of the computational geometry and dimensions..... | 106 |
| Figure 4-11. Correlation between the pixel intensity and the concentration of Rhodamine B in glycerol-water solution. | 111 |
| Figure 4-12. Normalised fluorescent marker concentration on the top of the hydrogel at the completion of the 180 minute experiment, once the working fluid had been removed from the flow rig | 112 |
| Figure 4-13. The mean normalised concentration distribution of Rhodamine B atop the hydrogel during the 180 minute experiment. | 113 |
| Figure 4-14. Cross-sectional view of the marker concentrations within each hydrogel. The blood analogue fluid flowed from left to right in each case. | 114 |
| Figure 4-15. Computational results showing the normalised fluorescent marker concentration within the hydrogel at the culmination of 3 hours and 15 minutes... | 115 |
| Figure 5-1. Geometries and dimensions. | 120 |
| Figure 5-2. Velocity vector distributions in Model I..... | 128 |
| Figure 5-3. Velocity magnitude contour plot in Model II..... | 129 |
| Figure 5-4. Flow development and C_p distribution in Model III..... | 131 |
| Figure 5-5. Velocity magnitude and flow pathlines in three further malapposed strut geometries..... | 134 |
| Figure 5-6. The impact of stent malapposition on the haemodynamics and drug transport of stented arteries. | 136 |
| Figure 5-7. The impact of incomplete stent apposition on the area-weighted average concentration (AWAC) of drug in the arterial tissue. | 137 |

| | |
|--|-----|
| Figure 5-8. Contours of the nomalised drug concentration obtained with Model II. | 138 |
| Figure 5-9. Contours of the nomalised drug concentration obtained with Model III. | 139 |
| Figure 6-1. Geometry and Boundary Conditions..... | 142 |
| Figure 6-2. Magnetic flux density contours of the magnetic drug-eluting stent strut used in this study. | 147 |
| Figure 6-3. The magnetically-altered haemodynamics of oxygenated blood in a vessel with a well-apposed drug-eluting stent strut..... | 149 |
| Figure 6-4. The magnetically-altered haemodynamics of deoxygenated blood in a vessel with a well-apposed drug-eluting stent strut..... | 150 |
| Figure 7-1. A non-streamlined, square profile strut geometry (a) is contrasted with a streamlined, semicircular profile strut geometry (b) in this study. | 154 |
| Figure 7-2. Three stented renal artery geometries were used in this study in conjunction with the two strut profile geometries shown earlier..... | 156 |
| Figure 7-3. The impact of strut profile shape on the flow and drug transport from well-apposed and malapposed struts. | 163 |
| Figure 7-4. The impact of strut profile geometry on the wall shear stresses acting on the arterial tissue near the stent strut. | 165 |
| Figure 7-5. The impact of strut profile shape on the wall shear stresses acting on the strut. Whereas high wall shear stresses (>6 Pa) occur around the top corners of Strut Profile I, no such regions were observed with Strut Profile II in either Geometry I or Geometry II. | 165 |
| Figure 7-6. The extent of recirculation zones (red) is diminished by 86% when Strut Profile II is used in place of Strut Profile I. | 166 |

Figure 7-7. The extent of endothelial dysfunction-inducing low wall shear stresses (blue) and platelet-activating high wall shear stresses (red) is significantly reduced once a more streamlined strut profile geometry is used..... 167

Figure 7-8. The normalised drug concentration distribution within a cross section of the lumen and tissue domains after a total simulation time of 24 hours. 168

Figure 8-1. The absence of a drug coating along the top of the streamlined stent strut, combined with the reduced prevalence of endothelial dysfunction-inducing low wall shear stresses, is expected to promote endothelialisation. 178

Nomenclature

| | |
|----------------|--|
| a | Coefficient used to calculate α |
| A | Recirculation zone area, m ² |
| $A_{hydrogel}$ | Total open area of the hydrogel membrane, m ² |
| $A_{orifice}$ | Area of the orifice on the side of each side-by-side diffusion cell, m ² |
| $A_{strainer}$ | Total open area of the cell strainer membrane, m ² |
| AWAC | Area-weighted average concentration |
| b | Coefficient used to evaluate α |
| B | Magnetic flux density, T |
| B_x | The x-component of the magnetic flux density field, T |
| B_y | The y-component of the magnetic flux density field, T |
| c | Normalised drug concentration |
| C | Local drug concentration or local Rhodamine B concentration (in Chapter 4 only), kg/m ³ |
| C_0 | Initial drug concentration at the strut surfaces, kg/m ³ |

| | |
|----------------|---|
| C_{do} | Initial concentration of Rhodamine B within the donor side-bi-side diffusion cell, kg/m ³ |
| CFD | Computational fluid dynamics |
| c_N | Normalised drug concentration achieved using the Newtonian model |
| c_{NN} | Normalised drug concentration achieved with a non-Newtonian model |
| c_P | Coefficient of pressure |
| C_{sample} | Concentrations of Rhodamine B within samples obtained from the recipient Side-Bi-Side diffusion cell, kg/m ³ |
| D_c | Diffusivity of paclitaxel in the stent coating |
| D_{fluid} | Diffusion coefficient of Rhodamine B in a glycerol-water solution, m ² /s |
| D_h | Hydraulic diameter of a square cross-section flow channel, m |
| $D_{hydrogel}$ | Diffusion coefficient of Rhodamine B in a PVA hydrogel, m ² /s |
| D_l | Diffusivity of paclitaxel in the blood in the arterial lumen, m ² /s |
| D_{strut} | Diffusion coefficient of Rhodamine B in a PDMS strut, m ² /s |
| D_t | Diffusivity of paclitaxel in the tissue |
| E | Electric field intensity, V/m |

| | |
|--------------|---|
| f_{coarse} | Coarse-grid solution |
| f_{fine} | Fine-grid solution |
| F^L | Lorentz force, N/m ³ |
| F^M | Magnetization force, N/m ³ |
| GCI | Grid convergence index |
| h | Half-height of an infinitely-long permanent rectangular magnet, m |
| H | Magnetic field intensity, A/m |
| H_{ct} | Haematocrit |
| ICEMA | Isocyanatoethylmethacrylate |
| I_D | Non-Newtonian drug concentration difference factor |
| I_L | Local non-Newtonian importance factor |
| J | Total current density, A/m ² |
| K | Boltzmann's constant, J/K |
| L_c | Coating thickness, m |
| L_{distal} | Length of the distal recirculation zone, mm |
| L_e | Entrance length, mm |

| | |
|-------------------|--|
| LIF | Laser-Induced Fluorescence |
| $L_{inter-strut}$ | Inter-strut distance, mm |
| $L_{proximal}$ | Length of the proximal recirculation zone, mm |
| \dot{m} | Mass flux of the drug species, kg/m ² s |
| M | Magnetization of blood, A/m |
| M_0 | Amount of solute initially found within a representative volume of Rhodamine B/PDMS film, kg |
| M_S | Magnetization of magnet, A/m |
| M_t | Amount of solute released into a ‘Side-Bi-Side’ diffusion cell chamber, kg |
| n | Direction normal to the arterial wall normalised by the inter-strut distance |
| N | Direction normal to the arterial wall, mm |
| p | Order of accuracy of the solution |
| P | Thermodynamic pressure, Pa |
| PDMS | Polydimethylsiloxane |
| PVA | Poly-(vinyl alcohol) |

| | |
|--------------------|---|
| Q | Volumetric flow rate, mL/s |
| Q_{high} | High volumetric flow rate, mL/s |
| Q_{low} | Low volumetric flow rate, mL/s |
| Q_{mean} | Mean volumetric flow rate, mL/s |
| r | Refinement factor |
| R | The molecular radius of Rhodamine B, m |
| Re | Reynolds number |
| Re^* | Reynolds number based on the width of a square cylinder |
| t | Time, s |
| T | Experimental temperature, °C or K |
| $t_{release}$ | Desired duration of drug release, s |
| V | Velocity vector of blood or blood analogue fluid, m/s |
| \bar{V} | Mean fluid velocity, m/s |
| \bar{V}_{∞} | Mean freestream velocity, m/s |
| V_{cell} | Volume of fluid within the recipient diffusion cell, m ³ |
| V_{strut} | Representative volume of Rhodamine B/PDMS film, m ³ |

| | |
|---------------------|---|
| V_x | Horizontal component of the fluid velocity at a grid cell, m/s |
| V_y | Vertical component of the fluid velocity at a grid cell, m/s |
| w | Half-width of an infinitely-long permanent rectangular magnet, m |
| WSS | Wall shear stress, Pa |
| ∇ | Gradient operator, m^{-1} |
| Δt | Time-step size, s |
| Δx | Horizontal dimension of a grid cell, m |
| Δy | Vertical dimension of a grid cell, m |
| α | Weighting factor used to calculate dynamic viscosity of glycerol-water solution |
| δ | Degree of stent malapposition, μm |
| $\delta_{hydrogel}$ | Thickness of a hydrogel membrane used to determine $D_{hydrogel}$, m. |
| δ_{max} | Maximum degree of stent malapposition, μm |
| $\delta_{strainer}$ | Thickness of a cell-strainer membrane used to determine D_{fluid} , m. |
| δ_{strut} | Half of the thickness of a Rhodamine B/PDMS film used to determine D_{strut} , m. |

| | |
|-----------------------|--|
| $\epsilon_{strainer}$ | Porosity of the cell-strainer membrane |
| γ | Weight fraction of glycerol in glycerol-water solution |
| $\dot{\gamma}$ | Shear strain rate, s^{-1} |
| λ | Wavelength of light generated by a mercury arc-discharge lamp, nm |
| μ | Dynamic viscosity of blood, $Pa \cdot s$ |
| $\bar{\mu}$ | Normalised mean viscosity |
| μ_0 | Permeability of free space, H/m |
| μ_g | Viscosity of glycerol, $Pa \cdot s$ |
| μ_{gw} | Viscosity of glycerol-water solution, $Pa \cdot s$ |
| μ_N | Dynamic viscosity of the Newtonian blood rheological model, $Pa \cdot s$ |
| μ_w | Viscosity of water, $Pa \cdot s$ |
| ν | Kinematic viscosity, m^2/s |
| ρ | Blood density, kg/m^3 |
| ρ_g | Density of glycerol, kg/m^3 |
| ρ_{gw} | Density of glycerol-water solution, kg/m^3 |
| ρ_w | Density of water, kg/m^3 |

| | |
|-----------------|---|
| σ | Electrical conductivity of blood, S/m |
| Φ | Electric potential field, V |
| χ | Magnetic susceptibility of blood |
| χ_{deoxyg} | Magnetic susceptibility of deoxygenated blood |
| χ_{oxyg} | Magnetic susceptibility of oxygenated blood |

Chapter 1

Introduction

1.1 The Emergence of Drug-Eluting Stents

1.1.1 Atherosclerosis

Atherosclerosis is a progressive disorder in which hard structures known as plaques accumulate on the inner walls of arteries. Plaques consist of cells (inflammatory and immune cells, endothelial cells and smooth muscle cells), lipids, connective tissues and debris. The progression of plaques over several decades can result in an abnormal narrowing, or stenosis, as may be seen in Figure 1-1. Blood flow at these stenosis sites is compromised, limiting the transport of oxygen, carbon dioxide and nutrients to organs and other parts of the body.

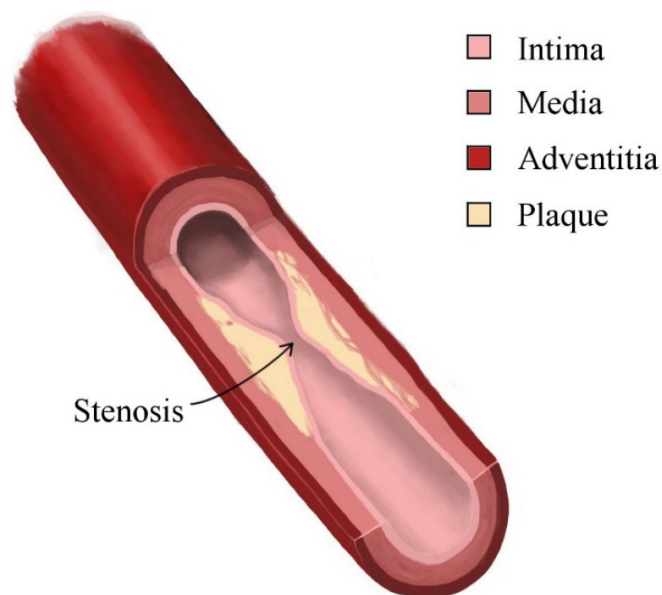


Figure 1-1. An artery with a stenosis.

This deprivation of blood flow can occur within any medium or large-sized artery and has potentially fatal consequences [1]. Atherosclerosis within the coronary arteries which supply blood to the heart is the primary cause of coronary artery

disease; this disease can culminate in angina (chest pain) or a myocardial infarction (heart attack), and is the leading cause of death in Australia, claiming 19,766 lives in 2013 alone [2]. When atherosclerosis afflicts the carotid arteries in the neck which supply blood to the brain, it manifests as carotid artery disease; this is the primary cause of strokes [3], which caused 8,304 fatalities in Australia in 2010 [4].

Atherosclerosis can also occur within the arteries which supply oxygen-rich blood to the legs, arms and pelvis (peripheral artery disease), as well as the renal arteries which supply blood to the kidneys (chronic kidney disease). Cumulatively, atherosclerosis became responsible for approximately 50% of deaths in industrialised nations by the start of the 21st century [5].

1.1.2 Angioplasty

In order to alleviate this burden, several methods have been proposed to restore blood flow at atherosclerosis sites [6]: a) angiogenesis (use of a laser catheter or gene therapy to promote the growth of small new vessels which bypass the blockage); b) angioplasty (compression of plaque through the insertion and expansion of a balloon catheter, as shown in Figure 1-2); c) atherectomy (removal of plaque using a catheter-based device); d) brachytherapy (delivery of gamma or beta radiation to the diseased sites), and; e) bypass grafting (providing an alternative route for blood flow around the blockage). Of these methods, angioplasty and bypass grafting are the most used for treating atherosclerosis [6,7]; however, unlike bypass grafting, whose hospitalisation can last over 14 days [8], most angioplasty patients can be discharged from the hospital in the morning after the operation and resume normal activities within a week [7].

Balloon Angioplasty

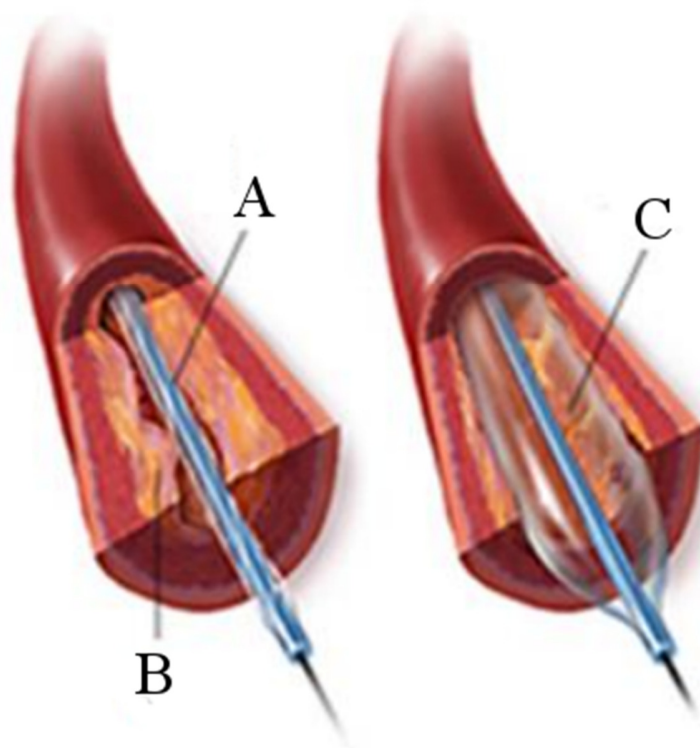


Figure 1-2. Balloon angioplasty involves the insertion of a balloon-tipped catheter (A) into a section of artery that is occluded by plaque (B). The expansion of the balloon (C) compresses the plaque against the artery wall. Blood flow through the artery is restored upon removal of the catheter. Images copyright of Medmovie [9] and modified with permission.

This association with shorter hospital stays and recovery times facilitated a steady increase in the popularity of angioplasty since the introduction of coronary angioplasty in the 1970s. In 2002, coronary angioplasty exceeded coronary artery bypass grafting in terms of the number of procedures performed annually in the

United States (657,000 vs. 515,000 respectively) [10]. The use of angioplasty has now also been extended to allow the treatment of carotid, renal, iliac, femoral, tibio-peroneal, subclavian, and other artery stenoses [11]. However, this expanded clinical use has also revealed a limitation in the form of a disease known as restenosis.

Restenosis is the recurrence of stenosis following intervention and typically occurs within 6 months of the initial procedure. Its diagnostic threshold is usually defined as being when the diameter of the lumen (the interior space of the artery through which blood flows) is decreased by more than 50% of the adjoining, healthy, sections of the vessel. As coronary angioplasty became widely adopted in the 1980s, restenosis was reported in up to 60% of patients [12-14].

There are three main mechanisms which underlie restenosis following angioplasty [15-17]: a) elastic recoil of the vessel wall; b) negative remodelling, and; c) neointimal hyperplasia. Elastic recoil occurs within 24 hours of balloon expansion and is a response to overstretching of the vessel wall. Negative remodelling is a reduction of the circumferential dimension of the entire artery [18] and is a compensatory reaction to injury, cellular proliferation and mechanical stresses imparted by blood flow [16]. Finally, neointimal hyperplasia is a proliferative response to injury whereby vascular smooth muscle cells and extracellular matrix accumulate to form a new inner layer, or neointima, within the arterial wall [19]. Unlike elastic recoil, negative remodelling and neointimal hyperplasia typically manifest weeks to months after balloon expansion. Intravascular ultrasound studies have shown that 60-80% of late lumen losses following angioplasty are due to negative remodelling, whilst the remaining 20-40% are due to neointimal hyperplasia [16]. These restenosis mechanisms may be seen in Figure 1-3.

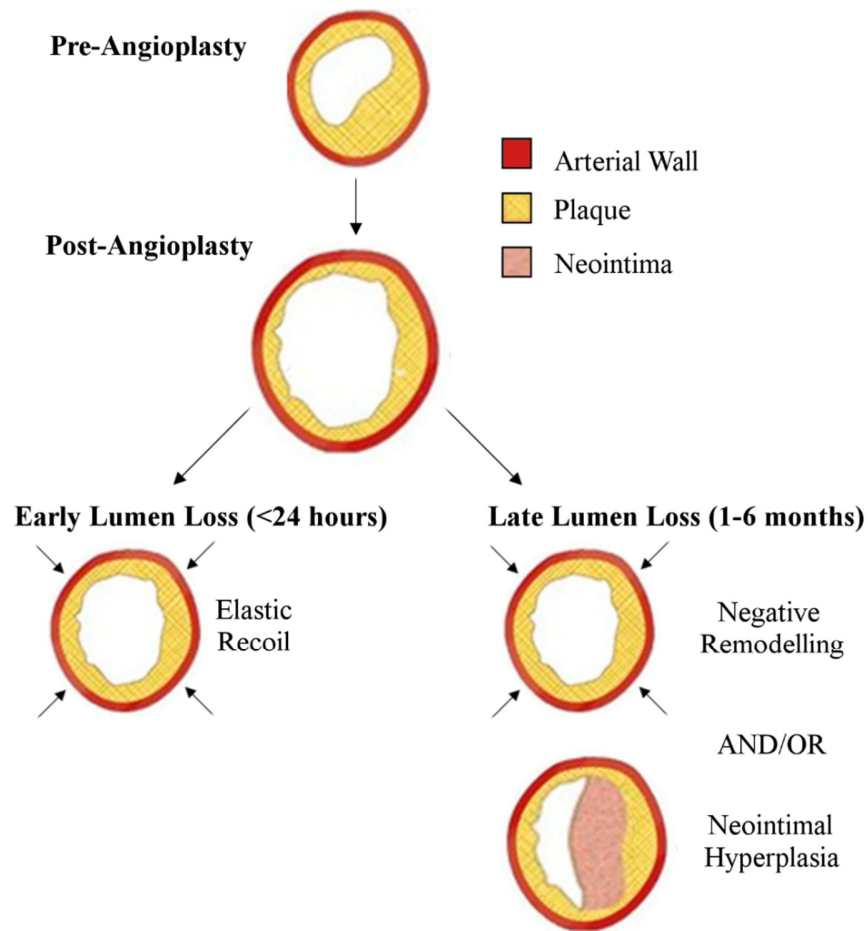


Figure 1-3. Mechanisms of Restenosis. Elastic recoil and negative remodelling are characterised by the contraction of the pre-existing wall mass, whilst neointimal hyperplasia is characterised by the accumulation of new arterial wall mass (neointima). Elastic recoil transpires within 24 hours of balloon expansion. Restenosis can also occur weeks to months after balloon expansion in the forms of negative remodelling and/or neointimal hyperplasia. Modified from Rajagopal and Rockson [20]. Copyright permission for reuse in this thesis has been obtained from *The American Journal of Medicine*. RightsLink License Number: 4200120240600.

1.1.3 Bare-Metal Stents

Restenosis rates steadily decreased because of improvements in physician experience, equipment and imaging, and patient lesion selection; however, a major breakthrough was not realised until the introduction of bare-metal stents in 1994 [19]. These

devices are small, metallic, wire-mesh tubes that are pre-loaded in a collapsed form onto a balloon catheter, fed through to the stenosis site and expanded, as shown in Figure 1-4. Once expanded, the stent acts as a mechanical scaffold which mitigates elastic recoil of the vessel and facilitates a larger post-procedural lumen diameter than angioplasty alone [19]. Bare-metal stents also restrict negative remodelling, despite causing more neointimal hyperplasia than angioplasty alone [21-23]. Serruys et al. showed that stenting reduced rates of coronary restenosis from 32% to 22% [24] and Fischman et al. showed that these rates reduced from 42% to 32% [25].

Stent Implantation

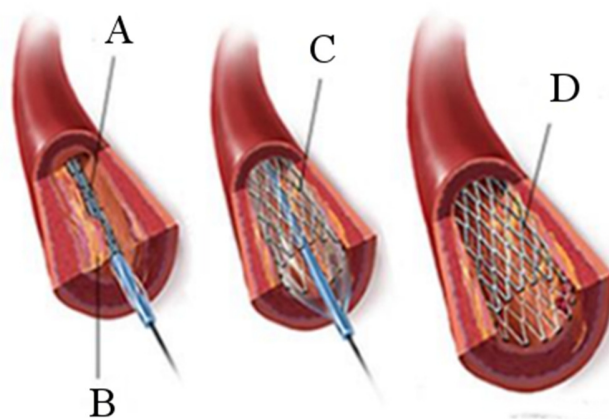


Figure 1-4. Bare-metal stent implantation within an occluded artery. A balloon-tipped catheter and stent (A) are fed through to the stenosis site (B). Inflation of the balloon results in the expansion of the stent and the arterial lumen alike (C). The deployed stent (D) is left within the artery to mitigate the risk of elastic recoil and negative remodelling. Images copyright of Medmovie [9] and modified with permission.

This ‘in-stent’ restenosis differs from restenosis following angioplasty in that it is primarily caused by neointimal hyperplasia as opposed to negative remodelling or elastic recoil. Neointimal hyperplasia in stented vessels may be caused by:

a) vascular trauma resulting from stent expansion, known as “overstretch

injury” [26]; b) the complex interactions between blood, the vessel wall and the metallic surface of the stent, which can affect the adsorption of plasma proteins and generate an inflammatory response [27]; and c) the alterations of blood flow due to the obstructing presence of the stent struts, which modify the mechanical stresses imparted on the endothelial cells which line the inner walls of arteries. An example of a stented vessel that has succumbed to in-stent restenosis caused by neointimal hyperplasia may be seen in Figure 1-5.

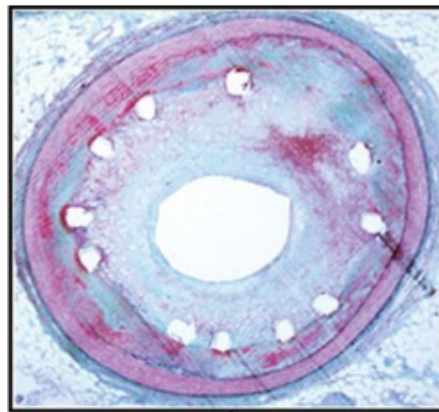


Figure 1-5. Photomicrograph representing the cross-sectional histology of an artery that has succumbed to in-stent restenosis caused by neointimal hyperplasia. The small, white spaces within the artery are the locations in which a stent strut was present. Taken from Nakano et al. [28]. Copyright permission for reuse in this thesis has been obtained from *European Heart Journal*. RightsLink License Number: 4202491244949.

1.1.4 Drug-Eluting Stents

Although in-stent restenosis rates were smaller than the restenosis rates associated with balloon angioplasty, the growing use of bare-metal stents resulted in an increased global burden of restenosis [19]. In an effort to alleviate this burden, intense work on stent development led to the introduction of drug-eluting stents. The Cypher Sirolimus-eluting stent (Cordis Corporation, Miami Lakes, FL, USA) and the TAXUS Express Paclitaxel-eluting stent (Boston Scientific, Natick, MA,

USA) became the first drug-eluting stents approved by the Food and Drug Administration for clinical use in 2003 and 2004 respectively. These devices were built upon their manufacturers' respective bare-metal stent, namely Cordis Corporation's Bx Velocity and Boston Scientific's Express platform. However, unlike these bare-metal stents, drug-eluting stents also feature a therapeutic drug housed within a polymer coating, as shown in Figure 1-6. These drugs reduce smooth muscle cell proliferation whilst the polymer coating regulates the rate of release of the drug.

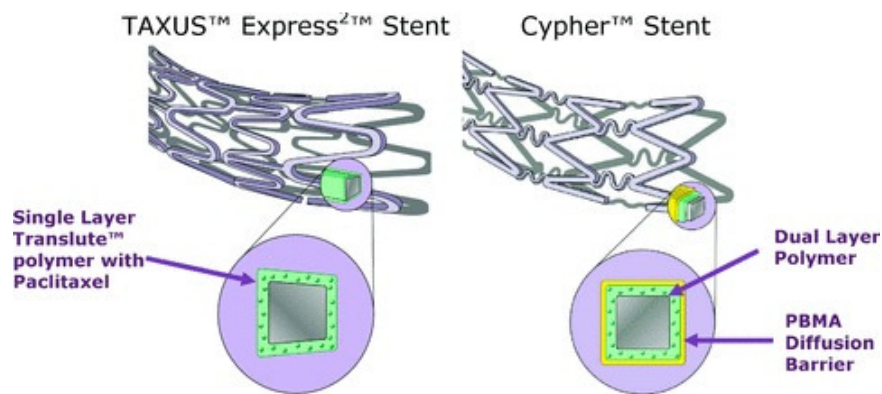


Figure 1-6. First generation drug-eluting stents. A therapeutic drug reduces neointimal hyperplasia whilst a polymer coating regulates the release of this drug. Taken from Pendyala et al. [29]. Copyright permission for reuse in this thesis has been obtained from *Journal of Interventional Cardiology*. RightsLink License Number: 4203660225959.

The elution of drug from these coatings into arterial tissue resulted in the reduced prevalence of neointimal hyperplasia and thus reduced the prevalence of in-stent restenosis. Whereas bare-metal stents were associated with in-stent restenosis rates of 20-50%, drug-eluting stents reduced these values to 3-20% [30-32]. This sparked enthusiasm for their further use and led to almost 90% of all stent patients receiving drug-eluting stents over bare-metal stents by the year 2006 [10].

1.2 The Limitations of Drug-Eluting Stents

Although drug-eluting stents have significantly reduced in-stent restenosis rates and the need for repeat intervention, limitations are still present. In-stent restenosis persists and its prevalence is non-negligible because of the widespread use of drug-eluting stents. Furthermore, the long-term safety of these devices has been brought into question because of studies which suggested that the window of thrombotic risk extends well beyond that of bare-metal stents [33,34].

Stent thrombosis is a rare condition in which blood clots form within stented arteries, potentially resulting in the reduction or total blockage of arterial blood flow. An example of an artery that has succumbed to stent thrombosis may be seen in Figure 1-7. This disease can occur over a wide range of time scales following stent implantation, with cases of acute (occurring in less than 24 hours), sub-acute (less than 30 days), late (greater than 30 days) and very late (greater than 12 months) stent thrombosis each documented.

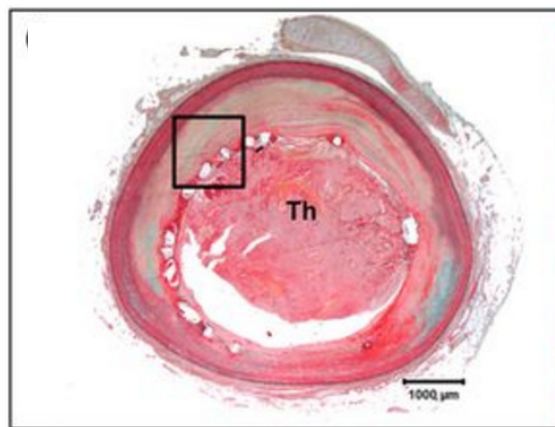


Figure 1-7. Histological section of an artery that has succumbed to stent thrombosis. The white spaces within the black square are the locations in which a stent strut was present, whilst 'Th' denotes the location of the thrombus. Taken from Byrne et al. [135]. Copyright permission for reuse in this thesis has been obtained from *European Heart Journal*. RightsLink License Number: 4202491383371.

The reported rates of late stent thrombosis are similar for both drug-eluting and bare-metal stents, at up to 0.7% [33,36,37] and 0.8% [36,38-40] respectively; however, drug-eluting stent late stent thrombosis has been associated with mortality rates as high as 45% [33,41], much higher than the rates of up to 20.8% associated with bare-metal stent late stent thrombosis [22,39]. Furthermore, the risk of very late stent thrombosis is greater for drug-eluting stents, with incidence rates of 0.6% and 0.7% in sirolimus and paclitaxel-eluting stents respectively in the 1-4 years following implantation [42]. In contrast, stent thrombosis only occurred in up to 0.2% of bare-metal stent patients during the same time period.

These discrepancies may arise due to the delayed arterial healing phenomenon that has been linked to drug-eluting stent use. Specifically, fibrin – a fibrous protein involved in the clotting of blood – has been shown to persist upwards of 8 months after drug-eluting stent implantation [43]. Furthermore, human necroscopy studies have shown that drug-eluting stents may not be fully covered by anticoagulant-expressing endothelial cells even years after implantation [44-46]. In contrast, bare metal stents show very little fibrin deposition more than 30 days after implantation [45] and are almost totally covered by endothelial cells 3-4 months after stent implantation [38,47]. Delayed arterial healing, in the form of peristrent fibrin deposition and incomplete endothelialisation, has been identified as the primary pathological substrate underlying late stent thrombosis [45].

Other factors – including patient, stent and procedural factors – have also been shown to promote stent thrombosis, as may be seen in Table 1-1. However, late stent thrombosis, like in-stent restenosis, may also be promoted by the non-physiological haemodynamics of stented vessels, in conjunction with these established

factors. The relationship between these factors and these non-physiological haemodynamics may also be seen in Table 1-1.

Table 1-1. Risk factors of late stent thrombosis and their potential haemodynamic impact. Modified from Koskinas et al. [49]. Copyright permission for reuse in this thesis has been obtained from *Journal of American College of Cardiology*. RightsLink License Number: 4200190643539.

| <i>Risk Factors</i> | <i>Haemodynamic Impact</i> |
|---|---|
| <i>Patient Factors</i> | |
| <i>Diabetes</i> | |
| <i>Advanced age</i> | |
| <i>Renal failure</i> | |
| <i>Low ejection fraction</i> | |
| <i>Acute coronary syndrome</i> | |
| <i>Premature antiplatelet therapy cessation</i> | |
| <i>Clopidogrel resistance</i> | |
| <i>Hypersensitivity to the drug or polymer</i> | |
| <i>Stent Factors</i> | |
| <i>Incomplete endothelialisation</i> | → Attenuation of physiologic wall shear stress-induced endothelial production of prostacyclin I ₂ , tissue plasminogen activator, and endothelial nitric oxide |
| <i>Stent strut and polymer thickness</i> | → Greater flow disturbances from thicker struts/polymer → low wall shear stresses |
| <i>Procedural Factors</i> | |
| <i>Bifurcation stenting</i> | → Adverse haemodynamic impact on the inherently complex wall shear stress environment |
| <i>Lesion complexity</i> | |
| <i>Multivessel disease</i> | |
| <i>Excessive stent length</i> | |
| <i>Incomplete stent apposition</i> | → Gaps between stent struts and the arterial wall → increased flow resistance → low wall shear stresses |
| <i>Overlapping stents</i> | → Greater flow disturbances → low wall shear stresses |
| <i>Expansive vascular remodelling</i> | → Reduced flow rate → low wall shear stresses |

1.3 The Adverse Haemodynamics of Drug-Eluting Stents

Stents

In arteries, blood flow exerts two types of stress on the arterial wall, which may be seen in Figure 1-8. Blood pressure is the force per unit area that acts perpendicular to an artery wall and is responsible for its cyclic extension and distension. Wall shear stresses, however, act at a tangent to the inner lining of the vessel wall and are the result of a “frictional” resistance caused by the viscous drag of blood against the wall. There is another important haemodynamic stress that is induced by the blood pressure, a circumferential stress known as the hoop stress, that can result in injury to the arterial wall. However, the primary focus of this thesis is to alleviate adverse fluid motions; hence, it was deemed to be out of the thesis’ scope to investigate this induced stress.

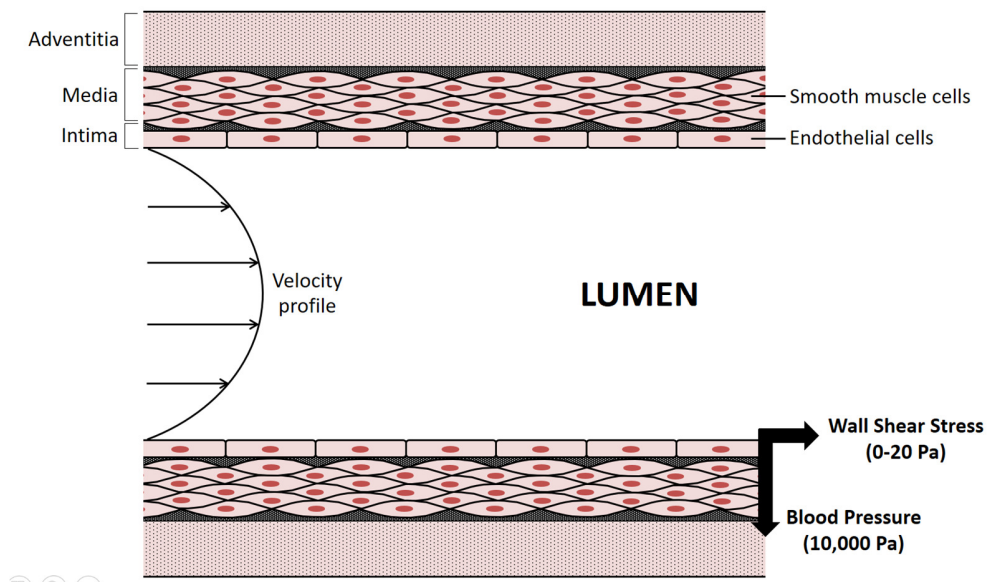


Figure 1-8. A diagram showing the two haemodynamic forces experienced in blood vessels. Wall shear stress and blood pressure values obtained from Hoskins and Hardman [48].

Blood pressure is by far the greater of the two stresses in Figure 1-8 in terms of magnitude, with the typical blood pressure of a healthy artery being approximately 10,000 Pa [48]. In contrast, the wall shear stresses in a healthy artery tend to fluctuate between just 0-20 Pa [48]. However, it is these relatively weak wall shear stresses which have been linked to the promotion of stent thrombosis and in-stent restenosis [49].

Non-physiological wall shear stresses arise due to the obstructing presence of the stent struts, as may be seen in Figure 1-9. The non-streamlined shape of commercial stent struts promotes flow separation, resulting in the development of recirculation zones proximal and distal to the struts [50]. These regions have been shown experimentally and numerically to correlate with regions of low wall shear stress, whilst high wall shear stresses are found over the surface of the struts [50,51].

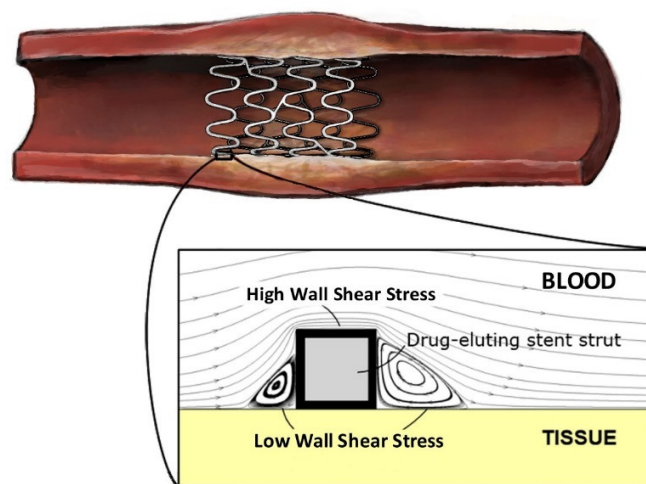


Figure 1-9. The presence of drug-eluting stents establishes localised regions of recirculating flow adjacent to the stent struts. These recirculation zones correlate with regions of low wall shear stress. Additionally, high wall shear stresses are found over the surface of the struts.

1.3.1 Haemodynamics and In-Stent Restenosis

Clinical and animal studies have consistently shown that low wall shear stresses correlate with the development of neointimal hyperplasia [52-56]. Low wall shear stresses (<0.5 Pa) affect the shape and alignment of endothelial cells [57], enhancing their permeability. This endothelial dysfunction allows underlying smooth muscle cells to proliferate and migrate from the media into the intima, as visualised in Figure 1-10.

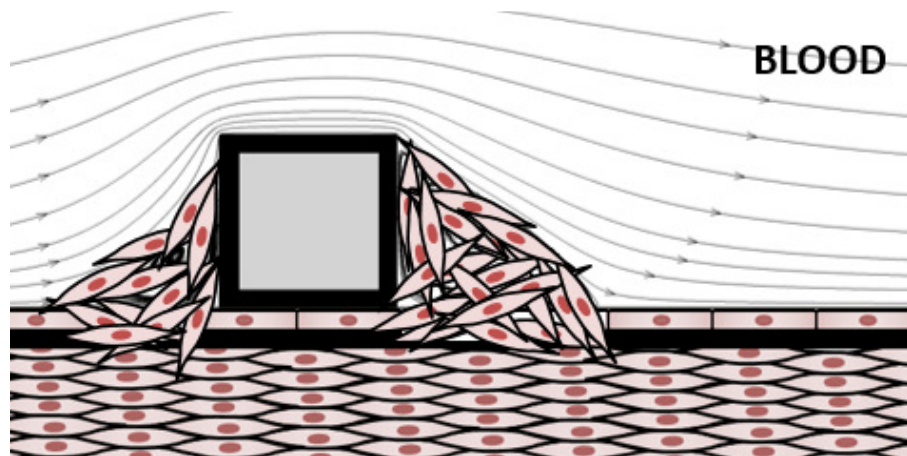


Figure 1-10. Endothelial dysfunction caused by low wall shear stresses promotes smooth muscle cell proliferation and migration.

Furthermore, in arteries with drug-eluting stents, re-endothelialisation is retarded pharmacologically [38,44,45,58], with the result that low wall shear stresses may act on shear-sensing smooth muscle cells directly via endothelium-independent mechanisms. In smooth, laminar flows, smooth muscle cell proliferation is inhibited through the reduced expression of platelet-derived growth factor from these cells, which enhances their proliferation. Additionally, these flows enhance the expression of transforming growth factor- β , which suppresses smooth muscle cell proliferation. In low shear stress environments, however, these vasculoprotective effects will not be

present; hence, smooth muscle cell proliferation is promoted in these regions, independently of the presence of an endothelium [59].

However, the relationship between low wall shear stresses and in-stent restenosis is complicated in drug-eluting stents by the antagonistic effects of flow-mediated drug transport. Specifically, past numerical studies have shown that vast quantities of drug accumulate within the recirculation zones adjacent to drug-eluting stent struts, as depicted in Figure 1-11.

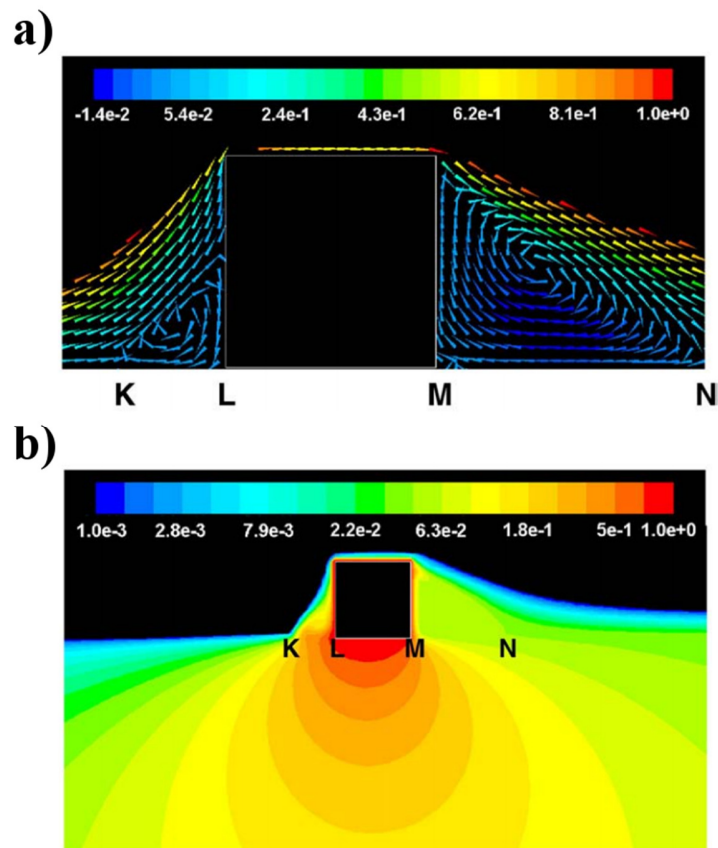


Figure 1-11. Flow-mediated drug transport. a) Recirculation zones, which form upstream and downstream of stent struts, allow the eluted drug matter to form drug pools of high concentration. b) The drug that accumulates in these recirculation zones can subsequently infiltrate the arterial tissue and serve as a secondary means of arterial drug uptake. Taken from Kolachalama et al. [60]. Copyright permission for reuse in this thesis has been obtained from *Journal of Controlled Release*. RightsLink License Number: 4200180794092.

This drug can subsequently infiltrate into arterial tissue and serve as a secondary mode of drug uptake [60], and potentially ameliorate the restenotic risk associated with these recirculation zones. It has even been suggested that drug deposition occurs less via contact between the drug coating and the arterial wall than via flow-mediated means from non-contacting strut surfaces [61].

1.3.2 Haemodynamics and Stent Thrombosis

Unlike in-stent restenosis, which develops progressively, the sudden occurrence of stent thrombosis hampers its direct assessment with regards to non-physiological shear stresses. Clotting has been shown to occur preferentially at sites of delayed arterial healing which are localised with vortical flow structures [49,62]. Low wall shear stresses may promote late stent thrombosis by inhibiting the proliferation of anticoagulant-expressing endothelial cells and retarding the endothelialisation of arterial and strut surfaces [63]. High wall shear stresses over the strut corners may further promote late-stent thrombosis by activating platelets to release platelet-aggregating factors such as thromboxane A₂ and adenosine diphosphate.

The activated platelets can subsequently enter downstream separation zones, as shown in Figure 1-12, and reach high concentrations because of the recirculating nature of flow in these zones [49]. This aggregation of platelets, combined with the reduction of anticoagulant-expressing endothelial cells (de-endothelialisation) in low wall-shear stress regions, may trigger thrombus formation [49].

The link between adverse haemodynamics and stent thrombosis is particularly important in arteries with incomplete stent apposition. This phenomenon, also referred to as stent malapposition, occurs when at least part of one

strut is not in direct contact with the arterial wall. It has been found to be present in 77% of drug-eluting stent patients with very late stent thrombosis [64].

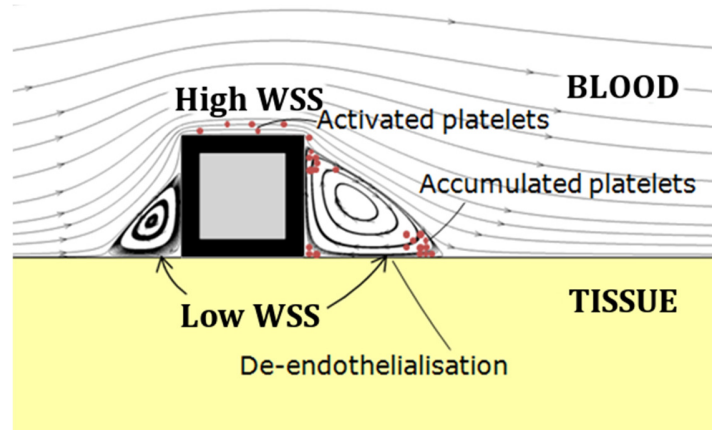


Figure 1-12. Platelets that are activated in regions with high wall shear stress (WSS) may subsequently accumulate in recirculation zones downstream of the stent struts. This aggregation, when combined with the reduced endothelial production of anticoagulants in low wall shear stress regions, can trigger thrombus formation.

As in the well-apposed strut in Figure 1-12, thrombosis in arteries undergoing stent malapposition may be linked to high shear stress-related platelet activation and endothelial dysfunction-inducing low wall shear stresses. These high wall shear stresses inhibit the formation of neointima [52] and have been shown to increase in magnitude and coverage as the degree of stent malapposition increases [65]. Both the higher wall shear stresses and the greater gap between the strut and the existing tissue can contribute towards the delayed coverage of malapposed struts by anticoagulant-expressing endothelial cells [65]. Platelets that are activated by exposure to these elevated wall shear stresses, or through contact with activated platelets or a dysfunctional endothelium, can then aggregate within downstream recirculation zones, as shown in Figure 1-13 [12]. This aggregation of platelets,

combined with the reduction of anticoagulant-expressing endothelial cells in low wall shear stress regions, can trigger thrombus formation.

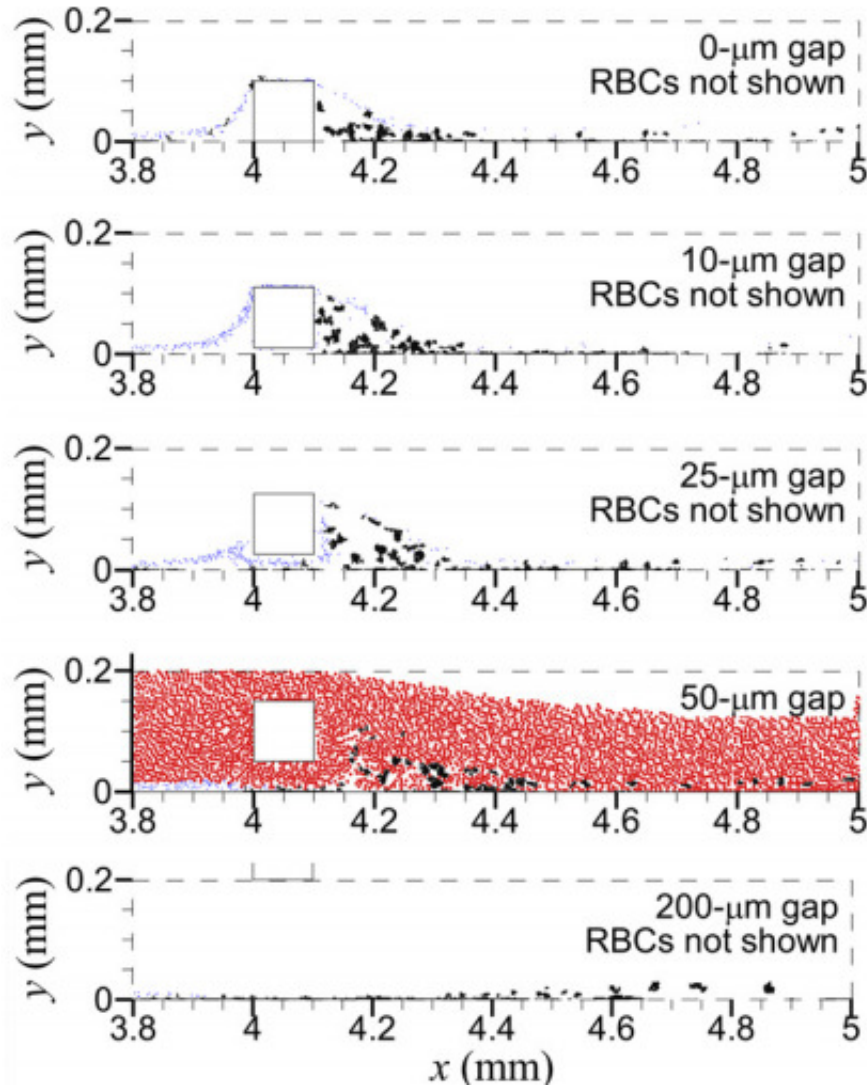


Figure 1-13. Locations of unactivated platelets (blue), activated platelets (black) and red blood cells (RBCs, red) after 1.58 seconds of simulating their transport, collision, activation, and adhesion and aggregation processes within coronary arteries featuring malapplied struts. A non-thrombogenic strut was assumed in this study, alongside a denuded endothelium and a platelet activation model that accounted for both the magnitude of and exposure time to shear stress. Taken from Chesnutt and Han [66].

Copyright permission for reuse in this thesis has been obtained from *Physical Biology*.

Copyright Clearance Center Confirmation Number: 11674622.

1.4 Modelling the Haemodynamics and Drug Transport of Stented Arteries

Although alleviating these adverse haemodynamics could result in improved drug-eluting stent safety, characterising the haemodynamics of stented arteries in-vivo has proven to be problematic. Ultrasound systems are only capable of measuring one velocity component and are therefore not well suited to studying the multi-directional flows of stented arteries [48]. Similarly, magnetic resonance imaging systems are hampered by low spatial and temporal resolutions, which limit the accuracy of wall shear stress measurements [67]. An alternative method of performing these haemodynamic studies is to simulate the blood flow numerically using computational fluid dynamics (CFD).

In recent years, CFD analyses have been used to non-intrusively provide an insight into the haemodynamic and drug transport environment of arteries treated with drug-eluting stents. It is important to ensure that blood is modelled accurately in these simulations because of: 1) the link between adverse haemodynamic phenomena and diseases such as in-stent restenosis and stent thrombosis [49], and; 2) the large quantities of drug which may be transported from stent surfaces into arterial tissue by luminal blood flow [61]. However, blood is a difficult fluid to model, owing to a combination of its shear-thinning non-Newtonian properties, its variability between individuals, its complex near-wall behaviour, and the pulsatile nature of its flow.

1.4.1 Modelling the Non-Newtonian Properties of Blood

Blood is a suspension of particles in an aqueous liquid medium known as plasma. The particles are comprised primarily of red blood cells, which take up approximately 97% of the total particulate volume, whilst the remaining 3% consist of white blood cells and platelets. The plasma which surrounds these particulates contains organic and inorganic salts, in addition to other small organic molecules. The total volume fraction of red blood cells in the blood is referred to as the hæmatocrit, and its value is around 40-45% for a typical, healthy human. In low strain rate flows ($<10 \text{ s}^{-1}$), red blood cells align together to form long chains known as rouleaux, as may be seen in Figure 1-14. Conversely, at high strain rates ($>200 \text{ s}^{-1}$), the cells separate and become aligned with the direction of blood flow. This causes a trend in which the apparent viscosity of blood decreases with increasing strain rate, which means that blood possesses shear-thinning non-Newtonian properties [68].

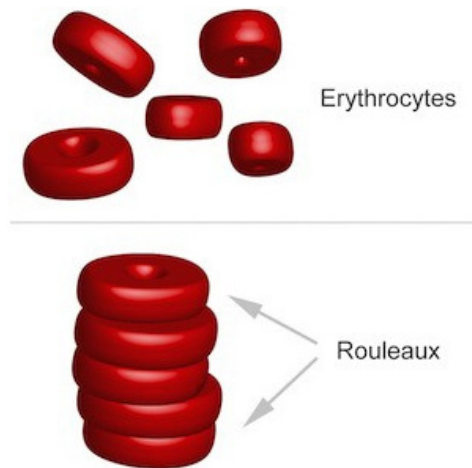


Figure 1-14. Long chains of red blood cells, known as rouleaux, form in regions of low strain rate. Conversely, at high strain rates, these cells separate and become aligned with the flow. This results in the apparent viscosity of blood decreasing as the strain rate increases, meaning that blood is a shear-thinning non-Newtonian fluid. Image copyright of ABC Corporation Bangladesh [69] and reused with permission.

Although blood is a non-Newtonian fluid, its flow in stented arteries has often been modelled numerically with a Newtonian blood model [61,70-73], meaning that its dynamic viscosity is assumed to be constant. Although this assumption greatly simplifies the modelling of blood, it has been found to only be acceptable in flows in which strain rates above 100s^{-1} are encountered [74]. Such strain rates are found in larger arteries and consequently some investigators have justified their assumption of blood being a Newtonian fluid by emphasising the large size of the arteries that they were modelling [70,72]. However, the separated flow regions that form proximal and distal to stent struts are characterised by low velocities, meaning that strain rates are modest in these separations. As non-Newtonian behaviour may significantly affect velocity distributions in these recirculation zones, it may also affect the rate at which drug is removed from the stent surface and convected by blood.

In order to capture the shear-thinning properties of blood, some computational studies of stented arteries [60,75,76] have implemented non-Newtonian blood rheological models [73,77-79]. Although each of these models has been created by parameter-fitting to experimental measurements of blood viscosity, they vary widely. Indeed, as shown in Figure 1-15, in some cases the prediction of blood viscosity at the same strain rate can differ by more than an order of magnitude. As blood viscosity not only differs significantly between males and females [80], but also between persons of the same sex [80], it is highly unlikely that any rheological model can be developed which would capture the highly variable properties of blood.

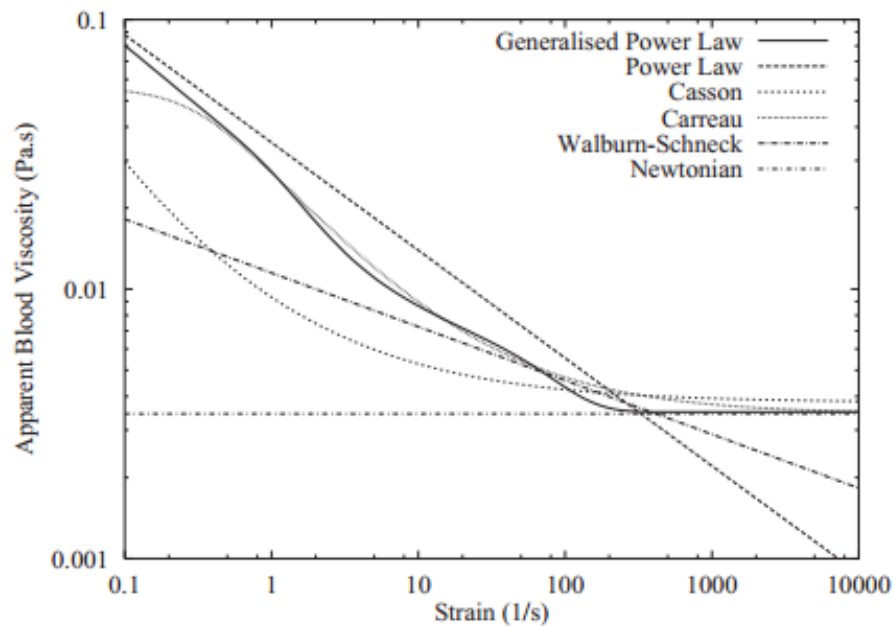


Figure 1-15. The viscosities predicted by the blood rheological models shown vary considerably at the same strain rates. Taken from Johnston et al. [81]. Copyright permission for reuse in this thesis has been obtained from *Journal of Biomechanics*. RightsLink License Number: 4200131112658.

1.4.2 Modelling the Individual Variations in Blood Behaviour

The primary causes of the individual variations in blood behaviour are variations in hæmatocrit [78]. Phillips et al. [70] showed that the hæmatocrit decreases significantly in the aftermath of the angioplasty procedures used in stent implantation, likely from blood loss and fluid resuscitation. They found that whereas the average hæmatocrit prior to the operation had been 40% in men and 38% in women, in the 12 hours following the procedure these values dropped to 34% and 33% respectively. The Carreau non-Newtonian blood rheological model has been utilised in some past numerical analyses of stented arteries [60,75] but unlike some other rheological models, such as the Walburn-Schneck and Casson models, it cannot simulate the effects of differences in hæmatocrit.

Hence, past analyses of steady-state drug deposition have not considered the effect of the reduced haematocrit on the resulting blood flow. It may be important to characterise these post-angioplasty reductions in haematocrit to better predict the early burst release of drug from strut coatings, which can take place within the first few days of stent implantation [6]. The burst release of Paclitaxel from the thermoplastic elastomer poly(styrene-b-isobutylene-b-styrene) (SIBS), the polymer carrier technology used on the TAXUS™ drug eluting stent, is shown in Figure 1-16.

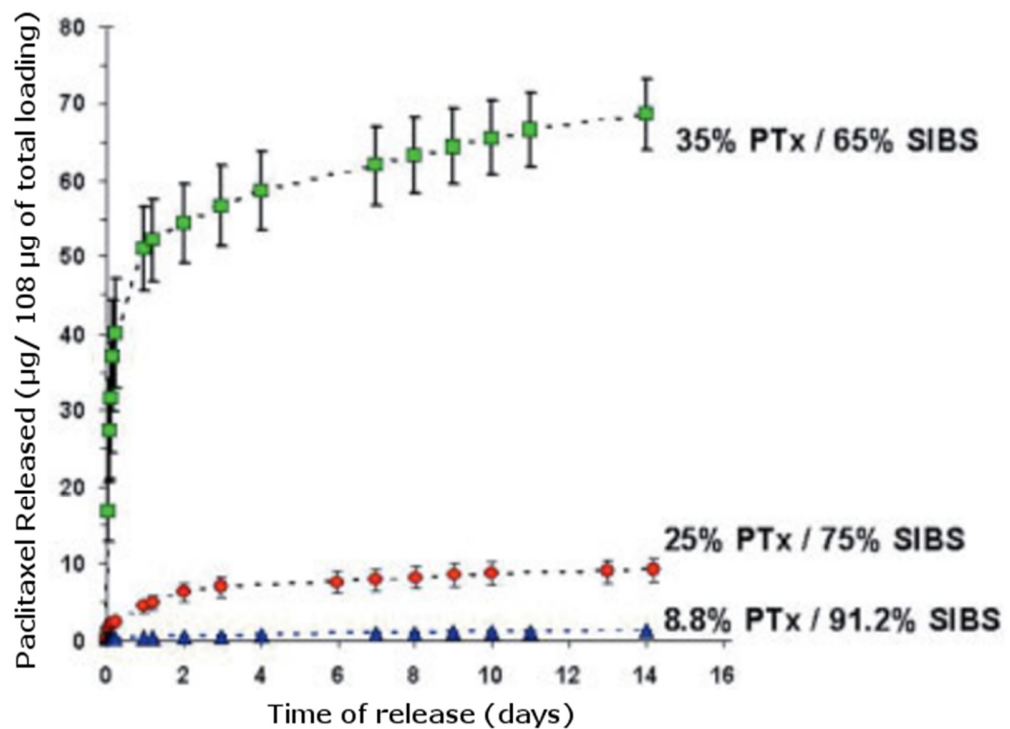


Figure 1-16. Burst release of Paclitaxel (PTx) from a poly(styrene-b-isobutylene-b-styrene) (SIBS) coating is believed to occur within two days of stent implantation. These in-vitro drug release profiles were obtained over 14 days in a phosphate buffered saline (PBS) Tween20 solution at 37°C. The SIBS polymer coatings contained 8.8, 25 and 35% (w/w) PTx. Modified from Renade et al. [82]. Copyright permission for reuse in this thesis has been obtained from *Journal of Biomedical Materials Research*. RightsLink License Number: 4203680145098.

1.4.3 Modelling the Near-Wall Behaviour of Blood

In addition to these non-Newtonian properties and individual variations, blood is also difficult to model due to its complex near-wall behaviour. Specifically, in steady, fully developed flow, red blood cells migrate towards the vessel axis, leaving a plasma-rich region near the walls which is relatively void of red blood cells [83]. This behaviour may be seen in Figure 1-17.

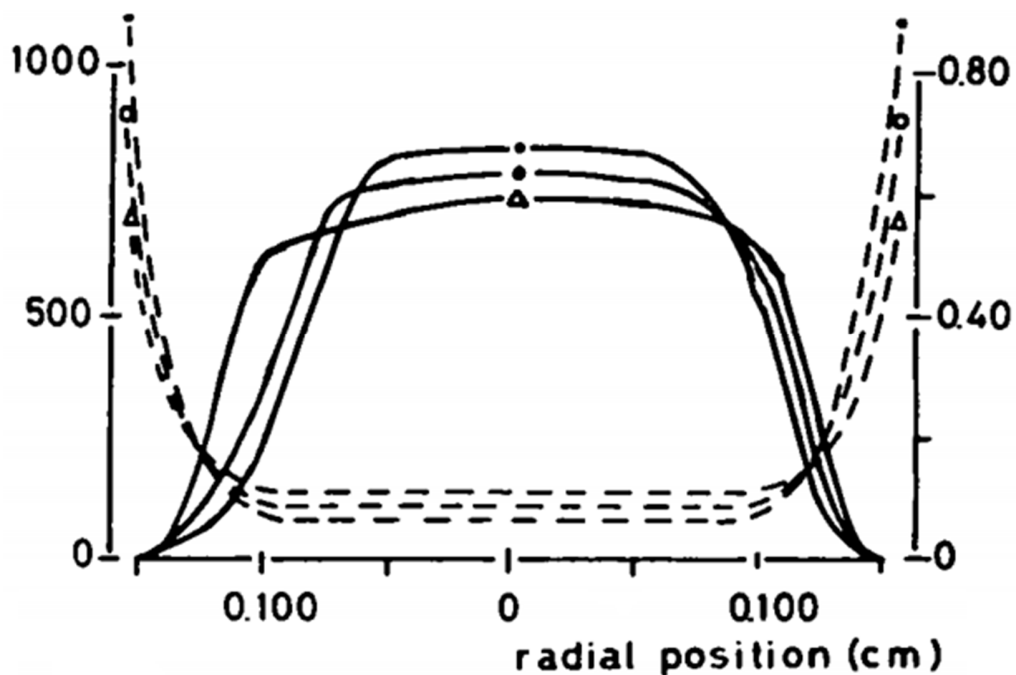


Figure 1-17. In steady, fully developed flow, red blood cells (—) migrate towards the centre of the vessel whilst platelets (- -) are displaced towards the vessel wall. These results were obtained with a haematocrit of 40% at wall shear rates of 1200 s⁻¹ (·), 760 s⁻¹ (•) and 240 s⁻¹ (Δ). Taken from Aarts et al. [83]. Copyright permission for reuse in this thesis has been obtained from *Arteriosclerosis, Thrombosis, and Vascular Biology*. RightsLink License Number: 4202490827951.

Prior numerical analyses have not taken this near-wall behaviour into consideration when investigating the drug transport of stented arteries. In order to study the full spectrum of rheological conditions achievable within the stented artery environment, it may be necessary to simulate the extreme cases of a boundary layer entirely depleted of red blood cells and a boundary layer rich in red blood cells. The fluid properties of plasma ($\rho = 1025 \text{ kg/m}^3$ and $\mu = 0.00122 \text{ Pa}\cdot\text{s}$ [84]) may be used to approximate the former case whilst non-Newtonian blood rheological models, such as those in Figure 1-15, may be used to represent the latter case.

1.4.4 Modelling the Pulsatility of Blood Flow

The pulsatility of blood flow further complicates the modelling of blood in stented arteries. This property has been shown to have minimal impact on the resulting drug distribution within a stented renal artery in both computational and in-vitro analyses [75]. Another study which compared Newtonian and non-Newtonian blood rheological models in a coronary artery model revealed just a 3.5% difference in average tissue drug concentration in steady flow conditions and even smaller differences in pulsatile flow conditions [60]. However, neither of these studies modelled the near-wall depletion of red blood cells when studying the impact of pulsatility on the drug transport of stented arteries. Furthermore, the diffusion of drug from the polymer coating was approximated in each of these numerical studies by assuming either a time-invariant, spatially uniform drug concentration [60] or an identical rate of drug depletion at each strut surface [75].

1.4.5 The Significance of Flow-Mediated Drug Transport

The assumption of a time-invariant, spatially uniform coating concentration has resulted in the assertion that flow-mediated drug transport is significant [61,60,85]. One study showed that almost 90% of the overall drug transport into the arterial tissue occurs from the stent surfaces that are not in contact with the tissue [61]. These results, shown in Figure 1-18, were also used to suggest that almost half of this deposition is contributed to from the top (adluminal) surface of the strut alone. It is not yet clear if this simplified drug transport model is valid; however, it is clear that this model is still being used in numerical studies [86,87].

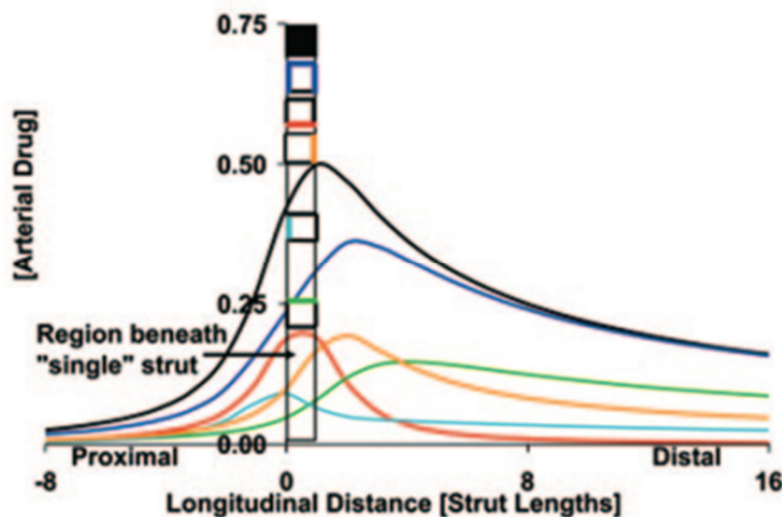


Figure 1-18. Drug concentration profiles obtained within a two-dimensional artery model featuring a single drug-eluting stent strut. These profiles were obtained at a depth of 1.5 strut lengths into the arterial tissue and are plotted as a function of axial distance along the tissue. The black line is the drug concentration profile obtained with a strut in which all strut surfaces possess a drug coating. Similarly, the dark blue line indicates the drug concentration profile obtained when the strut surface in contact with the tissue is not coated with drug but all other surfaces are coated. This study showed that the non-contacting surfaces of the strut yield almost 90% of the total drug uptake. Comparisons of the green and black lines also revealed that the top (adluminal) surface contributes about half of the total drug uptake alone. Taken from Balakrishnan et al. [61]. Copyright permission for reuse in this thesis has been obtained from *Circulation*.

RightsLink License Number: 4202490975741.

Another drug transport model has also been proposed in which the transient diffusion of drug within the polymer coating of drug-eluting stents is modelled [70,71]. Using this model, it was asserted that whilst the eluted drug preferentially deposits downstream of struts within the first 2 minutes of implantation, this distribution becomes more symmetric after 1 day [70]. Although the fractional drug release from the stent has been validated experimentally, the spatial distribution of drug within the tissue has not. Hence, a limitation of these models is a lack of validation of drug uptake characteristics, which in turn makes it difficult to assess the significance of flow-mediated drug transport.

1.4.6 Incomplete Stent Apposition

Similarly, it has been suggested that flow-mediated drug transport can yield high levels of drug uptake even in arteries with struts undergoing incomplete stent apposition. Past numerical studies of malapposed drug-eluting stent struts have been used to suggest that appreciable quantities of drug can be delivered into arterial tissue despite this lack of contact [61,75]. However, the diffusion of drug in these studies was simplified once again by the assumptions of a time-invariant, spatially uniform drug coating concentration [61] or an identical rate of drug depletion at each surface [75]. This flow-mediated drug transport from the malapposed strut may be seen in Figure 1-19.

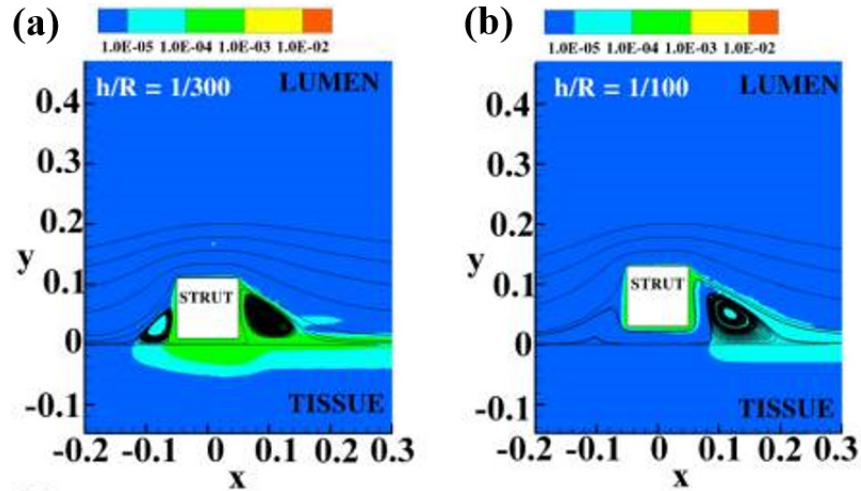


Figure 1-19. Numerical studies of malapposed drug-eluting stents showed that appreciable quantities of drug can be delivered into arterial tissue even when there is no direct contact between tissue and strut. However, these studies employed idealised drug transport models which did not factor in the non-uniform depletion of drug within the stent coating. Taken from O'Brien et al. [75]. Copyright permission for reuse in this thesis has been obtained from *Journal of Controlled Release*. RightsLink License Number: 4200120892194.

It may also be seen in this figure that the flow features surrounding malapposed struts are distinct from those surrounding struts that are in direct contact with the arterial tissue (well-apposed). Whereas well-apposed struts produce recirculation zones that remain attached to the strut, these zones detach from the strut at even mild degrees of malapposition, as shown in Figure 1-20 (10 μm gap). Furthermore, the proximal recirculation zone disappears whilst the distal zone increases in length at moderate malapposition distances (25 μm gap and 50 μm gap). Finally, at severe malapposition distances (200 μm gap), no recirculation zones are produced. Although this flow behaviour is well documented in two-dimensional computational fluid dynamics studies, it is not yet clear whether these features still transpire in three dimensional simulations. It is important to understand whether

and why these unique flow features actually transpire due to the aforementioned link between adverse haemodynamics and in-stent restenosis and stent thrombosis.

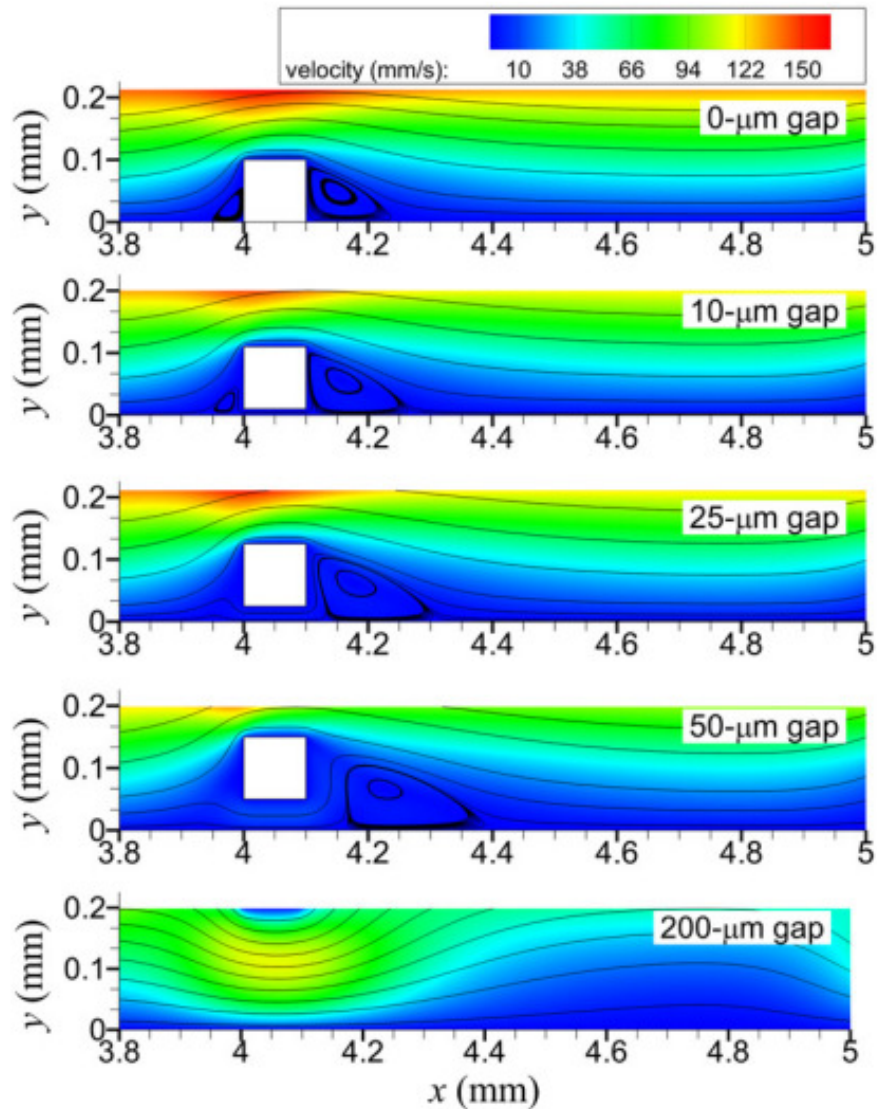


Figure 1-20. The impact of malposition distance on the flow in stented vessels. Whilst the recirculation zones remain attached to the stent strut in the well-apposed case, they detach even when the gap between the strut and the arterial wall is very small (10 μm). At moderate malposition distances (25 μm and 50 μm), the proximal recirculation zone disappears whilst the distal recirculation zone increases in length. Finally, for large degrees of malapposition (200 μm), the distal recirculation zone disappears. Taken from Chesnutt and Han [66]. Taken from Chesnutt and Han [88]. Copyright permission for reuse in this thesis has been obtained from *Physical Biology*. Copyright Clearance Center Confirmation Number: 11674622.

1.5 Alleviating the Adverse Haemodynamics of Arteries Treated with Drug-Eluting Stents

The majority of commercial drug-eluting stents have rectangular stent struts with slightly rounded corners but are typically non-streamlined, as may be seen in Table 1-2. This non-streamlined nature promotes the adverse haemodynamics discussed previously, but may also facilitate enhanced drug uptake.

Table 1-2. Strut profile geometries of various drug-eluting stents. Taken from Jimenez and Davies [89]. Copyright permission for reuse in this thesis has been obtained from *Annals of Biomedical Engineering*. Copyright Clearance Center Confirmation Number: 11677077.

| Stent | Company | Approximate geometry | Strut thickness (μm) | Drug coating (μm) |
|---------------|-------------------|----------------------|-----------------------------------|--------------------------------|
| Cypher | Cordis (J&J) | Trapezoid | 140 | 12.6 |
| Taxus Express | Boston Scientific | Trapezoid | 132 | 16 |
| Endeavor | Medtronic | Circular | 91 | 5.3 |
| Xience V | Abbott | Rectangular | 81 | 7.6 |
| Taxus Liberté | Boston Scientific | Rectangular | 97 | 15 |

One potential method of alleviating these adverse haemodynamics could involve making use of the biomagnetic properties of blood, which allow blood to interact with applied magnetic fields. These biomagnetic properties exist due to the high concentrations of iron oxides within mature red blood cells. Human red blood cells placed in strong magnetic fields, varying between 1 and 8 Tesla, were found to reorient with their disk plane parallel to the magnetic field [90]. These impacts on orientation were found to increase the viscosity of blood [91-93]. Blood also has a

high electrical conductivity which varies with haematocrit and temperature, as well as flow rate [94-96].

Numerical studies of oxygenated and deoxygenated blood have shown that these properties allow magnetic fields to considerably affect the shear stress distribution in flowing blood, particularly near the magnetic field source. Blood flow in both idealised [97,98] and more realistic artery geometries [99] is appreciably affected by magnetic fields surrounding a current conducting wire located external to the artery. Blood flow through a two-dimensional eccentric stenosis has also been shown to be impacted by the strength and positioning of an external permanent magnet [100]. However, the feasibility of using the biomagnetic properties of blood to alleviate the adverse haemodynamics found in arteries with drug-eluting stents has not yet been considered.

Numerical and in-vitro studies have also shown that the adverse haemodynamics of stented vessels can be alleviated simply by altering the shape of the strut profile of the stent. Circular arc stent strut profile geometries, when placed in flowing blood, have significantly smaller separation regions than rectangular profiled struts when both are of the same height, as shown in Figure 1-21 [89]. It may also be seen in this figure that reducing the height of the stent struts is also an effective method of reducing the extent of these separated flow regions. The maximum shear stress values on the surfaces of the haemodynamically favourable struts were approximately 50% lower than those of the rectangular struts. However, the impact of the strut profile geometry on the drug transport behaviour from drug-eluting stent struts was not analysed.

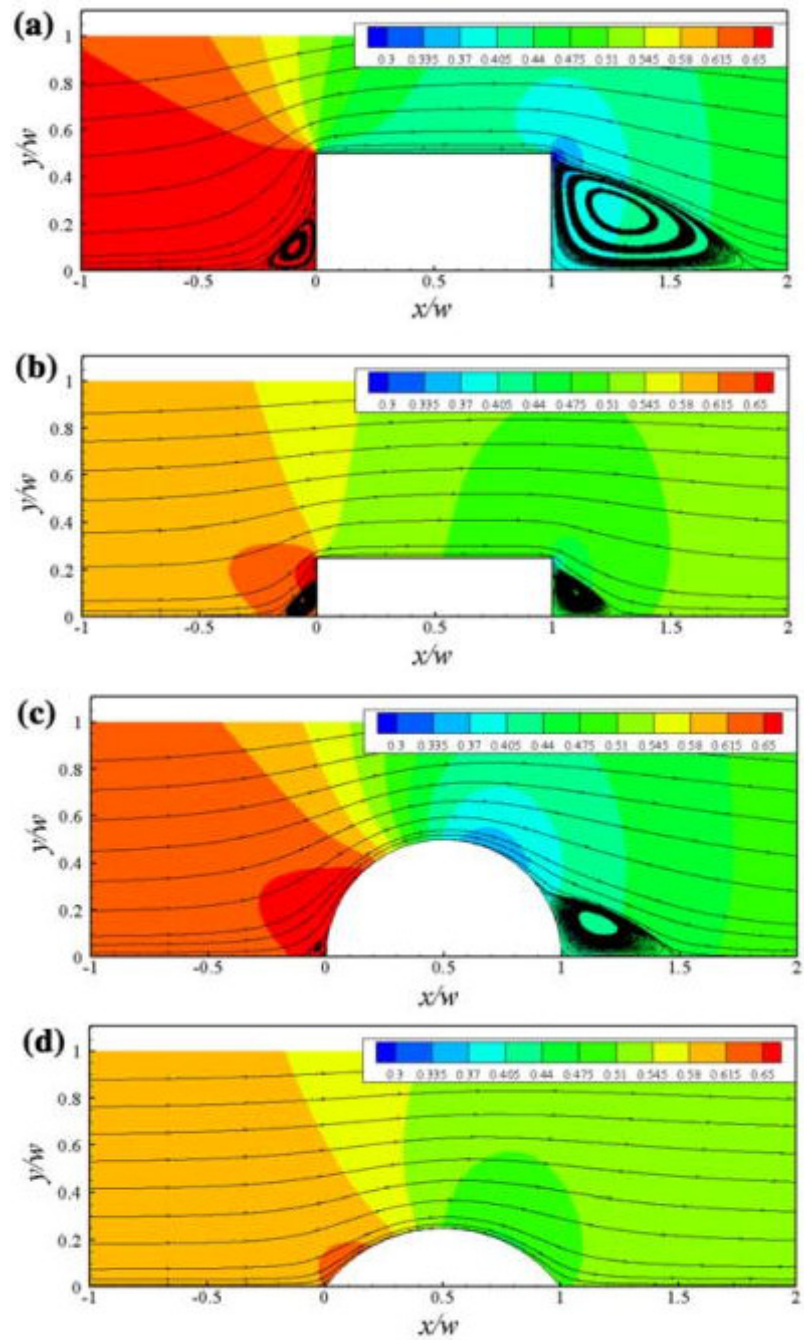


Figure 1-21. A more haemodynamic stent profile has been established as a potential method of alleviating adverse haemodynamics of arteries treated with drug-eluting stents. However, it is not yet known how these geometries affect drug uptake. Modified from Jimenez and Davies [89]. Copyright permission for reuse in this thesis has been obtained from *Annals of Biomedical Engineering*. Copyright Clearance Center Confirmation Number: 11677076.

1.6 Aims and Scope

There are two primary aims in this thesis. The first is to identify how arterial blood flow affects the drug transport details of arteries treated with drug-eluting stents. The second is to identify how to alleviate the adverse haemodynamics of these arteries without compromising drug uptake. A combination of computational fluid dynamics and in-vitro models are used to achieve these aims.

The impact of arterial blood flow on the drug transport details of arteries with drug-eluting stents is investigated in Chapters 2-5. In Chapter 2, the impact of blood's non-Newtonian properties and its complex near-wall behaviour on the transport of drug in stented arteries are studied numerically. Steady flow conditions and a constant drug coating concentration are assumed in this study. In Chapter 3, the additional effects of the depletion of drug with time in the stent coating and the pulsatility of blood flow are modelled. The drug transport results obtained are then validated against data obtained from an in-vitro benchtop model in Chapter 4. Finally, this validated numerical model is used to study the drug transport behaviour and the unique haemodynamics associated with incomplete stent apposition in Chapter 5.

Two potential methods of alleviating the adverse haemodynamics of stented arteries without compromising drug uptake are then investigated in Chapters 6 and 7. In Chapter 6, two-dimensional simulations are performed to investigate the feasibility of using magnetic struts to alleviate the adverse haemodynamics of stented arteries. Finally, two- and three-dimensional simulations are performed in Chapter 7 to investigate the feasibility of using haemodynamic strut profile geometries to simultaneously alleviate these adverse haemodynamics and enhance drug uptake.

Chapter 2

The Impact of Blood Rheology on Drug Transport in Stented Arteries: Steady Analyses

Chapter Aims

The haemodynamics of arteries treated with drug-eluting stents are believed to promote in-stent restenosis and stent thrombosis, and may also facilitate enhanced drug uptake. Hence, it is important to ensure that blood is modelled accurately when studying the haemodynamic and drug transport behaviour of stented arteries. The aim of this chapter is to elucidate how these behaviours are influenced by blood's highly variable non-Newtonian properties and by its complex near-wall behaviour.

2.1 Methods

2.1.1 Geometry

A series of two-dimensional CFD simulations were performed using the idealised geometry depicted in Figure 2-1. The lumen and the tissue were modelled as 3 mm tall and 1 mm tall fluid domains respectively. A single 0.1 mm square cross-section drug-eluting stent strut was also modelled halfway between the inlet and outlet of the computational domains, as may be seen in Figure 2-1. These dimensions are identical to those used in a prior analysis of stent-based drug therapy in the renal vasculature [75] and represents the application of established numerical techniques [60,61] to implants in non-coronary vasculatures, reflecting current clinical interest [101-104].

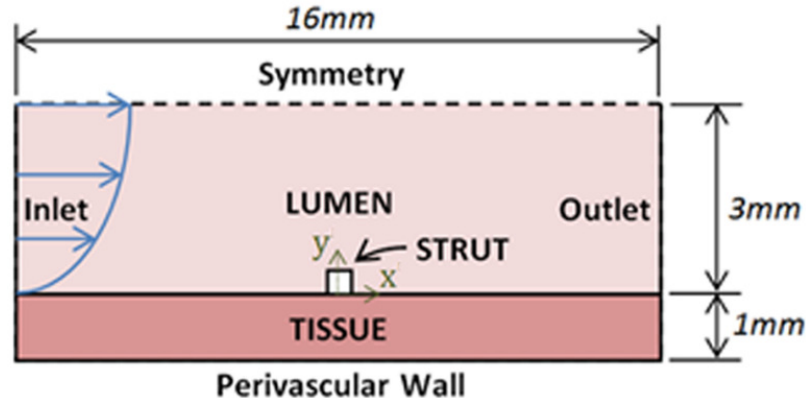


Figure 2-1. Geometry and boundary conditions. A single 0.1 mm square cross-section drug-eluting stent strut was positioned halfway between the inlet and outlet with one side of the strut in direct contact with the vessel wall. The co-ordinate system is defined such that $y = 0$ mm is defined at the lumen-tissue interface and $x = 0$ mm is located halfway between the inlet and the outlet. The flow is in the positive x-direction.

Although idealised, this geometry still captured the breadth of flow features present in more complex three-dimensional geometries. This included a single stent strut obstructing the near wall flow and generating regions adjacent to the strut where drug can pool [85]. A more realistic model of three-dimensional implants would likely consider multiple struts. When considered in this context, upstream struts act to shield downstream struts from flow, and superposition of drug occurs [61]. Flow-mediated drug uptake was previously found to be most significant at the foremost proximal strut – where the flow disruptions are largest and the contribution from neighbouring struts is quite small [61]. Hence, the geometry used in this study – a single stent strut isolated in the boundary layer of the flow – enhances the sensitivity of drug uptake to arterial flow changes. A square edge was similarly chosen in place of rounded or chamfered edges to yield the most exaggerated flow field.

2.1.2 Mathematical Model

In steady incompressible flow the equations of conservation of mass and momentum are written:

$$\nabla \bullet \mathbf{V} = 0, \tag{2-1}$$

and

$$\rho(\mathbf{V} \bullet \nabla \mathbf{V}) = -\nabla P + \nabla \bullet (\mu \nabla \mathbf{V}), \tag{2-2}$$

in which ρ is the blood density, μ is the dynamic viscosity of blood, \mathbf{V} is the velocity vector of blood in the lumen, P is the thermodynamic pressure and ∇ is the gradient operator.

The steady-state drug transport was represented in the lumen by

$$\mathbf{V} \bullet \nabla c = D_l \nabla^2 c, \quad (2-3)$$

and in the tissue by

$$D_t \nabla^2 c = 0. \quad (2-4)$$

c represents the normalised drug concentration, defined as the ratio of the local drug concentration, C , to the concentration of drug at the strut surfaces C_0 on which it is assumed to be uniform, viz

$$c = C/C_0, \quad (2-5)$$

and D_l and D_t represent the diffusivity of the drug in the blood and tissue respectively. Blood is assumed incompressible with a density of $\rho = 1060 \text{ kg/m}^3$.

The antiproliferative drug Paclitaxel served as a model compound in this analysis, chosen for its use as the active agent in drug-eluting stents and balloon catheters and for the large corpus of data regarding its vascular penetration and transport in blood and within arterial tissue. Its diffusivity coefficients are $D_l = 3.89 \times 10^{-11} \text{ m}^2/\text{s}$ [105] and $D_t = 3.65 \times 10^{-12} \text{ m}^2/\text{s}$ [106] respectively. A constant diffusivity of drug in blood was assumed, independent of local haematocrit or shear rate, since drug transport was modelled in the boundary layer in which such effects were assumed negligible. Specifically, erythrocytes are not in high concentration in the boundary layer and hence their impact on modulating the drug transport would be small. The flow rates in the boundary layer are also small and therefore assumed to be reasonably measured by a diffusivity measured statically [105]. Furthermore, the global diffusivity of drug in the tissue utilised in this study does not take into consideration the effects of tissue anisotropy and heterogeneity. More complex drug transport models have been described elsewhere which implement negative sink terms

to account for drug binding effects in the vascular wall [107]. However, the simplified convection-diffusion model used in this study will help to isolate the luminal flow patterns which enhance or diminish drug uptake.

The finite volume solver ANSYS FLUENT 14.5 (ANSYS Inc.) was used to perform the numerical simulations. A semi-implicit (SIMPLEC) algorithm coupled the pressure and velocity while a second order central differencing scheme spatially discretised the pressure and momentum variables. A second order upwind scheme was also used to discretise the scalar drug concentration.

2.1.3 Boundary Conditions

The elution of drug from the strut surfaces was modelled using a Dirichlet boundary condition, with $c = 1$. Continuity of flux was assumed at the lumen-tissue interface, while zero concentration, $c = 0$, was imposed at the inlet, implying that blood arrives from the inlet drug free. The walls of large veins and arteries are nourished with blood by a network of fine blood vessels, the “vasa vasorum”. This process of supplying blood to the artery walls can yield one of two boundary conditions at the perivascular wall: either saturation can be achieved, resulting in zero mass flux ($\partial c / \partial y = 0$), or the drug can be completely washed away ($c = 0$) [108]. In this study, the latter condition was assumed to be more realistic as the vasa vasorum are continuously replenished with fresh blood [71]. Finally, zero mass flux of drug was specified on the remaining boundaries.

To see the effects of different flow rates on the resulting drug distribution in the tissue, three flow rates were implemented: Q_{mean} representing the mean flow

during the cardiac cycle, while Q_{high} and Q_{low} were twice and half Q_{mean} respectively. These flow rates were then used in conjunction with each rheological model and a Poiseuille parabolic inlet velocity profile was implemented in each case. This allowed fully developed flow to be obtained with the Newtonian viscosity models. It should be noted that the Poiseuille parabolic profile does not simulate fully developed flow for the non-Newtonian blood rheological models. However, enough distance between the inlet and the strut was found to be present to ensure that fully developed flow was also closely approximated with the non-Newtonian models.

This may be seen in Figure 2-2, wherein the velocity profile obtained with a Power Law blood rheological model 8 mm away from the inlet (Line 1) is compared with the fully developed flow profile obtained with this rheological model (Line 2). These velocity profiles were both obtained within an unstented version of the geometry in Figure 2-1, in which the inlet had been extended upstream by 260 mm and in which no tissue domain was present. The similarity of the two velocity profiles, especially in the regions close the arterial wall ($y < 0.0005$ m), implies that the distances between the inlet and the strut are sufficient in this geometry to closely approximate fully developed flow for the Power Law model. As will be shown in later sections, this Power Law model displays the most significant non-Newtonian behaviour of any of the blood rheological models tested; hence there is sufficient distance between the inlet and the strut to ensure that fully developed flow is closely approximated for each of the blood rheological models tested.

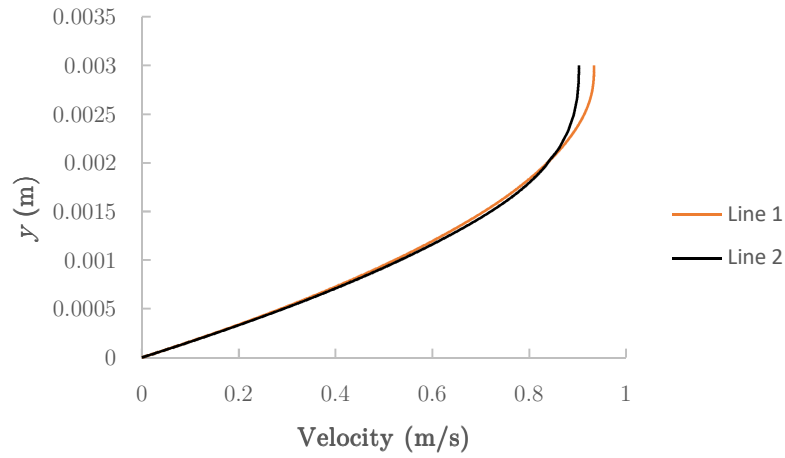


Figure 2-2. Comparison of the velocity profile obtained with the Power Law rheological model 8 mm away from the inlet (Line 1) with the fully developed flow profile obtained with this rheological model (Line 2).

A volumetric flow rate of 6.64 mL/s was used for Q_{mean} , which corresponds to a Reynolds number of 427 under the assumption of a constant dynamic viscosity, $\mu = 0.00345 \text{ Pa}\cdot\text{s}$. This is consistent with the mean flow conditions of the renal vasculature [75] and enabled blood flow to be modelled as laminar in all cases.

All remaining boundary conditions remained the same in each of the simulations performed. A uniform, zero gauge pressure boundary condition was specified at the outlet, whilst no-slip conditions were prescribed on the strut-lumen and lumen-tissue interfaces. A fixed wall assumption was also implemented in light of findings which suggest that stented arteries are considerably stiffer than non-stented arteries and that minimal arterial motion occurs [109]. Finally, a symmetry boundary condition was specified at the top of the 3 mm tall lumen domain in order to simulate a 6 mm diameter vessel.

2.1.4 Blood Rheological Models

A variety of blood models were implemented in conjunction with these boundary conditions to study the impact of blood rheology on the drug transport behaviour of stented arteries. In the first model, the Newtonian model, the dynamic viscosity is assumed to remain at a constant value of $\mu = 0.00345 \text{ Pa}\cdot\text{s}$ [73]. Five non-Newtonian blood rheological models – the Carreau, Casson, Generalised Power Law, Power Law, and Walburn-Schneck models – were then implemented to study the impact of blood's non-Newtonian properties on the drug transport behaviour. These models were chosen because they spanned the spectrum of viscosity variations with respect to strain-rate which have been observed in clinical data, as may be seen in Figure 2-3 [110-119]. Finally, a model with the fluid properties of plasma, $\rho = 1025 \text{ kg/m}^3$ and $\mu = 0.00122 \text{ Pa}\cdot\text{s}$ [120], was also implemented to account for near-wall red blood cell losses. The mathematical formulations of these models are given in

Table 2-1. Although the same inlet velocity profiles were used in conjunction with each of these viscosity models, it should be emphasised that the Reynolds number has a different definition for each case. Hence, Q_{low} , Q_{mean} and Q_{high} correspond with Reynolds numbers of 213.5, 427 and 854 for the Newtonian blood viscosity model only. For the Newtonian plasma viscosity model, these flow rates correspond to Reynolds numbers of 584, 1168 and 2336. However, due to the absence of a constant viscosity term, the Reynolds numbers cannot be defined for the non-Newtonian blood rheological models.

As shown in Figure 2-3, the apparent viscosity predicted by each rheological model is approximately constant for shear strain rates, $\dot{\gamma}$, greater than 400 s^{-1} . As $\dot{\gamma} \rightarrow 0 \text{ s}^{-1}$, however, each of the non-Newtonian models predicts a different increase in

the apparent viscosity of blood, thus demonstrating shear-thinning behaviour, so that at low strain rates they differ significantly from each other and from values obtained from viscometric data which is also presented in Figure 2-3. Whereas the Carreau model gives a maximum value of the absolute viscosity as the strain rate approaches zero, the viscosities of the Casson, Generalised Power Law, Power Law and Walburn-Schneck models each increase towards infinity. Furthermore, the original formulations of the Power Law and Walburn-Schneck models predict zero viscosities as $\dot{\gamma} \rightarrow \infty \text{ s}^{-1}$. Although the behaviour of blood as $\dot{\gamma} \rightarrow 0 \text{ s}^{-1}$ is still debated, zero viscosity at infinite $\dot{\gamma}$ is unphysical and hence limitations have been placed on the Power Law and Walburn-Schneck models to simulate the Newtonian behaviour of blood at high strain rates. The Generalised Power Law and Carreau model at high strain rates are each approximately asymptotic to the usually used value of the Newtonian model without any need for artificial limitations.

The original Casson model was developed for a yield-pseudo-plastic [115]. This means that unlike a fluid, which is defined by the fact that motion is induced if a shear stress is applied, a yield-pseudo-plastic behaves as if it were a solid if a shear stress less than the yield stress is applied. To alleviate these effects, a modified Casson model was proposed by Razavi et al. [121] in which no yield stress is present, and it was this model which was implemented in this current study. This modified Casson model was implemented with three hæmatocrit levels in order to determine how the hæmatocrit affects the haemodynamics and drug transport. The first of these models incorporated a hæmatocrit of 40%, typical of a healthy adult female [80], whilst the second incorporated a lowered, post-angioplasty hæmatocrit level of 33% [122]. Finally, the third Casson model implemented a hæmatocrit of 45%, normal for an adult male [80].

| BLOOD MODEL | EFFECTIVE VISCOSITY (PA · S) |
|-------------------------------------|---|
| Newtonian [73] | $\mu = 0.00345 \text{ Pa} \cdot \text{s}$ |
| Plasma [120] | $\mu = 0.00122 \text{ Pa} \cdot \text{s}$ |
| Power law (modified) [77] | $\mu = \begin{cases} m(\dot{\gamma})^{n_p-1}, & \dot{\gamma} < 427 \\ 0.00345 \text{ Pa} \cdot \text{s}, & \dot{\gamma} \geq 427 \end{cases},$ $m = 0.035, n_p = 0.6$ |
| Walburn-Schneck (modified) [123] | $\mu = \begin{cases} C_1 e^{C_2 H} e^{C_4 \left(\frac{TPMA}{H^2}\right)} \dot{\gamma}^{-C_3 H}, & \dot{\gamma} < 414, \\ 0.00345 \text{ Pa} \cdot \text{s}, & \dot{\gamma} \geq 414 \end{cases},$ $C_1 = 0.00797, C_2 = 0.0608, C_3 = 0.00499, C_4 = 14.585,$ $H = 40, TPMA = 25.9$ |
| Casson [79,124] | $\mu = 0.1 \left(\left[\sqrt{\eta} + \sqrt{\tau_y \left(\frac{1-e^{-m \dot{\gamma} }}{ \dot{\gamma} } \right)} \right]^2 \right),$ $\tau_y = (0.625H)^3, \eta = \eta_0(1-H)^{-2.5}, \eta_0 = 0.012, H = 40\%$ <p>(female normal), 33% (post – angioplasty) or 45% (male normal)</p> |
| Carreau [77] | $\mu = \mu_{\infty C} + (\mu_0 - \mu_{\infty C}) [1 + (\lambda \dot{\gamma})^2]^{(n_C-1)/2},$ $\lambda = 3.313, n_c = 0.3568, \mu_0 = 0.056 \text{ Pa} \cdot \text{s}, \text{ and}$ $\mu_{\infty C} = 0.00345 \text{ Pa} \cdot \text{s}$ |
| Generalised power law [73] | $\mu = \lambda \dot{\gamma} ^{n-1}, \lambda = \mu_{\infty G} + \Delta \mu \exp \left[- \left(1 + \frac{ \dot{\gamma} }{a} \right) \exp \left(- \frac{b}{ \dot{\gamma} } \right) \right],$ $n = n_{\infty} - \Delta n \exp \left[- \left(1 + \frac{ \dot{\gamma} }{c} \right) \exp \left(- \frac{d}{ \dot{\gamma} } \right) \right],$ $\mu_{\infty G} = 0.0035 \text{ Pa} \cdot \text{s}, n_{\infty} = 1.0, \Delta \mu = 0.025 \text{ Pa} \cdot \text{s},$ $\Delta n = 0.45, a = 50, b = 3, c = 50, \text{ and } d = 4$ |

Table 2-1. Blood rheological model equations.

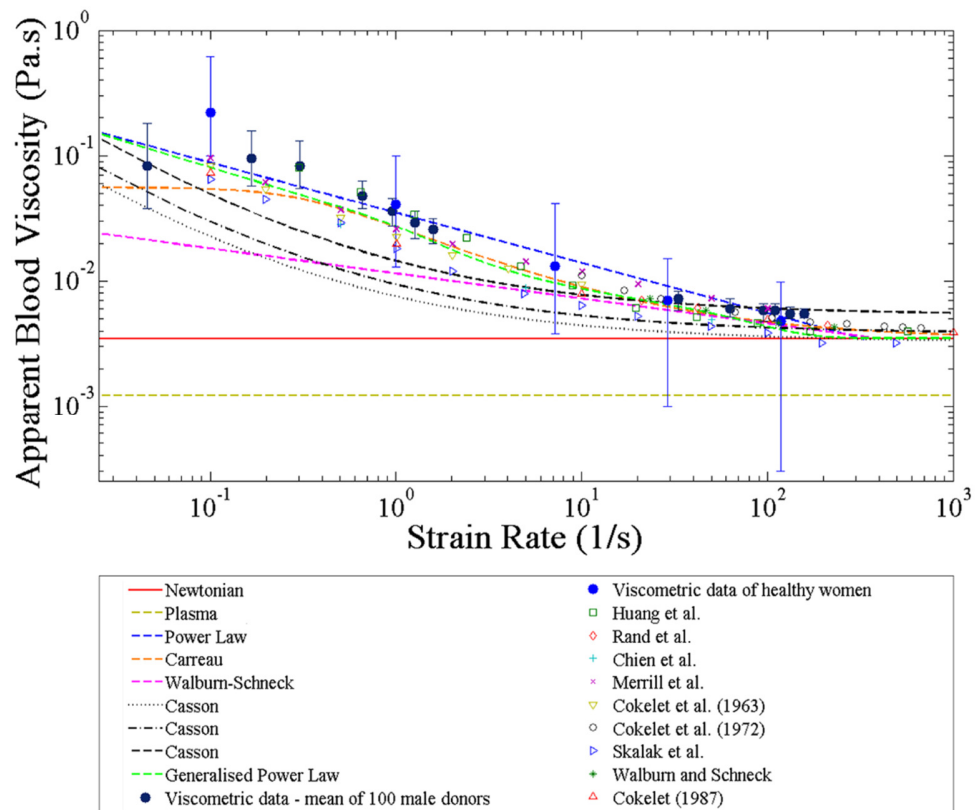


Figure 2-3. Experimental measurements of blood viscosity and non-Newtonian blood rheological models.

2.1.5 Grid Description and Refinement

Mesh convergence testing was carried out using the Newtonian model under mean flow conditions to ensure that the solutions obtained were independent of the size of the grid used. The mesh density used was greatest in the regions closest to the stent strut and near the interface between the tissue and lumen. This enabled the resolution of thin boundary layers which occurred along the no-slip boundaries defining the artery wall and the stent strut walls. Furthermore, the high mesh

density in the tissue and close to the stent strut facilitated the resolution of high drug concentration gradients.

The flow was deemed to be adequately resolved once the grid convergence index (GCI) corresponding to the recirculation lengths proximal and distal to the stent strut fell below 2%. This GCI is defined as [125]:

$$\text{GCI}_{fine\ grid} = \frac{3 \left| \frac{f_{fine} - f_{coarse}}{f_{fine}} \right|}{r^p - 1}, \quad (2-6)$$

where f_{fine} and f_{coarse} refer to either the proximal or distal recirculation length for a fine and coarse mesh respectively. r is the refinement factor, and p is the order of accuracy of the solution. In this study, $r = \sqrt{2}$ and $p = 2$.

Furthermore, the drug transport behaviour was deemed to be resolved once <2% change in the area-weighted average concentration (AWAC) of drug in a representative section of arterial tissue was observed between two successive mesh refinements. The representative area chosen was that of a rectangle bounded by the upper and lower extents of the tissue domain and the vertical lines $x = -0.35$ mm and $x = 0.35$ mm. This axial extent was chosen on the basis that a typical inter-strut distance is 7 struth widths [61]. It should be noted that the AWAC is an integral metric and, as such, differences are averaged out. Nonetheless, it was deemed prudent to ensure that the AWAC converged with each mesh refinement as it would be this metric that would be used to determine the magnitude of drug uptake in each of the simulations. The final mesh that was chosen contained 2,009,929 elements. More information about these grid convergence studies can be found in Appendix A.

2.2 Results and Discussion

2.2.1 Rheological Effects on Blood Flow

In each steady-state analysis performed, recirculating flow regions were observed to form proximal and distal to the stent strut, and were also observed to correspond with regions of high drug concentration, as found in past drug-eluting stent studies [60,75]. This phenomenon is shown in Figure 2-4 for a case employing the Newtonian blood viscosity model at an inlet flow rate of Q_{low} .

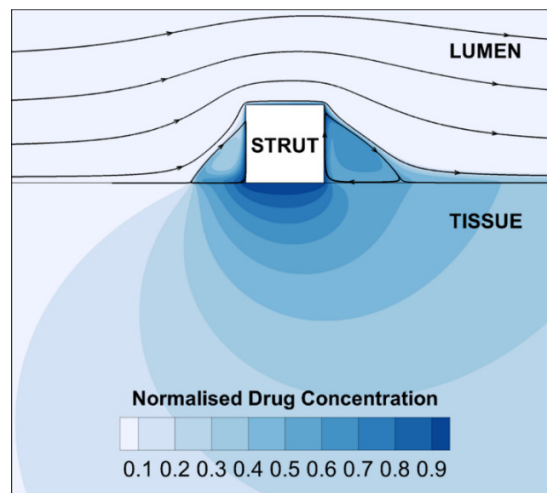


Figure 2-4. Drug concentration distribution and flow pathlines in the stented artery.

The lengths of these recirculating regions were affected by both the flow rate and the choice of blood rheological model, as may be seen in Figure 2-5 and Figure 2-6. Specifically, increases in the flow rate were associated with smaller proximal and larger distal recirculating flow regions for each rheological model investigated. The Newtonian model yielded larger proximal and distal recirculating regions than most of the non-Newtonian models at all flow rates, apart from two of the Casson models in the proximal region. In contrast, the Power Law model tended to produce the smallest recirculating flow regions, 18% smaller than the Newtonian

model in the proximal region and 24% smaller in the distal region at Q_{low} . This difference diminished as the flow rate increased, becoming 11% smaller in the proximal region and 6% lower than the Newtonian model in the distal region at Q_{high} . The Generalised Power Law, Walburn-Schneck and Carreau models produced similar recirculation length results to one another, smaller than the Newtonian model and generally larger than the Power Law model. Each of these non-Newtonian models also tended to converge towards the haemodynamic behaviour of the Newtonian model as the flow rate increased, although this behaviour was less evident in the three Casson models. It was also less evident in the model implementing plasma as the working fluid, which yielded a 24% smaller proximal recirculation length and a 59% larger distal recirculation length at Q_{high} .

To help ascertain why the non-Newtonian models tended to produce smaller recirculation regions, a new non-dimensional parameter, the *normalised mean viscosity*, $\bar{\mu}$, was introduced. This parameter, defined as

$$\bar{\mu} = \frac{\int_A \mu dA}{A\mu_N}, \quad (2-7)$$

measures the average value of the apparent blood viscosity, μ , in the area, A , of the proximal or distal recirculation zone being investigated, normalised by the dynamic viscosity associated with the Newtonian blood rheological model, $\mu_N = 0.00345 \text{ Pa}\cdot\text{s}$. As the size of the proximal and distal recirculation zones varied between models and flow rates, the value of A was different in each case investigated.

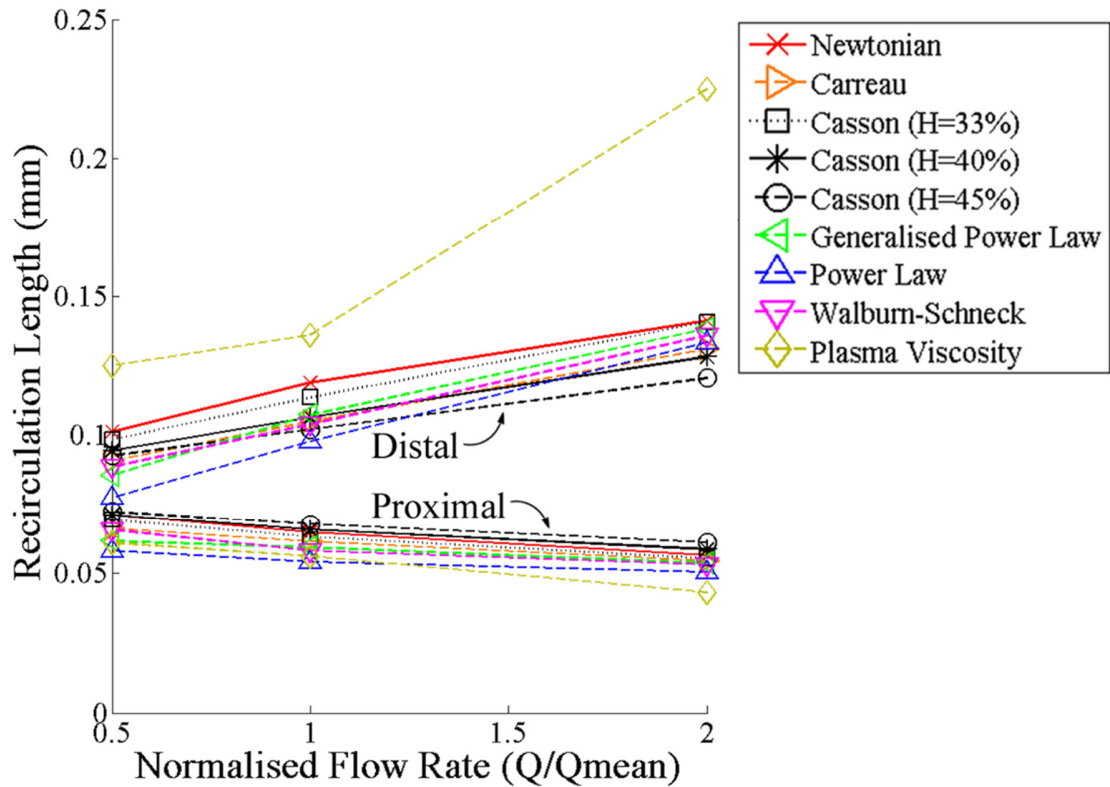


Figure 2-5. The effects of flow rate on the proximal and distal recirculation lengths. Increases in bulk flow rate were found to cause reductions in the proximal recirculation length and increases in the distal recirculation length produced by each rheological model.

Despite the significant differences between the rheological behaviour of the different models, the results of Figure 2-6 showed that the relationship between the recirculation lengths and $\bar{\mu}$ approximated linearity at most flow rates. This linear relationship indicates that the elevated viscosities of the non-Newtonian models in the recirculation zones is directly linked to smaller recirculation lengths as the higher viscosities mean that higher stresses are needed to generate the same shear rates so that there is greater resistance to motion. The R^2 index reveals that these linear trends are most noticeable at Q_{low} , in which $R^2 = 0.41$ in the proximal region and

0.62 in the distal region. However, these values dropped to 0.00 and 0.48 respectively at Q_{high} . The rheological models most responsible for this loss of linearity were the plasma model and the Casson models in which $H_{ct} = 40\%$ and 45% . These Casson models produced significantly larger proximal recirculation lengths than the Newtonian model at Q_{high} , despite having larger $\bar{\mu}$ values. Conversely, the plasma model yielded significantly larger distal recirculation lengths than the Newtonian model despite possessing a smaller $\bar{\mu}$. These discrepancies may be explained by the varying influence of non-Newtonian behaviour in each blood rheological model.

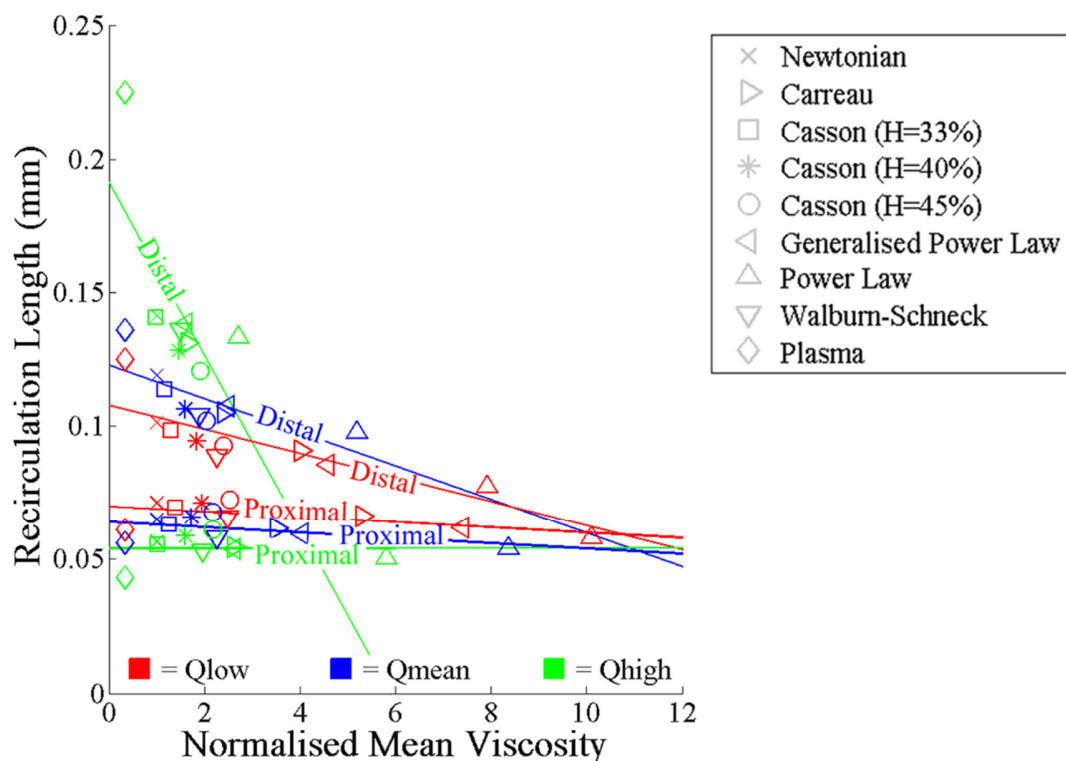


Figure 2-6. The effects of blood rheology on the proximal and distal recirculation lengths. The relationship between recirculation length and normalised mean viscosity, which measures the ratio of the average apparent viscosity in a recirculation zone and the Newtonian model's dynamic viscosity ($\mu_N = 0.00345 \text{ Pa}\cdot\text{s}$), was found to closely approximate linearity at each inlet flow rate. Furthermore, increases in normalised mean viscosity were found to cause reductions in recirculation length at each flow rate.

In order to quantify the significance of non-Newtonian flow behaviour, Ballyk et al. [73] introduced a concept referred to as the *non-Newtonian importance factor*:

$$I_L = \frac{\mu}{\mu_N}, \quad (2-8)$$

where μ is the apparent blood viscosity, while $\mu_N = 0.00345 \text{ Pa} \cdot \text{s}$ is the dynamic viscosity associated with blood at high strain rates. As non-Newtonian behaviour was generally most pronounced at low flow rates, only the results obtained at the lowest flow rate, Q_{low} , are shown in Figure 2-7.

The graphs of I_L obtained in this study confirm that the regions of highest dynamic viscosity occurred in both recirculation regions for each non-Newtonian blood rheology model. However, the Casson model in which $H_{ct} = 45\%$ was also found to yield high I_L values in high strain rate regions, such as near the tissue. As shown in Figure 2-3, this is because the apparent viscosity produced by this high hæmatocrit model is higher than the other blood viscosity models at strain rates above 100 s^{-1} . These high dynamic viscosities caused an increased resistance to blood flow, thereby reducing the size of the distal recirculation zone and increasing the size of the proximal zone. This could account for why this model produced significantly larger proximal recirculation lengths than the Newtonian model at each flow rate despite having larger $\bar{\mu}$ values, and why it yielded a significantly smaller distal recirculation length than the other models at Q_{high} .

These results also demonstrated that the magnitude of non-Newtonian behaviour is affected by the hæmatocrit level. The Casson model in which $H_{ct} = 33\%$ yielded smaller I_L values than the other Casson models in high and low strain rate regions alike. As shown in Figure 2-3, this is because the apparent viscosities produced by the Casson model decrease at all strain rates as the hæmatocrit level is

decreased. The decreased resistance to flow associated with this low haematocrit model yielded larger distal recirculation lengths. It also yielded smaller proximal recirculation lengths, although the reduced resistance to vortex formation in the proximal recirculating flow region antagonises this behaviour. Hence, this low-haematocrit Casson model was found to produce the haemodynamic environment most similar to that of the Newtonian model.

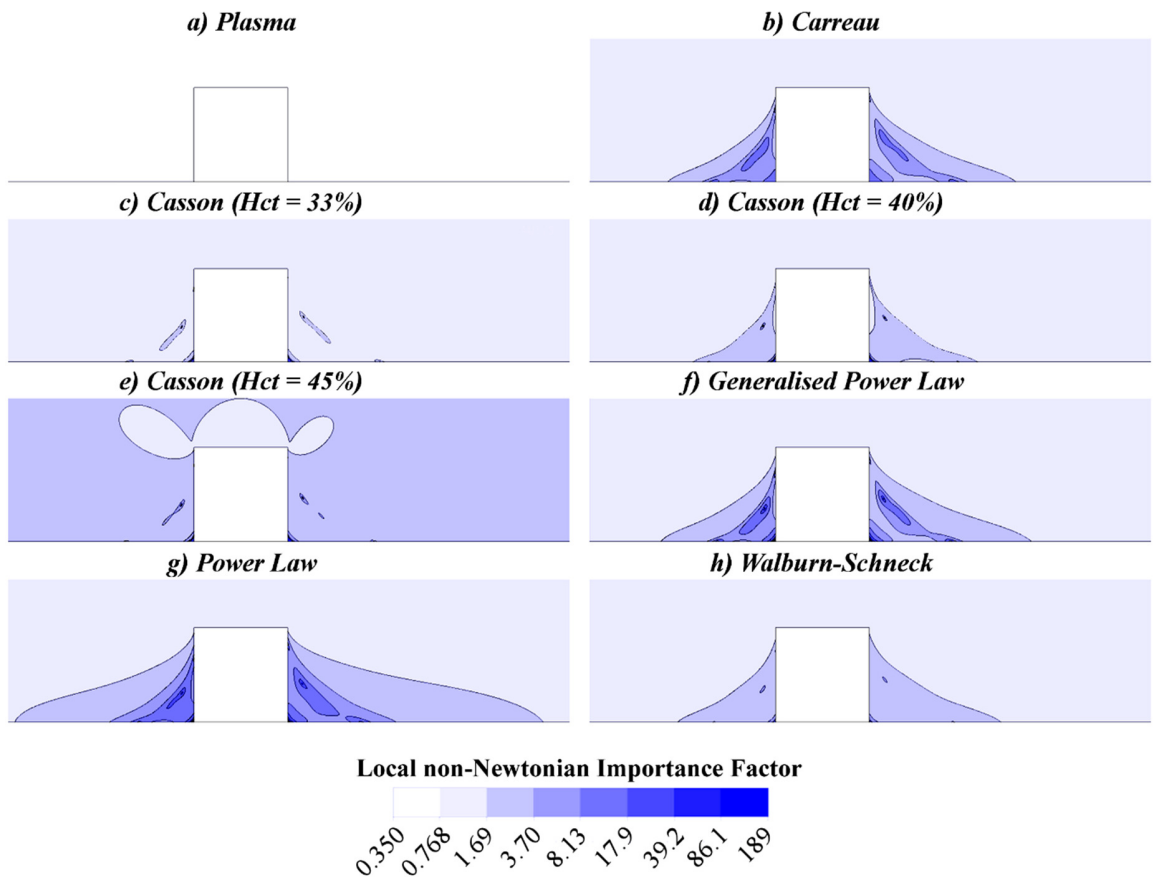


Figure 2-7. Local non-Newtonian importance factors, I_L . This non-dimensional parameter is used to illustrate the spatial variation in non-Newtonian behaviour for each blood rheological model. Although the plasma case (a) yielded a constant value of I_L , the remaining cases (b-h) showed that the most significant non-Newtonian behaviour occurs in the recirculation zones.

The smallest I_L values were associated with the plasma model, which yielded a constant I_L of 0.35. The associated decrease in resistance to flow in high strain rate regions and in recirculating flow regions resulted in the largest distal recirculation lengths of any of the models examined. It also yielded some of the smallest proximal recirculation lengths, although the reduced resistance to vortex formation in the proximal recirculating flow region opposes this behaviour somewhat. This antagonistic behaviour could explain why the plasma model's proximal recirculation lengths remained comparable to the other models at all flow rates whilst its distal lengths differed more dramatically.

2.2.2 Rheological Effects on Drug Transport

Fick's Law of diffusion states that the diffusive mass transfer across the lumen-tissue interface is proportional to the concentration gradient:

$$\dot{m} = -D_t \frac{\partial C}{\partial N}, \quad (2-9)$$

where \dot{m} is the mass flux of the drug species, D_t is the diffusivity of the drug in the tissue, and $\partial C/\partial N$ is the dimensional concentration gradient of drug. C is the concentration of drug and N is the direction normal to the lumen-tissue interface, taken positive in the positive y direction. Using the definition of the normalised drug concentration in Equation 2-5 and non-dimensionalising N in Equation 2-9, so that

$$n = \frac{N}{L_{inter-strut}}, \quad (2-10)$$

where $L_{inter-strut}$ is the same inter-strut distance used in the AWAC calculations, a normalised drug concentration gradient parameter was created which reveals the mass transport behaviour at the aforementioned representative section of the lumen-tissue interface as

$$\frac{\partial c}{\partial n} = -\frac{\dot{m}L_{inter-strut}}{C_0 D_t} \quad (2-11)$$

The normalised drug concentration gradient distribution associated with the Newtonian model in Figure 2-8 revealed five local peaks and troughs, labelled A, B, C, D and E. Although drug matter was evident in the proximal and distal segments, the concentration gradients at the lumen-tissue interface were only significant in magnitude in the far upstream (points A and B), and downstream (point E) regions. This behaviour could be readily explained by the pooling of drug in the proximal and distal regions driving diffusion processes, and local velocity vectors driving convection processes, as shown in Figure 2-9. In particular, it may be seen at point A, upstream of the proximal recirculation region, that low luminal drug concentrations and a velocity vector driving flow into the lumen give rise to highly negative $\partial c/\partial n$ values. Closer to the proximal strut surface, drug concentration gradients of more or less zero transpire, likely due to the low local velocities preventing convection, and a balance in luminal and tissue drug concentration preventing diffusion.

The results in this figure showed that whilst the presence of a proximal recirculation zone may be beneficial from a drug transport perspective, this is not the case for the distal recirculation zone. Specifically, integrating $\partial c/\partial n$ along the sections of the lumen-tissue interface occupied by the proximal and distal recirculation regions revealed that the distal zone detracted from the drug transport into the tissue ($\int (\partial c/\partial n)dx = -0.009$ mm) whilst the proximal zone enhanced drug transport ($\int (\partial c/\partial n)dx = 0.45$ mm). For the distal region, one can see that a larger recirculation region in which the drug can pool would act to dilute the luminal drug concentration, as well as a normal velocity vector (Figure 2-9) that acts to drive drug away from the tissue, minimising any convective transport processes. These

results are significant as indicate that designing haemodynamic stents struts which mitigate this distal recirculation zone may enhance drug uptake.

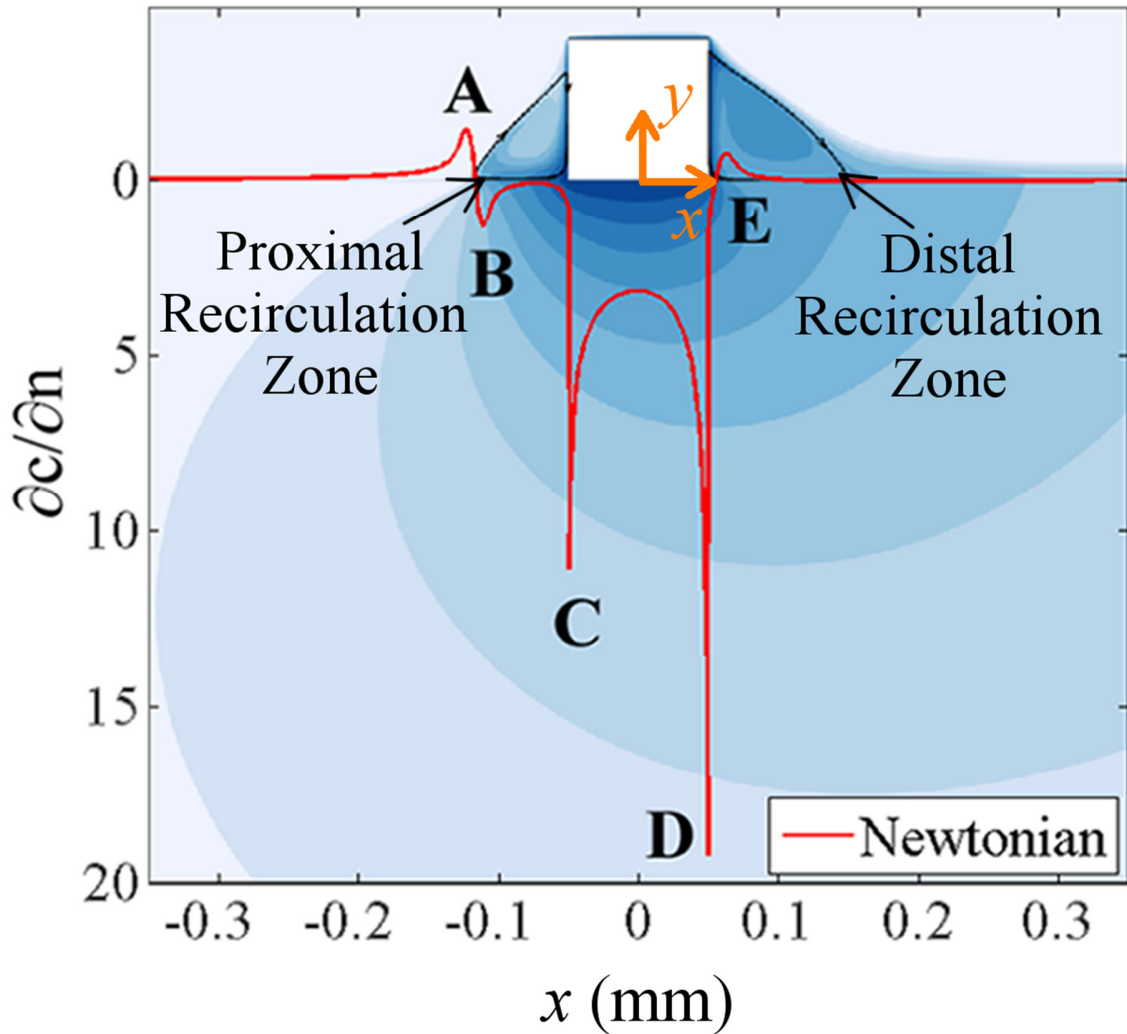


Figure 2-8. Diffusive mass transport behaviour. The plot of the normalised drug concentration gradient for the case in which blood is modelled as a Newtonian fluid revealed five peaks and troughs, labelled A, B, C, D and E. Local minima (A and E) show where drug is removed from the tissue while local maxima (B-D) show where it diffuses into the tissue.

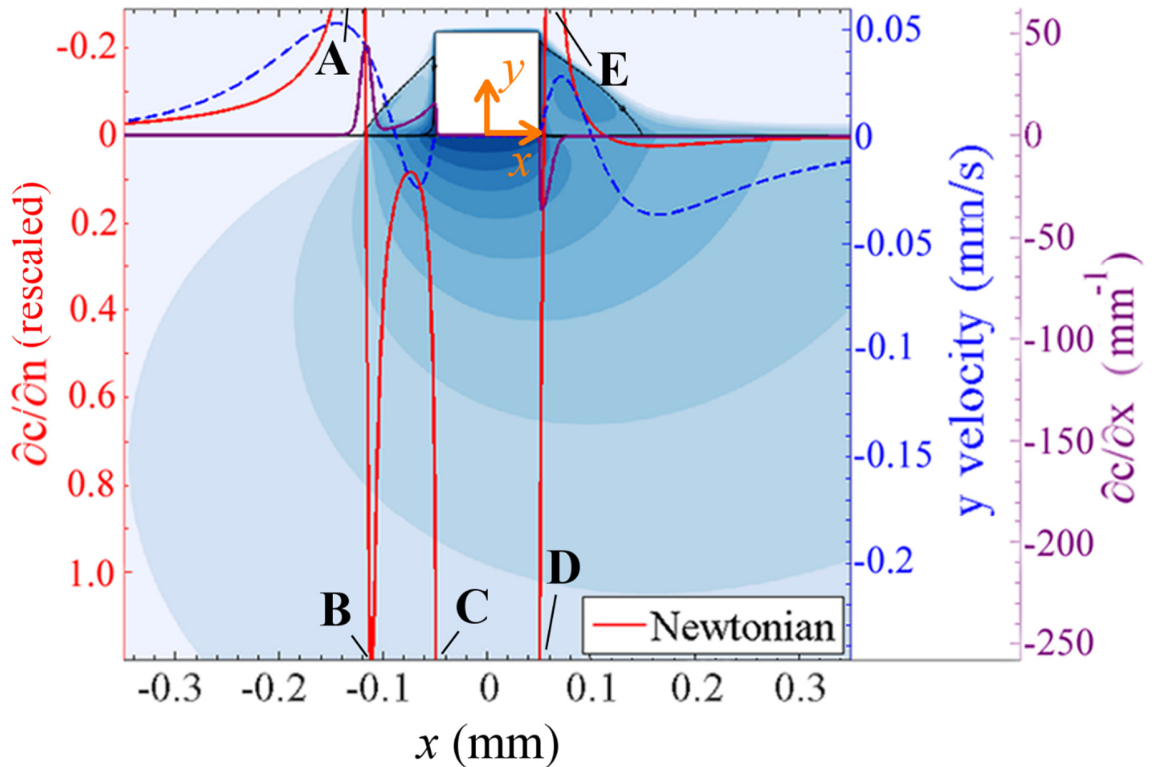


Figure 2-9. The effect of blood flow on the diffusive mass transport behaviour. The red line is a close-up of the $\partial c/\partial n$ line shown in Figure 2-8. The dashed blue line shows the distribution of the normal component of the blood velocity along a line 0.1 strut widths above the lumen-tissue interface. Comparison with the red $\partial c/\partial n$ line confirmed that the upward flow at points A and E resulted in loss of drug from the tissue due to convection. The purple $\partial c/\partial x$ line revealed that drug transport in the horizontal direction was significant between points A and B, and at points C and E.

An additional series of simulations were performed to investigate whether the distal recirculation zone displayed a similar tendency to drive drug out of the tissue with drugs other than Paclitaxel. These simulations were each performed with the Newtonian model at Q_{low} and whilst keeping the drug diffusivity in the tissue at a constant value of $D_t = 3.65 \times 10^{-12} \text{ m}^2/\text{s}$. The diffusivity in the lumen was varied with each simulation to establish diffusivity coefficient ratios of $D_l/D_t = 1, 10, 100, 1000, 10000$ and 100000 . Comparison of the graphs obtained in Figure 2-10 revealed higher concentration gradients – and hence greater drug transport across the lumen-tissue

interface - at lower D_l/D_t ratios. Although the drug concentration gradients across the lumen-tissue interface became insignificant as $D_l/D_t \geq 100$, a net loss of drug was nonetheless observed underneath the distal recirculation zone irrespective of D_l/D_t . Hence, the distal recirculation zone does display the tendency to remove drug from the tissue for non-Paclitaxel drugs although this behaviour diminishes as $D_l/D_t \geq 100$.

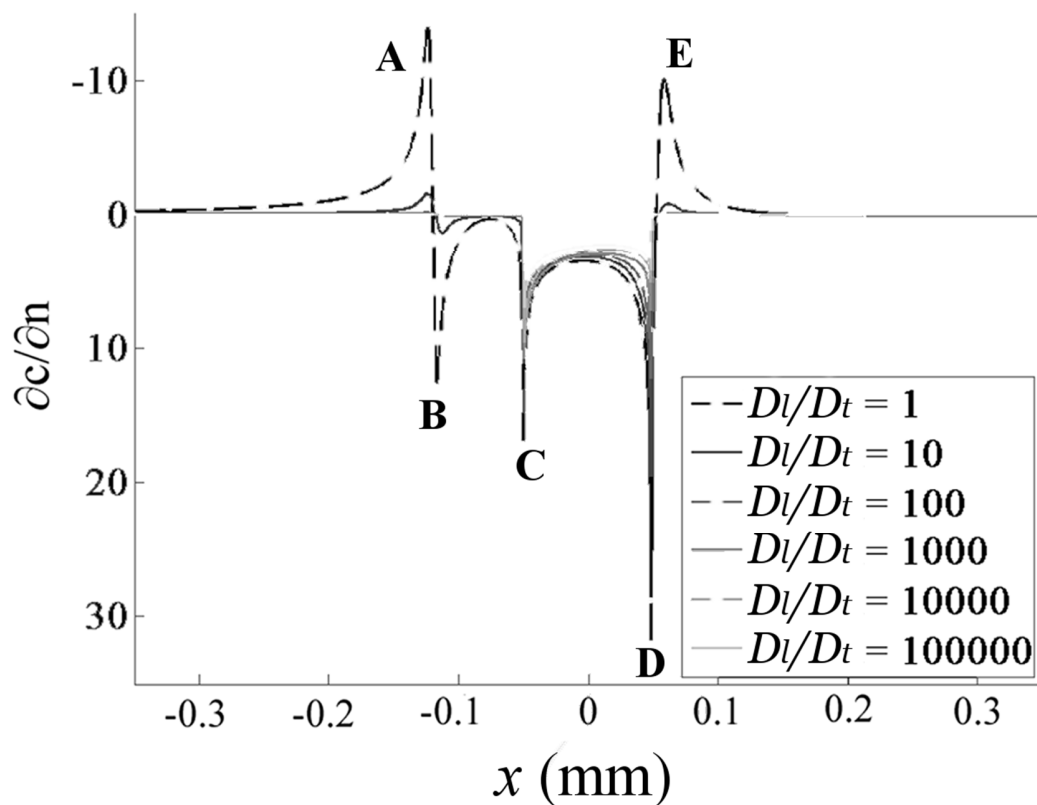


Figure 2-10. The effect of diffusion coefficient on the diffusive mass transport behaviour of stented arteries. The distal recirculation zone was found to remove drug from the tissue for non-Paclitaxel drugs, although this behaviour diminished as $D_l/D_t \geq 100$.

Similar drug concentration gradient profiles to the Newtonian model were observed in the non-Newtonian and plasma cases in Figure 2-11 as well, although with magnitudes scaled. Particularly, the magnitudes of the peaks and troughs

differed by up to 59% from those of the Newtonian model. These differences could be attributed to the fact that a change in the models would act to 1) vary the local velocity – but not to the extent that it would change the balance of convection and diffusion – and 2) vary the relative size of the recirculation regions. Hence the Newtonian model, with its larger recirculation regions, generally yielded the highest magnitude $\partial c/\partial n$ values of the blood models whilst the Power Law model’s smaller recirculation regions yielded the smallest values. The plasma model yielded the highest magnitude $\partial c/\partial n$ values overall, likely because of the high local velocities facilitated by its lower viscosity.

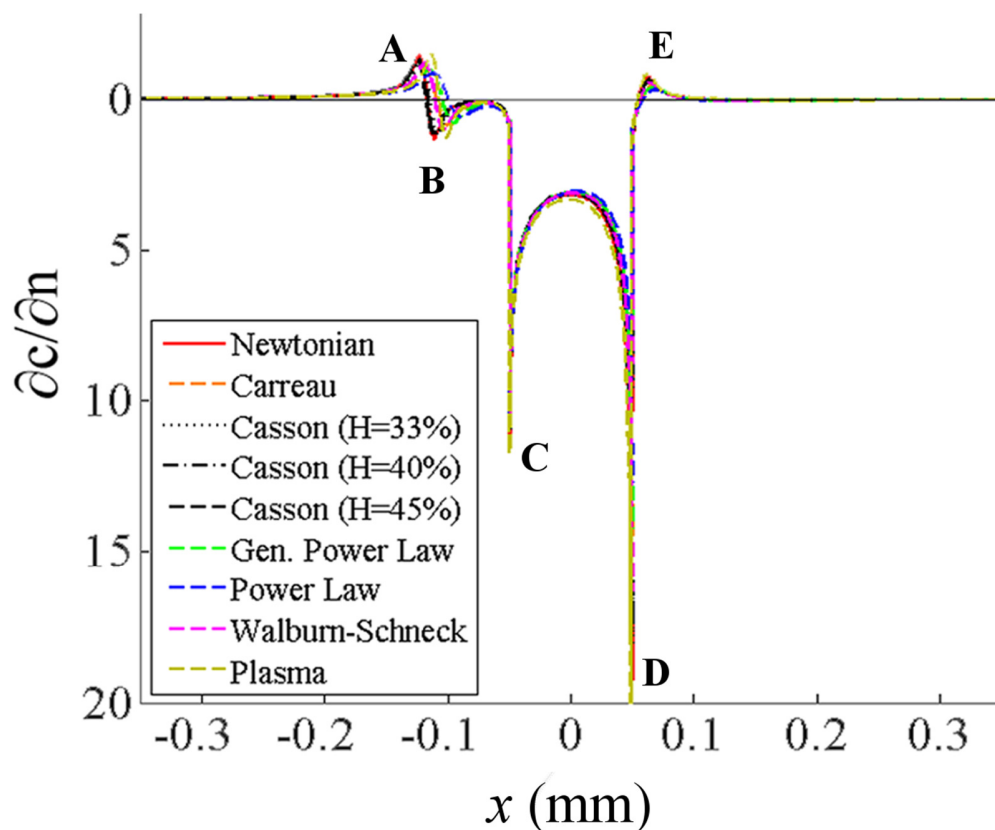


Figure 2-11. The effect of blood rheological model on the diffusive mass transport behaviour of stented arteries. The non-Newtonian blood rheological models produced similar $\partial c/\partial n$ patterns to the Newtonian model; however, their local maxima and minima were up to 59% smaller in magnitude.

The highest $\partial c/\partial n$ values were found at the strut-tissue interface, particularly at the corners at points C and D in each case. Examination of the high magnitude longitudinal concentration gradient ($\partial c/\partial x$) values at these points in Figure 2-9b revealed that large quantities of drug were removed longitudinally from beneath the strut. It was this removal of drug beneath the strut which facilitated the high $\partial c/\partial n$ values between points C and D and especially at the strut corners themselves. A similar phenomenon was observed at point B, which also featured high magnitude $\partial c/\partial x$ values due to the loss of drug upstream, facilitating a local $\partial c/\partial n$ peak. A higher magnitude $\partial c/\partial n$ was observed at point D than at point C due to the velocity vector aft of point D which drives drug out of the tissue (and thereby enhances the concentration gradient in the y direction). The impact of flow and blood rheological model selection on the magnitude of drug uptake can be assessed using comparisons of the AWAC values obtained with each simulation.

The AWAC of drug in the arterial tissue was dependent on both the flow rate and on the choice of the blood rheological model. An inverse relationship was found to exist between the AWAC and the flow rate, and, more precisely, between the AWAC and the sizes of the proximal and distal recirculating flow regions. The Newtonian model and the post-angioplasty Casson model ($H_{ct} = 33\%$), with their larger recirculation zones, therefore tended to produce the lowest AWAC of each of the blood rheological models at each flow rate while the Power Law model generally yielded the highest AWAC, as shown in Figure 2-12. However, these AWAC values deviated less than 5% from those of the Newtonian model at all of the flow rates tested. In fact, it was only when modelling plasma instead of blood that any

considerable deviations from the Newtonian model's AWAC were observed and even these only occurred at Q_{high} . This suggests that globally the Newtonian model is appropriate to use in place of non-Newtonian blood rheological models in studies seeking to quantify the magnitude of arterial drug uptake. The clinical significance of these results is that they convey that the magnitude of drug uptake in stent-based drug delivery is relatively invariant of individual variations in blood rheology. However, transient simulations implementing pulsatile inlet velocity profiles may be needed to confirm whether or not the plasma model's AWAC deviates significantly from the Newtonian model's over several cardiac cycles.

Although these results appear to convey that the Newtonian blood viscosity model is appropriate for use in drug-eluting stent studies, they have neglected to account for the effects of blood rheology on the spatial distribution of drug in the tissue. To investigate this, another new parameter, the *non-Newtonian drug concentration difference factor*, I_D , was introduced. This parameter represents the difference between the normalised drug concentration of the concerned non-Newtonian rheological model and the Newtonian model at the same flow rate, divided by the integrated absolute concentration gradient along a representative length of the lumen-tissue interface:

$$I_D = \frac{c_{NN} - c_N}{\int_{-0.35 \text{ mm}}^{0.35 \text{ mm}} \left| \frac{\partial c_N}{\partial n} \right| dx}. \quad (2-12)$$

As earlier, this representative length is chosen to lie between the points $x = -0.35 \text{ mm}$ and $x = 0.35 \text{ mm}$ along the line $y = 0 \text{ mm}$. The subscripts NN and N indicate non-Newtonian and Newtonian cases respectively.

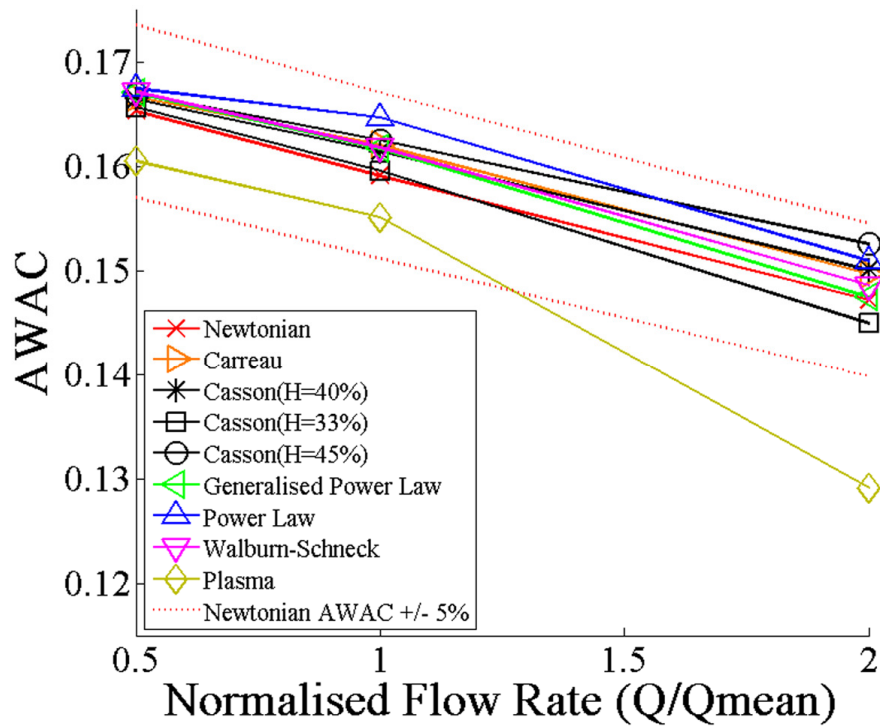


Figure 2-12. The effect of blood rheological model and flow rate on the average tissue drug concentration.

The effect of blood rheology on the distribution of drug in the artery wall was ascertained by a comparison of the I_D plots at the three flow rates investigated. The results of this study are shown in Figure 2-13. Once again, only the results corresponding with a flow rate of Q_{low} are displayed, as this is where non-Newtonian effects were generally most pronounced. The regions highlighted in red ($I_D > 0$) depict where the non-Newtonian blood model predicts a greater drug concentration, whilst the blue regions ($I_D < 0$) show where the Newtonian model predicts a higher drug concentration. Regions in which $|I_D| > 0.06$ were deemed to correlate with regions in which the non-Newtonian model's spatial distribution of drug matter departed significantly from that of the Newtonian model.

Although the Newtonian model was deemed adequate for predicting the AWAC, the presence of regions with high $|I_D|$ established that non-Newtonian effects were significant when investigating the spatial distribution of drug matter in stented arteries. The drug pools which formed in the smaller recirculating flow regions generally associated with the non-Newtonian models were significantly more concentrated than those of the Newtonian models, as conveyed by the red areas found immediately proximal and distal to the stent struts in Figure 2-13. Although the smaller recirculation regions of the non-Newtonian models did facilitate higher concentration drug pools, the strain rates associated with the Newtonian model were greater in the regions of the recirculation zones which were close to the lumen-tissue interface. These higher strain rates facilitated an increased convective transport of drug and may account for why I_D became negligibly small near the proximal lumen-tissue interface in each case, despite the higher concentrations of the drug pools in the non-Newtonian cases. I_D did not become negligible, however, at the distal lumen-tissue interface as the drug matter which reached the interface was already significantly more dilute in the Newtonian case. The result of these effects is that the Newtonian model tended to yield higher tissue drug concentrations upstream of the strut whilst the non-Newtonian models produced higher concentrations in the downstream region. The combination of these effects could account for why the AWAC values of the non-Newtonian models deviated less than 5% from that of the Newtonian model despite the significant differences in drug spatial distribution which were observed.

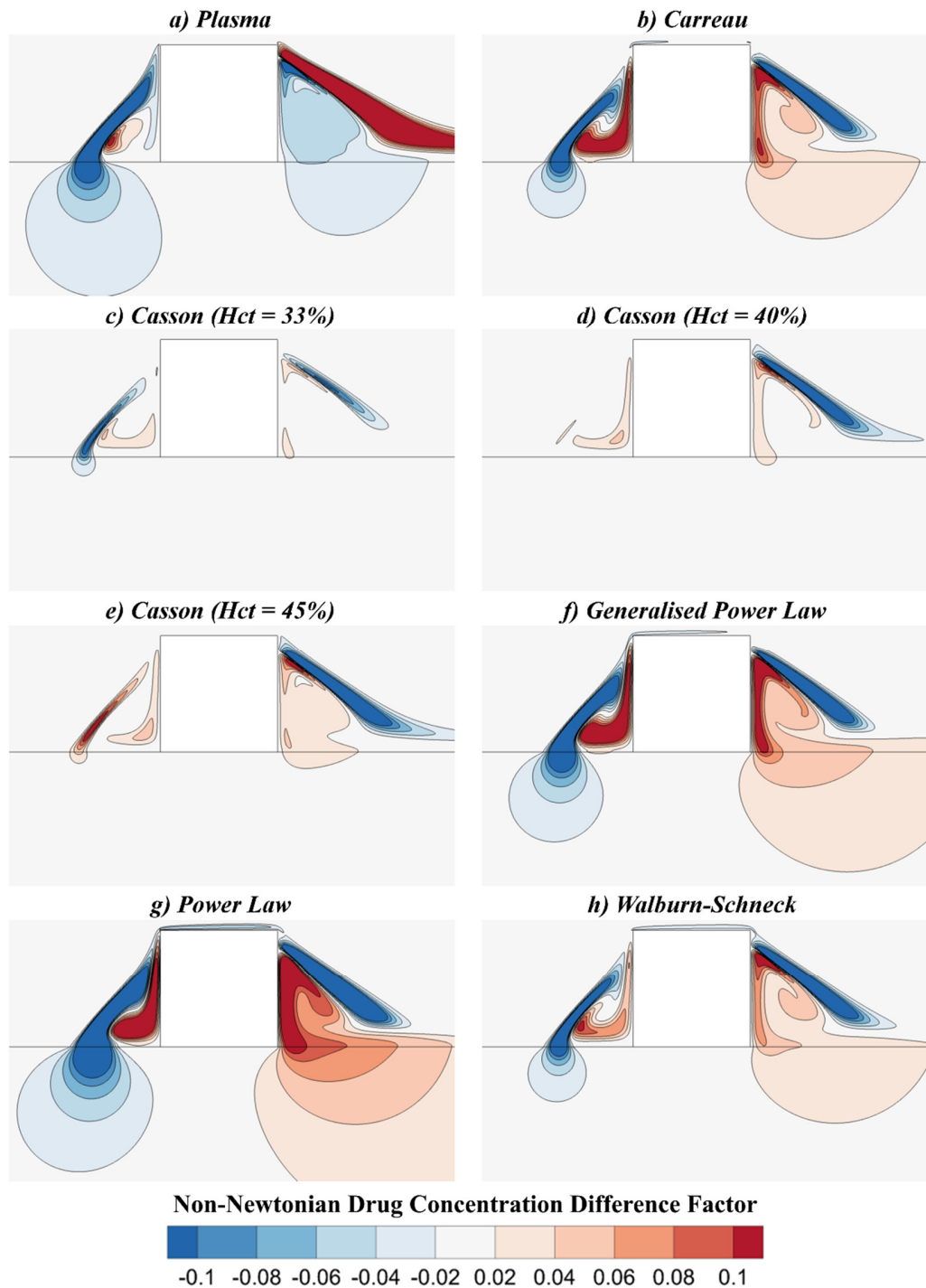


Figure 2-13. Contour plots of the non-Newtonian drug concentration difference factor, I_D . The regions highlighted in red ($I_D > 0$) depict where the non-Newtonian blood model predicts a greater drug concentration, whilst the blue regions ($I_D < 0$) show where the Newtonian model predicts a higher drug concentration.

Although a non-Newtonian blood rheological model may more accurately describe the spatial distribution of drug in arterial tissue, it is difficult to convey which model is best suited to this task. Comparison of the results obtained with the three Casson models revealed that patients with higher hæmatocrits may yield higher drug uptake globally but particularly in regions distal to the stent struts. However, as the Power Law model typically yielded the most significant non-Newtonian behaviour, it is suggested that both Newtonian and Power Law models be implemented in future studies concerned with drug transport details. This method may be used to determine a range of potential drug transport behaviours and thus be of potential use to stent designers. A plasma model may also be appropriate to incorporate on the basis of the relatively low tissue drug concentrations that it yields in both upstream and downstream tissue aspects. However, transient simulations implementing a pulsatile inlet velocity may be needed to confirm if these results depart significantly with those achieved with the Power Law and Newtonian models over several cardiac cycles.

2.3 Outcomes

Non-Newtonian effects were generally most pronounced at low flow rates and the choice of blood rheological model was found to influence flow patterns and drug transport. The largest non-Newtonian haemodynamic and drug transport effects were observed in the Power Law model, while these effects were more modest in cases employing the Walburn-Schneck, Casson, Carreau and Generalised Power Law models. This non-Newtonian behaviour typically manifested through significantly reduced proximal and distal recirculation lengths when compared with the Newtonian model. An additional blood plasma model was also implemented to account for red blood cell

depletion in the near-wall regions. This model yielded smaller proximal and larger distal recirculation lengths than the Newtonian model.

In each model investigated, the flow separation regions which formed downstream of the stent struts were found to remove drug from the tissue. These results, when considered in conjunction with relevant experimental data, could lead to the design of more haemodynamic drug-eluting stent struts which mitigate this distal recirculation zone and potentially enhance drug uptake.

Numerical methods allowed an appreciation of the subtle but still significant differences in drug delivery due to blood rheology. It was found that non-Newtonian effects can be significant and the choice of a non-Newtonian rheological model is contextually important. Specifically, a Newtonian model was globally found to be appropriate to use in studies seeking to quantify the magnitude of arterial drug uptake, although non-Newtonian effects were found to impact the spatial distribution of drug in the tissue. It was therefore suggested that both Newtonian and Power Law rheological models be implemented in future numerical studies concerned with drug transport details, in order to establish a range of potential drug concentration distributions. A plasma model may also be appropriate to incorporate on the basis of its relatively small tissue concentrations in both proximal and distal regions.

Clinically, these results conveyed that the magnitude of drug uptake in stent-based drug delivery is invariant of individual variations in blood rheology. Moreover, it was also suggested that patients with higher haematocrits may yield higher drug concentrations globally but particularly in regions distal to the stent struts. However, these results are limited in that a uniform coating concentration was implemented in this study. Further transient simulations implementing a pulsatile inlet velocity may be needed to confirm if these results still manifest over several cardiac cycles.

Chapter 3

The Impact of Blood Rheology on Drug Transport in Stented Arteries: Pulsatile Analyses

Chapter Aims

The first aim of this study is to elucidate how blood's non-Newtonian properties, complex near-wall behaviour, and the pulsatility of its flow affect the haemodynamics and drug transport of stented arteries. However, unlike Chapter 2 and other numerical studies dealing with this topic, the non-uniform depletion of drug at the stent surfaces is modelled. The second aim of this study is to assess the validity of neglecting this non-uniform depletion, whilst the third aim is to reveal whether flow-mediated drug transport is truly significant.

3.1 Methods

3.1.1 Geometry

A series of two-dimensional CFD analyses were performed using the idealised two-dimensional renal artery geometry depicted in Figure 3-1. The vessel lumen was modelled as a 3 mm tall fluid domain with a single 0.1mm square cross-section drug-eluting stent strut, positioned halfway between the inlet and outlet. The arterial tissue was modelled as a 1 mm thick fluid domain. These dimensions are identical to those used in Chapter 2; however, an additional 15 μm thick drug coating was added onto the strut in order to more accurately simulate the elution of drug.

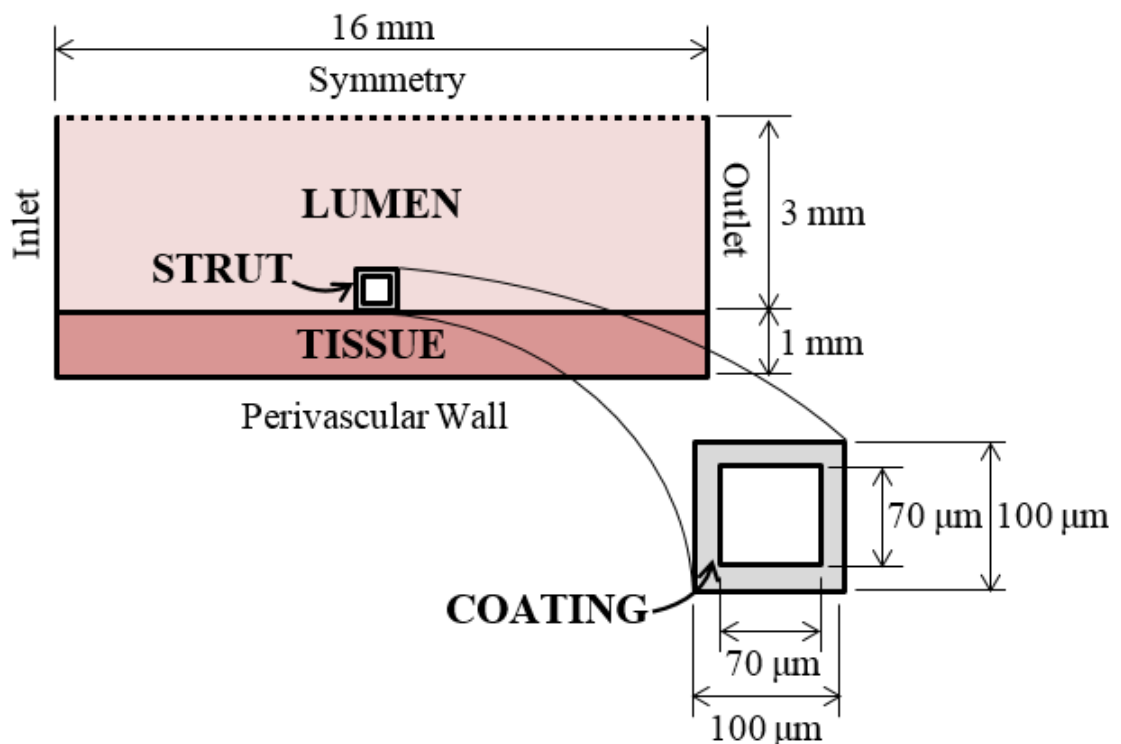


Figure 3-1: Geometry and dimensions. Unlike the geometry used in the previous chapter, a 15 μm thick drug coating was modelled in the current geometry to simulate the depletion of drug within the coating.

3.1.2 Mathematical Model

The incompressible, laminar blood flow through the lumen was modelled using a combination of the equations of conservation of mass,

$$\nabla \bullet \mathbf{V} = 0, \quad (3-1)$$

and conservation of momentum,

$$\rho \left[\frac{\partial \mathbf{V}}{\partial t} + \mathbf{V} \bullet \nabla \mathbf{V} \right] = -\nabla P + \nabla \bullet (\mu \nabla \mathbf{V}). \quad (3-2)$$

In these equations, ρ is the density of blood, μ is the dynamic viscosity of blood, \mathbf{V} is the velocity vector of blood in the lumen, P is the thermodynamic pressure, ∇ is the gradient operator and t is the time. Three different blood models were used to simulate this luminal blood flow.

The traditionally used Newtonian blood model was implemented first. This model features a constant dynamic viscosity of $\mu = 0.00345 \text{ Pa} \cdot \text{s}$, based on blood's lowest viscosity limit. This Newtonian assumption greatly simplifies the modelling of blood and was shown in Chapter 2 to be an appropriate model to use when seeking to quantify the magnitude of drug uptake. A constant blood density of $\rho = 1060 \text{ kg/m}^3$ is used in conjunction with this model.

Blood was then modelled as a shear-thinning non-Newtonian fluid using a Power Law blood rheological model. The mathematical formulation of this model's dynamic viscosity with respect to the shear strain rate, $\dot{\gamma}$, is given in Table 3-1. This model was chosen as it generally yielded the smallest recirculating flow regions and highest drug uptake of any of the blood rheological models tested in Chapter 2. A constant blood density of $\rho = 1060 \text{ kg/m}^3$ was once again ascribed.

Finally, blood was modelled with the fluid properties of plasma, with a constant density of $\rho = 1025 \text{ kg/m}^3$ and a constant dynamic viscosity of $\mu = 0.00122 \text{ Pa}\cdot\text{s}$. This model was implemented to account for the migration of red blood cells towards the vessel axis in steady, fully-developed flow, which leaves behind a plasma-rich region near the walls [83]. In Chapter 2, it also yielded the largest recirculating flow regions and the lowest drug uptake of any of the blood viscosity models.

With these three models, the full spectrum of rheology can be considered, including the extreme cases where the boundary layer is rich with red blood cells and entirely depleted of them. For brevity, the Newtonian blood and Newtonian plasma models will henceforth be referred to as the Newtonian and plasma models respectively. The constitutive equations used to define the three viscosity models may be seen in Table 3-1.

Table 3-1: Blood rheological model equations

| Blood model | Effective viscosity | Density |
|------------------------------|--|------------------------------|
| Newtonian [73] | $\mu = 0.00345 \text{ Pa}\cdot\text{s}$ | $\rho = 1060 \text{ kg/m}^3$ |
| Plasma [84] | $\mu = 0.00122 \text{ Pa}\cdot\text{s}$ | $\rho = 1025 \text{ kg/m}^3$ |
| Power law (modified) [77] | $\mu = \begin{cases} 0.035(\dot{\gamma})^{-0.4} \text{ Pa}\cdot\text{s}, & \dot{\gamma} < 427 \text{ s}^{-1} \\ 0.00345 \text{ Pa}\cdot\text{s}, & \dot{\gamma} \geq 427 \text{ s}^{-1} \end{cases}$ | $\rho = 1060 \text{ kg/m}^3$ |

Drug transport in the lumen was modelled using a scalar convection-diffusion equation,

$$\frac{\partial c}{\partial t} + \mathbf{V} \cdot \nabla c = D_l \nabla^2 c, \quad (3-3)$$

whilst drug transport in the tissue and strut coating were characterised using diffusion-only equations,

$$\frac{\partial c}{\partial t} = D_t \nabla^2 c \quad (3-4)$$

and

$$\frac{\partial c}{\partial t} = D_c \nabla^2 c. \quad (3-5)$$

c is the normalised drug concentration, defined as the non-dimensional ratio of the local drug concentration, C , to the maximum concentration of drug in the strut coating, C_0 , viz

$$c = C/C_0, \quad (3-6)$$

and D_b , D_t and D_c represent the diffusivity of the drug in the blood, tissue and coating respectively.

Paclitaxel again served as the model drug in this analysis. As in Chapter 2, diffusivity coefficients of $D_b = 3.89 \times 10^{-11} \text{ m}^2/\text{s}$ [105] and $D_t = 3.65 \times 10^{-12} \text{ m}^2/\text{s}$ [106] were used to simulate the diffusion of this drug within blood and within the arterial tissue respectively. The diffusivity coefficient of Paclitaxel within the coating was then determined based on the desired duration of drug release using Equation 3-7 [126]:

$$D_c = \frac{L_c^2}{t_{release}}, \quad (3-7)$$

where L_c is the coating thickness and $t_{release}$ is the drug release duration [70]. A 10 day drug release duration was specified, based on the release rate of the TAXUS-MR (moderate release) paclitaxel-eluting stent [127]. Given the coating thickness of $L_c = 15 \text{ }\mu\text{m}$, this resulted in a diffusivity coefficient of $D_c = 2.60 \times 10^{-16} \text{ m}^2/\text{s}$.

The solution of Equations 3-1 to 3-5 was accomplished using the finite volume solver, ANSYS FLUENT 14.5 (ANSYS Inc.). A semi-implicit (SIMPLEC)

algorithm coupled the pressure and velocity whilst a second order central differencing scheme spatially discretised the pressure and momentum variables. Temporal discretisation was achieved with a second order implicit scheme whilst a second order upwind scheme was used to discretise the scalar drug concentration.

3.1.3 Boundary Conditions

To investigate the effects of pulsatility, two inlet velocity boundary conditions were used in conjunction with the three blood models described earlier, giving rise to a total of six simulations. Firstly, three simulations – one for each blood model – were performed with a steady, Poiseuille parabolic inlet velocity profile, corresponding to a volumetric flow rate of $Q = 6.64$ mL/s. This is the same as the mean flow rate, Q_{mean} , that was used in the steady-state simulations of Chapter 2. This flow rate corresponds to a Reynolds number of 427 under the assumption of a constant dynamic viscosity, $\mu = 0.00345$ Pa·s, and is consistent with the mean flow conditions of the renal vasculature [75]. Three further simulations were then performed with a physiologically realistic renal artery waveform, obtained by Taylor et al. [128] using a finite element model of the three-dimensional pulsatile flow in the abdominal aorta. Each cycle of this waveform lasted a period of $T = 0.9$ s and yielded a mean volumetric flow rate of $Q_{mean} = 6.64$ mL/s, identical to the flow rate of the steady inlet flow profile. Unlike the steady profile, however, the oscillatory nature of the pulsatile inlet flow rate waveform meant that a Poiseuille parabolic inlet velocity profile could not be assumed. An analytical solution for the inlet velocity profile of pulsatile flows through straight tubes was previously derived by Womersley [129]. However, as this solution was derived for Newtonian flows, it was deemed more appropriate in this study to assign a time-varying uniform velocity, $\bar{u}(t)$, to the inlet

boundary and let this ‘plug flow’ profile develop using an extended inlet. This time-varying uniform velocity was defined as follows:

$$\bar{u}(t) = \frac{Q(t)}{\pi R^2}, \quad (3-8)$$

where $Q(t)$ is the time-varying flow rate and R is the vessel radius. A comparison of the two flow rate waveforms is depicted in Figure 3-2.

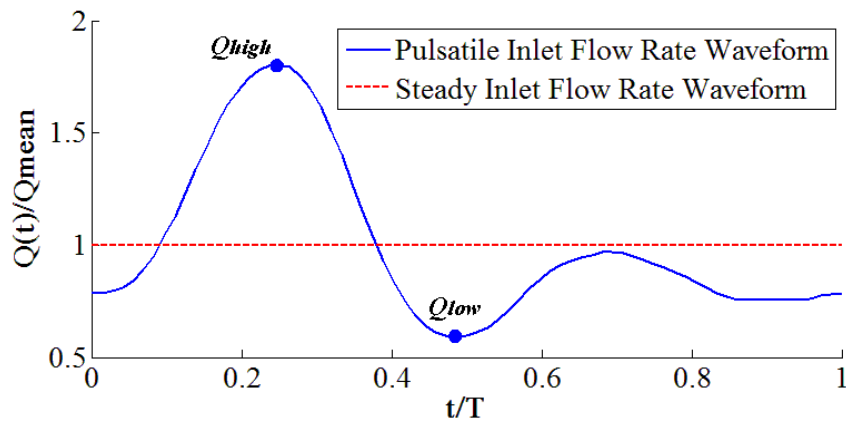


Figure 3-2: Pulsatile and steady inlet velocity profiles were used in this study. The mean flow rate of the Pulsatile waveform is identical to that of the steady waveform. A Poiseuille parabolic inlet velocity profile was used with the steady waveform whilst a plug-flow profile was used with the pulsatile waveform.

It should be noted that the distance that a fluid travels before becoming fully developed, known as the entrance length, can be calculated for laminar flows using Equation 3-9,

$$L_e \approx 0.05 ReD \quad (3-9)$$

In this equation, L_e is the entrance length, Re is the Reynolds number within the channel and D is the diameter of the channel. At a steady flow rate of $2Q_{mean}$, a Reynolds number of 854 is produced with the Newtonian blood viscosity model, which yields an entrance length of 256 mm. This is much longer than the distance between the inlet and the strut in the current geometry. However, less than 5%

difference in recirculation length was observed with this geometry when using a uniform inlet velocity profile instead of a parabolic profile, at steady flow rates of $2Q_{mean}$ and using the Newtonian blood viscosity model. Hence, sufficient distance between the inlet and the strut was assumed to be present to ensure that the flow near the strut approximates its fully developed state.

All remaining haemodynamic boundary conditions were kept the same in each of the six simulations. A uniform, zero gauge pressure boundary condition was specified at the outlet, whilst no-slip conditions were prescribed on the strut-lumen and lumen-tissue interfaces. A fixed-wall assumption was also implemented again [109]. Finally, a symmetry boundary condition was specified at the top of the lumen domain in order to simulate a 6 mm diameter vessel.

Each of the simulations also employed identical boundary conditions to simulate the time-varying release of drug from the strut coating. Initially, a normalised drug concentration of unity was assigned throughout this coating whilst all other lumen and tissue regions were assumed to be devoid of drug. A normalised drug concentration of $c = 0$ was imposed at the inlet, implying that drug-free blood arrives from the inlet. This same boundary condition was ascribed to the perivascular wall, using the assumption that drug would not be able to penetrate to the very bottom of the tissue. Continuity of flux was assumed at the lumen-tissue interface, as well as the strut-tissue and strut-lumen interfaces. Finally, zero flux of drug was specified on each of the remaining boundaries within the lumen, tissue and strut.

3.1.4 Spatial and Temporal Discretisation

Prior to performing the simulations, these boundary conditions were employed in a mesh convergence study to ensure that the results obtained are independent of the

size of the grid used. Using the steady inlet boundary condition in conjunction with the Newtonian model, the flow and drug transport were deemed to be adequately resolved with a mesh containing 149,726 elements. This mesh was subsequently used in each of the simulations that are discussed in this chapter.

The flow was deemed to be resolved once the grid convergence index (GCI) [125],

$$\text{GCI}_{\text{fine grid}} = \frac{3 \left| \frac{f_{\text{fine}} - f_{\text{coarse}}}{f_{\text{fine}}} \right|}{r^p - 1}, \quad (3-10)$$

corresponding to the recirculation lengths proximal and distal to the stent strut fell below 2%. In this equation, f_{fine} and f_{coarse} refer to either the proximal or distal recirculation length for a fine and coarse mesh respectively. r is the refinement factor, and p is the order of accuracy of the solution. In this case, $r = \sqrt{2}$ and $p = 2$. These GCI values were obtained using steady-state solutions in which the flow parameters remained constant with respect to time.

The drug transport behaviour was deemed to be mesh-independent once less than 2% change in area-weighted average concentration (AWAC) of drug was observed in a representative area of tissue between two successive mesh refinements. This representative area was chosen as that of a rectangle bounded by the upper and lower extents of the tissue and axial extents 3.5 strut widths either side of the strut. This 3.5 strut width figure was chosen on the basis that a typical inter-strut distance is 7 strut widths [61].

The fixed time-step that was chosen had to be sufficiently small to resolve the transient drug release. During a 60 s simulation, the AWAC values obtained with a time-step size of $\Delta t = 0.1$ s were identical to the results obtained when $\Delta t = 0.01$ s. Hence, this value of Δt was used in conjunction with the 149,726 element

mesh in the three studies employing a steady inlet velocity boundary condition.

However, 24 hour simulations were also performed with this boundary condition and for these simulations it was determined that a time-step size of $\Delta t = 30$ s yielded an identical AWAC to that obtained when $\Delta t = 1$ s. This larger time-step was therefore used for these longer simulations.

In the studies employing a pulsatile inlet velocity boundary condition, a time-step had to be chosen that resolved both transient drug release and the cyclical changes of velocity. A small time-step of $\Delta t = 20$ μ s was needed in this pulsatile flow study to satisfy the Courant-Friedrichs-Lewy condition. In this condition, the Courant number, CFL , was maintained below unity to ensure that the solution did not become unstable. For a two-dimensional case, the Courant number is defined as:

$$CFL = \frac{V_x \Delta t}{\Delta x} + \frac{V_y \Delta t}{\Delta y}, \quad (3-11)$$

where V_x and V_y are the horizontal and vertical velocities of blood in a grid cell, and Δx and Δy are the horizontal and vertical dimensions of this cell. Due to the small nature of the chosen time-step, a total solution time of 60 s was deemed to be the best compromise of computational time and accurate representation of drug transport.

Despite the extra complexity of the current model, a much coarser mesh was made possible than in the steady-state simulations because of the lower concentrations of drug within the arterial tissue. Specifically, an area-weighted average concentration (AWAC) of only 2.37×10^{-5} was produced after 60 s of drug transport, over three orders of magnitude lower than the AWAC of 0.159 obtained with the steady-state model. As a result, much lower drug concentration gradients were apparent within the present model, which meant that a much coarser mesh could be used to accurately resolve the drug transport behaviour. Further information about the meshes and time-steps used in this study may be seen in Appendix A.

3.2 Results and Discussion

3.2.1 Rheological Effects on Blood Flow

To study the impact of blood rheology on the haemodynamics of the stented vessel, the wall shear stresses along the lumen-tissue interface were obtained for each simulation. Cycle-averaged wall shear stress distributions were attained with each of the pulsatile flow simulations and compared against the wall shear stress distributions obtained with the steady flow boundary condition. These distributions may be seen in Figure 3-3 for the region where $-0.35 \text{ mm} \leq x \leq 0.35 \text{ mm}$. For reference, the mean shear stresses at arterial walls have been previously calculated to be between 1 and 7 Pa [130]. Among the steady flow simulations, both the Power Law Model and the Newtonian model produced wall shear stresses that fell within this range. However, the low dynamic viscosity of the Plasma model yielded a peak wall shear stress of only 0.38 Pa. This is much lower than the expected wall shear stress range stated above because this range was calculated using the assumptions of a constant blood viscosity of $0.0035 \text{ Pa} \cdot \text{s}$ [130].

The results of this analysis showed that pulsatility can strongly affect the magnitude of wall shear stresses along the lumen-tissue interface. The cycle-averaged wall shear stress distribution yielded higher wall shear stresses than the steady flow results obtained with like blood rheological models over the axial extent depicted in Figure 3-3. When the Newtonian model was used, the mean cycle-averaged wall shear stress exceeded the mean wall shear stress of the steady flow model by 36%. Similarly, the mean cycle-averaged wall shear stresses achieved with the plasma and Power Law models were greater than the mean wall shear stresses of the steady flow

models by 88% and 29% respectively. Hence, a steady flow assumption cannot be used to approximate the mean shear stress environment of a stented artery; however, it can be used to provide a conservative estimate of the extent low wall shear stress regions.

Pulsatile (cycle-averaged) vs. Steady

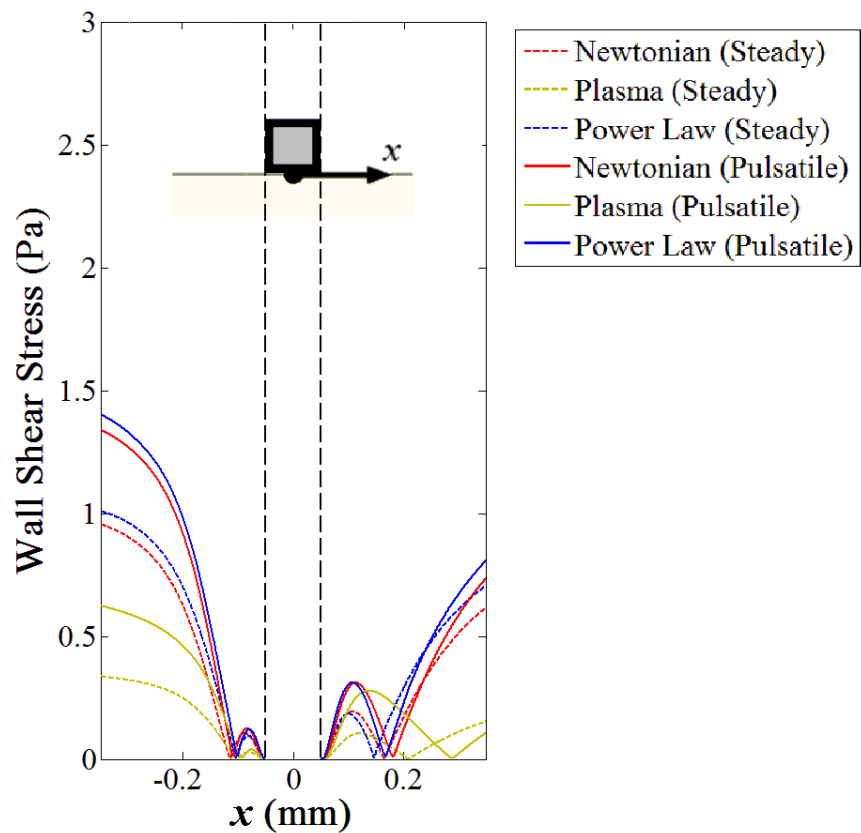


Figure 3-3: Wall shear stress distributions along the lumen-tissue interface.

These results also illustrated that the choice of blood rheological model can influence the magnitude of wall shear stresses. The Power Law model yielded a 9.4% greater mean cycle-averaged wall shear stress than the Newtonian model along the representative section of the lumen-tissue interface shown in Figure 3-3. Meanwhile,

the plasma model yielded a 52% smaller mean cycle-averaged wall shear stress than the Newtonian model. Hence, it is advised that both Power Law and plasma models be implemented in conjunction with the Newtonian model to calculate the range of shear stresses which may be achieved inside a stented artery.

3.2.2 Rheological Effects on Drug Transport

Despite the strong influence of pulsatility and the choice of blood rheological model on the haemodynamics of the vessel, these factors had little impact on the simulated drug transport behaviour. Throughout the sixty seconds, each of the six simulations yielded almost identical AWAC values, as may be seen in Figure 3-4. These results convey that the global drug uptake throughout stented arteries are only modestly affected by pulsatility and the choice of blood rheological model.

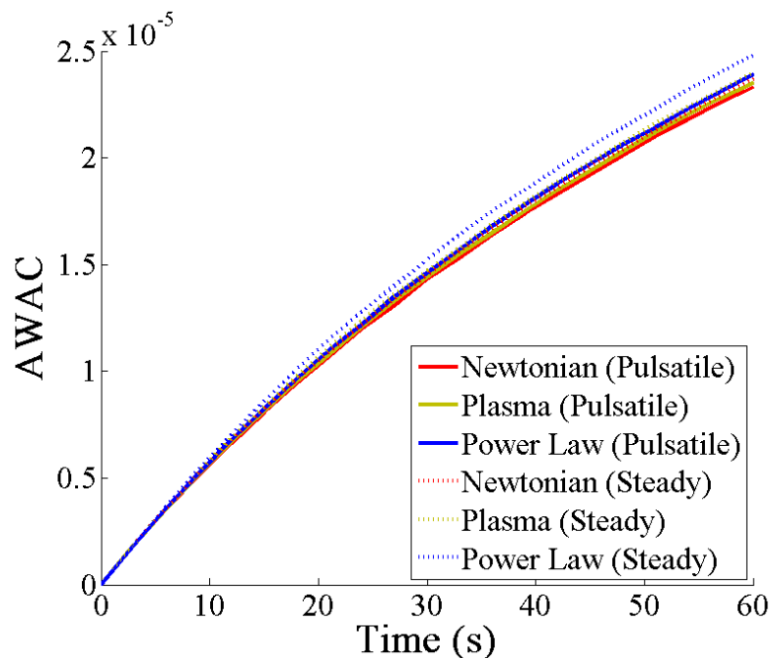


Figure 3-4. The impact of blood rheological model selection and pulsatility on the area-weighted average concentration (AWAC) of drug in the arterial tissue.

Furthermore, the results presented in Figure 3-5 show that there is minimal difference in the spatial distribution of drug within the arterial tissue at the culmination of the 60 second study period. As expected, localised regions of high drug concentration can be observed in the lumen in the regions where recirculating flow occurs. However, unlike the steady-state results of Chapter 2, these drug concentrations are not high enough to strongly impact the spatial distribution of drug within the tissue. Additionally, it may be seen Figure 3-5 that the concentrations of drug within the recirculation zones are even lower in the pulsatile flow cases than in the steady flow cases. This implies that even if flow-mediated drug transport is stronger at lower flow rates – as was observed in Chapter 2 – its impact is nullified over several cardiac cycles. Hence, these results imply that the drug distributions throughout stented arteries are only modestly affected by the pulsatility of blood flow and the choice of blood rheological model.

To see if these differences are still negligible at extended time periods, the normalised drug concentration, c , was calculated along each strut face at the culmination of 60 seconds. Although a unity value of c was initially assigned throughout the coating, these values decreased considerably at the outer surfaces of the coating after 60 seconds had elapsed, as may be seen in Figure 3-6. These results also showed that drug depletes much more rapidly at the coating surfaces exposed to blood flow than at the tissue interface; hence, the assumptions used in some numerical studies, whereby each strut face possesses time-invariant drug concentrations or identical rates of drug depletion, are inadequate.

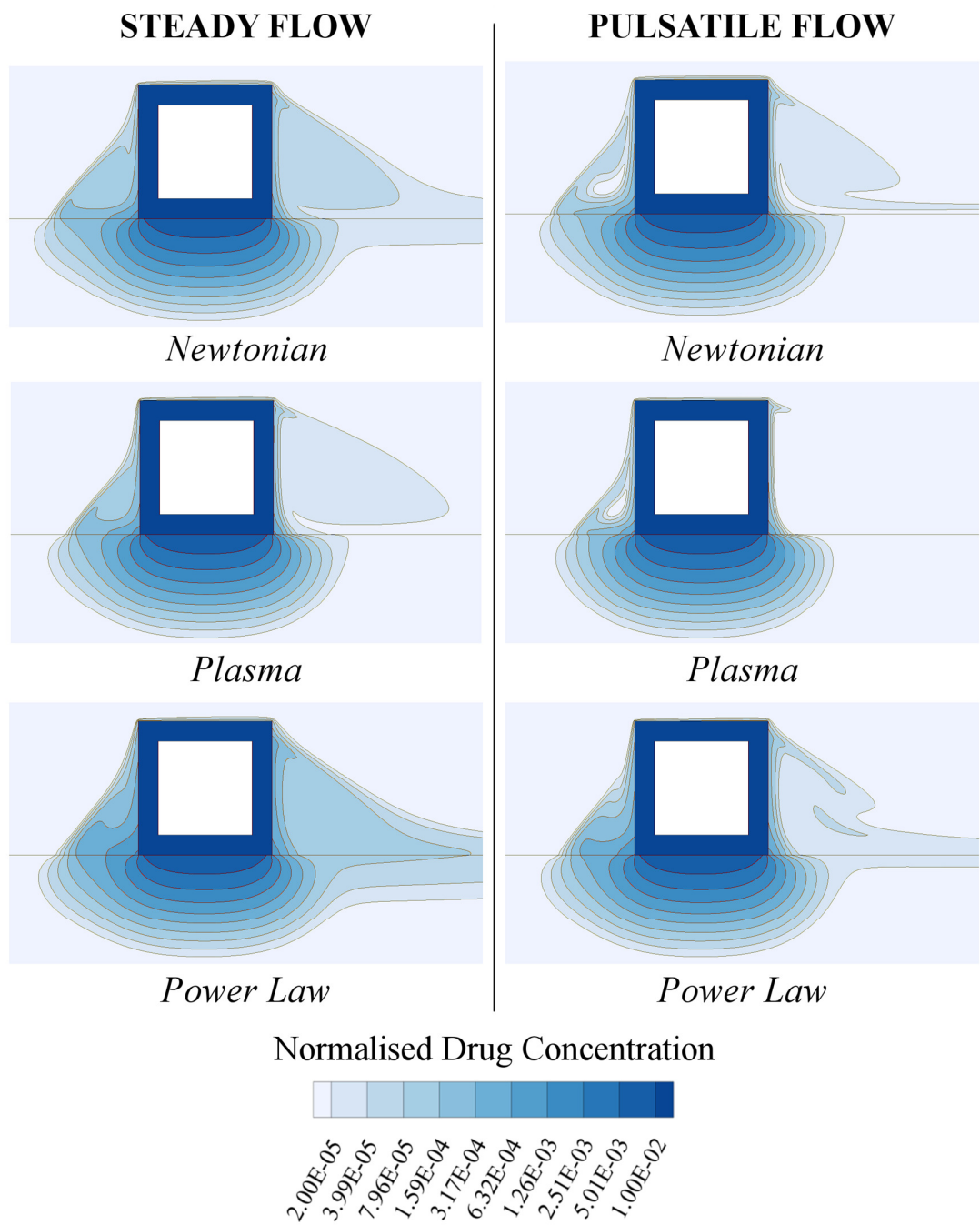


Figure 3-5. Normalised drug concentration distribution at the culmination of 60 seconds.

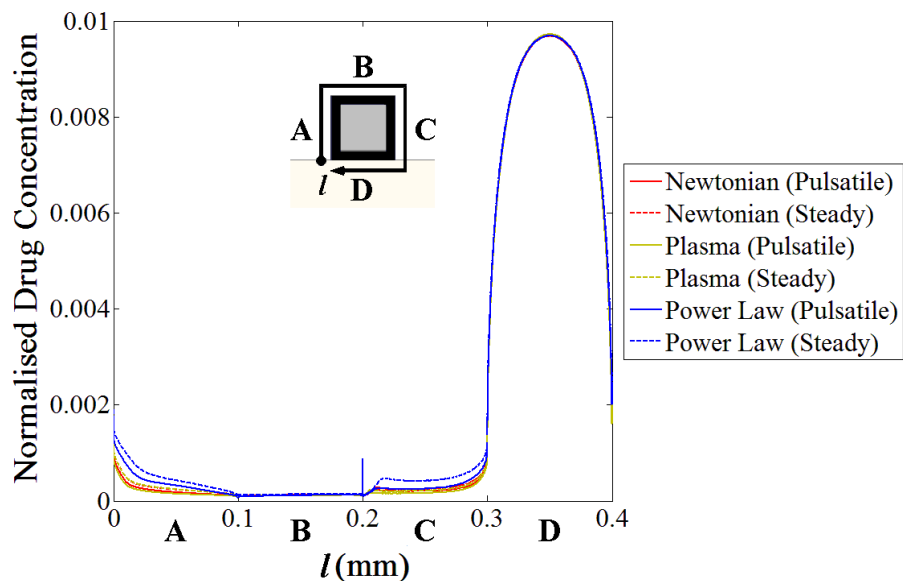


Figure 3-6. Normalised drug concentration at the outer surfaces of the strut coating after 60 seconds. Although pulsatility and the choice of blood rheological model do impact the drug concentration at sides A and C, they have little impact on the concentration at side D. The drug depletes more readily at the strut surfaces exposed to blood flow than at side D, which accounts for the similar magnitude of drug uptake achieved with each model.

These results also imply that the contribution of flow-mediated drug transport becomes less significant as time goes on. The fact that no significant differences in drug transport behaviour were noted between any of the models at the 60 second mark – in which time the drug pools either side of the strut visibly start depleting – therefore implies that no significant differences will ever transpire. Hence, the frequently used assumptions that blood is a Newtonian fluid and that its flow is steady are safe to use when investigating drug uptake.

To illustrate the insignificance of flow-mediated drug uptake, two additional steady-flow simulations were performed in which the drug was allowed to elute from the stent strut over a period of 24 hours. Unlike the previous simulations, a time-step size of $\Delta t = 30$ s was used in this study as the AWAC produced yielded less than 1%

difference to the values obtained with a time-step of $\Delta t = 0.1$ s. A large time-step could be used in these studies as the flow is laminar and steady, meaning that no changes to the flow field were observed throughout the 24 hour simulation. Hence, the Courant-Friedrichs-Lewy condition did not have to be met and the time-step only had to be small enough to resolve the time-varying drug transport behaviour.

The normalised drug concentration results shown in Figure 3-7a were obtained using the drug transport model described in this chapter in conjunction with the Newtonian blood viscosity model. Conversely, the results shown in Figure 3-7b were obtained using a drug transport model which disallowed the transport of drug from the coating into the arterial lumen. This was accomplished by specifying a zero drug flux boundary condition on the inner edges of the coating-lumen interface and imposing the condition $c = 0$ on the outer edges of this interface. A unity normalised drug concentration was specified throughout the strut coating at the start of each simulation; however, only the second case eliminated flow-mediated drug transport.

When the contours of Figure 3-7a and Figure 3-7b are rescaled in a and b respectively, it is apparent that both models yield very similar drug transport behaviour within the arterial tissue. The model which allowed flow-mediated drug transport produced an AWAC of 1.92×10^{-5} , almost identical to the value of 1.91×10^{-5} achieved with the model which negated flow-mediated drug transport. Hence, flow-mediated drug transport does not strongly influence drug uptake at any location within the arterial tissue.

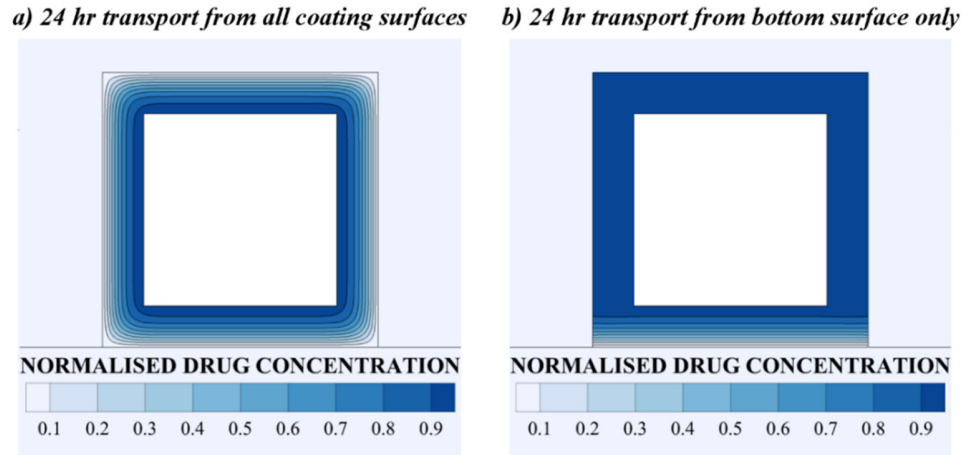


Figure 3-7. The normalised drug concentration at the strut coating obtained with two different drug transport models at the conclusion of 24 hours. The first model (a) was the same model used in each of the preceding analyses and facilitated drug transport from every strut surface. Conversely, the second model (b) only allowed drug to be transported into the tissue from the bottom strut surface, thereby eliminating flow-mediated drug uptake.

The significance of flow-mediated drug transport is vastly overestimated in steady-state simulations, which cannot model the depletion of drug at the stent coating. To illustrate this, a steady-state solution obtained in Chapter 2 with the Newtonian blood viscosity model is shown in Figure 3-8c. In contrast to the normalised drug concentration distributions of Figure 3-8a and Figure 3-8b, these results are highly asymmetrical. Furthermore, with an AWAC of 0.159, they are also significantly higher in concentration. Ergo, the drug transport behaviour of drug-eluting stents is not well represented by steady-state models and it is important to model the depletion of drug from the stent coating.

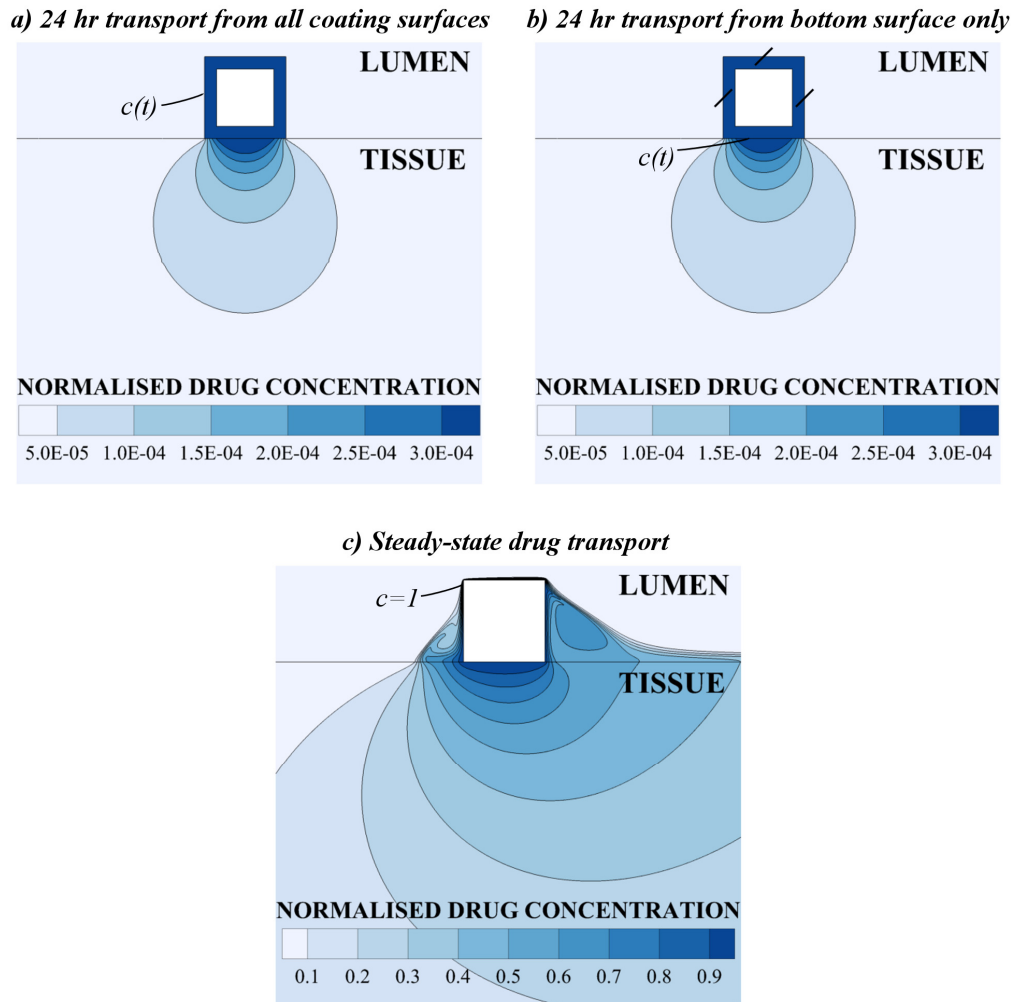


Figure 3-8. Comparison of the normalised drug concentration contours obtained with various drug transport models. The first model (a) facilitates drug transport from each strut surface. The second model (b) does not allow flow-mediated drug transport yet yields a near-identical spatial distribution of drug to the first model. Steady flow and transient drug transport assumptions were used in both of these models. Finally, steady-state drug transport models (c) vastly overestimate the magnitude of drug transport into the arterial wall, as well as the contribution of flow-mediated drug transport.

3.3 Outcomes

In this study, a series of computational fluid dynamics simulations were performed to investigate the impact of blood rheology on the drug transport behaviour of an artery treated with a drug-eluting stent. A Newtonian blood viscosity model was contrasted with a Power Law non-Newtonian blood viscosity model and a Newtonian plasma viscosity model to study the full spectrum of blood rheological behaviour. Unlike previous studies of the impact of blood rheology on drug transport, depletion of drug from the coating was modelled in the simulation to mimic the time-dependent loss of drug at each face of the stent strut.

The choice of fluid model significantly affected the magnitude of wall shear stresses near the stent strut. The Power Law model yielded the highest wall shear stresses whilst the plasma model produced the lowest wall shear stresses. Pulsatility was also shown to affect the magnitude of wall shear stresses, with higher stresses occurring at high flow rates. Indeed, the cycle-averaged wall shear stresses obtained from the pulsatile analyses were substantially higher than the wall shear stresses obtained in the steady flow analyses. Hence, a steady flow assumption cannot be used to approximate the mean shear stress environment of a stented artery; however, it could be used to provide a conservative estimate of the extent of low wall shear stress regions. It was also shown that both Power Law and plasma models should be implemented in conjunction with the Newtonian model to calculate the range of shear stresses which may be achieved inside a stented artery.

However, neither pulsatility nor the choice of blood rheological model were found to significantly affect either the magnitude or spatial distribution of drug within the arterial tissue. It was also shown that the assumptions that blood is a Newtonian fluid and that its flow is steady are appropriate to use when investigating

the global distribution of the drug resulting from drug-eluting stent use. Steady-state simulations, however, were found to be unrealistic, as the drug concentrations at the strut boundaries are heavily time-dependent. It was therefore concluded that the depletion of drug from each strut surface should be modelled and that flow-mediated drug transport does not globally affect drug uptake.

Chapter 4

The Impact of Blood Rheology on Drug Transport in Stented Arteries: Experimental Validation

Chapter Aims

It was shown in the preceding chapter that flow-mediated drug transport in arteries treated with drug-eluting stents is negligible. This is in stark contrast to the results of previous numerical studies, which showed that non-contacting strut surfaces can contribute up to 90% of arterial drug uptake. The aim of this study is to validate the drug transport model used in the preceding chapter, and to show if flow-mediated drug transport is truly negligible.

4.1 Methods

4.1.1 Experimental Framework

The validation of this drug transport model was established through a modified version of the pre-existing in-vitro framework developed by O'Brien et al. [75]. In this framework, the stented artery environment was modelled using an acrylic flow rig, a hydrogel and a polydimethylsiloxane (PDMS) strut loaded with a fluorescent marker, as shown in Figure 4-1a. The flow of a blood analogue fluid through this flow rig was used to mimic arterial blood flow, whilst the hydrogel and the PDMS strut mimicked arterial tissue and a stent strut respectively. Ultimately, the drug transport from a drug-eluting stent strut into arterial tissue was represented via the diffusion of a fluorescent marker from this PDMS strut into the hydrogel.

The concentrations of the fluorescent marker within the hydrogel were monitored using the Laser-Induced Fluorescence (LIF) technique. In this technique, a green light was used to excite the eluted marker, causing it to emit light of a nominal frequency. The intensities of the emitted light were measured using an epi-fluorescence microscope and the fluorescent marker concentrations were subsequently ascertained from these light intensities. The marker concentrations were monitored over a period of 180 minutes whilst a peristaltic pump transported blood analogue fluid through the flow rig. The temperature of this fluid at the flow rig outlet was also monitored over the 180-minute period using a thermocouple, as may be seen in Figure 4-1b. The complete experimental procedure may be seen in Appendix B.

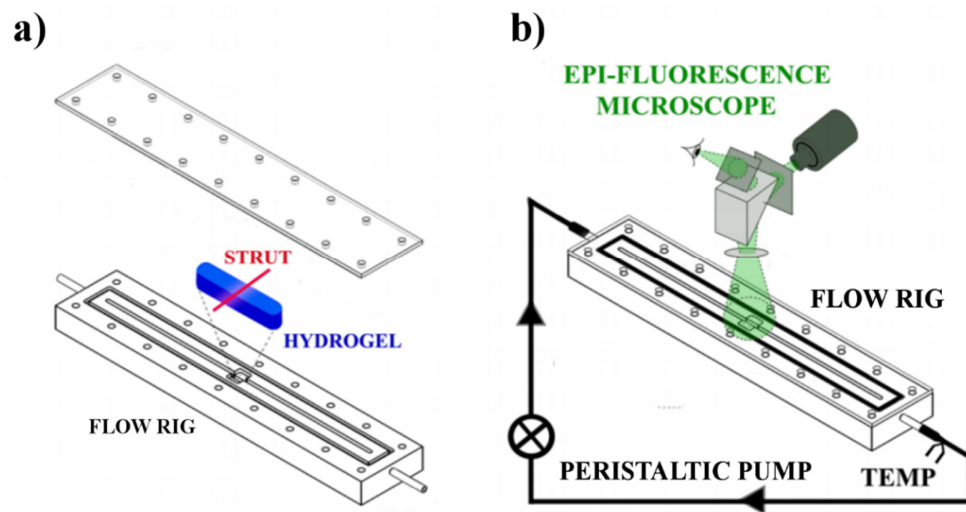


Figure 4-1. Schematic of the acrylic flow rig assembly (a) and the equipment used to monitor the drug uptake within the channel (b). Image copyright of O'Brien et al. [75] and modified with permission.

Flow Rig

The same flow rig used in the study by O'Brien et al. [75] was used in the current study. It was constructed from a clear acrylic block and featured a 3 mm square cross-section channel. The channel was sealed by securing a 3 mm thick acrylic lid onto the channel using 18 x M3 screws. A rubber o-ring encircling the channel ensured that the blood analogue fluid did not leak out of the rig.

The centre of the channel features a recess used to accommodate the hydrogel and two small acrylic blocks, shown in Figure 4-2, that are used to clamp the strut onto the hydrogel. These acrylic blocks were each secured onto the flow rig using $2 \times$ M1.2 screws. Meanwhile, the hydrogel recess was designed to allow the hydrogel to sit flush against the channel wall so that only its top surface is exposed to fluid flow.

The channel was also designed to be long enough to ensure that the flow of the blood analogue fluid is fully developed prior to reaching the hydrogel. Given the

square cross section of the channel, the distance that the laminar flow travels before becoming fully developed, known as the entrance length, could be calculated using Equation 4-1.

$$L_e \approx 0.05 ReD_h \quad (4-1)$$

In this equation, L_e is the entrance length, Re is the Reynolds number within the square channel and D_h is its hydraulic diameter. Given that $D_h = 0.003$ m and that a Reynolds number of 427 is desired to match the mean flow conditions of the renal vasculature [75], an entrance length of $L_e = 0.064$ m was calculated. In contrast, the square channel runs a total length of 0.124 m before reaching the hydrogel, thereby guaranteeing that the flow is fully developed before reaching the strut.

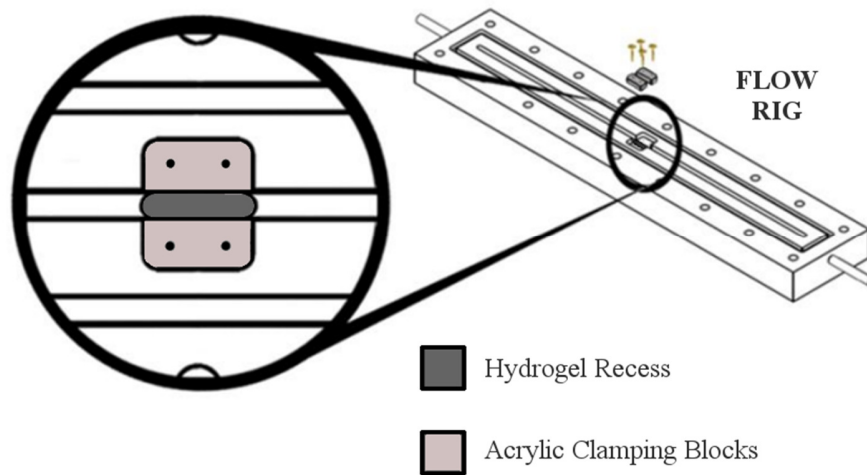


Figure 4-2. Close-up of the hydrogel recess and the acrylic blocks that are used to clamp the strut onto the hydrogel. Image copyright of O'Brien et al. [75] and modified with permission.

Blood Analogue Fluid

The blood analogue fluid that flows through this channel is a solution of glycerol (40 wt.%) and deionised water (60 wt.%). This fluid was chosen for its

optical transparency and because it possesses a similar dynamic viscosity and density to real blood.

The density of the glycerol-water solution, ρ_{gw} , was calculated analytically using the densities of glycerol, ρ_g , and water, ρ_w , viz:

$$\rho_{gw} = \gamma\rho_g + (1 - \gamma)\rho_w. \quad (4-2)$$

In this equation, γ is the weight fraction of glycerol in the solution. At an experimental temperature, T (in °C), say 23°C, $\rho_w = 997 \text{ kg/m}^3$ and $\rho_g = 1258 \text{ kg/m}^3$. Given that $\gamma = 0.4$, the density of the glycerol-water solution at 23°C is $\rho_{gw} = 1101 \text{ kg/m}^3$.

The viscosity of the glycerol-water solution, μ_{gw} , was calculated using an empirical formula [131],

$$\mu_{gw} = 0.001(1000\mu_w)^\alpha(1000\mu_g)^{1-\alpha}, \quad (4-3)$$

where μ_w and μ_g refer to the dynamic viscosities of water and glycerol respectively.

The superscript, α , is a weighting factor which varies between 0 and 1, and is given by the formula:

$$\alpha = 1 - \gamma + \frac{ab\gamma(1 - \gamma)}{a\gamma + b(1 - \gamma)}, \quad (4-4)$$

where

$$a = 0.705 - 0.0017T, \quad (4-5)$$

and

$$b = (4.9 + 0.036T)a^{2.5}. \quad (4-6)$$

For a temperature of $T = 23^\circ\text{C}$, a weighting factor of $\alpha = 0.819$ is produced. The dynamic viscosities of water and glycerol were also calculated using empirical formulae [131], specifically

$$\mu_w = 0.001790 \exp\left(\frac{(-1230 - T)T}{36100 + 360T}\right), \quad (4-7)$$

and

$$\mu_g = 12.1 \exp\left(\frac{(-1233 + T)T}{9900 + 70T}\right). \quad (4-8)$$

At 23°C, the values of μ_w and μ_g were calculated to be 9.35×10^{-4} Pa·s and 1.078 Pa·s respectively. Substituting these values into Equation 4-2, the viscosity of the blood analogue solution at 23°C was calculated to be $\mu_{gw} = 0.00334$ Pa·s.

Pump

The flow of this blood analogue solution through the flow channel was achieved using a LongerPump BT600-2J peristaltic pump. The rotational speed of the rollers within the pump were adjusted to achieve a Reynolds number of 427, consistent with the mean flow conditions of the renal vasculature [75]. This Reynolds number, Re , was calculated using the formula

$$Re = \frac{\rho_{gw} \bar{V} D_h}{\mu_{gw}}, \quad (4-9)$$

where \bar{V} is the mean velocity of the blood analogue fluid and D_h is the hydraulic diameter of the square, acrylic channel. Given that $D_h = 0.003$ m, a mean velocity of $\bar{V} = 0.432$ m/s was needed to achieve a Reynolds number of 427. This meant that the blood analogue fluid was pumped through the channel at a flow rate of 3.89 mL/s.

Temperature

The temperature of this pumped fluid was monitored using a thermocouple every 30 minutes. At no point during any of the experiments was the temperature of the fluid measured to be more than 1°C above or below 23°C. It was important to

regulate this temperature since the transport characteristics of the fluorescent marker into the fluid and hydrogel are strongly affected by temperature changes.

Hydrogel

The hydrogel used in this study was fabricated from a poly-(vinyl alcohol) (PVA, 16kDa, 98% hydrolysed) functionalised with 7 methacrylate crosslinks via reaction with 2-isocyanatoethylmethacrylate (ICEMA), using the method of Bryant et al. [132]. This hydrogel was used due to its optical transparency and due to its high porosity of 80%, similar to the 61% porosity of the arterial media [133]. The method used to create these hydrogels may be seen in Appendix C and the dimensions of the final product may be seen in Figure 4-3.

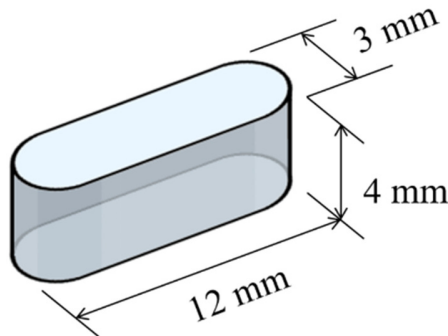


Figure 4-3. Hydrogel dimensions.

Strut

A single strip of polydimethylsiloxane (PDMS) loaded with a Rhodamine B fluorescent marker was placed atop this hydrogel, where it served as the drug-eluting stent strut analogue. The amorphous nature of the PDMS polymer facilitated a matrix-type delivery, consistent with the release of drug from a drug-eluting stent [134]. However, a metallic stent platform was not included in this strut due to ease of manufacture and because the flat nature of the hydrogel allowed the strut to

lie on top without needing structural support. Hence, the PDMS strut was essentially used to model the polymer drug coating of a drug-eluting stent strut rather than the stent platform itself.

Each strut was manufactured by mixing a 7:1 base/agent mass ratio PDMS solution (Sylgard® 184 Silicone Elastomer) with Rhodamine B powder (Sigma-R6626). 0.01 g of Rhodamine B were added to each gram of PDMS solution and Ethyl alcohol was added to allow the powder to be evenly mixed. Once the alcohol had evaporated, a thin 100 μm film was created with this mixture, using the method described in Appendix D. Once cured, this film was cut into 450 μm slices to produce struts with the dimensions shown in Figure 4-4.

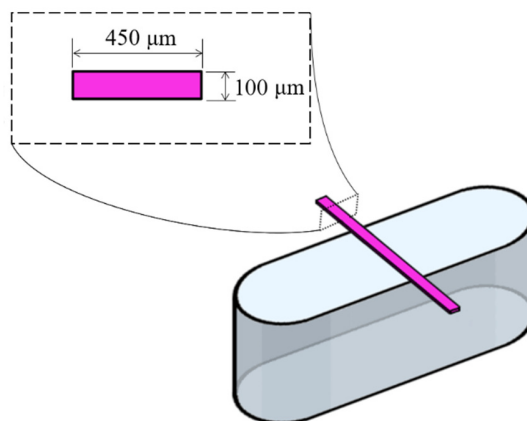


Figure 4-4. Strut dimensions.

Fluorescent Marker

The choice of Rhodamine B as the fluorescent marker was made for three reasons. Firstly, the absorption wavelength of Rhodamine B is 542-554 nm (green light) and the efficiency of the mercury lamp used in this study is highest when working in this green spectrum. Secondly, the use of a hydrogel meant that a hydrophilic marker had to be used. Lastly, the size of the drug affects its transport [135] and hence the

marker had to have a similar molecular size to Paclitaxel, the drug used in the computational analyses of Chapters 2 and 3.

Epifluorescence microscope

The distribution of this marker throughout the hydrogel was monitored using an inverted epifluorescence microscope (Nikon Eclipse TE2000). During this process, green light was emitted from a 100W mercury arc-discharge lamp and shone through the microscope's objective onto the hydrogel and strut. The lamp generates a localised peak in intensity at a wavelength of $\lambda = 546$ nm, within the absorption wavelength range of Rhodamine B. This causes the fluorescent marker to emit light of a nominal wavelength of $\lambda = 627$ nm. A $4\times$ magnification objective was used as it facilitated the visualisation of both the strut and the localised regions of the hydrogel in which significant Rhodamine B uptake transpired.

Images of the distribution of this marker were taken with a PCO pixelfly CCD camera that was mounted onto the microscope. These images were taken in 30 minute intervals after the flow rig had been filled with glycerol-water. The blood analogue fluid was pumped through the flow rig for a total time of 180 minutes. Following this, the hydrogel was removed from the acrylic flow rig and sliced in half to reveal the cross-sectional marker distribution. Finally, images of these distributions were captured using the camera. An exposure time of 400 ms was used to capture each image and the mercury lamp shutter was closed when not taking these images to minimise photobleaching. This experiment was repeated once more, yielding a total of two 180 minute experiments and four cross-sectional images. However, before these results could be used to validate the computational model of

Chapter 3, the diffusion coefficients of Rhodamine B in glycerol-water, the hydrogel and the strut needed to be determined.

4.1.2 Diffusion Studies

These diffusion coefficients were obtained experimentally using a pair of side-by-side diffusion cells (SIDE-BI-SIDE, PermeGear). These diffusion cells both consisted of a 3 mL fluid chamber surrounded by a water jacket, as may be seen in Figure 4-5. The flow of water via a peristaltic pump through these jackets regulated the temperature of the fluid within the two chambers to within 0.5°C of 23°C. A sampling port atop each fluid chamber allowed samples to be collected from the cells whilst magnetic stirrers ensured that the collected samples are well-mixed. A flat 9 mm diameter orifice was present on the side of each chamber and these orifices were aligned in the manner depicted in Figure 4-5. Finally, a membrane surrounded by a rubber washer was placed between the orifices of both cells, which were then clamped together to establish a seal.

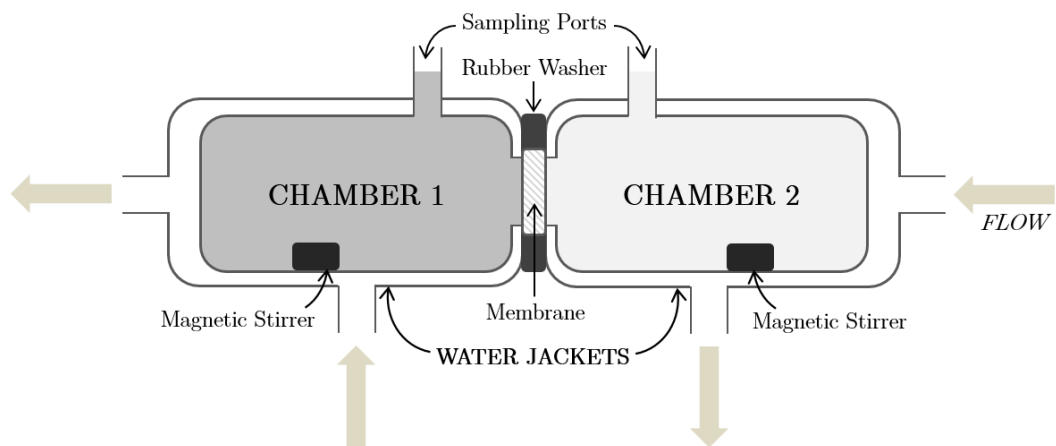


Figure 4-5. 'Side-Bi-Side' diffusion cell schematic.

Unique membranes were used to measure the diffusion coefficients of Rhodamine B within the glycerol-water solution, the hydrogel and the strut respectively. The diffusion coefficient of Rhodamine B in glycerol-water, D_{fluid} , was measured using a 50 μm thick cell strainer (Corning, 431751) with a pore size of 70 μm and a porosity of 23%. A 1 mm thick hydrogel film with a porosity of 80% was then used to measure the diffusion coefficient of Rhodamine B in the hydrogel, $D_{hydrogel}$. Finally, the diffusion coefficient of Rhodamine B within the PDMS strut, D_{strut} , was measured using a 100 μm thick film of the Rhodamine B/PDMS mixture used to manufacture the strut. A more detailed account of the steps performed in these diffusion studies may be seen in Appendix E.

When measuring D_{strut} , both reservoirs were filled with the glycerol-water solution. This diffusion coefficient was calculated using the formula [136]

$$\frac{M_t}{M_0} \approx 4 \sqrt{\frac{D_{strut} t}{(\delta_{strut})^2 \pi}}, \quad (4-10)$$

where M_t is the amount of solute released into the chamber at time t , M_0 is the amount of solute initially found within a representative volume of the film, and $2\delta_{strut}$ is the film thickness. This representative volume was defined as:

$$V_{strut} = A_{orifice} \delta_{strut}, \quad (4-11)$$

where $A_{orifice}$ is the area of the orifice on the side of each chamber and $2\delta_{strut}$ is the thickness of the Rhodamine B/PDMS film. Given that $2\delta_{strut} = 100 \mu\text{m}$ and $A_{orifice} = 6.4 \times 10^{-5} \text{ m}^2$, the representative volume of the film was calculated to be $V_{strut} = 3.2 \times 10^{-9} \text{ m}^3$. As the films had a density of $9.7 \times 10^2 \text{ kg/m}^3$ and contained 1 wt.% Rhodamine B, the initial mass of solute within this volume is $M_0 = 3.1 \times 10^{-8} \text{ kg}$. Hence, only the value of M_t needed to be monitored with respect to time to determine D_{strut} .

When measuring D_{fluid} , only Chamber 2 was filled with glycerol-water whilst Chamber 1 featured glycerol-water with 0.01 kg/m^3 of Rhodamine B. The cell containing Chamber 1 is thus referred to as the donor cell whilst the cell containing Chamber 2 is referred to as the recipient cell. D_{fluid} was determined using the equation [105]

$$D_{fluid} = \frac{V_{cell} \delta_{strainer}}{C_{d0} A_{strainer}} \frac{\partial C}{\partial t}, \quad (4-12)$$

where V_{cell} is the volume of fluid in the recipient cell, $\delta_{strainer}$ is the thickness of the cell-strainer membrane, C_{d0} is the initial concentration of Rhodamine B within the donor cell, and $A_{strainer}$ is the total open area of the cell strainer membrane. This open area is defined as:

$$A_{strainer} = A_{orifice} \epsilon_{strainer}, \quad (4-13)$$

where $\epsilon_{strainer}$ is the porosity of the membrane. Furthermore, $V = 3 \times 10^{-6} \text{ m}^3$, $\delta_{strainer} = 5 \times 10^{-5} \text{ m}$ and $C_{d0} = 0.01 \text{ kg/m}^3$. Hence, only the time rate of change of Rhodamine B concentration in the recipient chamber was needed to determine D_{fluid} .

$D_{hydrogel}$ was determined in the same manner as D_{fluid} except that the hydrogel film was clamped between the donor and recipient cells in place of the cell strainer. In this case,

$$D_{hydrogel} = \frac{V_{cell} \delta_{hydrogel}}{C_{d0} A_{hydrogel}} \frac{\partial C}{\partial t}, \quad (4-14)$$

where $\delta_{hydrogel}$ is the thickness of the hydrogel film and $A_{hydrogel}$ is the total open area of the hydrogel membrane. This open area is defined as:

$$A_{hydrogel} = A_{orifice} \epsilon_{hydrogel}, \quad (4-15)$$

where $\epsilon_{hydrogel}$ is the porosity of the hydrogel. Given that $\epsilon_{hydrogel} = 0.8$ and that $A_{orifice}$ is unchanged, a total open area of $A_{hydrogel} = 5.09 \times 10^{-5} \text{ m}^2$ was calculated. Furthermore, the hydrogel thickness is $\delta_{hydrogel} = 1 \times 10^{-3} \text{ m}$ and $C_{d0} = 0.01 \text{ kg/m}^3$.

Hence, only the time rate of change of the Rhodamine B concentration in the recipient chamber was needed to determine $D_{hydrogel}$.

The concentrations of the solute in each of the recipient chambers were measured using a microplate reader (INFINITE 200PRO, Tecan) through comparison with a standard dilution series. 100 μL aliquots were taken from the recipient chambers at staggered intervals over five hours when measuring $D_{hydrogel}$ and D_{strut} and over 75 minutes when measuring D_{fluid} . The recipient cells were then replenished with 100 μL of glycerol-water to ensure that 3 mL of fluid was always contained within the cell. The collected samples were contained within black Eppendorf tubes to minimise photobleaching, diluted with 900 μL of glycerol-water, and then stored within a refrigerator to minimise evaporation.

The reason for diluting these samples was to allow 100 μL of the solution to be extracted from the Eppendorf tubes and transferred into the wells of a black 96-well solid-bottomed microplate. These samples, as well as 100 μL samples of the standard dilution series were then read using the microplate reader. As may be seen in Figure 4-6, the fluorescence intensities of the light emitted from the standard dilution series are proportional to the concentrations of Rhodamine B within each sample.

The concentrations of Rhodamine B within the collected samples could therefore be obtained by dividing the intensity by the gradient of the linear regression line. However, because these samples were diluted, the concentrations of the samples that were originally extracted from the recipient cells had to be obtained using the following equation:

$$C = \frac{Intensity}{3.00 \times 10^7} \times Dilution\ Factor. \quad (4-16)$$

Given a dilution factor of 10, the concentrations obtained were substituted into Equations 4-9, 4-11 and 4-13 to obtain the values of D_{strut} , D_{fluid} and $D_{hydrogel}$.

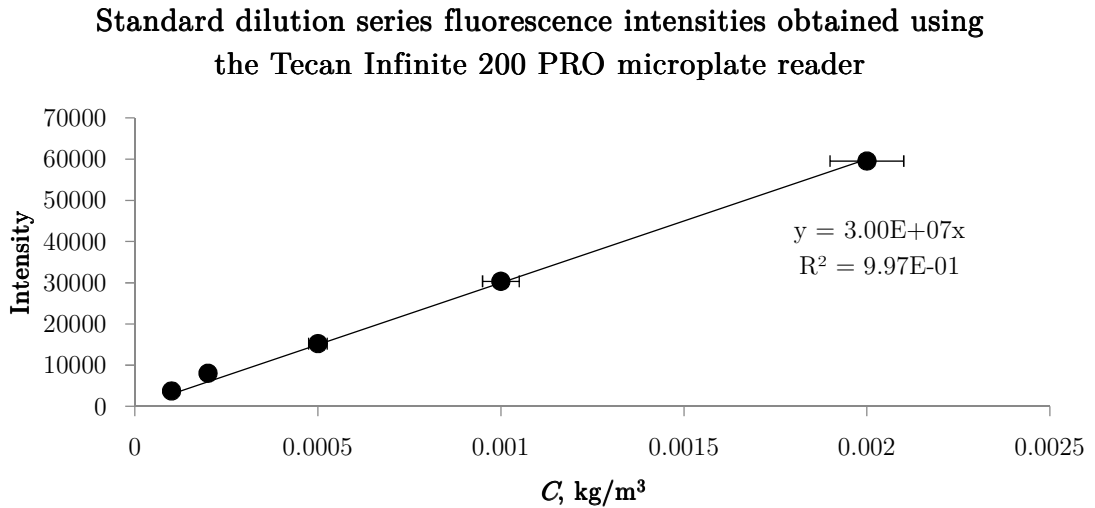


Figure 4-6. The plate readings of the standard dilutions revealed a linear relationship between the intensity of the emitted light and the concentration of Rhodamine B within each sample. The absolute errors in the concentration and intensity of the standard dilution series are shown.

To determine D_{strut} , the relationship between the proportion of solute released (M_t/M_0) and the square root of the time of elution was plotted. These results, shown in Figure 4-7 for three different trials, illustrate that a linear relationship was well approximated in each case. Using Equation 4-9 and the gradients of the three linear trendlines in Figure 4-7, a coefficient of $D_{strut} = 4.03 \pm 0.88 \times 10^{-15} \text{ m}^2/\text{s}$ was calculated. This is larger than the diffusivity of Paclitaxel within the drug coating that was used in Chapter 3, $D_c = 2.60 \times 10^{-16} \text{ m}^2/\text{s}$, but only by a factor of 15.5.

Diffusion of Rhodamine B from Rhodamine B/PDMS films

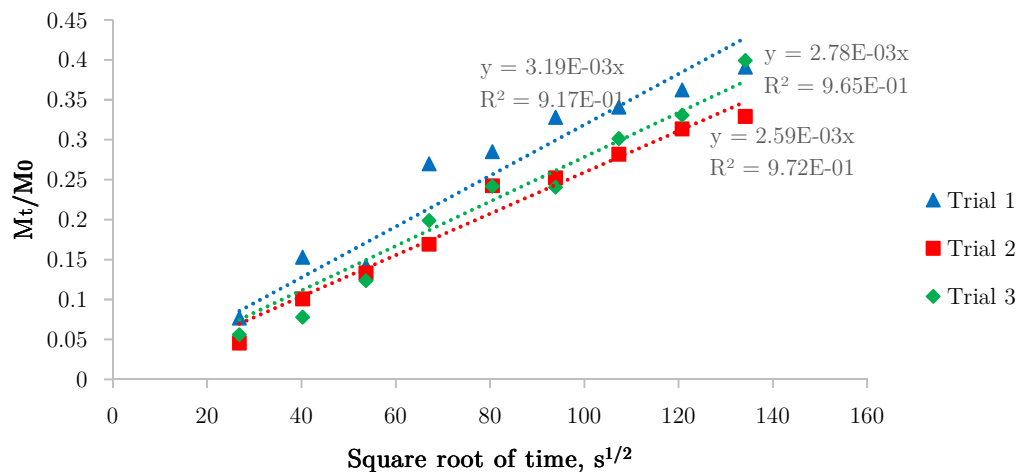


Figure 4-7. Relationship between the proportion of Rhodamine B released from the PDMS/Rhodamine B membrane and the square-root of the time of elution.

The variations in the three tests are most likely to have been caused by non-uniform Rhodamine B concentrations on the surfaces of the three PDMS/Rhodamine B films. These non-uniformities can arise because the marker readily diffuses from the surfaces of the films, even onto the glass slides used to make them. Additionally, although measures were taken to mitigate UV exposure during the diffusion studies, it is conceivable that this could also account for some of the differences between the three trials in Figure 4-7.

To determine D_{fluid} , the concentration of Rhodamine B in the recipient chamber was plotted against the time of elution, as may be seen in Figure 4-8. A linear regression analysis was then performed for each of the three trials and the gradients of these regression lines, $\partial C/\partial t$, were substituted into Equation 4-11. Only 75 minutes' worth of data were collected as the Rhodamine B concentrations in the recipient cells were greater than 10% of the initial donor cell concentration beyond this time. The cell strainer possessed a porosity of 23% and its pore size of 70 μm is

almost 40,000 times larger than the diameter of the Rhodamine B molecule, meaning that negligible impedance occurs through the membrane. A diffusion coefficient of $D_{fluid} = 1.38 \pm 1.03 \times 10^{-10} \text{ m}^2/\text{s}$ was subsequently produced from these three analyses; however, only Trial 2 yielded more than three data-points in which the Rhodamine B concentrations were within 10% of the donor cell's initial Rhodamine B concentration, $C_0 = 0.01 \text{ kg}/\text{m}^3$. Hence, only the value of $D_{fluid} = 6.59 \times 10^{-11} \text{ m}^2/\text{s}$ that was obtained with Trial 2 was used in this validation study.

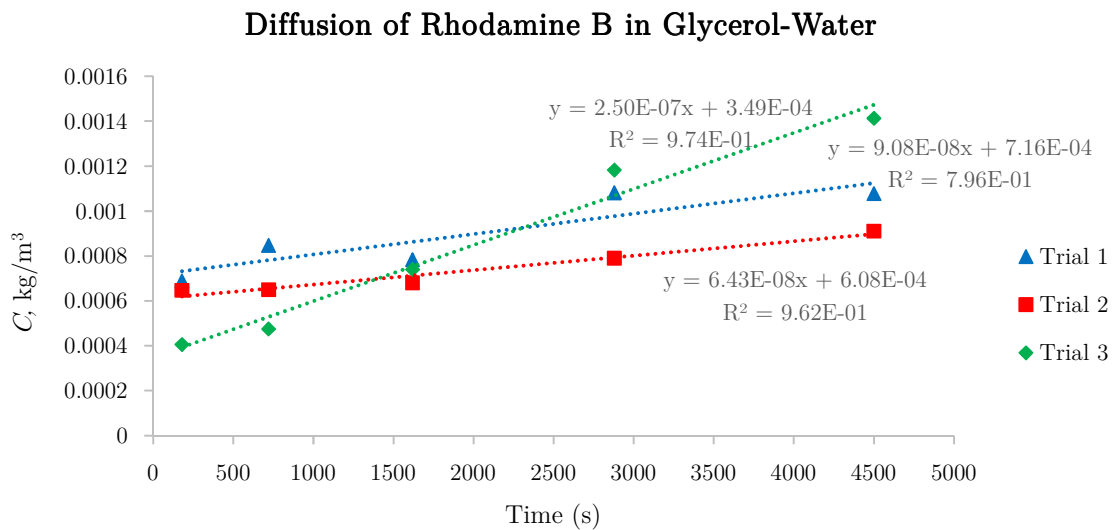


Figure 4-8. Relationship between the concentration of Rhodamine B in the receptor cell and the time of elution through a cell strainer membrane.

The large variations between these trials are likely due to two main reasons. Firstly, unlike the PDMS/Rhodamine B films, the cell-strainer membranes used in these trials are permeable. This means that great difficulty is encountered in keeping the fluids within the donor and recipient cells separate whilst filling up the cells. It is for this reason why there are such large differences in the initial concentrations of Rhodamine B within the glycerol water in Figure 4-8. Secondly, as in the previous diffusion study, it is also conceivable that UV exposure could account for some of the

differences between the three trials. Due to the large variations observed, the value of $D_{fluid} = 6.59 \times 10^{-11} \text{ m}^2/\text{s}$ was compared against a theoretical value to assess its accuracy.

To ensure that this diffusion coefficient is accurate, the Stokes-Einstein equation was used to estimate the diffusion coefficient of the solute within the working fluid. This equation takes the following form:

$$D_{fluid} = \frac{kT}{6\pi\mu_{gw}R}, \quad (4-17)$$

where k is Boltzmann's constant, T is the temperature of the fluid and R is the radius of the Rhodamine B molecule. Given that $k = 1.3807 \times 10^{-23} \text{ J/K}$, $T = 296 \text{ K}$ and that the diameter of the Rhodamine B molecule is $2R = 1.7 \times 10^{-9} \text{ m}$, a theoretical diffusion coefficient of $D_{fluid} = 7.64 \times 10^{-11} \text{ m}^2/\text{s}$ was calculated. Hence, the experimentally obtained diffusion coefficient, $D_{fluid} = 6.59 \times 10^{-11} \text{ m}^2/\text{s}$, conforms to expectations. It is also only 1.7 times higher than the diffusion coefficient of Paclitaxel within blood that was used in the preceding chapters, $D_l = 3.89 \times 10^{-11} \text{ m}^2/\text{s}$.

This similar diffusion coefficient ensures that the Peclet number, which defines the relative amounts of convective/diffusive transport of drug, is also similar to that of Paclitaxel within blood. This Peclet number, Pe , is defined as

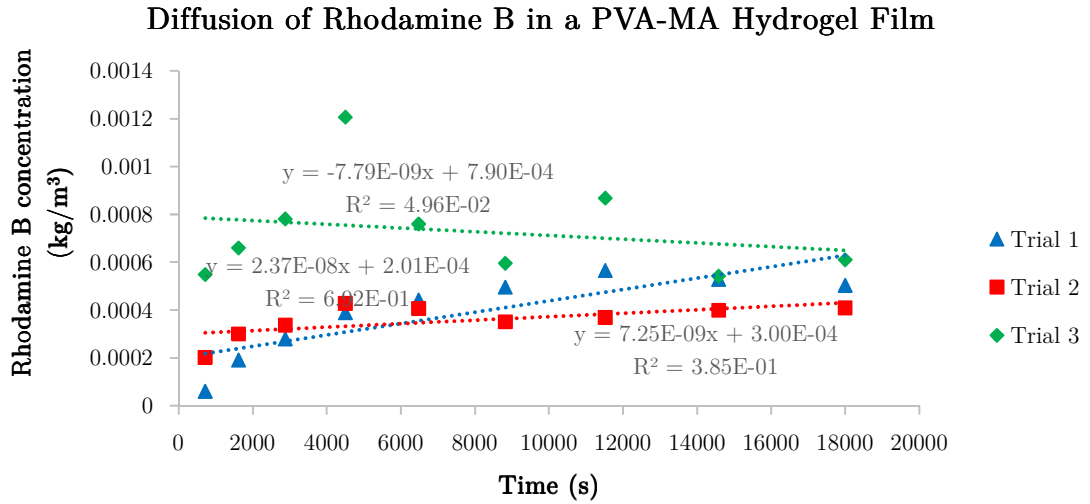
$$Pe = ReSc, \quad (4-18)$$

where Re is the Reynolds number and Sc is the Schmidt number, a dimensionless number defined as the ratio of the momentum diffusivity and the mass diffusivity. For the case of Paclitaxel within blood, $Sc = (\mu/\rho)/D_l$, whilst for Rhodamine B within the blood analogue fluid, $Sc = (\mu_{gw}/\rho_{gw})/D_{fluid}$. As a Reynolds number of 427 is desired to match the mean flow conditions of the renal vasculature, the Peclet

number of Rhodamine B within the blood analogue fluid was calculated to be 3.57×10^7 . Meanwhile, the Peclet number of Paclitaxel within blood was calculated to be 1.70×10^7 . The similarity of these Peclet numbers ensures that the transport kinetics of the fluorescent marker within the blood analogue fluid are similar to Paclitaxel within blood.

The value of $D_{hydrogel}$ was also calculated by plotting the Rhodamine B concentration in the recipient chamber against the time of diffusion, as may be seen in Figure 4-9. A linear regression analysis was then performed for each of the three trials and the gradients of these regression lines, $\partial C/\partial t$, were substituted into Equation 4-13. A diffusion coefficient of $D_{hydrogel} = 4.55 \pm 9.28 \times 10^{-11} \text{ m}^2/\text{s}$ was produced from these results. This high standard deviation was caused by Trial 3, which showed that the recipient chamber's Rhodamine B concentration decreases with respect to time. This physically unrealistic result is likely due to improper mixing of the recipient chamber caused by an incorrectly aligned magnetic stirrer. The remaining trials produced diffusion coefficients of $D_{hydrogel} = 1.40 \times 10^{-10} \text{ m}^2/\text{s}$ and $4.27 \times 10^{-11} \text{ m}^2/\text{s}$ respectively; however, these results also featured data-points that showed decreases in Rhodamine B concentration with respect to time. These data points were subsequently excluded from the analysis, yielding the truncated plot of Figure 4-9b. As only Trial 1 produced more than four viable data-points, the value of $D_{hydrogel} = 2.53 \times 10^{-10} \text{ m}^2/\text{s}$ was used in the ensuing computational analysis. However, due to the high variability of these results, the lowest value of $D_{hydrogel}$, $D_{hydrogel} = 4.27 \times 10^{-11} \text{ m}^2/\text{s}$, was also used. This way, even though the quality of the measured data for this diffusion study is questionable, the full range of potential hydrogel diffusivities could be tested in the ensuing computational study.

a)



b)

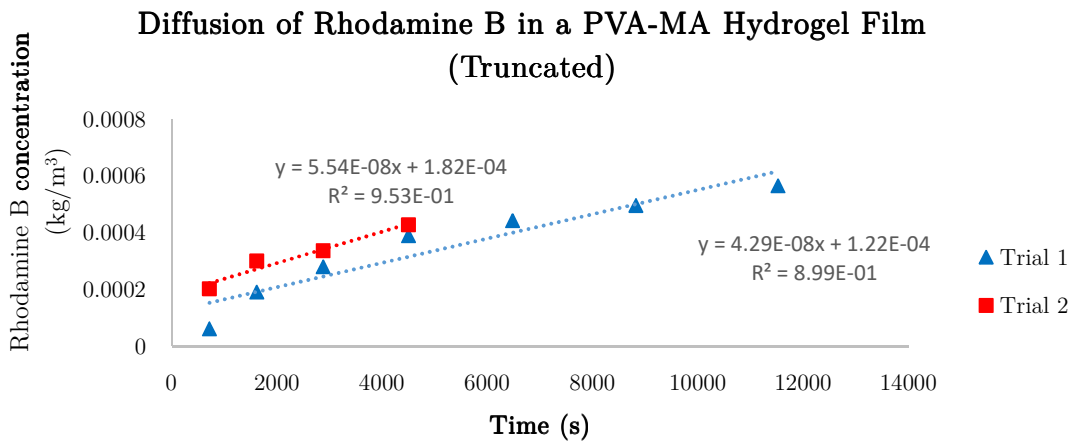


Figure 4-9. Relationship between the concentration of Rhodamine B in the recipient cell and the time of elution through a cell strainer membrane.

4.1.3 Computational Framework

Using these diffusion coefficients, a series of computational fluid dynamics simulations were then performed to compare with the in-vitro results. The model

used is the same as that used in Chapter 3, except that the properties and dimensions are specific to the experiment.

Geometry

The two-dimensional geometry used in this CFD study is depicted in Figure 4-10.

The vessel lumen was modelled as a 3 mm tall fluid domain with a single $100 \times 450 \mu\text{m}$ strut positioned halfway between the inlet and outlet. Arterial tissue was modelled as a 3 mm thick, homogeneous fluid domain. These dimensions are identical to those of the acrylic channel strut and the hydrogel respectively. It should be noted that it would have been more accurate to simulate the channel as a three-dimensional prism with zero-slip conditions on the side walls of the channel; however, as the main purpose of these simulations was to validate that flow-mediated drug transport is not significant, a two-dimensional model was deemed to be sufficient.

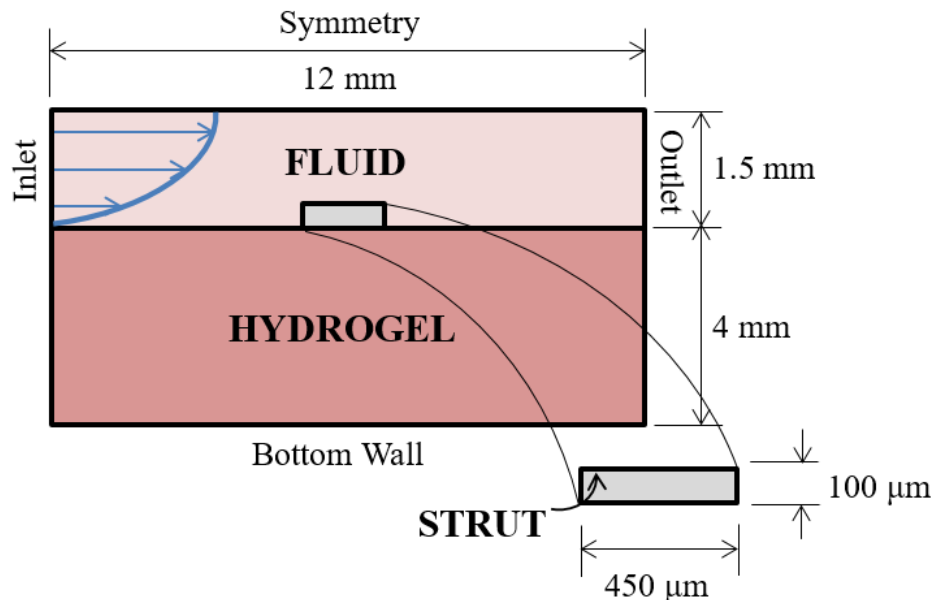


Figure 4-10. Schematic of the computational geometry and dimensions.

Mathematical Model

The flow of the incompressible, laminar blood analogue fluid through the channel was modelled using a combination of the equations of conservation of mass,

$$\nabla \cdot \mathbf{V} = 0, \quad (4-19)$$

and conservation of momentum,

$$\rho_{gw} \left[\frac{\partial \mathbf{V}}{\partial t} + \mathbf{V} \cdot \nabla \mathbf{V} \right] = -\nabla P + \nabla \cdot (\mu_{gw} \nabla \mathbf{V}). \quad (4-20)$$

In these equations, \mathbf{V} is the velocity vector of glycerol-water in the channel, P is the thermodynamic pressure, ∇ is the gradient operator and t is the time. The dynamic viscosity and density of the glycerol-water fluid previously obtained using Equations 4-1 and 4-2, $\mu_{gw} = 0.00334 \text{ Pa}\cdot\text{s}$ and $\rho_{gw} = 1101 \text{ kg/m}^3$, were both ascribed to the model.

Transport of the fluorescent marker in the glycerol-water mixture was modelled using a scalar convection-diffusion equation,

$$\frac{\partial c}{\partial t} + \mathbf{V} \cdot \nabla c = D_{fluid} \nabla^2 c, \quad (4-21)$$

whilst transport in the hydrogel and strut were characterised using diffusion-only equations,

$$\frac{\partial c}{\partial t} = D_{hydrogel} \nabla^2 c \quad (4-22)$$

and

$$\frac{\partial c}{\partial t} = D_{strut} \nabla^2 c \quad (4-23)$$

respectively. In these equations, c is the normalised fluorescent marker concentration, defined as the ratio of the local fluorescent marker concentration, C , to the maximum concentration of fluorescent marker in the strut coating, C_0 , viz

$$c = C/C_0. \quad (4-24)$$

Furthermore, D_{fluid} , $D_{hydrogel}$, and D_{strut} are the diffusivity coefficients of Rhodamine B in glycerol-water, in the hydrogel and in the strut respectively. Specifically, the experimentally derived combination of $D_{fluid} = 6.59 \times 10^{-11} \text{ m}^2/\text{s}$ and $D_{strut} = 4.03 \times 10^{-15} \text{ m}^2/\text{s}$ were used throughout the 180 minute experiment. Both experimentally derived values of $D_{hydrogel}$, $D_{hydrogel} = 2.53 \times 10^{-10} \text{ m}^2/\text{s}$ and $D_{hydrogel} = 4.27 \times 10^{-11} \text{ m}^2/\text{s}$, were then implemented in separate studies. Using these coefficients, the marker transport throughout the 180 minute experiment could be simulated.

However, an additional 10 minute period had to be simulated before and after the experiment, in which no fluid passed through the flow rig yet strut-hydrogel contact persisted. These 10 minute periods were due to the time needed to clamp/unclamp the strut from the hydrogel and to fasten/unfasten the 18×M3 screws that secure the acrylic lid of the flow channel. For this reason, an additional condition whereby $D_{fluid} = 0 \text{ m}^2/\text{s}$ was specified when simulating the 10 minutes preceding and following the main 180-minute simulation.

The solution of Equations 4-17 to 4-21 was accomplished using the finite volume solver, ANSYS FLUENT 16.2 (ANSYS Inc.). A semi-implicit (SIMPLEC) algorithm coupled the pressure and velocity whilst a second order central differencing scheme spatially discretised the pressure and momentum variables. Temporal discretisation was achieved with a second order implicit scheme whilst a second order upwind scheme was used to discretise the scalar fluorescent marker concentration.

Boundary Conditions

The haemodynamic boundary conditions used in Chapter 3 for a steady flow simulation were maintained in the current study. A steady, Poiseuille parabolic

velocity profile corresponding with a Reynolds number of 427 was specified at the inlet. A uniform, zero gauge pressure boundary condition was specified at the outlet, whilst no-slip conditions were ascribed to the strut-fluid and fluid-hydrogel interfaces. No-slip conditions were also specified on remaining boundaries. Finally, all wall boundaries were treated as rigid.

The drug transport boundary conditions of Chapter 3 were also maintained in order to simulate the Rhodamine B transport in the current study. Initially a normalised marker concentration of unity was specified throughout the strut whilst all other fluid and hydrogel regions were assumed to be devoid of the marker. A normalised marker concentration of $c = 0$ was imposed at the inlet, implying that Rhodamine B-free blood arrives from the inlet. This is the same boundary condition that was ascribed to the bottom wall, using the assumption that the marker would not permeate to the bottom of the hydrogel. Continuity of flux was assumed at the fluid-hydrogel interface as well as the fluid-strut and hydrogel-strut interfaces. Finally, zero flux of the marker was specified on each of the remaining boundaries within the fluid and hydrogel domains.

Spatial and Temporal Discretisation

Prior to performing the simulations, these boundary conditions were employed in a mesh convergence study to ensure that the results obtained are independent of the size of the grid used. The flow was deemed to be resolved once the grid convergence index (GCI) corresponding to the recirculation lengths proximal and distal to the stent strut fell below 2%. The GCI is defined as [125]:

$$\text{GCI}_{fine\ grid} = \frac{3 \left| \frac{f_{fine} - f_{coarse}}{f_{fine}} \right|}{r^p - 1}, \quad (4-25)$$

where f_{fine} and f_{coarse} refer to either the proximal or distal recirculation length for a fine and coarse mesh respectively. r is the refinement factor, and p is the order of accuracy of the solution. In this case, $r = \sqrt{2}$ and $p = 2$.

The drug transport behaviour was deemed to be mesh-independent once less than 2% change in area-weighted average concentration (AWAC) of the fluorescent marker was observed in a representative area of hydrogel between two successive mesh refinements. This representative area was chosen as that of a rectangle bounded by the upper and lower extents of the hydrogel and axial extents 3.5 strut widths either side of the strut. This axial extent was chosen on the basis that a typical inter-strut distance is 7 strut widths [61]. The results of this study were obtained using a time-step of $\Delta t = 30$ s over a total solution time of 24 hours. The flow and drug transport were deemed to be adequately resolved with a mesh containing 276,358 elements. More information on these grid convergence studies can be found in Appendix A.

4.2 Results and Discussion

4.2.1 Experimental Results

The relationship between the brightness of the observed images and the concentration of Rhodamine B in a glycerol-water solution may be seen in Figure 4-11. A linear trend is observed, meaning that the fluorescence intensities that are observed can be directly converted into results in terms of the concentration of Rhodamine B. Using this correlation, the concentrations of Rhodamine B in the hydrogel could be obtained at the conclusion of the three hour experiment. These concentrations were normalised against the mean concentration of Rhodamine B

within the struts (9.7 kg/m^3) to produce a normalised distribution of drug within the tissue, just like in the numerical simulations in the previous chapters.

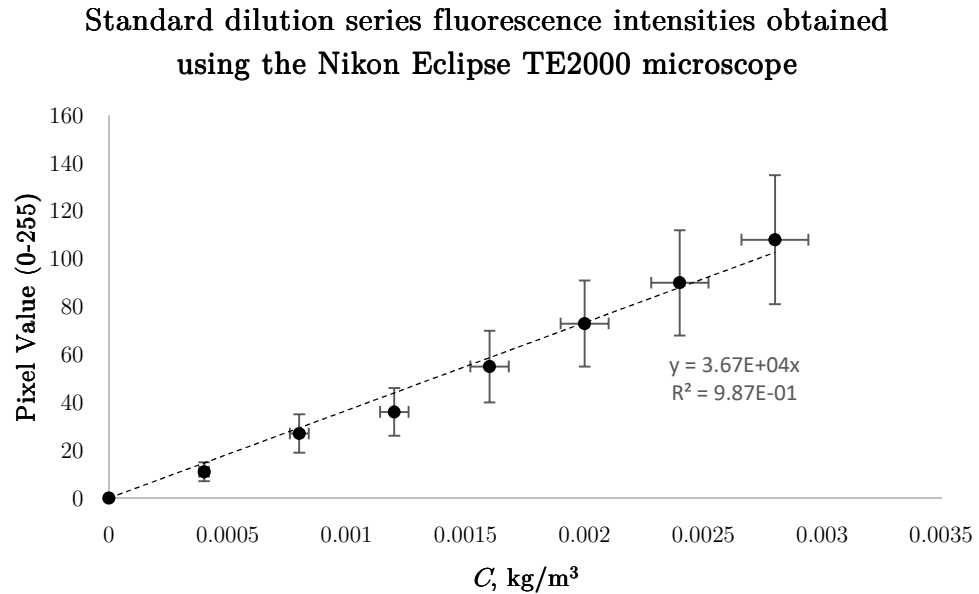


Figure 4-11. Correlation between the pixel intensity and the concentration of Rhodamine B in glycerol-water solution. Note that whilst the absolute errors in the concentrations of the standard dilutions series are shown, it is the standard deviations that are shown for the Pixel value.

Using this transformation, the images of the fluorescence intensity obtained at the completion of the 180 minute experiment were converted into the form of a normalised concentration. These results may be seen in Figure 4-12.

Despite being set up in the same manner, the two cases did produce slightly different marker concentrations. Specifically, higher concentrations are achieved in both the proximal and distal aspects of the hydrogel in Case 2. It is hypothesised that this difference arose due to higher marker concentrations at the strut surfaces in Case 2. Furthermore, unlike the symmetrical drug concentration distributions that

were observed in Chapter 3, higher concentrations are evident in the distal aspect than the proximal aspect in the current study.

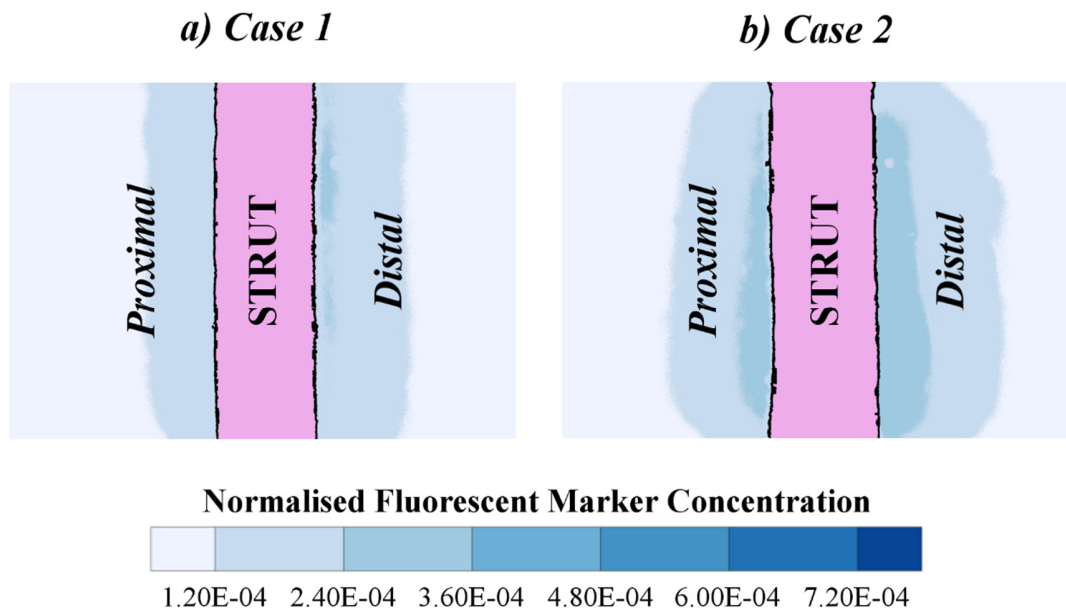


Figure 4-12. Normalised fluorescent marker concentration on the top of the hydrogel at the completion of the 180 minute experiment, once the working fluid had been removed from the flow rig. Both Case 1 (a) and Case 2 (b) were set up in the same manner and although there is some degree of variation, the diffusion of the marker into the proximal and distal aspects of the hydrogel is apparent in both cases.

To investigate why this asymmetry occurs, a series of marker concentration graphs were plotted with each strut throughout the 180 minute experiment. These results, shown in Figure 4-13, show that the higher concentrations in the distal aspect are most pronounced within the first 30 minutes of the experiment. As the experiment progresses, however, the difference between the proximal and distal concentration peaks becomes less noticeable. This reflects the notion that flow-mediated drug uptake becomes less significant as time wears on. Nonetheless, the concentrations shown in Figure 4-12 and Figure 4-13 are only of the top surface of

the hydrogel and do not show if this asymmetry persists more deeply into the hydrogel.

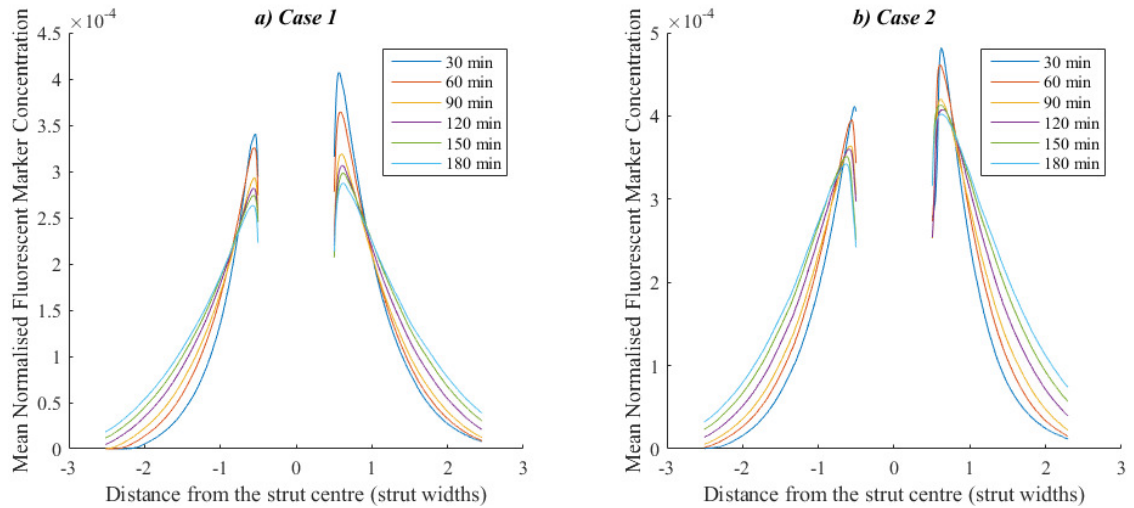


Figure 4-13. The mean normalised concentration distribution of Rhodamine B atop the hydrogel during the 180 minute experiment.

To show how deeply the Rhodamine B penetrated into the tissue, the hydrogels in both cases were sliced in half at the end of the experiment and the cross-sectional distribution of marker shown. It was important to ensure that the hydrogel was sliced down the middle, as Case 2 in Figure 4-12 appears to show that the Rhodamine B concentrations are lower near the sides of the hydrogel. These cross-sectional marker distributions, shown in Figure 4-14, do differ in magnitude but are each very symmetrical. As in Figure 4-12 and Figure 4-13, it is believed that these differences between cases arise due to inhomogeneous Rhodamine B distributions along the coating surface. As mentioned previously, it is difficult to completely eliminate these non-uniformities as the marker readily diffuses from the outer surface of the strut. Hence, a limitation of this study is this difficulty in controlling the spatial homogeneity of the Rhodamine B across the outer strut

surfaces. Nonetheless, the symmetric nature of each distribution implies that the impact of flow-mediated drug transport is very low.

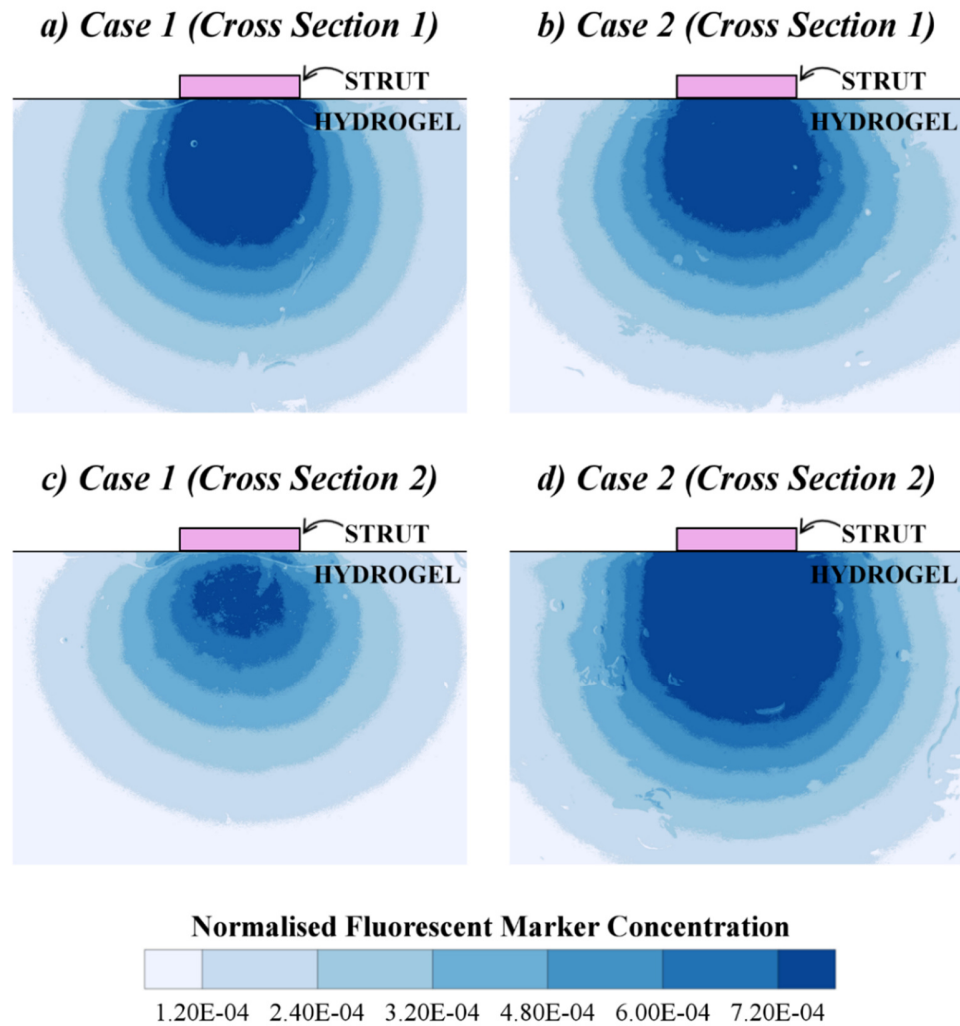


Figure 4-14. Cross-sectional view of the marker concentrations within each hydrogel. The blood analogue fluid flowed from left to right in each case. Note that the strut has been put into this image purely to illustrate the scale of the image and its true position is not necessarily illustrated. Also, the Cross Section 2 images (c and d) have been flipped vertically to facilitate the direct comparison with the Cross Section 1 images (a and b).

4.2.2 Numerical Results

The numerical results obtained after the three hours of simulated fluid flow and fluorescent marker release may be seen in Figure 4-15. In both of the cases depicted, the previously obtained values of D_{fluid} and D_{strut} were used; however, the larger value of $D_{hydrogel}$ was implemented in Figure 4-15a whilst the lower value was used in Figure 4-15b. This smaller $D_{hydrogel}$ yielded a normalised fluorescent marker distribution that closely approximated the results of Figure 4-14, whilst the larger $D_{hydrogel}$ produced lower concentrations than in the experiments. However, the distribution of the marker was symmetrical about the strut in both simulations, similar to the experiments. These results can therefore be used to validate the drug transport model of Chapter 3 and also validate the finding that flow-mediated drug transport is negligible.

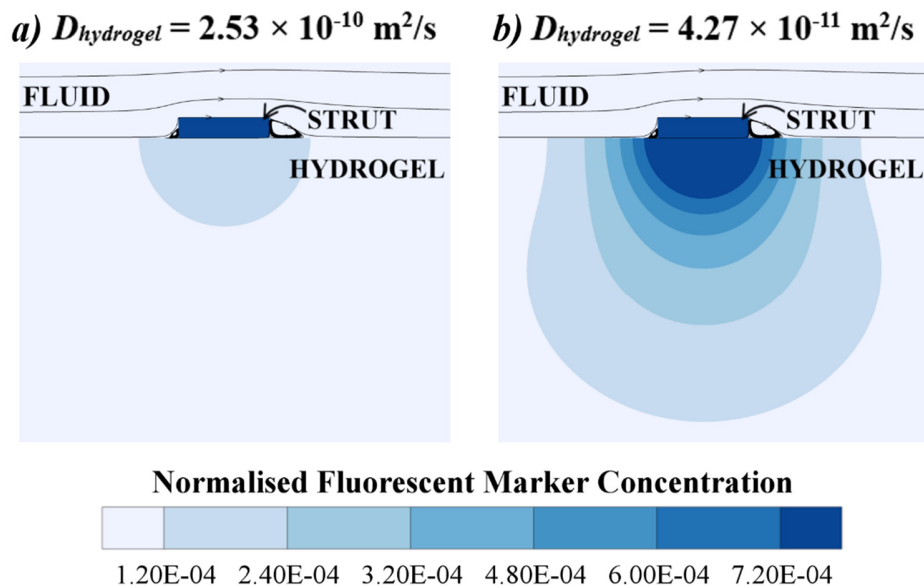


Figure 4-15. Computational results showing the normalised fluorescent marker concentration within the hydrogel at the culmination of 3 hours and 15 minutes. In the first case (a) the high value of $D_{hydrogel}$ that was obtained in the diffusion study was implemented. In the second case (b), the lower value was used.

4.3 Outcomes

An in-vitro model was used to validate the computational model introduced in Chapter 3. In this model, the elution of drug from a stent strut was modelled through the diffusion of a fluorescent dye, Rhodamine B, from a PDMS strut. The transport of this dye into a flowing glycerol-water solution and into a hydrogel was used to represent the transport of antiproliferative drugs into blood and arterial tissue respectively. The distribution of the fluorescent dye within the hydrogel was observed using an epifluorescence microscope.

These results revealed a close likeness between the marker distributions produced by computational and in-vitro analyses. Despite differences in the magnitude of Rhodamine B transport, this similarity in spatial distribution conveyed that the drug transport model of Chapter 3 – in which the depletion of drug within the coating was modelled - is an accurate method of modelling the drug transport behaviour of stented arteries. It also conveyed that flow-mediated drug transport into the vessel is negligible.

Chapter 5

The Haemodynamics and Drug Transport Behaviour Associated with Incomplete Stent Apposition

Chapter Aims

In recent numerical studies, it has been suggested that significant quantities of drug can be transported from malapposed drug-eluting stent struts into arterial tissue. The first aim of this study is to implement the validated drug transport model of Chapter 3 to see if this is truly the case. The second aim is to ascertain whether the flow features that have been documented in two-dimensional studies still transpire in more realistic geometries.

5.1 Methods

Computational fluid dynamics simulations were used to ascertain why the unique flow features of malapposed struts transpire. The flow pathlines obtained with two-dimensional simulations are contrasted with those obtained with a three-dimensional malapposed ring to test whether the flow features obtained with two-dimensional models are realistic. Comparisons of the velocity and pressure distributions obtained with the two-dimensional models are used to explain why these features develop. The impact of these features on the haemodynamics of the stented vessel are then revealed through comparisons of the wall shear stress distributions.

Furthermore, a coupled computational fluid dynamics and mass transport model is used to elucidate the impact of stent malapposition on the drug transport environment of stented arteries. The validated mass transport model introduced in Chapter 3 is used in this study, in conjunction with two-dimensional models featuring stent strut geometries at varying degrees of malapposition. The impact of malapposition distance on the drug transport behaviour of stented arteries is revealed using drug concentration contours and by comparing the magnitude of drug uptake for each geometry.

5.1.1 Geometries

The first geometry used in this study, Model I, is three-dimensional in nature and is shown in Figure 5-1a. In this geometry, the vessel is modelled as a cylinder with 6 mm diameter and a total length of 16 mm. The stent strut geometry was represented using a single, malapposed ring with a 100 μm square profile. The malapposition distance, defined as the gap between the strut and the tissue, was

varied between $\delta = 0$ mm and a maximum value of $\delta_{max} = 100$ μm . As only the haemodynamics of this geometry were investigated, the arterial tissue was left out of this model.

Six further simulations were then performed using Model II, shown in Figure 5-1b. The malapposition distance of a single 0.1 mm square profile strut was varied with each simulation so that $\delta = 0$ μm , 10 μm , 25 μm , 50 μm , 75 μm , and 100 μm . Each strut was positioned halfway between the inlet and the outlet of a 3 mm tall fluid domain used to model the arterial lumen. A 1 mm thick fluid domain was also implemented into the model to enable the measurement of drug uptake in the arterial tissue.

An additional six simulations were then performed using Model III, shown in Figure 5-1c. The six geometries used in this model were identical to those of Model II except that a 15 μm thick drug coating was included in the model. This coating facilitated a more realistic simulation of the depletion of drug at the strut surfaces and was used to determine whether malapposed struts are capable of yielding significant drug uptake.

The dimensions of these geometries were consistent with those used in the prior analyses of stent-based drug therapy in the renal vasculature in Chapters 2 and 3. Although these geometries were simplified, they captured the characteristic haemodynamic and drug-transport phenomena native to stented arteries whilst eliminating some of the obscuring phenomena of more complex geometries. This made them ideal for studying the effect of stent malapposition on the haemodynamics and drug transport in stented arteries.

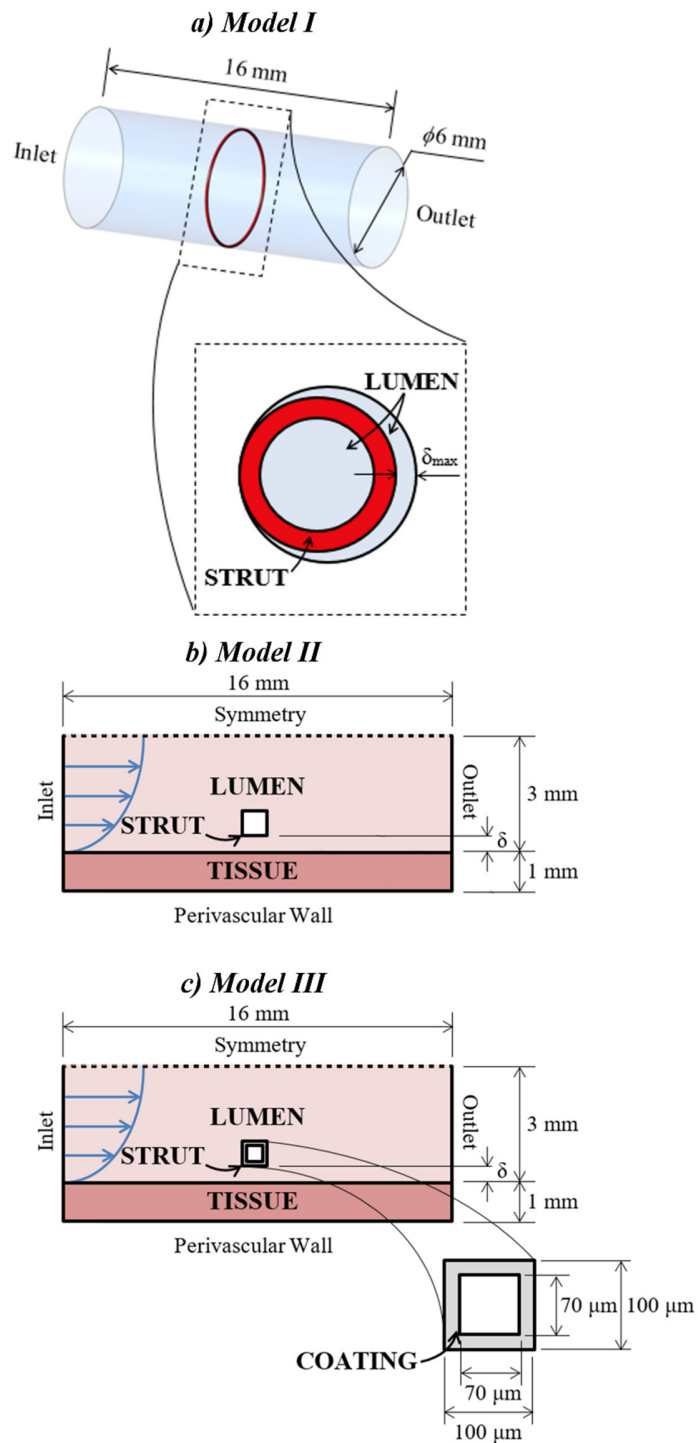


Figure 5-1. Geometries and dimensions. Model I (a) is a three-dimensional renal artery geometry featuring a malapposed strut ring. Two-dimensional simulations were carried out using Model II (b) and Model III (c). A coating was implemented into Model III to more accurately simulate drug elution from the strut.

5.1.2 Mathematical Model

In each geometry, the blood flowing through the lumen was modelled as a Newtonian, incompressible fluid undergoing laminar flow. This was accomplished using a combination of the equations of conservation of mass,

$$\nabla \bullet \mathbf{V} = 0, \quad (5-1)$$

and conservation of momentum. In Model I and Model II, the following formulation of the equations of conservation of momentum were used:

$$\rho(\mathbf{V} \bullet \nabla \mathbf{V}) = -\nabla P + \nabla \bullet (\mu \nabla \mathbf{V}), \quad (5-2)$$

In Model III, however, the drug coating depletes with respect to time and hence a steady-state solution – in which all flow and drug transport variables remain constant – could not be achieved. Hence, for these geometries only, the following formulation of the equations of conservation of momentum was used:

$$\rho \left[\frac{\partial \mathbf{V}}{\partial t} + \mathbf{V} \bullet \nabla \mathbf{V} \right] = -\nabla P + \nabla \bullet (\mu \nabla \mathbf{V}). \quad (5-3)$$

In these equations, ρ is the blood density, μ is the dynamic viscosity of blood, \mathbf{V} is the velocity vector of blood in the lumen, P is the thermodynamic pressure, ∇ is the gradient operator and t is the time.

Several assumptions were used to simplify these haemodynamic models.

Blood was modelled with uniform density, $\rho = 1060 \text{ kg/m}^3$, and laminar flow conditions were assumed due to the low Reynolds numbers ($\text{Re} < 1300$ [137]) found in the renal vasculature. A constant viscosity of $\mu = 0.00345 \text{ Pa} \cdot \text{s}$, based on blood's lowest viscosity limit, was ascribed to the blood for three main reasons: firstly, it was shown in Chapter 2 to yield more exaggerated flow disturbances than non-Newtonian blood rheological models; secondly, the low and high wall shear stress thresholds used in this study were originally obtained using this model [66,138], and; finally, the

choice of blood rheological model has negligible impact on the drug transport behaviour of stented arteries, as shown in Chapter 3.

The equations used to model this drug transport behaviour were slightly different in Model II and Model III. As in Chapter 2, the steady-state drug transport in Model II was represented in the lumen by

$$\mathbf{V} \bullet \nabla c = D_l \nabla^2 c, \quad (5-4)$$

and in the tissue by

$$D_t \nabla^2 c = 0. \quad (5-5)$$

In Model III, however, the drug transport in the lumen was represented by

$$\frac{\partial c}{\partial t} + \mathbf{V} \bullet \nabla c = D_l \nabla^2 c, \quad (5-6)$$

whilst drug transport in the tissue and strut coating were characterised using

$$\frac{\partial c}{\partial t} = D_t \nabla^2 c \quad (5-7)$$

and

$$\frac{\partial c}{\partial t} = D_c \nabla^2 c. \quad (5-8)$$

In these equations, c is the normalised drug concentration. This parameter is defined as the ratio of the local drug concentration, C , to the maximum concentration of drug in the strut coating, C_0 , viz:

$$c = C/C_0, \quad (5-9)$$

and D_l , D_t and D_c represent the diffusivity of the drug in the blood, tissue and coating respectively.

Paclitaxel served as the model drug in this analysis once again. Its diffusivity coefficients in blood and arterial tissue are $D_l = 3.89 \times 10^{-11} \text{ m}^2/\text{s}$ [105] and $D_t = 3.65 \times 10^{-12} \text{ m}^2/\text{s}$ [106] respectively. For studies using Model III, the diffusivity coefficient of Paclitaxel within the coating was calculated based on the formula

$$D_c = \frac{L_c^2}{t_{release}}, \quad (5-10)$$

where L_c is the coating thickness and $t_{release}$ is the desired duration of drug release. A 10 day drug release duration was specified, based on the release rate of the TAXUS-MR (moderate release) paclitaxel-eluting stent [127]. Given the coating thickness of $L_c = 15 \text{ }\mu\text{m}$, this resulted in a diffusivity coefficient of $D_c = 2.60 \times 10^{-16} \text{ m}^2/\text{s}$.

The solutions of Equations 5-1 to 5-10 were obtained through use of the finite volume solver ANSYS FLUENT 14.5 (ANSYS Inc.). A semi-implicit (SIMPLEC) algorithm coupled the pressure and velocity whilst a second order central differencing scheme spatially discretised the pressure and momentum variables. A second order upwind scheme was used to discretise the scalar drug concentration.

5.1.3 Boundary Conditions

All haemodynamic boundary conditions remained the same in each model. A steady, fully-developed inlet velocity profile corresponding with a Reynolds number of 427 was specified for each geometry, consistent with the mean flow conditions of the renal vasculature [75]. A uniform, zero gauge pressure boundary condition was specified at the outlet, whilst no-slip conditions were ascribed to the strut-lumen and lumen-tissue interfaces. A fixed-wall assumption was also implemented in light of findings which suggest that stented arteries are considerably stiffer than unstented ones and that minimal arterial motion occurs [109]. Finally, a symmetry boundary condition was specified on the top of the two-dimensional lumen domains, as may be seen in Figure 5-1b and Figure 5-1c.

Unlike these haemodynamic boundary conditions, the drug transport boundary conditions differed with each model. As Model I was only used to study

the haemodynamics of an artery with a malapposed strut, no drug transport boundary conditions were implemented into this model. In Model II, however, the elution of drug from the strut surface was modelled using a Dirichlet boundary condition, in which $c = 1$ on each strut boundary. In Model III, a normalised drug concentration of unity was initially ascribed throughout the coating, whilst all other lumen and tissue regions were assumed to be devoid of drug. Once the flow in each of the Model III geometries had been resolved, continuity of flux was assigned at the strut-lumen and strut-tissue interfaces. Zero flux of drug was also specified on the inner boundaries of the coating. These conditions caused the drug to deplete within the coating, meaning that, unlike Model II, a steady state could not be achieved. As a result, a computational period of 24 hours was used in conjunction with this model.

All remaining drug transport boundary conditions were identical in both Model II and III. A normalised drug concentration of $c = 0$ was imposed at the inlet, implying that drug-free blood arrives from the inlet. This same boundary condition was ascribed to the perivascular wall, using the assumption that drug would not be able to penetrate to the very bottom of the tissue. Continuity of flux was assumed at the lumen-tissue interface, as well as the strut-tissue and strut-lumen interfaces. Finally, zero flux of drug was specified on each of the remaining boundaries within the lumen and tissue.

5.1.4 Spatial and Temporal Discretisation

These same boundary conditions were also used in a series of mesh independence studies, performed to ensure that the solutions obtained were independent of the size of the grid used. The mesh densities in each geometry were greatest in the regions closest to the stent strut and also near the interface between the tissue and lumen.

This enabled the resolution of thin boundary layers which occurred along the no-slip boundaries defining the artery wall and the stent strut walls. Furthermore, the high mesh densities in the tissue and close to the stent struts facilitated the resolution of high drug concentration gradients in Models II and III.

A Grid Convergence Index (GCI) criterion was used to ensure that the solutions obtained with each geometry were independent of the mesh density. This GCI was defined as [125]:

$$\text{GCI}_{fine\ grid} = \frac{3 \left| \frac{f_{fine} - f_{coarse}}{f_{fine}} \right|}{r^p - 1}, \quad (5-11)$$

where f_{fine} and f_{coarse} may refer to the area of wall exposed to recirculating flow, the recirculation length or the average tissue drug concentration, for a fine and coarse mesh respectively. r is the refinement factor, and p is the order of accuracy of the solution. For each geometry, $r = \sqrt{2}$ and $p = 2$.

In Model I, mesh independence was judged to be achieved once the GCI corresponding to the area of arterial wall exposed to recirculating flow fell below 5%. For each of the six geometries which comprise Model II and Model III, the flow behaviour was deemed to be resolved once the GCI corresponding to the lengths of the recirculation zones fell below 2%. The drug transport behaviour in Model II and Model III were deemed to be resolved once less than 2% change in the area-weighted average concentration (AWAC) of drug within a representative area of arterial tissue was observed between successive mesh refinements. These AWAC-based mesh refinement studies were only performed for the geometries in which the greatest drug uptake were observed. Furthermore, the AWAC for Model III was measured after a total simulation time of 24 hours. A time-step of 30 s was used in these simulations as it was found to yield an identical AWAC over a 24 hour period when compared to

a time-step size of 1 s. The final meshes corresponding with Model I, the six Model II geometries and the six Model III geometries contained the number of elements shown in Table 5-1. More information on the grid convergence studies used to obtain these meshes may be found in Appendix A.

Table 5-1: Final mesh sizes.

| Model (geometry) | NO. OF ELEMENTS |
|----------------------------|-----------------|
| I | 5,003,861 |
| II | |
| $\delta = 0 \mu\text{m}$ | 2,009,929 |
| $\delta = 10 \mu\text{m}$ | 2,197,105 |
| $\delta = 25 \mu\text{m}$ | 2,239,387 |
| $\delta = 50 \mu\text{m}$ | 2,335,819 |
| $\delta = 75 \mu\text{m}$ | 2,436,187 |
| $\delta = 100 \mu\text{m}$ | 2,534,587 |
| III | |
| $\delta = 0 \mu\text{m}$ | 149726 |
| $\delta = 10 \mu\text{m}$ | 166206 |
| $\delta = 25 \mu\text{m}$ | 179004 |
| $\delta = 50 \mu\text{m}$ | 193224 |
| $\delta = 75 \mu\text{m}$ | 200334 |
| $\delta = 100 \mu\text{m}$ | 207444 |

Note that significantly more elements were needed in Model II to achieve grid convergence than in Model III, despite the geometries being identical apart from the presence of a drug coating in Model III. This is because whilst the depletion of drug within the drug coating of Model III was modelled, this was not the case in Model II. As a result, the total drug uptake in Model II ($\delta = 0 \mu\text{m}$) was over four orders of magnitude greater than in Model III ($\delta = 0 \mu\text{m}$). The concentration gradients in the

tissue were therefore much stronger in Model II than in Model III and a much denser mesh was required to ascertain the drug transport behaviour.

5.2 Results and Discussion

5.2.1 The Haemodynamics of Arteries with Malapposed Struts

Comparisons of the velocity vector distributions of Model I with the flow pathlines of Model III revealed that the same flow features appear in the two-dimensional and three-dimensional models. As may be seen in Figure 5-2, when $\delta = 0 \mu\text{m}$ in the three-dimensional model, recirculation zones form which are attached to the proximal and distal face of the strut. These zones were only found downstream of the strut when $\delta = 50 \mu\text{m}$ and $\delta = 100 \mu\text{m}$, however, and they were also detached from the strut in both cases. These recirculation zones, highlighted in blue in Figure 5-2, remained attached to the vessel wall irrespective of the malapposition distance; however, they were observed to increase in length and shorten in height as δ was increased. This same behaviour was also observed in the two-dimensional results obtained using Model II, which may be seen in Figure 5-3. Note that the haemodynamic results of Model III have not been shown due to being identical to those obtained with Model II. From these results, it can be concluded that two-dimensional computational fluid dynamics models are suitable to use when modelling the haemodynamics of arteries featuring malapposed stent struts.

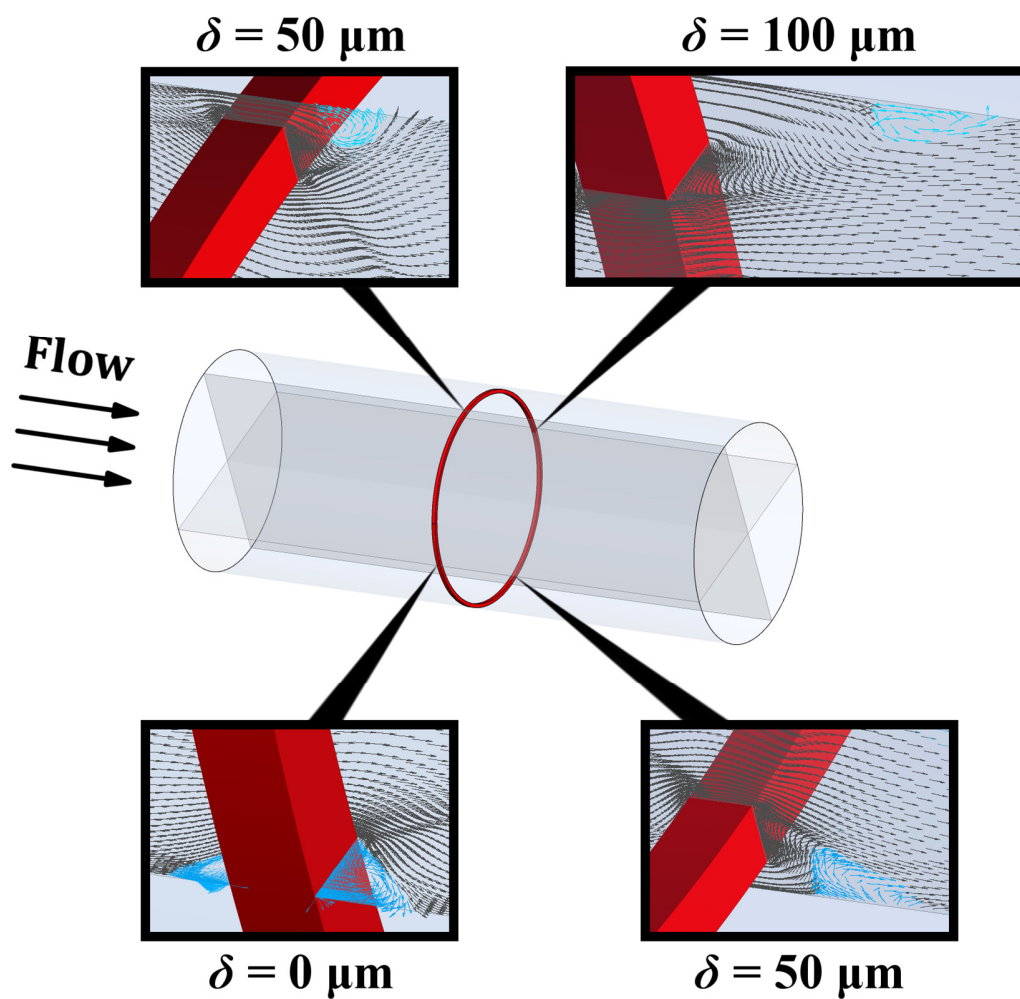


Figure 5-2. Velocity vector distributions in Model I. Recirculation zones, shown in blue, are attached to the proximal and distal strut surfaces when $\delta = 0 \mu\text{m}$. These zones become separated from the strut and form only downstream of it when $\delta = 50 \mu\text{m}$ and $\delta = 100 \mu\text{m}$. The recirculation zones are attached to the vessel wall in each case.

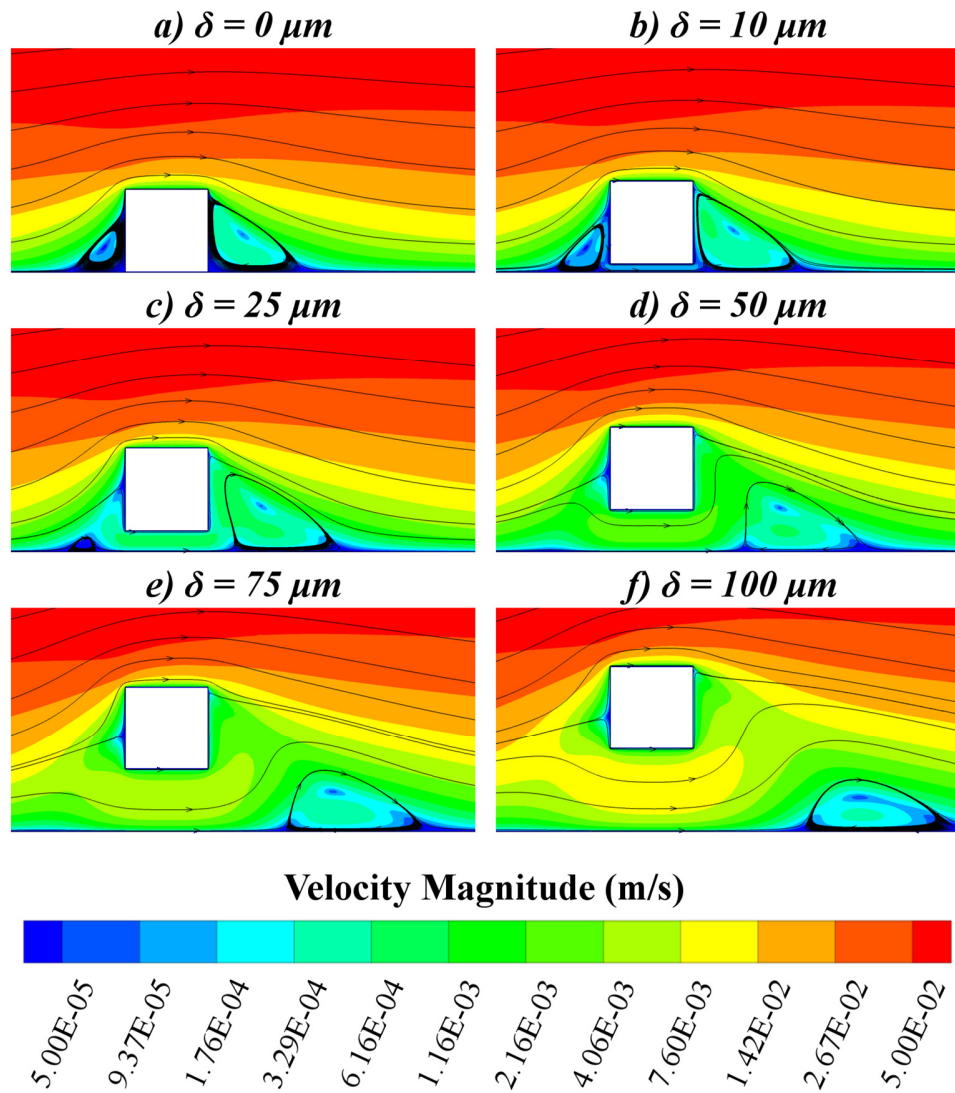


Figure 5-3. Velocity magnitude contour plot in Model II. The recirculation zones formed in these geometries displayed the same behaviour as those formed in the three-dimensional model in Figure 5-2.

The velocity magnitude contour plots in Figure 5-3 were used in conjunction with the plots of the coefficient of pressure in Figure 5-4 to explain why these flow characteristics transpire. This coefficient of pressure, C_P , was defined as:

$$C_P = \frac{P}{\frac{1}{2}\rho\bar{V}_\infty^2}, \quad (5-12)$$

where \bar{V}_∞ is the mean freestream velocity of blood at the inlet, and ρ and P are the blood density and the thermodynamic pressure respectively. This coefficient of pressure was monitored only using the geometry in Model III in which $\delta = 25 \mu\text{m}$. Using a time-step size of 0.00002 s, the flow was allowed to develop from an initialised solution in which the blood flow was stationary throughout the geometry. The pathlines and C_P distributions obtained at the time-points where $t = 0.00088$ s, 0.0016 s and 0.0048 s may be seen in Figure 5-4a, Figure 5-4b and Figure 5-4c respectively. Finally, the pathlines and C_P contours obtained once the flow had ceased changing with respect to time may be seen in Figure 5-4d.

It may be seen in Figure 5-4a that the pressure at point D is higher than at point C. This adverse pressure gradient is caused by the rapid expansion of flow as it exits the region underneath the strut at point C. This gradient retards the flow passing between points C and D and leads to the separation of this flow from the arterial wall, as may be seen in Figure 5-4b. It is this adverse pressure gradient which gives rise to the distal recirculation zones shown in Figure 5-3b-f.

Similarly, it may be seen in Figure 5-4c that the pressure at point B is higher than at point A. This adverse pressure gradient exists because the flow moving down the proximal face of the strut decelerates as it comes in close proximity to the arterial wall at point B. This gradient retards the flow passing between these points and leads to the separation of this flow from the arterial wall, as may be seen in Figure 5-4d. It is this adverse pressure gradient which causes the formation of the proximal recirculation zones in the geometries of Figure 5-3b-c.

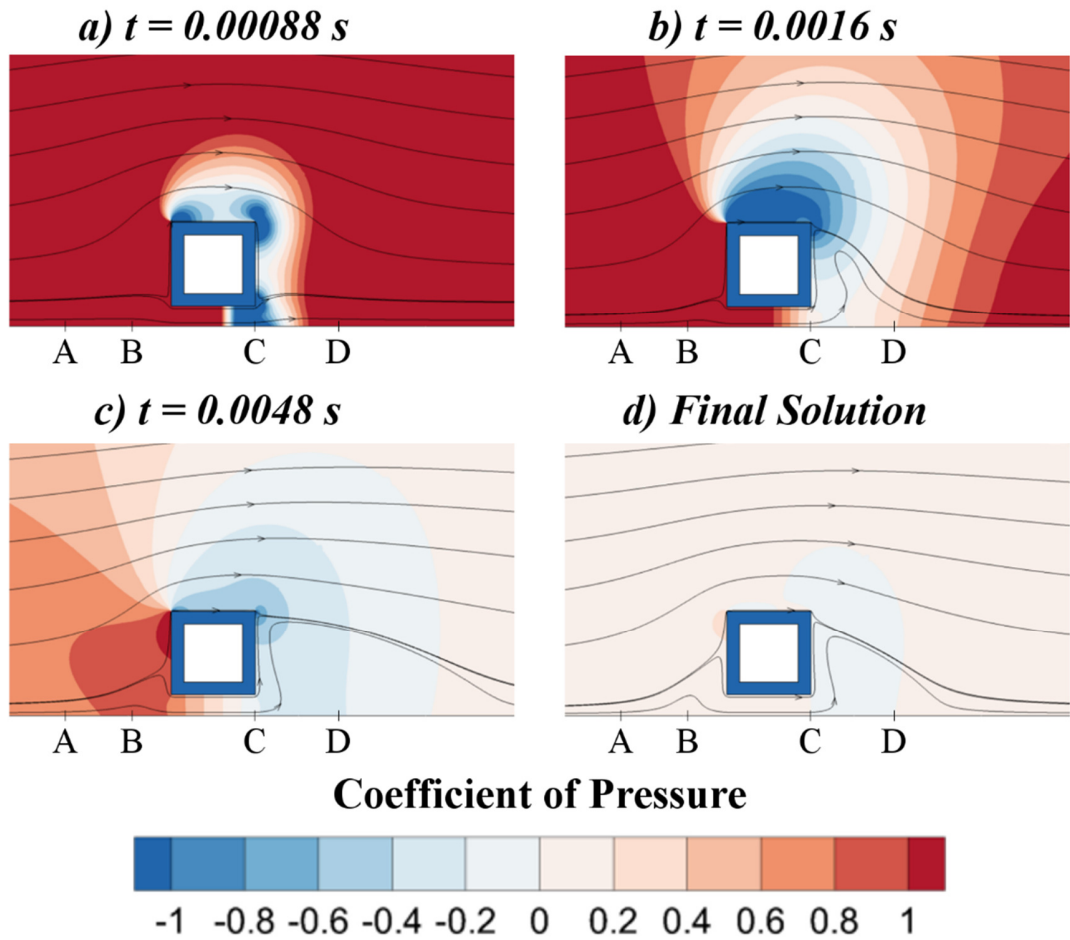


Figure 5-4. Flow development and C_p distribution in Model III for the geometry in which $\delta = 25 \mu\text{m}$. The flow develops from an initialised solution in which the blood is stationary to a final solution in which all flow parameters cease to change with respect to time.

Another adverse pressure gradient may be seen on the top-right corner of the strut in Figure 5-4a. As in a backward-facing step, this gradient is caused by the sudden expansion of the flow above the strut as it passes this corner. In the well-apposed geometry of Figure 5-3a, this gradient causes the flow to detach at the top-right corner and establish a recirculation zone which is attached to strut and tissue alike. In the malapposed geometries of Figure 5-3b-f, however, two streams approach this corner, merge and then flow away without detaching from the strut surfaces.

Instead of forming on the strut surfaces, the aforementioned distal recirculation zones of Figure 5-3b-f initiate at the tissue itself. This implies that the adverse pressure gradient at the tissue boundary is strong enough to cause flow separation whilst the gradient at the strut corners is not.

These factors explain why recirculation zones form in arteries with malapposed struts, as well as why they are attached to the vessel wall and not the strut; however, there are other characteristics of these zones which have not yet been explained. Namely, the following outcomes may be observed in Figure 5-3 as the malapposition distance is increased: the proximal recirculation zone reduces in size; the distal recirculation zone reduces in height and increases in length; the distance between the recirculation zones and the strut increases, and; the apex of the distal recirculation zone shifts closer to the centre of the zone.

The reducing size of the proximal recirculation zone can be explained by comparing the velocity magnitude contours of Figure 5-3c-d and the coefficient of pressure plots of Figure 5-4. Namely, the velocity of the blood flowing underneath the strut increases with respect to δ , a result of the inherently higher freestream velocity of fluid located farther away from the tissue boundary. The pressure beneath the stent strut decreases as a result of this increased velocity. Hence, the adverse pressure gradient between points A and B in Figure 5-4a would be smaller in geometries with greater malapposition and result in smaller proximal recirculation zones.

Similarly, the changes to the distal recirculation zone as δ increases can also be explained through examination of Figure 5-3. Specifically, the momentum of fluid exiting the region below the strut increases with respect to the malapposition distance. This increased momentum establishes a longer, less skewed recirculation

zone due to inertia effects, and also causes the zone to be displaced further downstream. However, the adverse pressure gradient between points C and D in Figure 5-4a reduces as the malapposition distance is increased. This is the result of the reduced expansion ratio – the ratio of the height of the expanded region to the constricted region – of the fluid flowing beneath the strut. This phenomenon accounts for the reduced size and eventual removal of the distal recirculation zone in Figure 5-5.

It may also be observed in Figure 5-5 that the distal recirculation zone does eventually decrease in size with respect to increasing malapposition distance. This is consistent with past findings which showed that at low Reynolds numbers, the flow past a square cylinder persists without separating from the cylinder surfaces [139]. Specifically, this phenomenon was observed at Reynolds numbers of $Re^* \leq 1$, where Re^* is the Reynolds number based on the width of the cylinder. Using the strut width and the inlet velocity at a point level with the top strut surface, a maximum value of $Re^* = 1.8$ was calculated in Figure 5-3. However, as the Reynolds number increases, the magnitude of viscous forces is expected to decrease until flow separation occurs at the trailing edges of the cylinder.

For illustrative purposes, three further simulations were performed to see when the flow separates from the trailing edges of the strut. The malapposition distances were increased in these geometries to $\delta = 150 \mu\text{m}$, $\delta = 500 \mu\text{m}$ and $\delta = 1000 \mu\text{m}$, yielding Reynolds numbers of $Re^* = 2.3$, $Re^* = 5.1$ and $Re^* = 8.5$ respectively. For comparison, flow detaches from the surface of circular cylinders at around $Re^* = 5$. The velocity magnitude and flow pathlines obtained with these geometries may be seen in Figure 5-5.

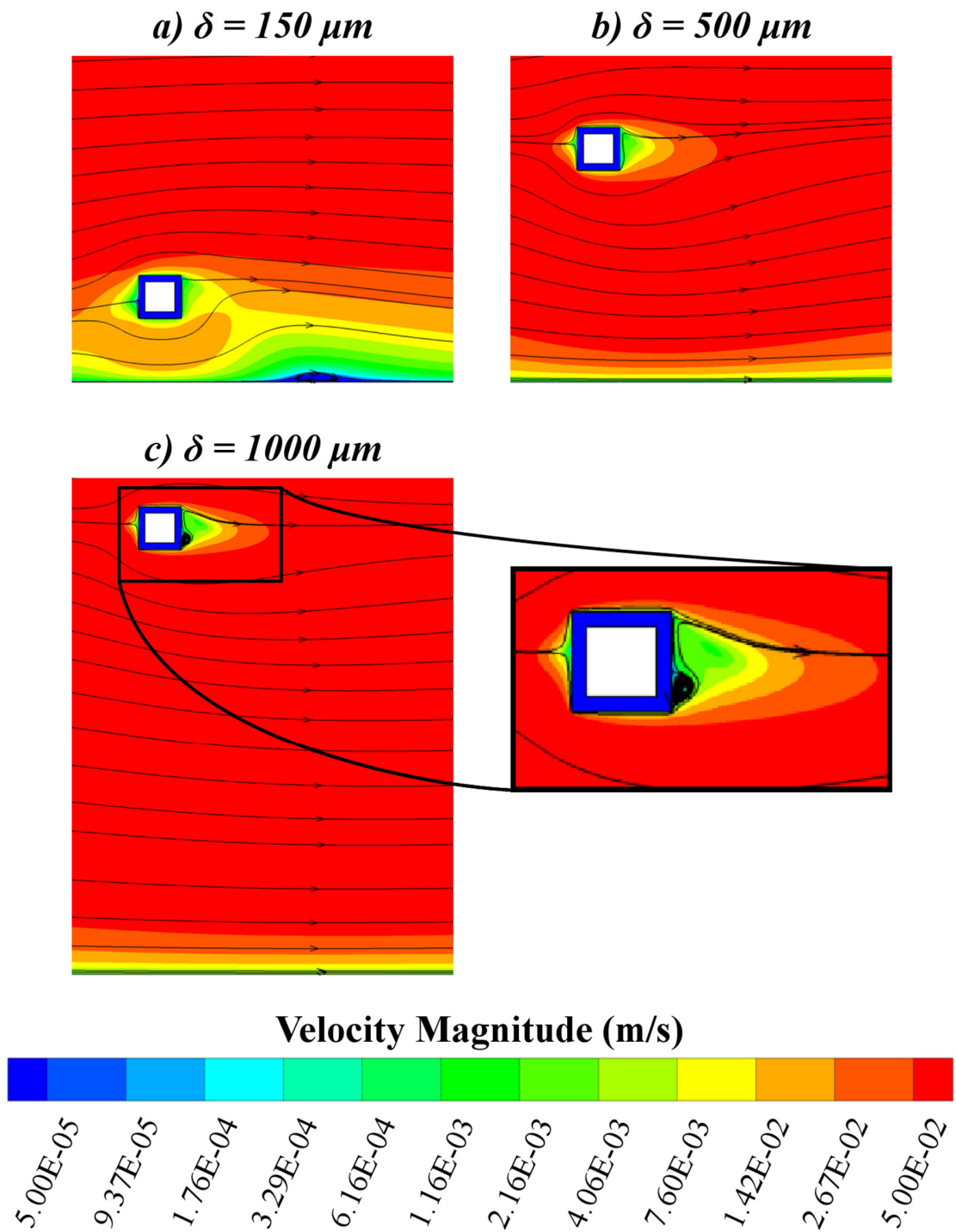


Figure 5-5. Velocity magnitude and flow pathlines in three further malapposed strut geometries.

These results show that the flow can separate from the strut, although only at very large malapposition distances greater than $\delta = 500 \mu\text{m}$. In Figure 5-5a, the distal recirculation zone is significantly smaller and further downstream of the strut than in any of the geometries in Figure 5-3. When the malapposition distance is increased in Figure 5-5b, this distal recirculation zone disappears entirely. However, when the malapposition distance increases further, a recirculation zone does form on the strut itself, as may be seen in Figure 5-5c. These results confirm that as the Reynolds number increases, the magnitude of viscous forces decreases until flow separation occurs at the trailing edges of the cylinder.

The impact of these haemodynamic phenomena on the wall shear stress distribution within the artery may be seen in Figure 5-6. Endothelial dysfunction-inducing low wall shear stresses below 0.5 Pa [57] were observed adjacent to the struts in each case, as may be seen in Figure 5-6a. It may also be seen that these low wall shear stresses occurred directly underneath the struts whilst $\delta \leq 25 \mu\text{m}$. Furthermore, platelet-activating high wall shear stresses exceeding 6 Pa [66] were also observed on the upper corners of the strut in each case, as may be seen in Figure 5-6b. The extent of these low and high wall shear stresses tended to increase with respect to the malapposition distance, as shown in Figure 5-6c. This is in agreement with the results of prior studies [65,140] and conveys the need to model malapposed stent geometries when seeking to alleviate the adverse haemodynamics of stented arteries.

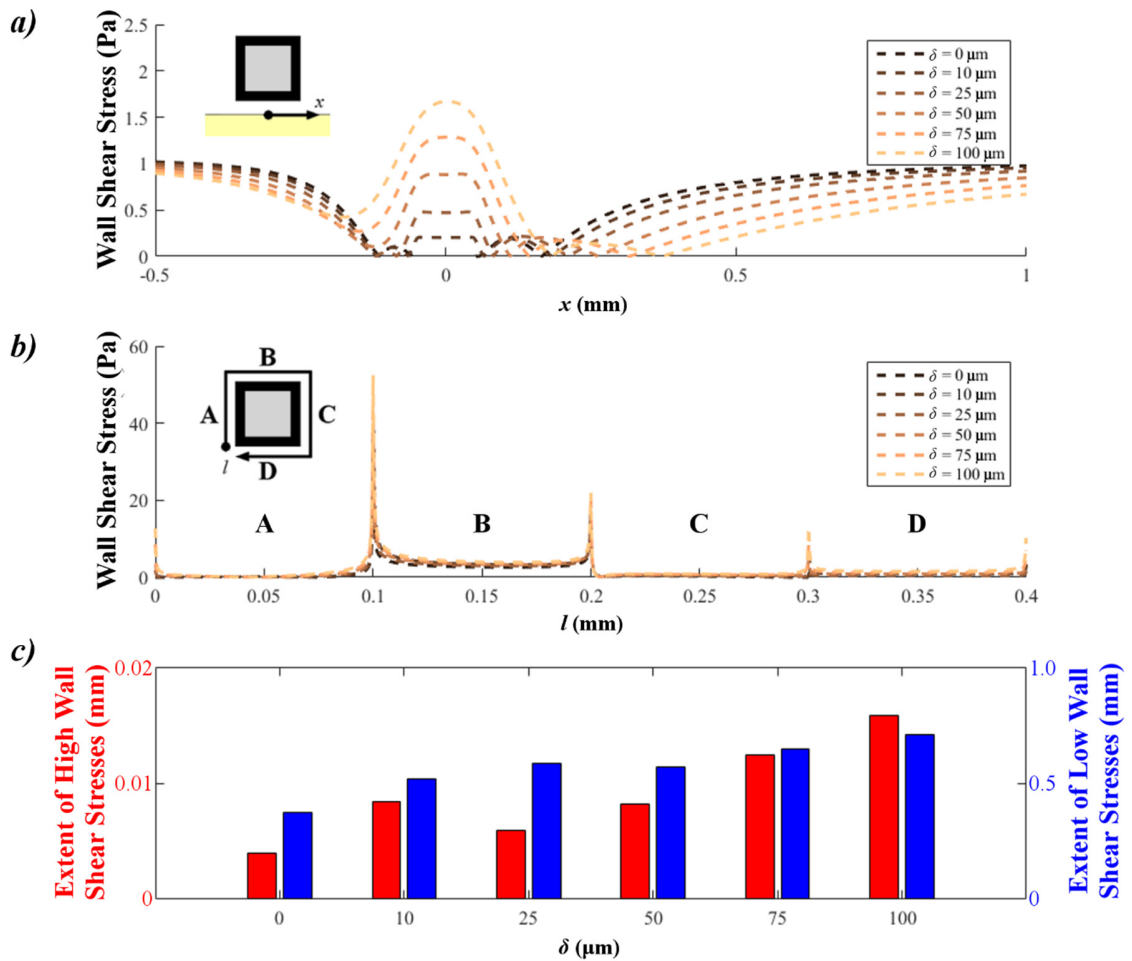


Figure 5-6. The impact of stent malapposition on the haemodynamics and drug transport of stented arteries. a) Regions of low wall shear stress (<0.5 Pa) could be observed along the lumen-tissue interface both upstream and downstream of the struts. b) Regions of elevated wall shear stress (>6 Pa) were observed on the top corners of the strut in each case. c) The extent of low wall shear stresses along the tissue and high wall shear stresses along the strut generally increased with respect to the malapposition distance.

5.2.2 The Drug Transport Behaviour of Malapposed Struts

Comparison of the drug-transport behaviour of Model II and Model III revealed that modelling the depletion of drug within the strut coating vastly affects the uptake of drug in the arterial tissue. In Figure 5-7, the AWAC of drug was calculated for each

geometry in both models. As in previous studies which utilised a uniform, time-invariant drug coating concentration, the results in Figure 5-7a – obtained with Model II – showed that malapposed struts can facilitate significant levels of drug uptake. However, if the depletion of drug within the strut coating is taken into consideration, then it is clear from the results of Figure 5-7b that stent malapposition significantly compromises drug uptake; whereas a 6.5% increase in AWAC is observed in Model II when comparing the malapposed case where $\delta = 10 \mu\text{m}$ to the well-apposed case, a 93% decrease in AWAC is observed in Model III. Note that the AWAC values shown in these graphs represent the average normalised drug concentration throughout the entire tissue domain.

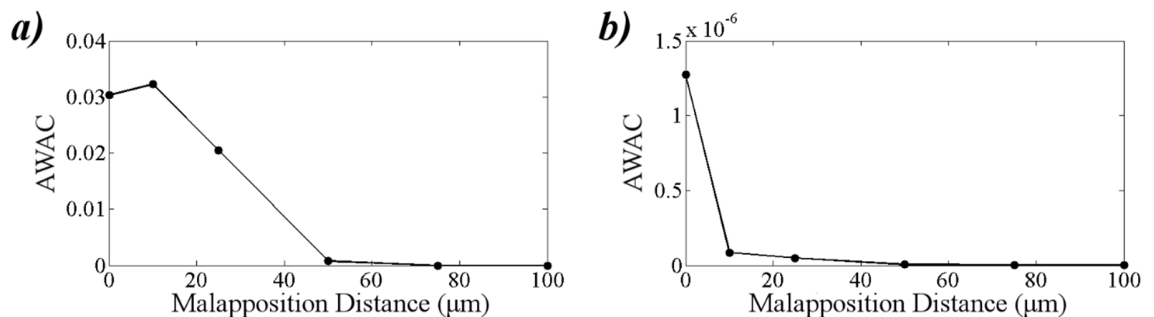


Figure 5-7. The impact of incomplete stent apposition on the area-weighted average concentration (AWAC) of drug in the arterial tissue. In the simulations performed using Model II (a), significant drug uptake was noted even when the strut was not in direct contact with arterial tissue. In Model III however (b), significant depletion of drug was noted even for very small stent malapposition distances.

This disparity between the two drug transport models is further illustrated in the contours of the normalised drug concentration in Figure 5-8 and Figure 5-9. Using these results, it is concluded that the drug uptake from malapposed drug

eluting stent struts is negligible and that the depletion of drug within the stent coating needs to be implemented into numerical models.

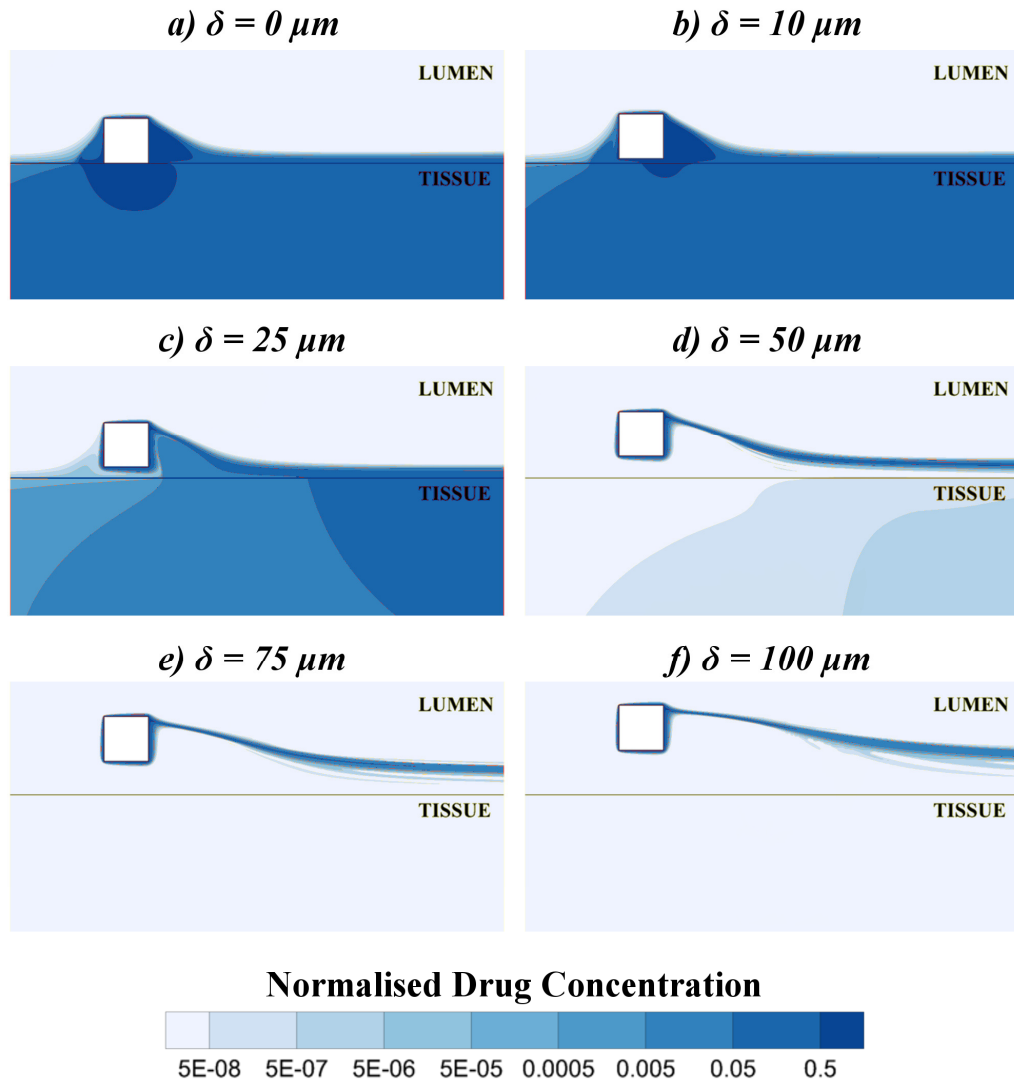


Figure 5-8. Contours of the normalised drug concentration obtained with Model II. As the depletion of drug within the coating was not modelled in these cases, significant drug uptake was noted even when $\delta = 25 \mu\text{m}$.

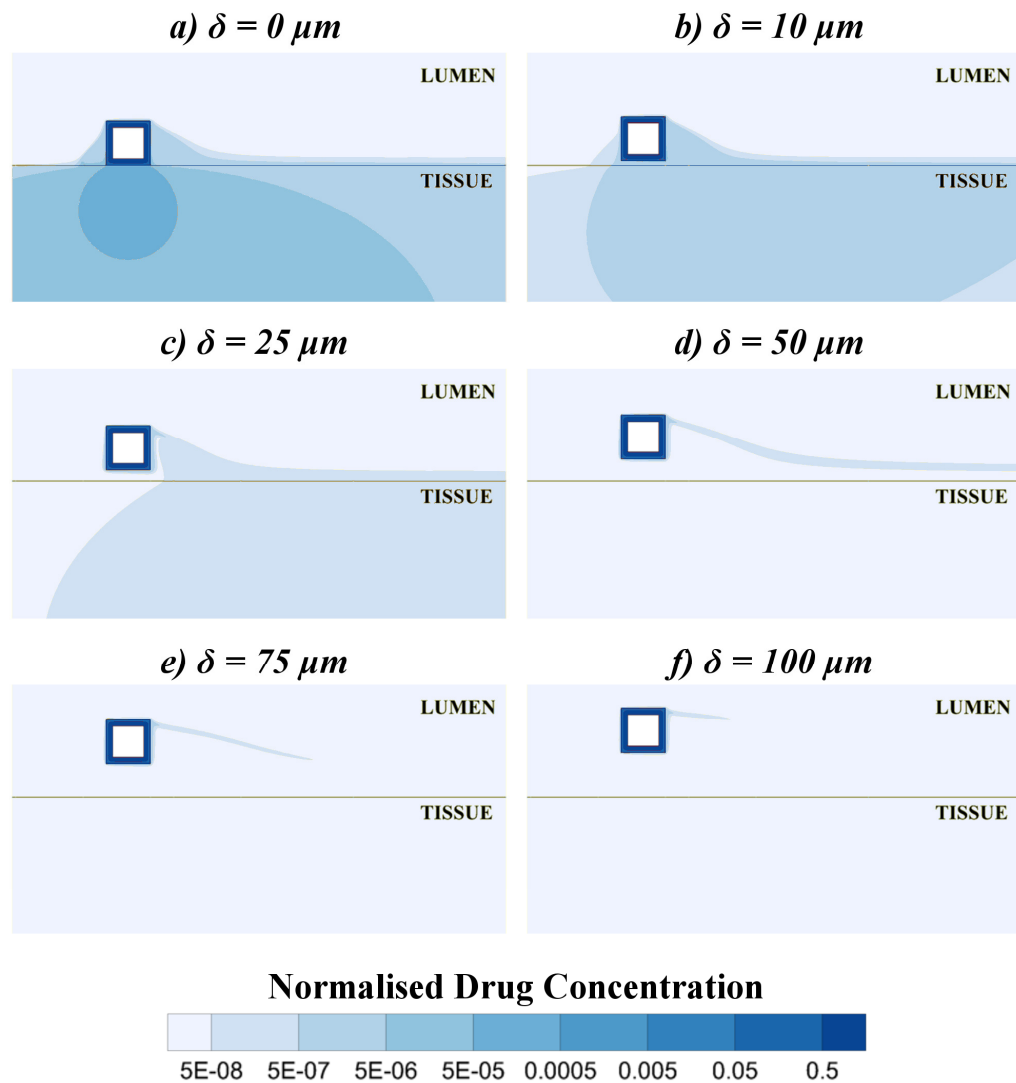


Figure 5-9. Contours of the normalised drug concentration obtained with Model III. As the depletion of drug within the coating was modelled in these cases, even a small malapposition distance of $\delta = 10 \mu\text{m}$ yielded negligible drug uptake.

5.3 Outcomes

Using two-dimensional CFD simulations, it was shown in this study that larger stent malapposition distances yield an increased prevalence of platelet-activating high wall shear stresses and endothelial dysfunction-inducing low wall shear stresses. It was also shown that increasing this malapposition distance yields a significant reduction

in the transport of antiproliferative drug into the tissue. The combined lack of drug in the vessel wall and continued presence of low wall shear stress regions is thought to account for the increased restenotic risk associated with malapposed drug-eluting stent struts. Hence, it is particularly important to ensure that the adverse haemodynamics of arteries treated with drug-eluting stents are alleviated when stent malapposition occurs.

Chapter 6

The Localised Haemodynamics of Drug-Eluting Stents are not Improved by the Presence of Magnetic Struts

Chapter Aims

Blood, a biomagnetic fluid, experiences two forces when in the vicinity of magnets:

1) magnetisation forces which reorient red blood cells to align with the magnetic field, and 2) Lorentz forces which oppose the flow of blood. The aim in this chapter is to investigate whether these forces can be used to attenuate the haemodynamic disturbances that are produced by stent struts and thus alleviate the risk of in-stent restenosis and stent thrombosis.

6.1 Methods

6.1.1 Geometry

To achieve the aim of this chapter, a series of two-dimensional CFD simulations were performed using the idealised stented-vessel geometry depicted in Figure 6-1. In this geometry, the vessel lumen was modelled as a 3 mm tall fluid domain with a single 0.1 mm square cross-section drug-eluting stent strut positioned halfway between the inlet and outlet. One side of the strut was in direct contact with the vessel wall, whilst the other three sides were exposed to luminal blood flow. The magnetic source is the stent platform itself, which is located within a 15 μm thick coating.

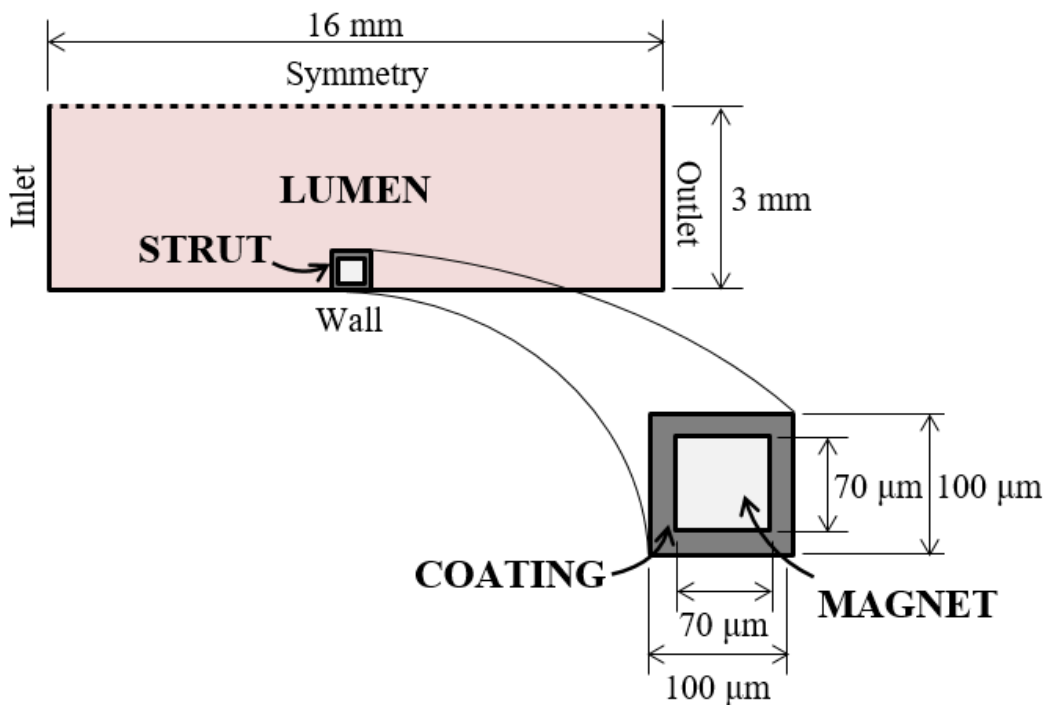


Figure 6-1. Geometry and Boundary Conditions. A single 0.1 mm square cross-section drug-eluting stent strut was positioned halfway between the inlet and outlet with one side of the strut in direct contact with the vessel wall. The magnetic source is the stent platform.

The dimensions used were consistent with those of the stented renal artery geometries of Chapters 2 and 3, reflecting the current clinical interest in non-coronary vessels [101,102]. Furthermore, the square-edged, two-dimensional nature of the geometry enabled the modelling of a worst case scenario in which the flow is perpendicular to the strut and in which flow disturbances are maximised. This made it the ideal geometry for studying the validity of the magnetic drug-eluting stent concept.

6.1.2 Mathematical Model

The blood flowing through this idealised geometry was modelled using a combination of the continuity (Equation 6-1), momentum (Equation 6-2) and Maxwell equations (Equations 6-3 to 6-7).

$$\nabla \cdot \mathbf{V} = 0 \quad (6-1)$$

$$(\mathbf{V} \cdot \nabla) \mathbf{V} = \nu \nabla^2 \mathbf{V} + \frac{1}{\rho} [-\nabla P + \underbrace{\mathbf{J} \times \mathbf{B}}_{\mathbf{F}^L} + \underbrace{\mu_0 (\mathbf{M} \cdot \nabla) \mathbf{H}}_{\mathbf{F}^M}] \quad (6-2)$$

$$\nabla \cdot \mathbf{B} = \nabla \cdot [\mu_0 (\mathbf{H} + \mathbf{M})] = 0 \quad (6-3)$$

$$\nabla \cdot \mathbf{J} = 0 \quad (6-4)$$

$$\nabla \times \mathbf{H} = \mathbf{J} \quad (6-5)$$

$$\mathbf{J} = \sigma (\mathbf{E} + \mathbf{V} \times \mathbf{B}) = \sigma (-\nabla \Phi + \mathbf{V} \times \mathbf{B}) \quad (6-6)$$

$$\nabla^2 \Phi = \nabla \cdot (\mathbf{V} \times \mathbf{B}) \quad (6-7)$$

\mathbf{V} is the velocity vector of blood in the lumen and ∇ is the gradient operator. In the momentum equation, ρ is the blood density, ν is the kinematic viscosity of blood, P is the thermodynamic pressure and t is the time. The two additional body forces, \mathbf{F}^L

and \mathbf{F}^M , act on the blood due to interactions with the magnetic field; \mathbf{F}^L is the Lorentz force, which opposes the motion of electrically conducting fluids in an imposed magnetic fields, and \mathbf{F}^M is the magnetisation force, which is an attractive or repulsive response to magnetic field gradients. In the Maxwell equations, \mathbf{J} , \mathbf{B} , \mathbf{M} , \mathbf{E} and \mathbf{H} are the total current density, magnetic flux density, magnetisation, electric field intensity and magnetic field intensity respectively. μ_0 is the permeability of free space, σ is the electrical conductivity of blood and, finally, Φ is an electric potential field resulting from the movement of blood within the magnetic field.

Several assumptions were used to simplify this haemodynamic model. Blood was modelled with a uniform density, $\rho = 1060 \text{ kg/m}^3$, and laminar flow conditions were assumed due to the low Reynolds numbers ($Re < 1300$ [137]) in the renal vasculature. A constant viscosity of $\nu = 3.3 \times 10^{-6} \text{ m}^2/\text{s}$, based on blood's lowest viscosity limit, was ascribed to the blood as it yields more exaggerated recirculating flow regions than other blood rheological models, as shown in Chapter 2. Furthermore, blood was modelled as a conducting fluid with a constant electrical conductivity of $\sigma = 0.8 \text{ S/m}$. This conductivity has been measured to be 0.7 S/m in stationary blood [96] and increases by $\sim 10\%$ when subjected to medium shear rates as viscous forces alter erythrocyte orientation [94]. Conductivity is also dependent on temperature and hematocrit, although these effects and the effect of shear rate were neglected for simplicity. Additionally, a simplified magnetisation model was implemented in which temperature and density dependencies were neglected. In this model,

$$\mathbf{M} = \chi \mathbf{H}, \tag{6-8}$$

where χ is the magnetic susceptibility of blood. Oxygenated blood is diamagnetic, indicating that it is repelled away from the direction of increasing magnetic field

intensity, so that it possesses a negative magnetic susceptibility [91], $\chi_{oxyg} = -6.6 \times 10^{-7}$. Conversely, deoxygenated blood is paramagnetic, signifying that it is attracted towards the direction of increasing magnetic field intensity; thus it has a positive magnetic susceptibility [141], $\chi_{deoxyg} = 3.5 \times 10^{-6}$. Both χ values were implemented to broaden the range of stented vessel environments in which the feasibility of the magnetic drug-eluting stent concept was evaluated. Finally, the magnetisation field and the magnetic field were assumed to be parallel, enabling the magnetisation force in Equation 6-2 to be rewritten as

$$\mathbf{F}^M = \mu_0 M \nabla H, \quad (6-9)$$

where $M = |\mathbf{M}|$ and $H = |\mathbf{H}|$.

The solution of Equations 6-1 to 6-9 was accomplished through use of the finite volume solver ANSYS FLUENT 14.5 (ANSYS Inc.). A semi-implicit (SIMPLEC) algorithm coupled the pressure and velocity whilst a second order central differencing scheme spatially discretised the pressure and momentum variables. A second order upwind scheme was used to discretise the Cartesian components of the induced magnetic field vector. The inbuilt magnetohydrodynamics module of ANSYS FLUENT 14.5 was used to calculate the Lorentz body force whilst the magnetisation body force was implemented into the solver using user-defined functions.

6.1.3 Boundary Conditions

In the process of resolving these body forces, the magnetic fields surrounding the stent strut boundary were defined in the same way as the fields surrounding infinitely-long permanent rectangular magnets. The intensity of these magnetic fields, \mathbf{H} , is related to the magnetic flux density, \mathbf{B} , by the equation $\mathbf{B} = \mu_0(\mathbf{M} + \mathbf{H})$;

however, as $\mathbf{M} \ll \mathbf{H}$, the simplified form, $\mathbf{B} = \mu_0 \mathbf{H}$, was used in this analysis. Two magnetic flux density field configurations were studied, the first with poles at the top and bottom of the strut and the second with poles facing fore and aft of the strut. The x - and y -components of the first configuration are described [142] as,

$$B_x(x, y) = \frac{\mu_0 M_S}{4\pi} \left\{ \ln \left[\frac{(x+w)^2 + (y-h)^2}{(x+w)^2 + (y+h)^2} \right] - \ln \left[\frac{(x-w)^2 + (y-h)^2}{(x-w)^2 + (y+h)^2} \right] \right\} \quad (6-10)$$

and

$$B_y(x, y) = \frac{\mu_0 M_S}{2\pi} \left\{ \tan^{-1} \left(\frac{2h(x+w)}{(x+w)^2 + y^2 - h^2} \right) - \tan^{-1} \left(\frac{2h(x-w)}{(x-w)^2 + y^2 - h^2} \right) \right\}, \quad (6-11)$$

whilst the components of the second configuration are described [142] as,

$$B_x(x, y) = \frac{\mu_0 M_S}{2\pi} \left\{ \tan^{-1} \left(\frac{2w(y+h)}{(y+h)^2 + x^2 - w^2} \right) - \tan^{-1} \left(\frac{2w(y-h)}{(y-h)^2 + x^2 - w^2} \right) \right\} \quad (6-12)$$

and

$$B_y(x, y) = \frac{\mu_0 M_S}{4\pi} \left\{ \ln \left[\frac{(y+h)^2 + (x-w)^2}{(y+h)^2 + (x+w)^2} \right] - \ln \left[\frac{(y-h)^2 + (x-w)^2}{(y-h)^2 + (x+w)^2} \right] \right\}. \quad (6-13)$$

On the assumption of a coating thickness of 15 μm , the height and width of the infinitely-long permanent rectangular magnet in both configurations was $2h = 2w = 70 \mu\text{m}$. The value of M_S was varied in order to yield peak magnetic flux densities of $B_{max} = 0 \text{ T}$, 4T and 8T at the strut surface. The magnetic flux density fields of the top-bottom pole configuration and the fore-aft pole configuration are visualised in Figure 6-2a and Figure 6-2b respectively for a case where $B_{max} = 1 \text{ T}$.

Excepting these changes in magnet strength and orientation, all haemodynamic boundary conditions remained the same in each simulation. A steady, fully-developed inlet velocity profile corresponding to a Reynolds number of 427 was used, consistent with mean flow conditions in the renal vasculature [75]. A uniform, zero gauge pressure boundary condition was specified at the outlet, whilst no-slip conditions were assigned to the strut-lumen and lumen-tissue interfaces. A symmetry boundary condition was also specified at the top of the lumen domain, as shown in Figure 6-1. Finally, the arterial wall was treated as rigid and electrically insulating (i.e. $\partial\Phi/\partial n = 0$, where n is the direction normal to the wall) whilst zero induced magnetic flux density at the inlet and outlet was also specified.

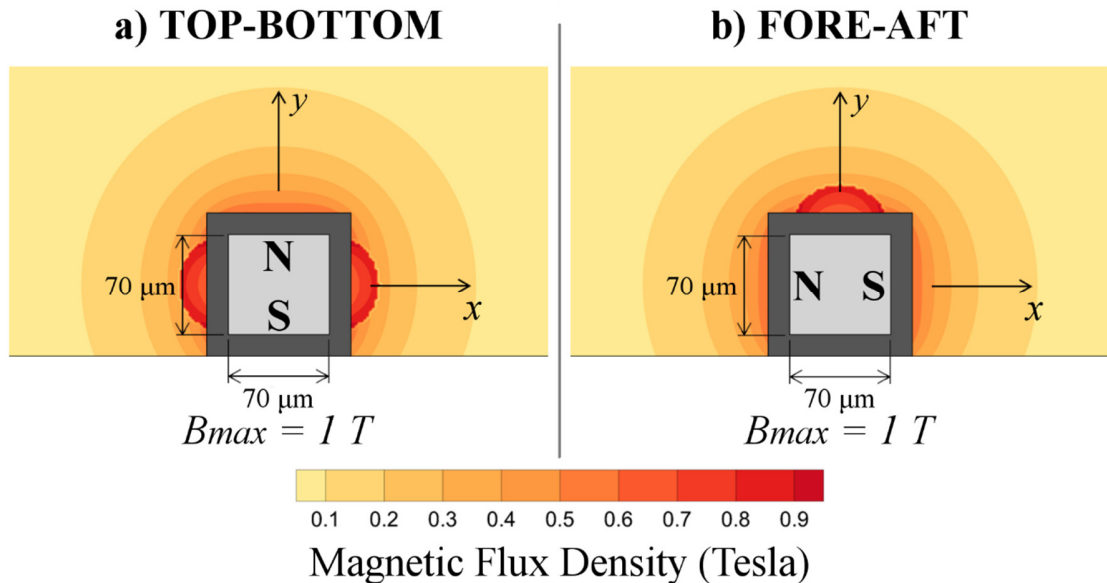


Figure 6-2. Magnetic flux density contours of the magnetic drug-eluting stent strut used in this study. The magnet has been modelled as an infinitely long permanent rectangular magnet with height $2h = 70\ \mu\text{m}$ and width $2w = 70\ \mu\text{m}$. Cases in which $B_{max} = 1\ \text{T}$ are depicted for the configurations in which the poles are a) on the top and bottom strut faces, and b) on the fore and aft strut faces. Note that the positions of the north and south poles are interchangeable in each case and do not affect the results.

6.1.4 Grid Description

These same boundary conditions were also used in a series of mesh independence studies, performed to ensure the reliability of the subsequent magnetic drug-eluting stent cases. The mesh densities used in these studies were greatest in the regions closest to the stent strut and also near the arterial wall. This enabled the resolution of thin boundary layers along the strut and arterial walls. The flow was deemed to be resolved once the grid convergence indexes (GCI) corresponding to the lengths of recirculation zones fell below 2%. This GCI was defined as [125]:

$$\text{GCI}_{\text{fine grid}} = \frac{3 \left| \frac{f_{\text{fine}} - f_{\text{coarse}}}{f_{\text{fine}}} \right|}{r^p - 1}, \quad (6-14)$$

where f_{fine} and f_{coarse} refer to either the proximal or distal recirculation length for a fine and coarse mesh respectively. r is the refinement factor, and p is the order of accuracy of the solution. Using values of $r = 2$ and $p = 2$, the blood flow around the strut was found to be adequately resolved with a mesh containing 225,064 elements. More information regarding these mesh convergence studies may be found in Appendix A.

6.2 Results and Discussion

The results obtained using this mesh may be seen in Figure 6-3 and Figure 6-4 respectively. It may be seen in Figure 6-3 that oxygenated blood is only noticeably affected by the presence of the magnetic strut when the top-bottom configuration magnet is used and when $B_{\text{max}} = 8$ T. This configuration, shown in Figure 6-3a(iii), yielded a slightly taller proximal recirculation zone and an enlarged secondary vortex

within this zone. Similarly, it may be seen in Figure 6-4 that deoxygenated blood is only noticeably affected by the presence of a magnetic strut when a top-bottom configuration magnet is used and when $B_{max} \geq 4$ T. This configuration yielded a proximal recirculation zone with reduced height and an enlarged secondary vortex within the distal recirculation zone, as may be seen in Figure 6-4a(ii) and Figure 6-4a(iii). In contrast, the fore-aft magnet configuration had negligible impact on the haemodynamics of the stented vessel in either oxygenated or deoxygenated blood.

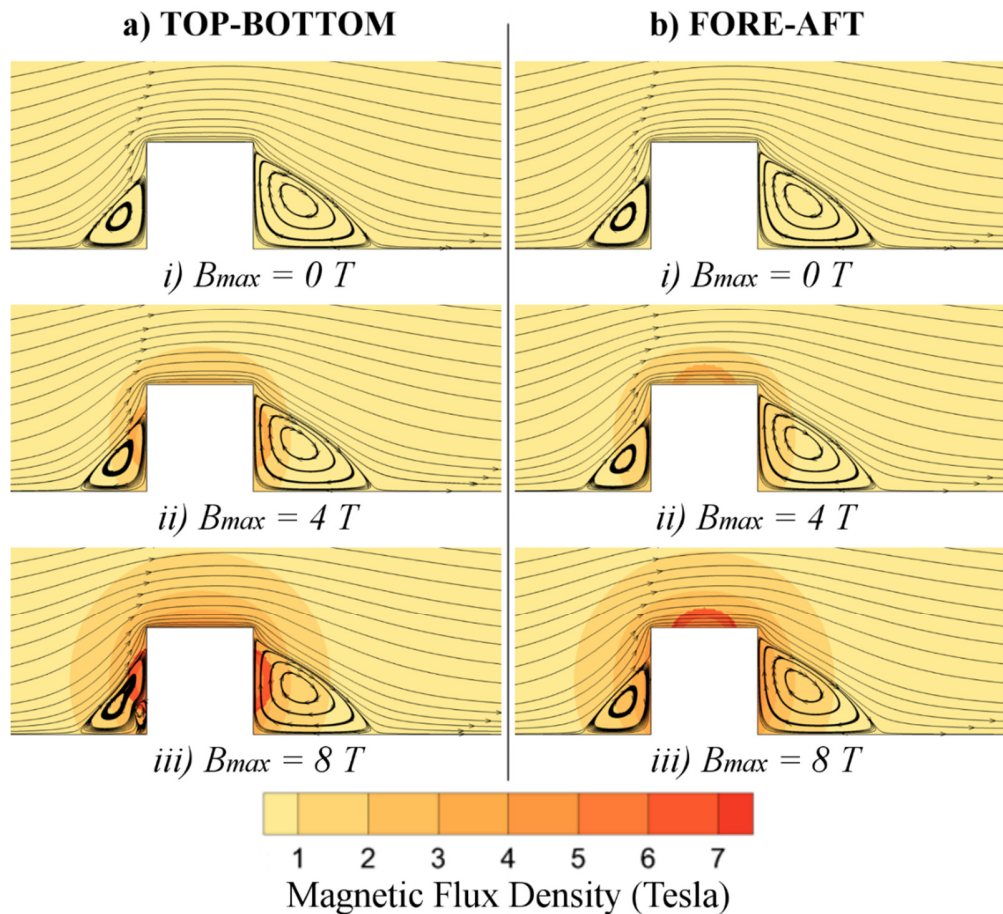


Figure 6-3. The magnetically-altered haemodynamics of oxygenated blood in a vessel with a well-apposed drug-eluting stent strut.

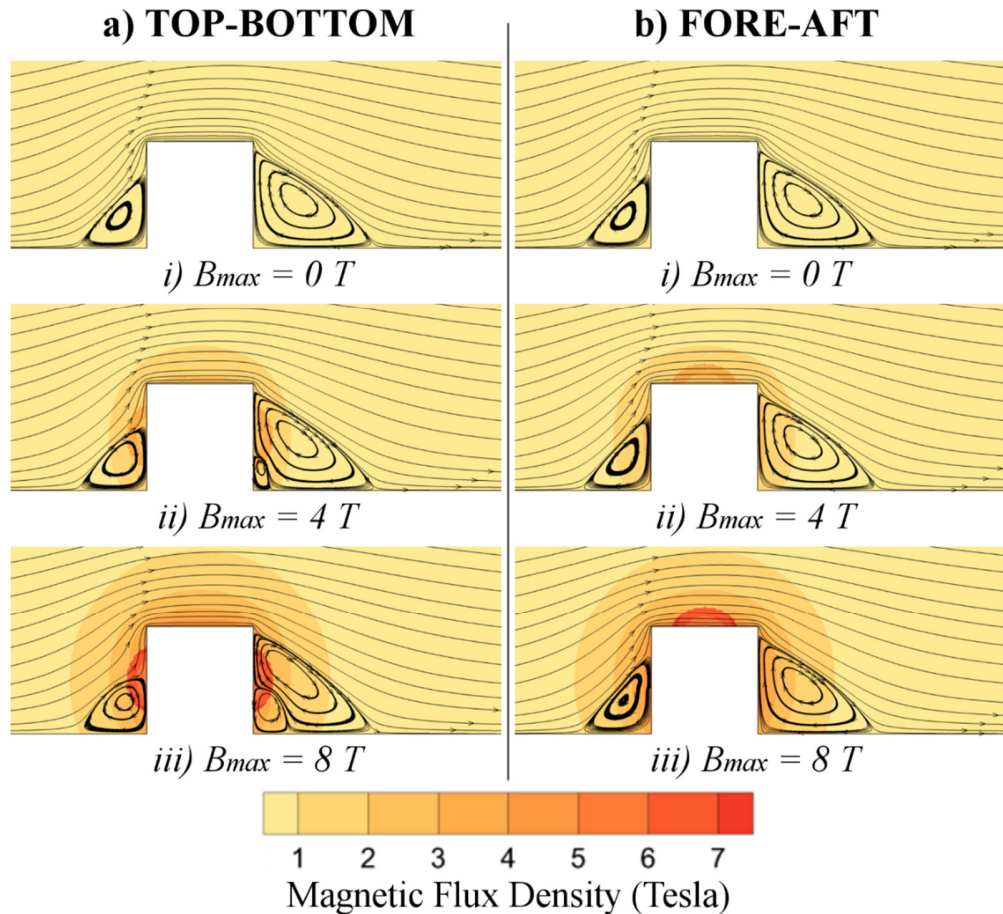


Figure 6-4. The magnetically-altered haemodynamics of deoxygenated blood in a vessel with a well-apposed drug-eluting stent strut.

The differences between Figure 6-3 and Figure 6-4 are due to the different magnetic susceptibilities of oxygenated and deoxygenated blood; whereas oxygenated blood is repelled away from the direction of increasing magnetic flux density, deoxygenated blood accelerates towards this direction. Hence, as oxygenated blood within the proximal recirculation zone moves down the strut face – in the same direction that magnetic flux density increases for the Top-Bottom configuration

magnet – the blood decelerates. When the magnet is strong enough, as occurs in Figure 6-3a(iii), the fluid velocity reduces to zero along the strut face and causes the flow to separate from that surface. This accounts for the enlarged secondary recirculation zone within the proximal recirculation zone of Figure 6-3a(iii). Similarly, as deoxygenated blood within the distal recirculation zone moves up the strut face – in the same direction that magnetic flux density decreases in the Top-Bottom configuration magnet – it decelerates. When the magnet is strong enough, as occurs in Figure 6-4a(iii), flow separation occurs, establishing the large secondary vortex within the distal recirculation zone.

The differences in height of the proximal recirculation zones in cases involving the Top-Bottom configuration magnet can similarly be explained by the differences in magnetic susceptibility. The magnet causes deoxygenated blood flowing along the top of the proximal recirculation zone to be accelerated towards the strut, thereby flattening the recirculation zone. On the other hand, oxygenated blood flowing along the top of the proximal recirculation zone is repelled, thereby extending the height of this recirculation zone. However, as shown in Table 6-1, no major reductions to the proximal or distal recirculation lengths along the lumen were observed with either Top-Bottom or Fore-Aft pole configurations, in both oxygenated and deoxygenated blood. Hence, the localised haemodynamics of drug-eluting stents are not improved by the presence of magnetic struts.

Table 6-1: The effect of magnetic flux density and orientation on recirculation length in oxygenated and deoxygenated blood.

| NON-MAGNETIC STRUT | | | | | |
|--------------------------------------|---------------|---------------------|----------|-------------------|----------|
| Magnet orientation | B_{max} (T) | $L_{proximal}$ (mm) | % Change | L_{distal} (mm) | % Change |
| n/a | 0 | 0.065 | n/a | 0.115 | n/a |
| MAGNETIC STRUT IN OXYGENATED BLOOD | | | | | |
| Magnet orientation | B_{max} (T) | $L_{proximal}$ (mm) | % Change | L_{distal} (mm) | % Change |
| Top-Bottom | 4.0 | 0.065 | 0% | 0.115 | 0% |
| Top-Bottom | 8.0 | 0.065 | 0% | 0.115 | 0% |
| Fore-Aft | 4.0 | 0.065 | 0% | 0.116 | 0.9% |
| Fore-Aft | 8.0 | 0.065 | 0% | 0.116 | 0.9% |
| MAGNETIC STRUT IN DEOXYGENATED BLOOD | | | | | |
| Magnet orientation | B_{max} (T) | $L_{proximal}$ (mm) | % Change | L_{distal} (mm) | % Change |
| Top-Bottom | 4.0 | 0.065 | 0% | 0.115 | 0% |
| Top-Bottom | 8.0 | 0.064 | -1.5% | 0.115 | 0% |
| Fore-Aft | 4.0 | 0.065 | 0% | 0.114 | -0.9% |
| Fore-Aft | 8.0 | 0.065 | 0% | 0.112 | -2.6% |

6.3 Outcomes

In this CFD study, the feasibility of using magnetic drug-eluting stent struts to mitigate the adverse haemodynamics which precipitate stent thrombosis was studied. However, even at unrealistically strong magnetic flux densities of 8.0 T, this magnetic strut concept only minimally affected the length of the low wall shear stress-producing recirculation zones adjacent to the strut. Hence, the magnetic strut concept was determined to be unsuitable for mitigating the non-physiological shear stresses that precipitate stent thrombosis.

Chapter 7

Streamlining Drug-Eluting Stents to Improve their Haemodynamic and Drug Transport Behaviour

Chapter Aims

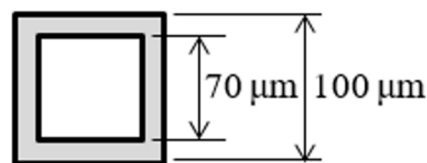
The non-streamlined nature of current commercial drug-eluting stent strut designs promotes an adverse haemodynamic environment that may precipitate in-stent restenosis and stent thrombosis. The aim of this chapter is to see if a streamlined drug-eluting stent strut design can be used to alleviate this adverse haemodynamic environment whilst simultaneously enhancing drug uptake.

7.1 Methods

7.1.1 Geometry

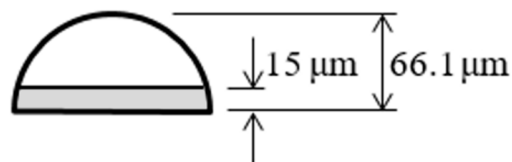
A series of two- and three-dimensional CFD simulations were performed to see if these possibilities can be achieved. In each of these simulations, the haemodynamics and drug transport behaviour of a square profile strut geometry were compared against a geometry with a more streamlined, semicircular strut profile. Both struts, shown in Figure 7-1, are comprised of a stent platform and a drug coating. The area of the stent platform and the thickness of the drug coating is identical in both cases. However, whilst all surfaces of Strut Profile I are coated, only an abluminal coating is modelled in Strut Profile II.

a) *Strut Profile I*



 Stent Platform

b) *Strut Profile II*



 Drug Coating

Figure 7-1. A non-streamlined, square profile strut geometry (a) is contrasted with a streamlined, semicircular profile strut geometry (b) in this study. The cross-sectional area of the stent platform and the thickness of the drug coating is the same in both cases. However, whilst all four sides of Strut Profile I feature a drug coating, this coating is present only in the abluminal face of Strut Profile II.

A coating was present only on the abluminal face of Strut Profile II for three main reasons. Firstly, it reduces the overall thickness of the strut, thereby reducing flow disturbances. Secondly, the antiproliferative drug coating impedes re-endothelialisation [143,147]; hence, an absence of drug along the top of the struts may enhance the endothelial coverage of the struts [148]. Finally, the drug transport from non-contacting surfaces was shown to be negligible in Chapter 3; hence the coating is only necessary in the region where the strut contacts the tissue.

As both stent profiles had the same amount of stent platform material, this contact region was larger in Strut Profile II than in Strut Profile I. Despite having only 39% of the drug coating volume of Strut Profile I, it is anticipated that the enhanced contact region of Strut Profile II will yield greater drug uptake. Strut Profile II is therefore anticipated to not only alleviate the adverse haemodynamics of stented arteries, but also improve the drug transport behaviour.

These two strut profiles were used in conjunction with the three stented renal artery geometries illustrated in Figure 7-2. The first of these geometries, shown in Figure 7-2a, is a two-dimensional geometry featuring a single, well-apposed drug-eluting stent strut. The second geometry was identical to the first except that the strut is malapposed with a 50 μm gap between the bottom of the strut and the tissue, as shown in Figure 7-2b. The final stented renal artery geometry is three-dimensional and features two struts that have been offset from one another by 2 mm. Note that a complete 360° geometry was established for this three-dimensional study in case secondary flows were observed, which could cause disturbances that would move across the interfaces in an axisymmetric model.

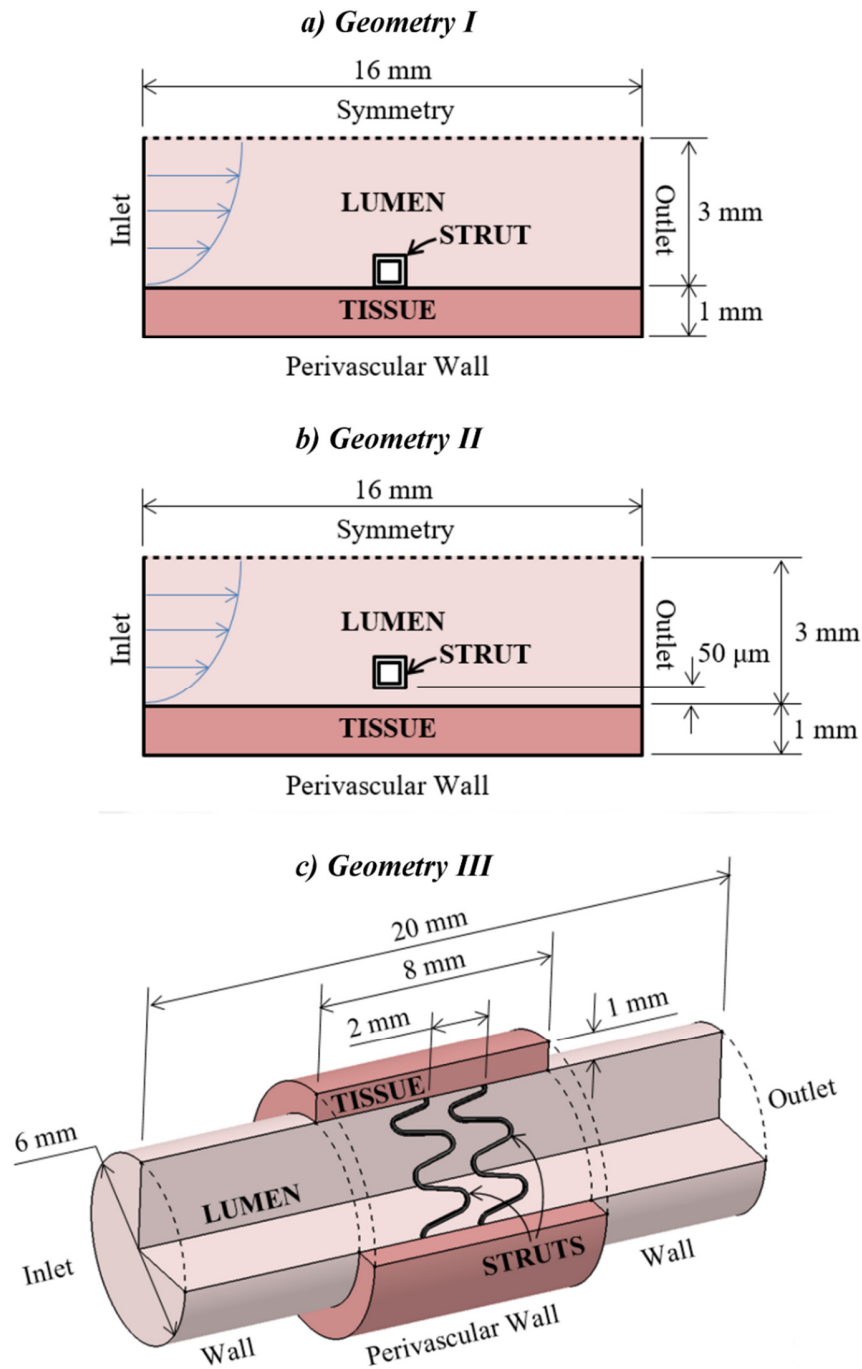


Figure 7-2. Three stented renal artery geometries were used in this study in conjunction with the two strut profile geometries shown earlier. The first geometry (a) is a two-dimensional model featuring a single, well-apposed drug-eluting stent strut. The second geometry (b) is also a two-dimensional model but features a single, malapposed drug-eluting stent strut. Finally, a more realistic three-dimensional geometry (c) is implemented, featuring two well-apposed drug-eluting stent struts.

In each of these geometries, the flow field and drug concentration distribution was modelled in the lumen, whilst drug concentration distributions were also modelled in the coating and tissue. In the two-dimensional geometries, the lumen was modelled as a 3 mm tall fluid domain and the arterial tissue was modelled as a 1 mm thick, homogeneous fluid domain. In the three-dimensional geometry, the lumen was modelled as a 6 mm diameter fluid domain and a 1 mm thick fluid domain was once again used to model the arterial tissue. The struts were modelled halfway between the inlet and outlet in each case. Note that whilst only Strut Profile I is depicted in Figure 7-2, these geometries were also used in conjunction with Strut Profile II.

7.1.2 Mathematical Model

The blood flowing through these geometries was modelled as a Newtonian, incompressible fluid undergoing laminar flow using the formulation of the Navier-Stokes equations shown below.

$$\nabla \bullet \mathbf{V} = 0 \quad (7-1)$$

$$\rho \left[\frac{\partial \mathbf{V}}{\partial t} + \mathbf{V} \bullet \nabla \mathbf{V} \right] = -\nabla P + \nabla \bullet (\mu \nabla \mathbf{V}). \quad (7-2)$$

In these equations, \mathbf{V} is the velocity vector of blood in the lumen, ∇ is the gradient operator, ρ is the blood density, μ is the dynamic viscosity of blood, and P is the thermodynamic pressure.

Several assumptions were used to simplify this haemodynamic model. Blood was modelled with uniform density, $\rho = 1060 \text{ kg/m}^3$, and laminar flow conditions were assumed due to the low Reynolds numbers ($Re < 1300$ [137]) in the renal vasculature. A constant viscosity of $\mu = 0.00345 \text{ Pa}\cdot\text{s}$, based on blood's lowest viscosity limit, was ascribed to the blood for three main reasons: firstly, it yields

more exaggerated flow disturbances than non-Newtonian blood rheological models; secondly, the wall shear stress thresholds used in this study were originally obtained using Newtonian models [66,138], and; finally, the choice of blood rheological model has negligible impact on the drug transport behaviour of stented arteries, as shown in Chapter 3.

Drug transport in the lumen was modelled using a scalar convection-diffusion equation,

$$\frac{\partial c}{\partial t} + \mathbf{V} \cdot \nabla c = D_l \nabla^2 c, \quad (7-3)$$

whilst drug transport in the tissue and strut coating were characterised using diffusion-only equations,

$$\frac{\partial c}{\partial t} = D_t \nabla^2 c \quad (7-4)$$

and

$$\frac{\partial c}{\partial t} = D_c \nabla^2 c \quad (7-5)$$

respectively. In these equations, c is the normalised drug concentration, defined as the ratio of the local drug concentration, C , to the maximum concentration of drug in the strut coating, C_0 , viz

$$c = C/C_0. \quad (7-6)$$

Furthermore, D_l , D_t and D_c represent the diffusivity of the drug in the blood, tissue and coating respectively.

Paclitaxel served as the model drug in this analysis, chosen for its use as the active agent in drug-eluting stents and for the large corpus of data regarding its transport. Its diffusivity coefficients in blood and arterial tissue have been observed to be $D_l = 3.89 \times 10^{-11} \text{ m}^2/\text{s}$ [105] and $D_t = 3.65 \times 10^{-12} \text{ m}^2/\text{s}$ [106] respectively. The

diffusivity coefficient of Paclitaxel within the coating was calculated based on the formula

$$D_c = \frac{L_c^2}{t_{release}}, \quad (7-7)$$

where L_c is the coating thickness and $t_{release}$ is the desired duration of drug release [70].

A 10-day drug release duration was specified, based on the release rate of the TAXUS-MR (moderate release) paclitaxel-eluting stent [127]. Given the coating thickness of $L_c = 15 \mu\text{m}$, this resulted in a diffusion coefficient of

$$D_c = 2.60 \times 10^{-16} \text{ m}^2/\text{s}.$$

The solution of these equations was accomplished through use of the finite volume solver ANSYS FLUENT 16.2 (ANSYS Inc.). A semi-implicit (SIMPLEC) algorithm coupled the pressure and velocity whilst a second order central differencing scheme spatially discretised the pressure and momentum variables. Temporal discretisation was achieved with a second order implicit scheme whilst a second order upwind scheme was used to discretise the scalar drug concentration.

7.1.3 Boundary Conditions

The same haemodynamic boundary conditions were used in each geometry where possible. A steady, fully-developed inlet velocity profile corresponding with a Reynolds number of 427 was specified, consistent with the mean flow conditions of the renal vasculature [75]. A uniform, zero gauge pressure boundary condition was also used, whilst no-slip conditions were prescribed on the strut-lumen and lumen-tissue interface. A symmetry boundary condition was also specified on the top of the lumen domains in the two-dimensional geometries, as may be seen in Figure 7-2. No

such boundary condition was required in Geometry III; however, an additional no-slip condition was ascribed to the ‘wall’ boundaries depicted in Figure 7-2c.

Each of the simulations also employed identical boundary conditions to simulate the time-varying release of drug from the strut coating. Initially, a normalised drug concentration of unity was assigned throughout this coating whilst all other lumen and tissue regions were assumed to be devoid of drug. A normalised drug concentration of $c = 0$ was imposed at the inlet, implying that drug-free blood arrives from this boundary. This same boundary condition was ascribed to the perivascular wall, using the assumption that drug would not be able to penetrate to the very bottom of the tissue. Continuity of flux was assumed at the lumen-tissue interface, as well as the strut-tissue and strut-lumen interfaces. Finally, zero flux of drug was specified on each of the remaining boundaries within the lumen, tissue and strut. Using these boundary conditions, drug release was simulated from the strut into the tissue and lumen over a period of 24 hours.

7.1.4 Grid Description and Refinement

These same boundary conditions were also used in a series of mesh independence studies, performed to ensure that the solutions obtained were independent of the size of the grid used. The mesh densities in each geometry were greatest in the regions closest to the struts and near the interface between the tissue and lumen. This enabled the resolution of thin boundary layers which occurred along the no-slip boundaries defining the artery wall and the stent strut walls. Furthermore, the high mesh densities in the tissue and close to the stent struts facilitated the resolution of high drug concentration gradients.

The flow around these struts in the two-dimensional studies was deemed to be resolved once the grid convergence index (GCI) [125],

$$\text{GCI}_{\text{fine grid}} = \frac{3 \left| \frac{f_{\text{fine}} - f_{\text{coarse}}}{f_{\text{fine}}} \right|}{r^p - 1}, \quad (7-8)$$

corresponding to the extent of recirculation zones fell below 2% in the two-dimensional cases. In this equation, f_{fine} and f_{coarse} refer to the length of recirculating flow regions for a fine and coarse mesh respectively. r is the refinement factor, and p is the order of accuracy of the solution. In this case, $r = \sqrt{2}$ in the two-dimensional cases and $p = 2$. For the three-dimensional cases, the flow through both geometries was deemed to be adequately resolved once $\leq 5\%$ change in the area of coverage of recirculating flow regions was observed between two successive mesh refinements.

The drug transport behaviour was deemed to be resolved once convergence of the average concentration of drug within the tissue was obtained between successive mesh refinements. In Geometry I, grid convergence was deemed to be obtained once less than 2% change in the area-weighted average concentration (AWAC) of drug throughout the tissue domain was noted between refinements. The resulting tissue grid was then re-used in Geometry II. In Geometry III, the volume-weighted average concentration (VWAC) of drug throughout the tissue was monitored between refinements. Unlike the two-dimensional geometries, 2% change in VWAC could not be achieved due to the high computational demands associated with this geometry; hence, grid independence was assumed to occur once a 5% change in VWAC occurred between successive refinements. The mesh density was approximately doubled with each mesh refinement and the AWAC and VWAC were each measured after 24 hours of simulation time. As in Chapter 3, a time-step of 30 s was used in each simulation.

The final mesh sizes for each strut and artery geometry are shown in . More information regarding these mesh convergence studies may be seen in Appendix A. Table 7-1. More information regarding these mesh convergence studies may be seen in Appendix A.

Table 7-1. Final mesh sizes.

| Geometry | No. of Elements |
|-------------------------------|------------------------|
| I (strut profile I) | 149,726 |
| I (strut profile II) | 109,792 |
| II (strut profile I) | 193,224 |
| II (strut profile II) | 135,336 |
| III (strut profile I) | 22,613,628 |
| III (strut profile II) | 20,481,254 |

7.2 Results and Discussion

7.2.1 Two-dimensional simulations

The impact of these different strut profile geometries on the drug transport behaviour of these devices may be seen in the normalised drug concentration contours of Figure 7-3. In Figure 7-3a and Figure 7-3b, it is apparent that both strut profile geometries produced very symmetric drug concentration distributions at the culmination of the 24 hour simulation period. However, Strut Profile II, with its enhanced coating-tissue contact region, yielded an AWAC of 2.11×10^{-6} , 66% larger than the AWAC of 1.27×10^{-6} achieved with Strut Profile I. In contrast, the AWAC achieved by Strut Profile I and Strut Profile II when malapposed was just 6.09×10^{-9} and 4.81×10^{-9} respectively. This lack of significant drug uptake may be seen in Figure 7-3c and Figure 7-3d, and is due to the absence of contact between the tissue and the struts.

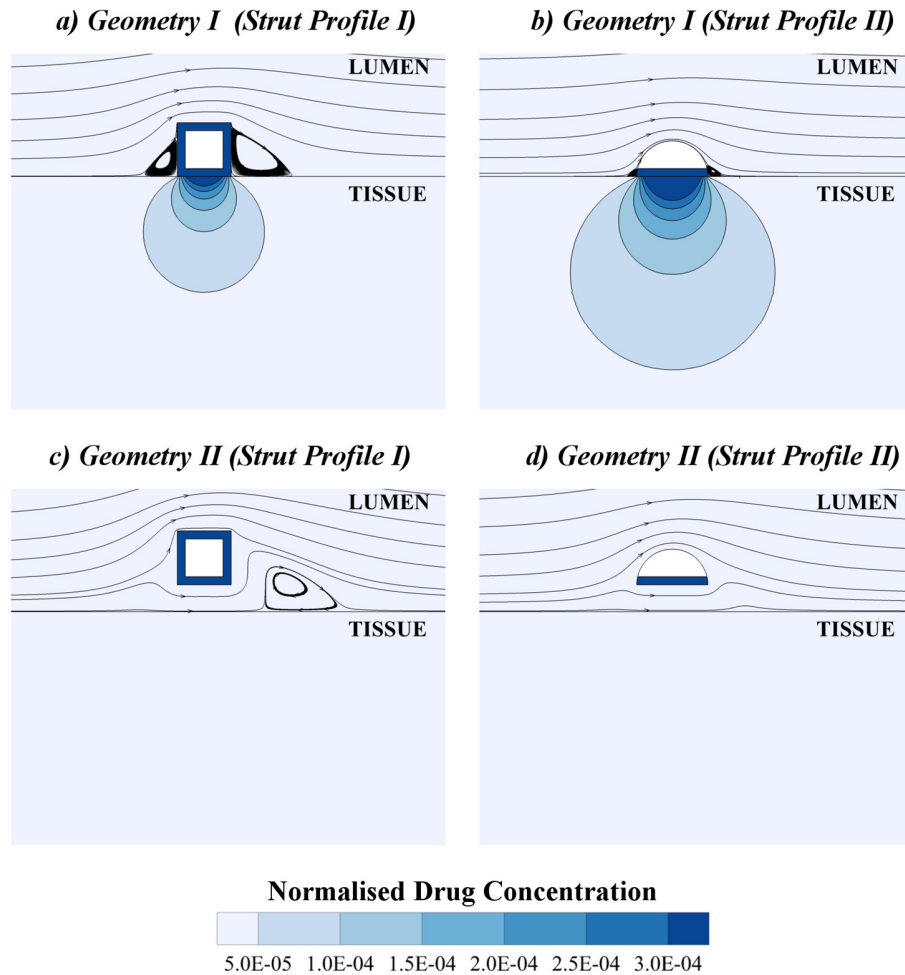


Figure 7-3. The impact of strut profile shape on the flow and drug transport from well-apposed and malapposed struts. In the well-apposed configuration, Strut Profile II produced proximal and distal recirculation zones that were 72% and 77% smaller, respectively, than those produced by Strut Profile I. With its enhanced coating-tissue contact, Strut Profile II also yielded 66% more drug uptake than Strut Profile I. In the Geometry II studies, recirculation zones were removed altogether once Strut Profile II was used in place of Strut Profile I. Neither profile yielded any significant drug uptake in this malapposed configuration.

It can also be seen in Figure 7-3 that altering the strut profile geometry can significantly affect the haemodynamics of stented vessels. Whereas Strut Profile I produced large recirculation zones in both well-apposed and malapposed

configurations, Strut Profile II significantly reduced or removed these zones. Specifically, in the Geometry I studies, the lengths of the proximal and distal recirculation zones reduced from 0.065 mm to 0.018 mm and from 0.115 mm to 0.027 mm respectively. Similarly, in the Geometry II studies, the 0.151 mm long recirculation bubble was removed altogether once Strut Profile II was used in place of Strut Profile I. The depletion of these recirculation zones helps to assuage the non-physiological wall shear stresses that act on the stent and tissue alike.

The impact of strut profile geometry on the magnitude of wall shear stresses acting on the tissue may be seen in Figure 7-4. In Geometry I, Strut Profile II yielded 59% less exposure to low wall shear stresses (<0.5 Pa) than Strut Profile I, as may be construed from Figure 7-4a. Similarly, in the malapposed configuration, Strut Profile II produced a 36% reduction in the extent of low wall shear stresses, as shown in Figure 7-4b. These results coincide with past findings that streamlined strut profile geometries can alleviate the low wall shear stresses that cause endothelial dysfunction [89].

Furthermore, this streamlined strut profile was also found to be effective in alleviating the platelet-activating high wall shear stresses along the top of the struts, as may be seen in Figure 7-5. These high wall shear stresses (>6 Pa [66]) occur around the top corners of Strut Profile I in both well-apposed and malapposed configurations, as shown in Figure 7-5a and Figure 7-5b respectively. In contrast, Strut Profile II yielded no such regions of high wall shear stress in either Geometry I or Geometry II and is thus less likely to cause platelet activation.

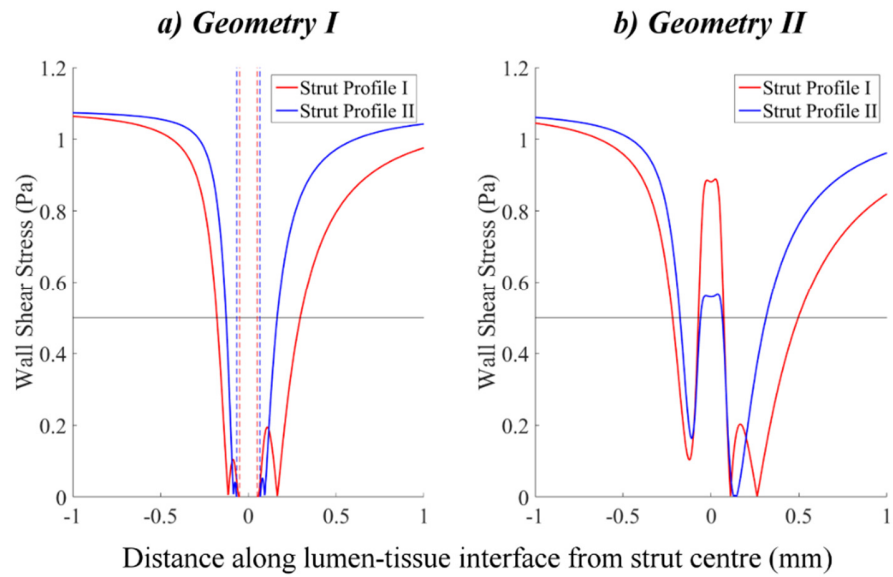


Figure 7-4. The impact of strut profile geometry on the wall shear stresses acting on the arterial tissue near the stent strut. In Geometry I, Strut Profile II yielded 59% less exposure to low wall shear stresses (<0.5 Pa) than Strut Profile I. Similarly, in Geometry II, Strut Profile II produced a 36% reduction in the extent of low wall shear stresses.

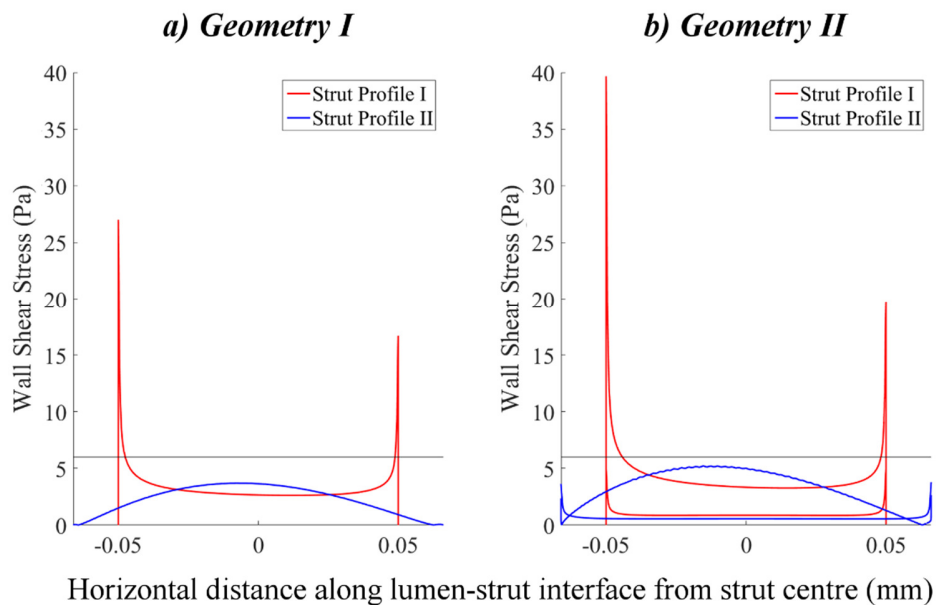


Figure 7-5. The impact of strut profile shape on the wall shear stresses acting on the strut. Whereas high wall shear stresses (>6 Pa) occur around the top corners of Strut Profile I, no such regions were observed with Strut Profile II in either Geometry I or Geometry II.

7.2.2 Three-dimensional simulations

The feasibility of using Strut Profile II to mitigate recirculation zones in realistic geometries was assessed by measuring the extent of negative wall shear stresses in Geometry III. These negative wall shear stress regions, shown in Figure 7-6, were defined as the regions in which the wall shear stress components in the freestream flow direction became negative in magnitude. The cumulative area of these regions, and therefore the cumulative extent of the recirculation zones, diminished by 86% when Strut Profile II was used in place of Strut Profile I.

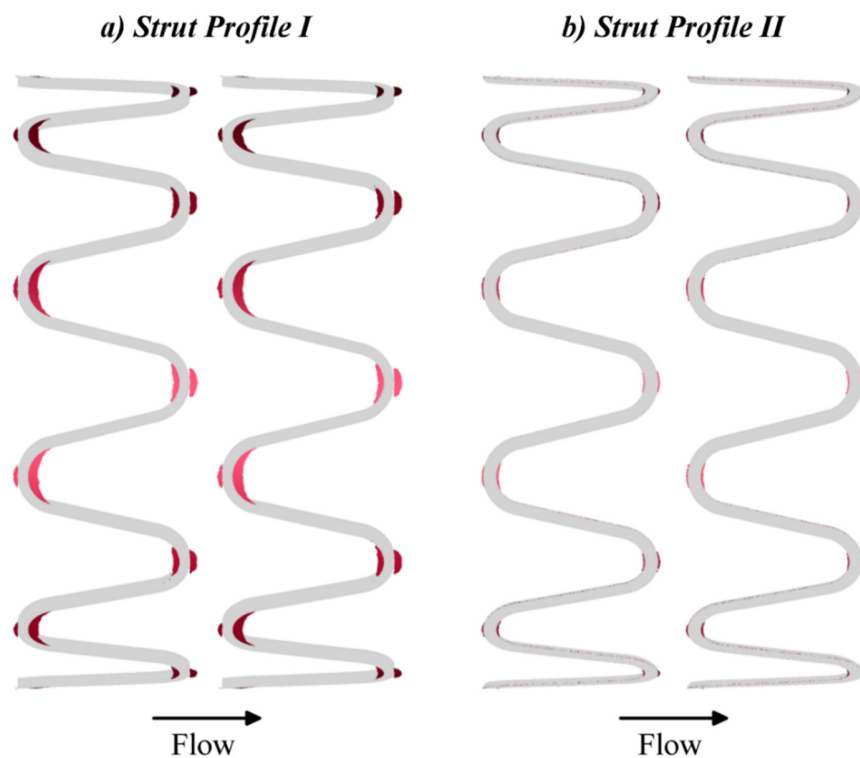


Figure 7-6. The extent of recirculation zones (red) is diminished by 86% when Strut Profile II is used in place of Strut Profile I.

The extent of non-physiological wall shear stresses in Geometry III also diminished when Strut Profile II was used in place of Strut Profile I, as shown in

Figure 7-7. The regions exposed to low wall shear stresses (<0.5 Pa) are shown in blue in this figure whilst the regions exposed high wall shear stress (>3 Pa) have been shown in red. The extent of the low wall shear stress regions acting on the strut and tissue was found to reduce by 58%. Neither strut profile produced shear stresses above the critical shear stress of 6 Pa; however, sustained exposure to high wall shear stresses of 3 Pa have been observed to cause platelet activation as well [149]. Although it is not clear if the circulating platelets are exposed to these shear stresses for long enough to cause activation, the extent of these high wall shear stress regions was reduced by 74% when Strut Profile II was used. These results corroborate the findings of Jimenez et al. [89], which showed that streamlined struts restrict the development of recirculation zones and high shear stress peaks over the strut surfaces. The reduction of platelet-activating high shear stresses and endothelial dysfunction-inducing low wall shear stresses in the Strut Profile II geometry is therefore expected to yield a reduced risk of stent thrombosis.

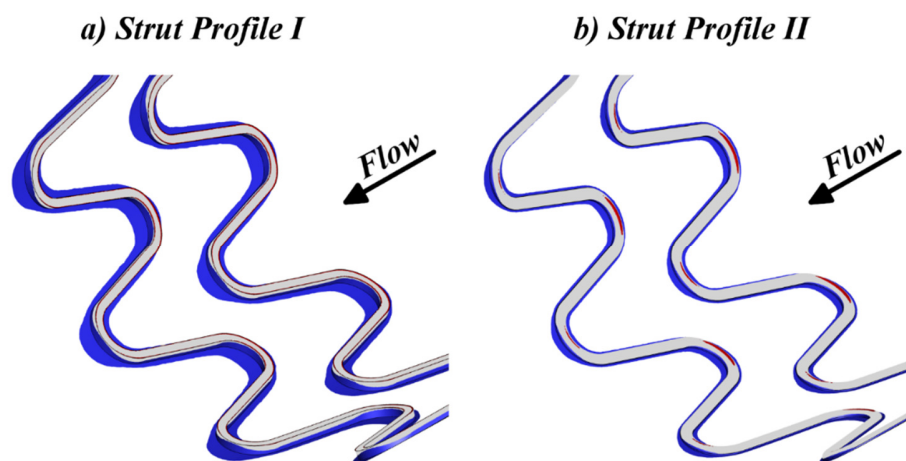


Figure 7-7. The extent of endothelial dysfunction-inducing low wall shear stresses (blue) and platelet-activating high wall shear stresses (red) is significantly reduced once a more streamlined strut profile geometry is used. Low wall shear stresses (<0.5 Pa) were reduced by 58% whilst high wall shear stresses (>3 Pa) were reduced by 74%.

Finally, the drug transport properties of the two strut profiles were compared to see if the likelihood of in-stent restenosis could also be assuaged. The VWAC of drug within the tissue in Geometry III was observed to be 0.93×10^{-5} and 1.60×10^{-5} for Strut Profile I and Strut Profile II respectively. Hence, Strut Profile II generated 72% more drug uptake than Strut Profile I despite its drug coating being 39% the size of the Strut Profile I coating. Furthermore, as may be seen in Figure 7-8, the drug that is eluted from the strut with the semicircular profile penetrates more deeply into the tissue, as well as further upstream and downstream. These results imply that the increased region of contact between Strut Profile II and the tissue enhances drug delivery whilst minimising the loss of drug to the blood stream.

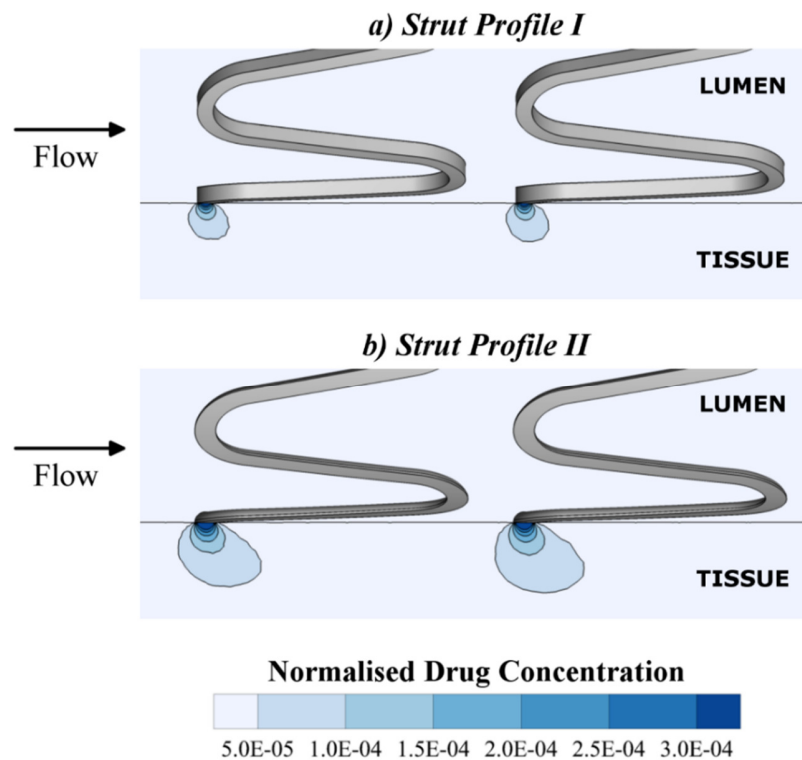


Figure 7-8. The normalised drug concentration distribution within a cross section of the lumen and tissue domains after a total simulation time of 24 hours. Strut Profile II generated 72% more drug uptake than Strut Profile I despite its drug coating being 39% the size of the Strut Profile I coating.

Hence, there are three main reasons why Strut Profile II could reduce the likelihood of in-stent restenosis. Firstly, the lack of drug coating along the top of the strut encourages the coverage of the struts by endothelial cells, which act as a barrier against smooth muscle cell proliferation. Secondly, its streamlined shape mitigates endothelial dysfunction-inducing low wall shear stresses. Finally, the enhanced coating-tissue contact region increases the transport of antiproliferative drug into the arterial tissue.

7.3 Outcomes

Two different drug-eluting stent strut profile shapes were compared to investigate whether a streamlined strut profile can be used to simultaneously improve the haemodynamic and drug transport behaviour of stented arteries. The first of these struts featured a non-streamlined square profile with a continuous drug coating that enclosed the strut; the second strut featured a more streamlined semicircular profile and an abluminal drug coating. Using two- and three-dimensional simulations, this streamlined design was shown to significantly reduce the extent of recirculating flow regions, particularly in arteries undergoing incomplete stent apposition. It also reduced the extent of endothelial dysfunction-inducing low wall shear stresses and platelet-activating high wall shear stresses. Furthermore, despite having 61% less drug coating than the square-profiled strut, the semicircular design significantly enhanced the transport of antiproliferative agents into the tissue. These results convey that streamlined, abluminally coated drug-eluting stent struts could provide a feasible means of alleviating the adverse haemodynamics that precipitate stent thrombosis and in-stent restenosis whilst simultaneously enhancing drug uptake.

Chapter 8

Conclusions and Future Work

8.1 Thesis Significance

There were two major aims in this thesis. The first was to evaluate how blood flow impacts the drug transport behaviour of arteries treated with drug-eluting stents. The second was to identify how to alleviate the adverse haemodynamics of stented arteries without compromising drug uptake. For fluid dynamicists, the significance of pursuing these aims was in establishing a methodology for modelling the haemodynamic and drug transport behaviour of stented arteries. For device designers, the significance was in identifying how to improve the safety and efficacy of drug-eluting stents. In this chapter, the main findings of this thesis and the future work that is needed to bring these findings into fruition are outlined.

8.2 Arterial Blood Flow and its Impact on Stent-Based Drug Delivery

The study of blood flow in arteries treated with drug-eluting stents and its impact on drug delivery was performed using a combination of CFD and in-vitro analyses. Using CFD, the impact of blood's shear-thinning non-Newtonian properties, its complex near-wall behaviour, and the pulsatility of its flow on the haemodynamics of stented arteries was assessed. Additionally, two different drug transport models were implemented in these CFD studies to ascertain how these properties affect the transport of drug from the stent into arterial tissue. An in-vitro study was then performed to determine the validity of these drug transport models and the results were then used to determine the significance of flow-mediated drug transport. This investigation into the role of blood flow in stent-based drug delivery was concluded

by investigating the haemodynamics and the drug transport behaviour of arteries featuring malapposed stent struts.

The impact of blood's shear-thinning non-Newtonian properties and its complex near-wall behaviour on the haemodynamics of stented arteries was assessed using steady-state and transient CFD simulations. When implementing non-Newtonian blood rheological models in place of the traditional Newtonian model, the extent of recirculation zones reduced by up to 24% whilst mean cycle-averaged wall shear stresses increased by up to 9.4%. Of the non-Newtonian models studied, the Power model produced the most extreme non-Newtonian behaviour, whilst Walburn-Schneck, Casson, Carreau and Generalised Power Law models were less extreme. Another model possessing the properties of blood plasma was also implemented in these simulations to account for the paucity of red blood cells in near-wall regions. This model yielded recirculation length increases of up to 59% and a 52% reduction in mean cycle-averaged wall shear stresses. Hence, it was advised that both Power Law and plasma models be implemented in conjunction with the traditional Newtonian model in future studies concerned with the haemodynamics of stented arteries. This way, the full spectrum of rheological conditions achievable within the stented artery can be modelled.

The pulsatility of blood flow was also studied using CFD analyses and also shown to significantly impact the haemodynamics of stented arteries. The cycle-averaged wall shear stresses obtained in studies featuring a pulsatile inlet velocity waveform were significantly higher than the wall shear stresses obtained from steady flow analyses with like rheological models. When the Newtonian model was used, the mean cycle-averaged wall shear stress exceeded the mean wall shear stress of the steady flow model by 36%. Similarly, the mean cycle-averaged wall shear stresses

achieved with the plasma and Power Law models were greater than the mean wall shear stresses of the steady flow models by 88% and 29% respectively. A steady flow assumption therefore cannot be used to approximate the mean shear stress environment of a stented artery; however, this assumption could be used to conservatively estimate the extent low wall shear stress regions. It is clear from these results that the non-Newtonian properties of blood, its complex near-wall behaviour, and the pulsatility of its flow all strongly impact the haemodynamics of stented vessels; however, the impact of these properties on stent-based drug-delivery was found to be more complex and depended strongly on the drug transport model used.

When a uniform, time-invariant drug coating concentration was assumed in a series of steady-state CFD simulations, the choice of blood rheological model was found to be contextually important. As in the haemodynamic studies, the Power Law model produced the most significant non-Newtonian behaviour. However, the magnitude of drug uptake produced by this model deviated less than 5% from that obtained with the traditional, Newtonian model. These results implied that the Newtonian model is appropriate to use in studies seeking to quantify the magnitude of arterial drug uptake; however, the spatial distribution of these drugs was strongly influenced by the choice of blood rheological model. Specifically, the Newtonian model tended to yield higher tissue drug concentrations upstream of the strut whilst the non-Newtonian blood models produced higher concentrations in the downstream region. It was therefore suggested that Newtonian and Power Law models should be implemented in future studies concerned with drug transport details, to establish a range of potential drug concentration distributions.

However, the results obtained with transient CFD simulations, in which the time-dependent depletion of drug within the stent coating could be modelled, seemed

to contradict these findings. In these simulations, neither the non-Newtonian properties of blood, its complex near-wall behaviour, nor the pulsatility of its flow had any significant impact on the amount or distribution of drug within the arterial tissue. This is because the drug depletes much more rapidly at the coating surfaces that are exposed to blood flow than at the surfaces that are in contact with arterial tissue. The results obtained using this drug transport model implied that flow-mediated drug transport is negligible in arteries treated with drug-eluting stents. They also implied that the frequently used assumptions that blood is a Newtonian fluid and that its flow is steady are safe to use when investigating drug uptake.

To validate the drug transport models used in these CFD analyses, an additional in-vitro study was performed. In this experiment, a stented artery environment was mimicked using a polydimethylsiloxane strip (stent strut analogue), a polyvinyl alcohol hydrogel (tissue analogue) and a glycerol-water working fluid (blood analogue). The transport of Rhodamine B, a fluorescent marker, from the strip and into the hydrogel was used to analogously represent the drug transport from a stent strut into arterial tissue. The Rhodamine B distribution within the hydrogel was measured with an epifluorescence microscope and a symmetric distribution about the strut was revealed. The results obtained showed a close agreement with computational results obtained using the drug transport model in which the time-dependent depletion of drug within the stent coating was modelled. Hence, these experiments validated the finding that flow-mediated drug transport is negligible in arteries treated with drug-eluting stents. For fluid dynamicists, it also established that the non-uniform depletion of drug within the stent coating must be modelled when studying stent-based drug delivery.

Having established that flow-mediated drug transport is insignificant, the previously held notion that malapposed drug-eluting stent struts yield significant drug uptake was challenged with another series of CFD studies. Using the validated drug transport model, it was shown that the rapid rate of drug depletion at the surfaces of malapposed struts precludes significant drug transport into the tissue. Even when the gap between the strut and tissue was only 10 μm , a 93% reduction in drug uptake was observed when compared to a well-apposed strut after 24 hours of drug transport. This drug uptake was found to decrease even further as the gap between the strut and tissue increased.

In contrast, the extent of platelet-activating high wall shear stresses and endothelial dysfunction-inducing low wall shear stresses was observed in this study to increase with respect to the degree of malapposition. The combination of a lack of drug uptake and an increased prevalence of non-physiological wall shear stresses may account for the increased risk of in-stent restenosis and stent thrombosis that is associated with stent malapposition. Hence, these results convey the need for fluid dynamicists to model malapposed stent geometries when seeking to alleviate the adverse haemodynamics of stented arteries.

8.3 Alleviating the Adverse Haemodynamics of Arteries Treated with Drug-Eluting Stents without Compromising Drug Uptake

Two potential methods of alleviating these adverse haemodynamics without compromising drug uptake were identified. The first method involved the use of

magnetic stent struts to reduce the extent of separated flow regions. The second method involved using a more streamlined stent strut profile shape to mitigate non-physiological wall shear stresses whilst also enhancing the strut-tissue contact region to maximise drug transport. A series of CFD simulations were performed to see if these concepts could truly be used to alleviate the adverse haemodynamics of stented arteries. The drug transport behaviour of valid concepts was then tested using the validated drug transport model.

It was hypothesised that the magnetic strut concept could influence the flow around drug-eluting stents since blood is a biomagnetic fluid. However, it was shown that even at unrealistically strong magnetic flux densities of 8.0 T, a magnetic strut could only modestly affect the extent of low wall shear stress-producing recirculation zones. Specifically, the length of these recirculation zones reduced by only 2.6% in deoxygenated blood and no reductions in recirculation zone length were observed in oxygenated blood. The magnetic strut concept was therefore determined to be unsuitable for alleviating the adverse haemodynamics of stented arteries.

In contrast, it was found that altering the strut profile geometry of drug-eluting stents is a very effective method of improving the haemodynamics of stented arteries without compromising drug uptake. In these studies, a non-streamlined, square profile strut geometry with a continuous drug coating that enclosed the strut was compared against a streamlined, semicircular strut profile with an abluminal drug coating. The cross-sectional area of the stent platform and the thickness of the drug coating was the same in both geometries; however, the semicircular design possessed an enhanced strut-tissue contact region to maximise drug transport. As a result, three-dimensional simulations showed that, despite having 61% less drug coating than the square-profile strut, this semicircular design yielded 72% more drug

uptake. Furthermore, the cumulative extent of the recirculation zones diminished by 86% and the extent of low (<0.5 Pa) and high (>3 Pa) wall shear stress regions reduced by 58% and 74% respectively. These three-dimensional results were corroborated by two-dimensional simulations, which also showed that the semicircular geometry dramatically reduces the extent of non-physiological shear stresses in arteries with malapposed struts. Hence, these results conveyed that it is possible to alleviate the adverse haemodynamics that promote stent thrombosis and in-stent restenosis without compromising drug uptake.

For device designers, these results showed that the safety of drug-eluting stents may be improved by using streamlined semicircular-profiled drug-eluting stent struts with abluminal drug coatings. It is expected that endothelialisation will be promoted with these struts due to the absence of an antiproliferative drug coating along the top of the struts as well as the reduced extent of endothelial dysfunction-inducing low wall shear stresses. This enhanced endothelial coverage is illustrated in Figure 8-1, where it is compared with the impaired endothelialisation of a non-streamlined strut with a continuous drug coating. Given that endothelial cells act as a barrier against smooth muscle cell proliferation and express anticoagulants, these streamlined struts could mitigate in-stent restenosis and stent thrombosis rates. In-stent restenosis may also be alleviated by the enhanced drug uptake that these struts facilitate. Stent thrombosis may also be mitigated by the reduced prevalence of platelet-activating high wall shear stresses and the reduced size of recirculation zones, particularly in cases where strut malapposition transpires.

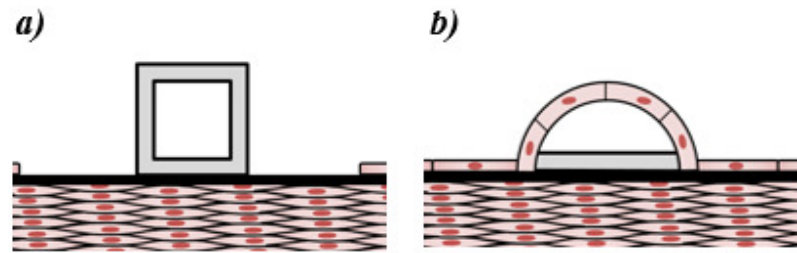


Figure 8-1. The absence of a drug coating along the top of the streamlined stent strut, combined with the reduced prevalence of endothelial dysfunction-inducing low wall shear stresses, is expected to promote endothelialisation. This improved endothelialisation is anticipated to help mitigate the rates of in-stent restenosis and stent thrombosis.

8.4 Limitations and Future Work

Although the semicircular strut profile alleviates the adverse haemodynamics that promote thrombosis and restenosis, further testing is needed to ensure that it is indeed safer than the current, non-streamlined alternatives. Whilst the simulations in this thesis showed that wider, more haemodynamic strut profile geometries can enhance drug transport, the extent of arterial injury following stent expansion was not investigated. Finite element simulations should therefore be performed to estimate how deeply various strut profile geometries become embedded within the arterial tissue and to estimate the extent of arterial injury caused.

It is also important to model the drug transport behaviour of these embedded struts to optimise the design of the drug coating. In this thesis, it was shown that only the drug coating surfaces that are in contact with the arterial tissue yield significant drug transport. However, only well-apposed and malapposed strut geometries were investigated for their drug transport behaviour. Given that stenting often involves overdilation to ensure well-apposedness, some degree of strut embedment is likely to occur. Hence, the drug coating may need to be extended

along the side walls of the strut, instead of only being present on the abluminal face, to optimise drug transport.

Furthermore, although the strut profile geometries tested featured the same amount of material, it is not clear if the streamlined strut is strong enough to support the vessel. Further finite element simulations should therefore be performed to test that these devices do not collapse or break under the stresses of the arterial environment. As this thesis was primarily focused on the haemodynamics of stented arteries and their impact on drug transport, these finite element simulations were deemed to be out of scope.

Another limitation of this thesis is that the fabricability of the semicircular profiled struts was not investigated. In a previous study, it was suggested that an elliptically profiled stent strut can be manufactured by chemically etching rectangular profiles obtained from conventional laser cut tubes [150]. It is anticipated that the same method can be used to manufacture semicircular profiled struts. However, further work will need to be performed to assess whether this manufacturing method is indeed valid.

Despite these limitations, the results presented in this thesis are valuable additions to scientific literature for fluid dynamicists and device designers alike, and it is hoped that they can be used to improve the safety and efficacy of future generations of drug-eluting stents.

References

- [1] National Heart, Lung, and Blood Institute. 2017. *What Is Atherosclerosis?*. [ONLINE] Available at: <https://www.nhlbi.nih.gov/health/health-topics/topics/atherosclerosis>. [Accessed 27 January 2017].
- [2] Heart Foundation. 2015. *Heart disease fact sheet*. [ONLINE] Available at: <http://heartfoundation.org.au/about-us/what-we-do/heart-disease-in-australia/heart-disease-fact-sheet>. [Accessed 27 January 2017].
- [3] Ku, D.N. & Woodruff, G.W., 1997. Blood flow in arteries. *Annual Review of Fluid Mechanics*, 29, pp.399–434.
- [4] Australian Institute of Health and Welfare 2013. Stroke and its management in Australia: an update. *Cardiovascular Disease Series*, 37.
- [5] Lusis, A.J., 2000. Atherosclerosis. *Nature*, 407(6801), pp.233–41. Available at: <http://www.ncbi.nlm.nih.gov/pubmed/11001066><http://www.pubmedcentral.nih.gov/articlerender.fcgi?artid=PMC2826222>.
- [6] Khan, W., Farah, S. & Domb, A.J., 2012. Drug eluting stents: Developments and current status. *Journal of Controlled Release*, 161(2), pp.703–712.

- [7] Frank, A.O., Walsh, P.W. & Moore, J.E., 2002. Computational fluid dynamics and stent design. *Artificial Organs*, 26(7), pp.614–621.
- [8] Peterson, E.D., Coombs, L.P., Ferguson, T.B., Shroyer, A.L., DeLong, E.R., Grover, F.L., Edwards, F.H. & STS National Cardiac Database Investigators, 2002. Hospital variability in length of stay after coronary artery bypass surgery: results from the Society of Thoracic Surgeon’s National Cardiac Database. *The Annals of thoracic surgery*, 74(2), pp.464–473. Available at: <http://www.ncbi.nlm.nih.gov/pubmed/12173830>.
- [9] Medmovie.com. 2013. *Coronary Angioplasty*. [ONLINE] Available at: http://medmovie.com/library_id/3255/topic/ahaw_0068a/. [Accessed 12 August 2016].
- [10] Hunter, W.L., 2006. Drug-eluting stents: beyond the hyperbole. *Advanced Drug Delivery Reviews*, 58(3), pp.347–349.
- [11] Krajcer, Z. & Howell, M.H., 2000. Update on endovascular treatment of peripheral vascular disease: new tools, techniques, and indications. *Texas Heart Institute Journal / from the Texas Heart Institute of St. Luke’s Episcopal Hospital, Texas Children’s Hospital*, 27(4), pp.369–385.
- [12] Moliterno, D.J. & Topol, E.J. 2002. Restenosis: epidemiology and treatment. In:
Topol, E.J., ed. *Textbook of Cardiovascular Medicine, 2nd ed.* Philadelphia: LippincottRaven, pp.1715-1750.

[13] Thornton, M., Gruentzig, A.R., Hollman, J., King, S.B. & Douglas, J.S., 1984. Coumadin and aspirin in prevention of recurrence after transluminal coronary angioplasty: a randomized study. *Circulation*, 69(4), pp.721–727.

Available at:

<http://ovidsp.ovid.com/ovidweb.cgi?T=JS&PAGE=reference&D=med2&NEWS=N&AN=6230174>.

[14] Holmes, D.R., Vlietstra, R.E., Smith, H.C., Vetrovec, G.W., Kent, K.M., Cowley, M.J., Faxon, D.P., Gruentzig, A.R., Kelsey, S.F., Detre, K.M. & Van Raden, M.J., 1984. Restenosis after percutaneous transluminal coronary angioplasty (PTCA): A report from the PTCA registry of the national heart, lung, and blood institute. *The American Journal of Cardiology*, 53(12).

[15] Hoffmann, R., Morice, M.C., Moses, J.W., Fitzgerald, P.J., Mauri, L., Breithardt, G., Schofer, J., Serruys, P.W., Stoll, H.P. and Leon, M.B., 2008.

Impact of late incomplete stent apposition after sirolimus-eluting stent implantation on 4-year clinical events: intravascular ultrasound analysis from the multicentre, randomised, RAVEL, E-SIRIUS and SIRIUS trials. *Heart (British Cardiac Society)*, 94(3), pp.322–328. Available at:

<http://www.ncbi.nlm.nih.gov/pubmed/17761505>.

[16] Mintz, G.S., Popma, J.J., Pichard, A.D., Kent, K.M., Satler, L.F., Wong, S.C., Hong, M.K., Kovach, J.A. and Leon, M.B., 1996. Arterial remodeling after coronary angioplasty: a serial intravascular ultrasound study. *Circulation*, 94(1), pp.35–43. Available at: <http://www.ncbi.nlm.nih.gov/pubmed/8964115>.

- [17] Muhlestein, J.B., Zidar, J.P. & Blazing, M.A., 2002. The vascular biology of restenosis: an overview. In: Stack, R.S., Roubil, G.S., O'Neill, W.W., ed. *Interventional cardiovascular medicine, principles and practice*. 2nd ed. Philadelphia: Churchill Livingstone.
- [18] Post, M.J., Borst, C. & Kuntz, R.E., 1994. The relative importance of arterial remodeling compared with intimal hyperplasia in lumen renarrowing after balloon angioplasty. A study in the normal rabbit and the hypercholesterolemic Yucatan micropig. *Circulation*, 89(6), pp.2816–2821. Available at: <http://circ.ahajournals.org/cgi/doi/10.1161/01.CIR.89.6.2816>.
- [19] Geary, R.L., Clowes, A.W. 2007. Epidemiology and pathogenesis of restenosis. In: Duckers, H.J., Nabel, E.G. and Serruys, P.W. ed. *Essentials of Restenosis: For the Interventional Cardiologist*. Totowa: Humana Press, pp.7-28.
- [20] Rajagopal, V. & Rockson, S.G., 2003. Coronary restenosis: A review of mechanisms and management. *American Journal of Medicine*, 115(7), pp.547–553.
- [21] Puel, J., Juilliere, Y., Bertrand, M.E., Rickards, A.F., Sigwart, U. & Serruys, P.W., 1988. Early and late assessment of stenosis geometry after coronary arterial stenting. *The American Journal of Cardiology*, 61(8), pp.546–553.
- [22] Cutlip, D.E., Baim, D.S., Ho, K.K., Popma, J.J., Lansky, A.J., Cohen, D.J., Carrozza, J.P., Chauhan, M.S., Rodriguez, O. & Kuntz, R.E., 2001. Stent thrombosis in the modern era: a pooled analysis of multicenter coronary stent clinical trials. *Circulation*, 103(15), pp.1967–1971.

- [23] Kimura, T., Nosaka, H., Yokoi, H., Iwabuchi, M. & Nobuyoshi, M., 1993. Serial angiographic follow-up after palmaz-schatz stent implantation: comparison with conventional balloon angioplasty. *Journal of the American College of Cardiology*, 21(7), pp.1557–1563.
- [24] Serruys, P.W., De Jaegere, P., Kiemeneij, F., Macaya, C., Rutsch, W., Heyndrickx, G., Emanuelsson, H., Marco, J., Legrand, V., Materne, P. & Belardi, J., 1994. A comparison of balloon-expandable-stent implantation with balloon angioplasty in patients with coronary artery disease. *New England Journal of Medicine*, 331(8), pp. 489-495.
- [25] Fischman, D.L., Leon, M.B., Baim, D.S., Schatz, R.A., Savage, M.P., Penn, L., Detre, K., Veltri, L., Ricci, D., Nobuyoshi, M. & Cleman, M., 1994. A randomized comparison of coronary-stent placement and balloon angioplasty in the treatment of coronary artery disease. *New England Journal of Medicine*, 331(8), pp.496–501. Available at: <http://www.nejm.org/doi/pdf/10.1056/NEJM199408253310802>.
- [26] Schwartz, R.S., Huber, K.C., Murphy, J.G., Edwards, W.D., Camrud, A.R., Vlietstra, R.E. & Holmes, D.R., 1992. Restenosis and the proportional neointimal response to coronary artery injury: results in a porcine model. *Journal of the American College of Cardiology*, 19(2), pp.267–274.
- [27] Hehrlein, C., Zimmermann, M., Metz, J., Ensinger, W. & Kubler, W., 1995. Influence of surface texture and charge on the biocompatibility of endovascular stents. *Coronary Artery Disease*, 6(7), pp.581–586.

- [28] Nakano, M., Otsuka, F., Yahagi, K., Sakakura, K., Kutys, R., Ladich, E.R., Finn, A.V., Kolodgie, F.D. & Virmani, R., 2013. Human autopsy study of drug-eluting stents restenosis: Histomorphological predictors and neointimal characteristics. *European Heart Journal*, 34(42), pp.3304–3313.
- [29] Pendyala, L., Jabara, R., Robinson, K. & Chronos, N., 2009. Passive and active polymer coatings for intracoronary stents: novel devices to promote arterial healing. *Journal of Interventional Cardiology*, 22(1), pp.37-48.
- [30] Morice, M.C., Serruys, P.W., Sousa, J.E., Fajadet, J., Ban Hayashi, E., Perin, M., Colombo, A., Schuler, G., Barragan, P., Guagliumi, G. & Molnar, F., 2002. Randomized study with the sirolimus-coated Bx velocity balloon-expandable stent in the treatment of patients with de novo native coronary artery lesions. A randomized comparison of a sirolimus-eluting stent with a standard stent for coronary revascularization. *The New England Journal of Medicine*, 346, pp.1773-1780.
- [31] Moses, J.W., Leon, M.B., Popma, J.J., Fitzgerald, P.J., Holmes, D.R., O'shaughnessy, C., Caputo, R.P., Kereiakes, D.J., Williams, D.O., Teirstein, P.S. & Jaeger, J.L., 2003. Sirolimus-eluting stents versus standard stents in patients with stenosis in a native coronary artery. *The New England Journal of Medicine*, 349(14), pp.1315–1323. Available at: <http://www.ncbi.nlm.nih.gov/pubmed/14523139>.
- [32] Stone, G.W., Ellis, S.G., Cox, D.A., Hermiller, J., O'shaughnessy, C., Mann, J.T., Turco, M., Caputo, R., Bergin, P., Greenberg, J. & Popma, J.J., 2004. A polymer-based, paclitaxel-eluting stent in patients with coronary artery disease.

The New England Journal of Medicine, 350(3), pp.221–231. Available at:

<http://www.ncbi.nlm.nih.gov/pubmed/14724301>.

[33] Iakovou, I., Schmidt, T., Bonizzoni, E., Ge, L., Sangiorgi, G.M., Stankovic, G., Airolidi, F., Chieffo, A., Montorfano, M., Carlino, M. & Michev, I., 2005.

Incidence, predictors, and outcome of thrombosis after successful implantation of drug-eluting stents. *The Journal of the American Medical Association*, 293(17), pp.2126–2130. Available at: <http://www.ncbi.nlm.nih.gov/pubmed/15870416>.

[34] McFadden, E.P., Stabile, E., Regar, E., Cheneau, E., Ong, A.T., Kinnaird, T., Suddath, W.O., Weissman, N.J., Torguson, R., Kent, K.M. & Pichard,

A.D., 2004. Late thrombosis in drug-eluting coronary stents after discontinuation of antiplatelet therapy. *Lancet*, 364(9444), pp.1519–1521.

[35] Byrne, R.A., Joner, M. & Kastrati, A., 2015. Stent thrombosis and restenosis: what have we learned and where are we going? The Andreas Grüntzig Lecture ESC 2014. *European Heart Journal*, 36(47), pp.3320-3331.

[36] Moreno, R., Fernández, C., Hernández, R., Alfonso, F., Angiolillo, D.J., Sabaté, M., Escaned, J., Bañuelos, C., Fernández-Ortiz, A. & Macaya, C., 2005.

Drug-eluting stent thrombosis: Results from a pooled analysis including 10 randomized studies. *Journal of the American College of Cardiology*, 45(6), pp.954–959.

[37] Ong, A.T.L., McFadden, E.P., Regar, E., de Jaegere, P.P., van Domburg, R.T. & Serruys, P.W., 2005. Late angiographic stent thrombosis (LAST) events

with drug-eluting stents. *Journal of the American College of Cardiology*, 45(12), pp.2088–2092.

[38] Farb, A., Burke, A.P., Kolodgie, F.D. & Virmani, R., 2003. Pathological mechanisms of fatal late coronary stent thrombosis in humans. *Circulation*, 108(14), pp.1701–1706.

[39] Heller, L.I., Shemwell, K.C. & Hug, K., 2001. Late stent thrombosis in the absence of prior intracoronary brachytherapy. *Catheterization and Cardiovascular Interventions*, 53(1), pp.23–28.

[40] Wang, F., Stouffer, G.A., Waxman, S. & Uretsky, B.F., 2002. Late coronary stent thrombosis: Early vs. late stent thrombosis in the stent era. *Catheterization and Cardiovascular Interventions*, 55(2), pp.142–147.

[41] Pfisterer, M., Brunner-La Rocca, H.P., Buser, P.T., Rickenbacher, P., Hunziker, P., Mueller, C., Jeger, R., Bader, F., Osswald, S., Kaiser, C. & Basket-Late Investigators, 2006. Late clinical events after clopidogrel discontinuation may limit the benefit of drug-eluting stents: an observational study of drug-eluting versus bare-metal stents. *Journal of the American College of Cardiology*, 48(12), pp.2584-2591.

[42] Stone, G.W., Moses, J.W., Ellis, S.G., Schofer, J., Dawkins, K.D., Morice, M.C., Colombo, A., Schampaert, E., Grube, E., Kirtane, A.J. & Cutlip, D.E., 2007. Safety and efficacy of sirolimus- and paclitaxel-eluting coronary stents. *New England Journal of Medicine*, 356(10), pp.998–1008. Available at: <http://www.nejm.org/doi/abs/10.1056/NEJMoa067193>.

- [43] Kandzari, D.E., 2006. Drug-eluting stent thrombosis: it's never too late. *Nature Clinical Practice Cardiovascular Medicine*, 3(12), pp.638-639.
- [44] Finn, A. V., Joner, M., Nakazawa, G., Kolodgie, F., Newell, J., John, M.C., Gold, H.K. and Virmani, R., 2007. Pathological correlates of late drug-eluting stent thrombosis: Strut coverage as a marker of endothelialization. *Circulation*, 115(18), pp.2435–2441.
- [45] Joner, M., Finn, A.V., Farb, A., Mont, E.K., Kolodgie, F.D., Ladich, E., Kutys, R., Skorija, K., Gold, H.K. & Virmani, R., 2006. Pathology of Drug-Eluting Stents in Humans. Delayed Healing and Late Thrombotic Risk. *Journal of the American College of Cardiology*, 48(1), pp.193–202.
- [46] Nakazawa, G., Finn, A.V., Joner, M., Ladich, E., Kutys, R., Mont, E.K., Gold, H.K., Burke, A.P., Kolodgie, F.D. & Virmani, R., 2008. Delayed arterial healing and increased late stent thrombosis at culprit sites after drug-eluting stent placement for acute myocardial infarction patients: An autopsy study. *Circulation*, 118(11), pp.1138–1145.
- [47] Grewe, P.H., Deneke, T., Machraoui, A., Barmeyer, J. & Müller, K.M., 2000. Acute and chronic tissue response to coronary stent implantation: Pathologic findings in human specimen. *Journal of the American College of Cardiology*, 35(1), pp.157–163.
- [48] Hoskins, P.R. & Hardman, D., 2014. Three-dimensional imaging and computational modelling for estimation of wall stresses in arteries. *The British Journal of Radiology*, 82, pp.S3-17.

- [49] Koskinas, K.C., Chatzizisis, Y.S., Antoniadis, A.P. & Giannoglou, G.D., 2012. Role of endothelial shear stress in stent restenosis and thrombosis: Pathophysiologic mechanisms and implications for clinical translation. *Journal of the American College of Cardiology*, 59(15), pp.1337–1349.
- [50] Jiménez, J.M., Prasad, V., Michael, D.Y., Kampmeyer, C.P., Kaakour, A.H., Wang, P.J., Maloney, S.F., Wright, N., Johnston, I., Jiang, Y.Z. & Davies, P.F., 2014. Macro- and microscale variables regulate stent haemodynamics, fibrin deposition and thrombomodulin expression. *Journal of the Royal Society, Interface / the Royal Society*, 11(94), p.20131079.
- [51] LaDisa, J.F., Guler, I., Olson, L.E., Hettrick, D.A., Kersten, J.R., Warltier, D.C. & Pagel, P.S., 2003. Three-dimensional computational fluid dynamics modeling of alterations in coronary wall shear stress produced by stent implantation. *Annals of Biomedical Engineering*, 31(8), pp.972–980.
- [52] Wentzel, J.J., Krams, R., Schuurbijs, J.C., Oomen, J.A., Kloet, J., van der Giessen, W.J., Serruys, P.W. & Slager, C.J., 2001. Relationship between neointimal thickness and shear stress after Wallstent implantation in human coronary arteries. *Circulation*, 103(13), pp.1740–1745.
- [53] LaDisa Jr., J.F., Olson, L.E., Moithen, R.C., Hettrick, D.A., Pratt, P.F., Hardel, M.D., Kersten, J.R., Warltier, D.C. & Pagel, P.S., 2005. Alterations in wall shear stress predict sites of neointimal hyperplasia after stent implantation in rabbit iliac arteries. *American Journal of Physiology: Heart and Circulatory Physiology*, 288(5), pp.H2465–H2475.

- [54] Papafaklis, M.I., Bourantas, C.V., Theodorakis, P.E., Katsouras, C.S., Naka, K.K., Fotiadis, D.I. & Michalis, L.K., 2010. The effect of shear stress on neointimal response following sirolimus- and paclitaxel-eluting stent implantation compared with bare-metal stents in humans. *Journal of the American College of Cardiology: Cardiovascular Interventions*, 3(11), pp.1181–1189.
- [55] Morlacchi, S., Keller, B., Arcangeli, P., Balzan, M., Migliavacca, F., Dubini, G., Gunn, J., Arnold, N., Narracott, A., Evans, D. & Lawford, P., 2011. Hemodynamics and in-stent restenosis: micro-CT images, histology, and computer simulations. *Annals of Biomedical Engineering*, 39(10), pp.2615–2626.
- [56] Chen, H.Y., Sinha, A.K., Choy, J.S., Zheng, H., Sturek, M., Bigelow, B., Bhatt, D.L. & Kassab, G.S., 2011. Mis-sizing of stent promotes intimal hyperplasia: impact of endothelial shear and intramural stress. *American Journal of Physiology: Heart and Circulatory Physiology*, 301(6), pp.H2254–H2263.
- [57] Malek, A.M., Alper, S.L. & Izumo, S., 1999. Hemodynamic shear stress and its role in atherosclerosis. *The Journal of the American Medical Association*, 282(21), pp.2035–2042.
- [58] Nakazawa, G., Finn, A.V., Vorpahl, M., Ladich, E.R., Kolodgie, F.D. & Virmani, R., 2011. Coronary responses and differential mechanisms of late stent thrombosis attributed to first-generation sirolimus- and paclitaxel-eluting stents. *Journal of the American College of Cardiology*, 57(4), pp.390–398.
- [59] Liu, S.Q., Tieche, C., Tang, D. & Alkema, P., 2003. Pattern formation of vascular smooth muscle cells subject to nonuniform fluid shear stress: role of

PDGF-beta receptor and Src. *American journal of physiology. Heart and circulatory physiology*, 285(3), pp.H1081- H1090. Available at: <http://www.ncbi.nlm.nih.gov/pubmed/12738619>.

[60] Kolachalama, V.B., Tzafiriri, A.R., Arifin, D.Y. & Edelman, E.R., 2009. Luminal flow patterns dictate arterial drug deposition in stent-based delivery. *Journal of Controlled Release*, 133(1), pp.24–30.

[61] Balakrishnan, B., Tzafiriri, A.R., Seifert, P., Groothuis, A., Rogers, C. & Edelman, E.R., 2005. Strut position, blood flow, and drug deposition: Implications for single and overlapping drug-eluting stents. *Circulation*, 111(22), pp.2958–2965.

[62] Nakazawa, G., Yazdani, S.K., Finn, A.V., Vorpahl, M., Kolodgie, F.D. & Virmani, R., 2010. Pathological findings at bifurcation lesions. The impact of flow distribution on atherosclerosis and arterial healing after stent implantation. *Journal of the American College of Cardiology*, 55(16), pp.1679–1687.

[63] Akagawa, E., Ookawa, K. & Ohshima, N., 2004. Endovascular stent configuration affects intraluminal flow dynamics and in vitro endothelialization. *Biorheology*, 41(6), pp.665–680. Available at: <http://www.ncbi.nlm.nih.gov/pubmed/15851843>.

[64] Cook, S., Wenaweser, P., Togni, M., Billinger, M., Morger, C., Seiler, C., Vogel, R., Hess, O., Meier, B. & Windecker, S., 2007. Incomplete stent apposition and very late stent thrombosis after drug-eluting stent implantation. *Circulation*, 115(18), pp.2426–2434.

[65] Foin, N., Gutiérrez-Chico, J.L., Nakatani, S., Torii, R., Bourantas, C.V., Sen, S., Nijjer, S., Petraco, R., Kouser, C., Ghione, M. & Onuma, Y., 2014.

Incomplete stent apposition causes high shear flow disturbances and delay in neointimal coverage as a function of strut to wall detachment distance: implications for the management of incomplete stent apposition. *Circulation: Cardiovascular Interventions*, 7(2), pp.180–189.

[66] Chesnutt, J.K. & Han, H.C., 2016. Computational simulation of platelet interactions in the initiation of stent thrombosis due to stent malapposition. *Physical Biology*, 13(1), p.016001.

[67] Boussel, L., Rayz, V., Martin, A., Acevedo-Bolton, G., Lawton, M.T., Higashida, R., Smith, W.S., Young, W.L. & Saloner, D., 2009. Phase-contrast magnetic resonance imaging measurements in intracranial aneurysms in vivo of flow patterns, velocity fields, and wall shear stress: Comparison with computational fluid dynamics. *Magnetic Resonance in Medicine*, 61(2), pp.409–417.

[68] Rodkiewicz, C.M., Sinha, P. & Kennedy, J.S., 1990. On the application of a constitutive equation for whole human blood. *Journal of Biomechanical Engineering*, 112(2), pp.198–206.

[69] ABC Corporation Bangladesh, (2013), *Advanced Rheology* [ONLINE]. Available at: <http://www.abc-bd.com/wp-content/uploads/2013/08/3.jpg> [Accessed 15 November 2016].

- [70] Balakrishnan, B., Dooley, J.F., Kopia, G. & Edelman, E.R., 2007. Intravascular drug release kinetics dictate arterial drug deposition, retention, and distribution. *Journal of Controlled Release*, 123(2), pp.100–108.
- [71] Mongrain, R., Faik, I., Leask, R.L., Rod , J. & Bertrand, O.F., 2007. Effects of diffusion coefficients and struts apposition using numerical simulations for drug eluting coronary stents. *Journal of Biomechanical Engineering*, 129(5), pp.733–742. Available at: <http://www.ncbi.nlm.nih.gov/pubmed/17887899>.
- [72] Zunino, P., D’Angelo, C., Petrini, L., Vergara, C., Capelli, C. & Migliavacca, F., 2009. Numerical simulation of drug eluting coronary stents: Mechanics, fluid dynamics and drug release. *Computer Methods in Applied Mechanics and Engineering*, 198(45–46), pp.3633–3644.
- [73] Ballyk, P.D., Steinman, D.A. & Ethier, C.R., 1994. Simulation of non-Newtonian blood flow in an end-to-side anastomosis. *Biorheology*, 31(5), pp.565–586.
- [74] Berger, S.A. & Jou, L.D., 2000. Flows in stenotic vessels. *Annual Review of Fluid Mechanics*, 32, pp.347–382.
- [75] O’Brien, C.C., Kolachalama, V.B., Barber, T.J., Simmons, A. & Edelman, E.R., 2013. Impact of flow pulsatility on arterial drug distribution in stent-based therapy. *Journal of Controlled Release*, 168(2), pp.115–124.
- [76] Mejia, J., Mongrain, R. & Bertrand, O.F., 2011. Accurate prediction of wall shear stress in a stented artery: newtonian versus non-newtonian models. *Journal*

of *Biomechanical Engineering*, 133(7), pp.1–8. Available at: <http://www.ncbi.nlm.nih.gov/pubmed/21823750>.

[77] Cho, Y.I. & Kensey, K.R., 1991. Effects of the non-Newtonian viscosity of blood on flows in a diseased arterial vessel. Part 1: Steady flows. *Biorheology*, 28, pp.241–262.

[78] Walburn, F.J. & Schneck, D.J., 1976. A constitutive equation for whole human blood. *Biorheology*, 13(3), pp.201-210.

[79] Fung, Y.C. & Cowin, S.C., 1994. Biomechanics: mechanical properties of living tissues, 2nd ed. *Journal of Applied Mechanics*, 61, p.1007.

[80] Billett, H.H. 1990. Hemoglobin and hematocrit. In: Walker, H.K., Hall, W.D. & Hurst, J.W. ed. *Clinical Methods: the History, Physical, and Laboratory Examinations*. 3rd ed. Boston: Butterworths.

[81] Johnston, B.M., Johnston, P.R., Corney, S. & Kilpatrick, D., 2004. Non-Newtonian blood flow in human right coronary arteries: Steady state simulations. *Journal of Biomechanics*, 37(5), pp.709–720.

[82] Ranade, S.V., Miller, K.M., Richard, R.E., Chan, A.K., Allen, M.J. & Helmus, M.N., 2004. Physical characterization of controlled release of paclitaxel from the TAXUS™ Express2™ drug-eluting stent. *Journal of Biomedical Materials Research Part A*, 71(4), pp.625-634.

[83] Aarts, P.A., van den Broek, S.A., Prins, G.W., Kuiken, G.D., Sixma, J.J. & Heethaar, R.M., 1988. Blood platelets are concentrated near the wall and red

blood cells, in the center in flowing blood. *Arteriosclerosis (Dallas, Tex.)*, 8(6), pp.819–824.

[84] Pedersen, L., Nielsen, E.B., Christensen, M.K., Buchwald, M. & Nybo, M., 2014. Measurement of plasma viscosity by free oscillation rheometry: imprecision, sample stability and establishment of a new reference range. *Annals of Clinical Biochemistry: An International Journal of Biochemistry and Laboratory Medicine*, 51(4), pp.495-498.

[85] Kolachalama, V.B., Levine, E.G. & Edelman, E.R., 2009. Luminal flow amplifies stent-based drug deposition in arterial bifurcations. *PLoS ONE*, 4(12), p.e8105.

[86] Rikhtegar, F., Edelman, E.R., Olgac, U., Poulikakos, D. & Kurtcuoglu, V., 2016. Drug deposition in coronary arteries with overlapping drug-eluting stents. *Journal of Controlled Release*, 238, pp.1–9.

[87] Chen, Y., Xiong, Y., Jiang, W., Yan, F., Guo, M., Wang, Q. & Fan, Y., 2015. Numerical simulation on the effects of drug eluting stents at different Reynolds numbers on hemodynamic and drug concentration distribution. *BioMedical Engineering OnLine*, 14(Suppl 1), p.S16. Available at: <http://www.biomedical-engineering-online.com/content/14/S1/S16>.

[88] Chesnutt, J.K. & Han, H.C., 2016. Computational simulation of platelet interactions in the initiation of stent thrombosis due to stent malapposition. *Physical Biology*, 13(1), p.016001.

[89] Jiménez, J.M. & Davies, P.F., 2009. Hemodynamically driven stent strut design. *Annals of Biomedical Engineering*, 37(8), pp.1483–1494.

- [90] Higashi, T., Yamagishi, A., Takeuchi, T., Kawaguchi, N., Sagawa, S., Onishi, S. & Date, M., 1993. Orientation of erythrocytes in a strong static magnetic field. *Blood*, 82(4), pp.1328–1334.
- [91] Motta, M., Haik, Y., Gandhari, A. & Chen, C.J., 1998. High magnetic field effects on human deoxygenated hemoglobin light absorption. *Bioelectrochemistry and Bioenergetics*, 47(2), pp.297–300.
- [92] Hall, W.F. & Busenberg, S.N., 1969. Viscosity of magnetic suspensions. *The Journal of Chemical Physics*, 51(1), pp.137-144.
- [93] McTague, J.P., 1969. Magnetoviscosity of Magnetic Colloids. *The Journal of Chemical Physics*, 51(1969), p.133. Available at: <http://link.aip.org/link/?JCP/51/133/1&Agg=doi>.
- [94] Frewer, R.A., 1974. The electrical conductivity of flowing blood. *Bio-Medical Engineering*, 9(12), pp.552–555. Available at: <http://www.scopus.com/inward/record.url?eid=2-s2.00016271061&partnerID=40&md5=820795b8194c7f07520630833f21332f>.
- [95] Jaspard, F. & Nadi, M., 2002. Dielectric properties of blood: an investigation of temperature dependence. *Physiological Measurement*, 23(3), pp.547–554. Available at: <http://www.ncbi.nlm.nih.gov/pubmed/12214762>.
- [96] Gabriel, S., Lau, R.W. & Gabriel, C., 1996. The dielectric properties of biological tissues: III. Parameteric models for the dielectric spectrum of tissues.

Physics in Medicine and Biology, 41(11), pp.2271–2293. Available at:

<http://www.ncbi.nlm.nih.gov/pubmed/8938026>.

[97] Tzirtzilakis, E.E., Sakalis, V.D., Kafoussias, N.G. & Hatzikonstantinou, P.M., 2004. Biomagnetic fluid flow in a 3D rectangular duct. *International Journal for Numerical Methods in Fluids*, 44(12), pp.1279–1298.

[98] Papadopoulos, P.K. & Tzirtzilakis, E.E., 2004. Biomagnetic flow in a curved square duct under the influence of an applied magnetic field. *Physics of Fluids*, 16(8), pp.2952-2962.

[99] Kenjereš, S., 2008. Numerical analysis of blood flow in realistic arteries subjected to strong non-uniform magnetic fields. *International Journal of Heat and Fluid Flow*, 29(3), pp.752–764.

[100] Khashan, S.A. & Haik, Y., 2006. Numerical simulation of biomagnetic fluid downstream an eccentric stenotic orifice. *Physics of Fluids*, 18(11), p.113601.

[101] Van Jaarsveld, B.C., Krijnen, P., Pieterman, H., Derkx, F.H., Deinum, J., Postma, C.T., Dees, A., Woittiez, A.J., Bartelink, A.K., Man int Veld, A.J. & Schalekamp, M.A., 2000. The effect of balloon angioplasty on hypertension in atherosclerotic renal-artery stenosis. Dutch renal artery stenosis intervention cooperative study group. *The New England Journal of Medicine*, 342(14), pp.1007–1014. Available at: <http://www.ncbi.nlm.nih.gov/pubmed/10749962>.

[102] White, C.J., Ramee, S.R., Collins, T.J., Jenkins, J.S., Escobar, A. & Shaw, D., 1997. Renal artery stent placement: Utility in lesions difficult to treat with

balloon angioplasty. *Journal of the American College of Cardiology*, 30(6), pp.1445–1450.

[103] Rocha-Singh, K., Jaff, M.R. & Rosenfield, K., 2005. Evaluation of the safety and effectiveness of renal artery stenting after unsuccessful balloon angioplasty: The ASPIRE-2 study. *Journal of the American College of Cardiology*, 46(5), pp.776–783.

[104] Dorros, G., Prince, C. & Mathiak, L., 1993. Stenting of a renal artery stenosis achieves better relief of the obstructive lesion than balloon angioplasty. *Catheterization and Cardiovascular Diagnosis*, 29(3), pp.191–198.

[105] Lovich, M.A., Creel, C., Hong, K., Hwang, C.W. & Edelman, E.R., 2001. Carrier proteins determine local pharmacokinetics and arterial distribution of paclitaxel. *Journal of Pharmaceutical Sciences*, 90(9), pp.1324–1335.

[106] Creel, C.J., Lovich, M.A. & Edelman, E.R., 2000. Arterial Paclitaxel Distribution and Deposition. *Circulation Research*, 86, pp.879–884.

[107] Lovich, M.A. & Edelman, E.R., 1996. Computational simulations of local vascular heparin deposition and distribution. *The American Journal of Physiology*, 271(5), pp.H2014-24. Available at: <http://www.ncbi.nlm.nih.gov/pubmed/8945921>.

[108] Finkelstein, A., McClean, D., Kar, S., Takizawa, K., Varghese, K., Baek, N., Park, K., Fishbein, M.C., Makkar, R., Litvack, F. & Eigler, N.L., 2003. Local

drug delivery via a coronary stent with programmable release pharmacokinetics. *Circulation*, 107(5), pp.777–784.

[109] Henry, F.S. 2000. Flow in stented arteries. In: Vendonck, P. & Perktold, K. ed. *Intra and Extra Corporeal Cardiovascular Fluid Dynamics*. Southampton: WIT Press.

[110] Dintenfass, L. 1985. *Blood viscosity, hyperviscosity & hyperviscosaemia*. 1st ed. Lancaster (Lancashire): MTP Press.

[111] Dintenfass, L., Julian, D.G. & Miller, G., 1966. Viscosity of blood in healthy young women: effect of menstrual cycle. *The Lancet*, 287(7431), pp.234-235.

[112] Copley, A.L., Huang, C.R. & King, R.G., 1973. Rheogoniometric studies of whole human blood at shear rates from 1000 to 0.0009 sec⁻¹. I. Experimental findings. *Biorheology*, 10(1), p.17.

[113] Rand, P.P.W., Lacombe, E., Hunt, H.E. & Austin, W.H., 1964. Viscosity of normal human blood under normothermic and hypothermic conditions. *Journal of Applied Physiology*, 19(1), pp.117–122.

[114] Chien, S., Usami, S.H.U.N.I.C.H.I., Taylor, H.M., Lundberg, J.L. & Gregersen, M.I., 1966. Effects of hematocrit and plasma proteins on human blood rheology at low shear rates. *Journal of Applied Physiology*, 21(1), pp.81-87.

[115] Merrill, E.W., Gilliland, E.R., Cokelet, G., Shin, H., Britten, A. & Wells, R.E., 1963. Rheology of human blood, near and at zero flow: effects of temperature and hematocrit level. *Biophysical Journal*, 3(3), pp.199–213.

- [116] Cokelet, G.R., Merrill, E.W., Gilliland, E.R., Shin, H., Britten, A. & Wells Jr, R.E., 1963. The rheology of human blood—measurement near and at zero shear rate. *Transactions of the Society of Rheology*, 7(1), pp.303-317.
- [117] Cokelet, G.R., Fung, Y.C., Perrone, N. & Anliker, M., 1972. *Biomechanics: its Foundation and Objectives*. Prentice-Hall, New York.
- [118] Skalak, R., Keller, S.R. & Secomb, T.W., 1981. Mechanics of blood flow. *Journal of Biomechanical Engineering*, 103(May), pp.102–115.
- [119] Cokelet, G.R., 1987. The rheology and tube flow of blood. In: Skalak, R., Chien, S., ed. *Handbook of Bioengineering*. New York: McGraw-Hill, pp.14.1-14.17.
- [120] Pedersen, L., Nielsen, E.B., Christensen, M.K., Buchwald, M. & Nybo, M., 2014. Measurement of plasma viscosity by free oscillation rheometry: imprecision, sample stability and establishment of a new reference range. *Annals of Clinical Biochemistry: An International Journal of Biochemistry and Laboratory Medicine*, 51(4), pp.495-498.
- [121] Razavi, A., Shirani, E. & Sadeghi, M.R., 2011. Numerical simulation of blood pulsatile flow in a stenosed carotid artery using different rheological models. *Journal of Biomechanics*, 44(11), pp.2021–2030.
- [122] Phillips, S.J., Spector, M., Zeff, R.H., Skinner, J.R., Toon, R.S., Grignon, A. and Kongtahworn, C., 1989. Hematocrit changes after uncomplicated

percutaneous transluminal coronary angioplasty. *The American Journal of Cardiology*, 64(14), p.940.

[123] Walburn, F.J. & Schneck, D.J., 1976. A constitutive equation for whole human blood. *Biorheology*, 13(3), pp.201-210.

[124] Moore, J.E. & Ku, D.N., 1994. Pulsatile velocity measurements in a model of the human abdominal aorta under simulated exercise and postprandial conditions. *Journal of Biomechanical Engineering*, 116(1), pp.107–111.

[125] Roache, P.J., 1997. Quantification of uncertainty in computational fluid dynamics. *Annual Review of Fluid Mechanics*, 29(1), pp.123–160. Available at: <http://www.annualreviews.org/doi/abs/10.1146/annurev.fluid.29.1.123>.

[126] Deen, W.M., 1998. *Analysis of transport phenomena, topics in chemical engineering (Vol. 3)*. Oxford University Press, New York.

[127] Colombo, A., Drzewiecki, J., Banning, A., Grube, E., Hauptmann, K., Silber, S., Dudek, D., Fort, S., Schiele, F., Zmudka, K. & Guagliumi, G., 2003. Randomized study to assess the effectiveness of slow- and moderate-release polymer-based paclitaxel-eluting stents for coronary artery lesions. *Circulation*, 108(7), pp.788–794. Available at: <http://www.ncbi.nlm.nih.gov/pubmed/12900339>.

[128] Taylor, C.A., Hughes, T.J. & Zarins, C.K., 1998. Finite element modeling of three-dimensional pulsatile flow in the abdominal aorta: relevance to atherosclerosis. *Annals of Biomedical Engineering*, 26(6), pp.975-987.

- [129] Womersley, J.R., 1955. Method for the calculation of velocity, rate of flow and viscous drag in arteries when the pressure gradient is known. *The Journal of physiology*, 127(3), pp.553-563.
- [130] Papaioannou, T.G. & Stefanadis, C., 2005. Vascular wall shear stress: basic principles and methods. *Hellenic J Cardiol*, 46(1), pp.9-15.
- [131] Cheng, N.S., 2008. Formula for the viscosity of a glycerol-water mixture. *Industrial and Engineering Chemistry Research*, 47(9), pp.3285–3288.
- [132] Bryant, S.J., Davis-Arehart, K.A., Luo, N., Shoemaker, R.K., Arthur, J.A. & Anseth, K.S., 2004. Synthesis and characterization of photopolymerized multifunctional hydrogels: Water-soluble poly(vinyl alcohol) and chondroitin sulfate macromers for chondrocyte encapsulation. *Macromolecules*, 37(18), pp.6726-6733.
- [133] Migliavacca, F., Gervaso, F., Prosi, M., Zunino, P., Minisini, S., Formaggia, L. & Dubini, G., 2007. Expansion and drug elution model of a coronary stent. *Computer Methods in Biomechanics and Biomedical Engineering*, 10(1), pp.63-73.
- [134] Higuchi, T., 1963. Mechanism of sustained-action medication. Theoretical analysis of rate of release of solid drugs dispersed in solid matrices. *Journal of Pharmaceutical Sciences*, 52(12), pp.1145-1149.
- [135] Hwang, C.W., Wu, D. & Edelman, E.R., 2003. Impact of transport and drug properties on the local pharmacology of drug-eluting stents. *International Journal of Cardiovascular Intervention*, 5(1), pp. 7-12.

- [136] Saltzman, W.M., 2001. *Drug delivery: engineering principles for drug therapy*. 1st ed. Oxford [England]: Oxford University Press.
- [137] Yamamoto, T., Ogasawara, Y., Kimura, A., Tanaka, H., Hiramatsu, O., Tsujioka, K., Lever, M.J., Parker, K.H., Jones, C.J., Caro, C.G. & Kajiya, F., 1996. Blood velocity profiles in the human renal artery by Doppler ultrasound and their relationship to atherosclerosis. *Arteriosclerosis, Thrombosis, and Vascular Biology*, 16(January 1996), pp.172–177.
- [138] LaDisa, J.F., Olson, L.E., Guler, I., Hettrick, D.A., Kersten, J.R., Warltier, D.C. & Pagel, P.S., 2005. Circumferential vascular deformation after stent implantation alters wall shear stress evaluated with time-dependent 3D computational fluid dynamics models. *Journal of Applied Physiology*, 98(3), pp.947-957.
- [139] Sen, S., Mittal, S. and Biswas, G., 2011. Flow past a square cylinder at low Reynolds numbers. *International Journal for Numerical Methods in Fluids*, 67(9), pp.1160-1174.
- [140] Poon, E.K.W., Barlis, P., Moore, S., Pan, W.H., Liu, Y., Ye, Y., Xue, Y., Zhu, S.J. & Ooi, A.S., 2014. Numerical investigations of the haemodynamic changes associated with stent malapposition in an idealised coronary artery. *Journal of Biomechanics*, 47(12), pp.2843–2851.
- [141] Haik, Y., Pai, V. & Chen, C. J. 1999. Biomagnetic fluid dynamics. In: Shyy, W., Narayanan, R, ed. *Fluid Dynamics at Interfaces*. Cambridge: Cambridge University Press, pp. 439-452.

- [142] Furlani, E. P., 2001. *Permanent magnet and electromechanical devices: materials, analysis, and applications*. Academic Press, San Diego, USA, Chap. 4., ISBN: 978-0-12-269951-1.
- [143] Nakazawa, G., Finn, A.V., John, M.C., Kolodgie, F.D. & Virmani, R., 2007. The significance of preclinical evaluation of sirolimus-, paclitaxel-, and zotarolimus-eluting stents. *The American Journal of Cardiology*, 100(8), pp.S36-S44.
- [144] Nakazawa, G., Finn, A.V. & Virmani, R., 2007. Vascular pathology of drug-eluting stents. *Herz Kardiovaskuläre Erkrankungen*, 32(4), pp.274-280.
- [145] Barilli, A., Visigalli, R., Sala, R., Gazzola, G.C., Parolari, A., Tremoli, E., Bonomini, S., Simon, A., Closs, E.I., Dall'Asta, V. & Bussolati, O., 2008. In human endothelial cells rapamycin causes mTORC2 inhibition and impairs cell viability and function. *Cardiovascular Research*, 78(3), pp.563-571.
- [146] Butzal, M., Loges, S., Schweizer, M., Fischer, U., Gehling, U.M., Hossfeld, D.K. & Fiedler, W., 2004. Rapamycin inhibits proliferation and differentiation of human endothelial progenitor cells in vitro. *Experimental Cell Research*, 300(1), pp.65-71.
- [147] Chen, T.G., Chen, J.Z. & Wang, X.X., 2006. Effects of rapamycin on number activity and eNOS of endothelial progenitor cells from peripheral blood. *Cell Proliferation*, 39(2), pp.117-125.

- [148] Eppihimer, M., 2013. Impact of polymer type and location on stent thrombogenicity and endothelial cell coverage. EuroIntervention. 2013. *EuroPCR Abstracts*.
- [149] Yin, W. Rouf, F., Shanmugavelayudam, S.K. & Rubenstein, D.A., 2014. Endothelial cells modulate platelet response to dynamic shear stress. *Cardiovascular Engineering and Technology*, 5(2), pp.145-153.
- [150] Mejia, J., Ruzzeh, B., Mongrain, R., Leask, R. & Bertrand, O.F., 2009. Evaluation of the effect of stent strut profile on shear stress distribution using statistical moments. *Biomedical Engineering Online*, 8(1), p.8.

Appendix A

Grid Convergence Studies

Grid Convergence in Chapter 2

The final grid used in this chapter may be seen in Figure A-1. As shown, the mesh densities are highest in the regions close to the stent strut and also near the tissue and lumen. The mesh is fully structured and features no skewed elements.

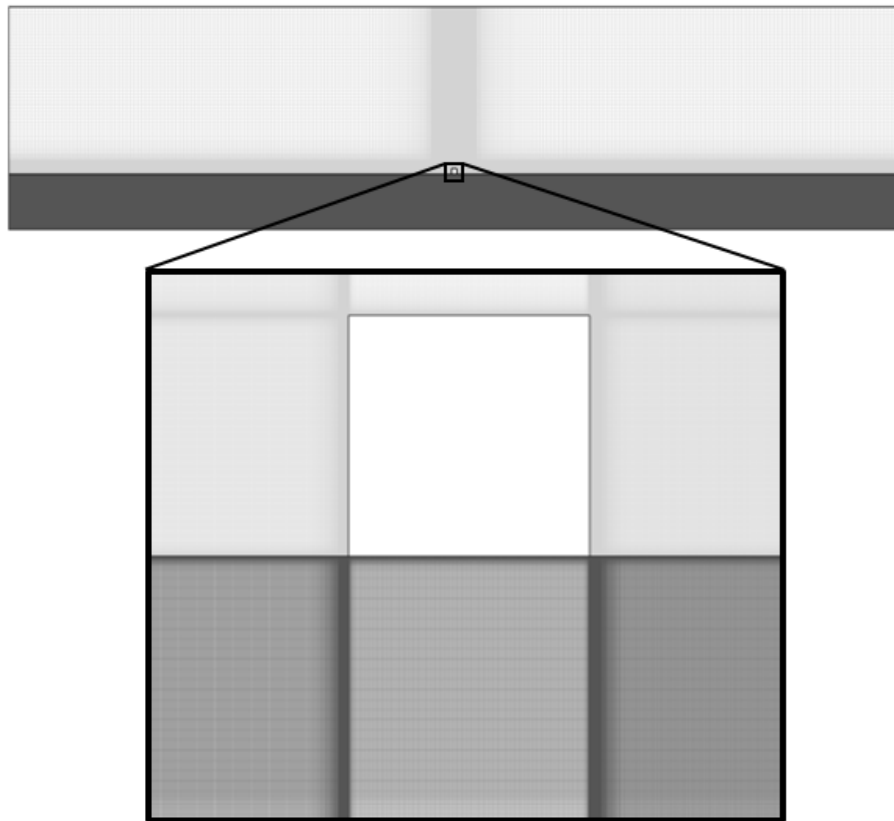


Figure A-1. The grid used in the steady-state simulations of Chapter 2. This mesh contains 2,009,929 elements.

The flow was deemed to be adequately resolved once the grid convergence index (GCI) corresponding to the recirculation lengths proximal and distal to the stent strut fell below 2%. These GCI values may be seen in Table A-1.

Table A-1. Grid convergence study in Chapter 2.

| Case | No. of Elements | $L_{proximal}$ (mm) | GCI | L_{distal} (mm) | GCI |
|------|-----------------|---------------------|-----|-------------------|-----|
| 1 | 1,003,861 | 0.065 | - | 0.115 | - |
| 2 | 2,009,929 | 0.065 | 0% | 0.115 | 0% |
| 3 | 4,028,702 | 0.065 | 0% | 0.115 | 0% |

Although the flow was clearly well defined by each mesh, the mesh independence of the drug-transport behaviour also needed to be evaluated. This was accomplished by comparing the area-weighted average concentration (AWAC) of drug within a representative area of arterial tissue. This representative area was chosen as that of a rectangle bounded by the upper and lower extents of the tissue and axial extents 3.5 strut widths either side of the strut. Mesh convergence was defined to occur once $\leq 2\%$ change was observed between two successive mesh refinements, similar to the drug transport convergence criteria used in prior numerical drug-eluting stent studies [4,5]. These results are listed in Table A-2 and the convergence is visualised in Figure A-2. As both the AWAC and the recirculation lengths were adequately resolved using the 2,009,929 element mesh, this mesh was subsequently used in all simulations in Chapter 2.

Table A-2. Mesh Independence of the Area-Weighted Average Concentration (AWAC) Drug Transport Variable.

| Case | No. of Elements | AWAC | % Change |
|------|-----------------|-------|----------|
| 1 | 1,003,861 | 0.156 | - |
| 2 | 2,009,929 | 0.159 | 1.9% |
| 3 | 4,028,702 | 0.160 | 0.6% |

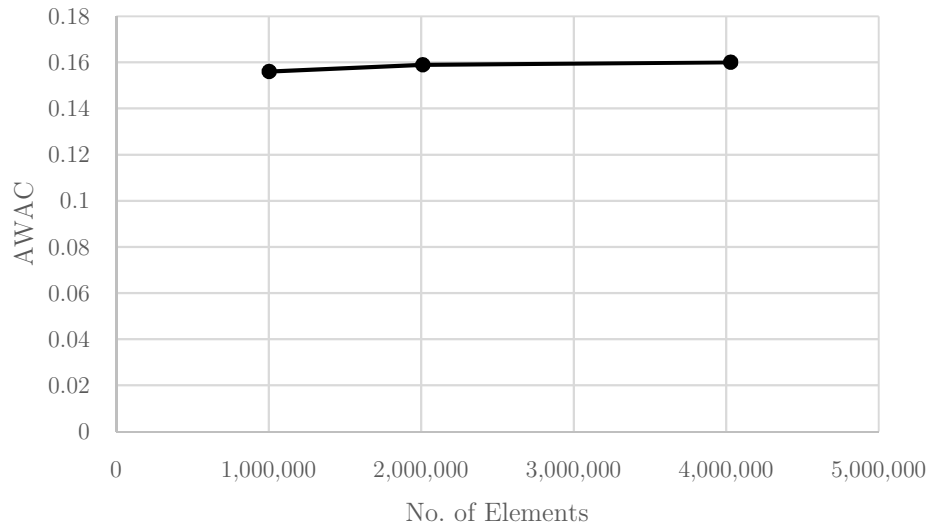


Figure A-2. Convergence of the AWAC variable with respect to the mesh size.

Grid Convergence in Chapter 3

The final mesh used in this chapter may be seen in Figure A-3. As in Chapter 2, the grid densities used in this mesh are highest in the regions close to the stent strut and also near the lumen-tissue interface. However, due to the very small time-step size that would have resulted if a mesh with no skewed elements was used, a different meshing strategy was used in these transient simulations.

Specifically, an o-grid was created around the strut, as shown in Figure A-3. This mesh is fully structured and contains 149,726 elements.

The flow through this grid was deemed to be adequately resolved once the grid convergence index (GCI) corresponding to the recirculation lengths proximal and distal to the stent strut fell below 2%. These grid convergence studies may be seen in Table A-3. As in the steady-state simulations of Chapter 2, the flow was found to be clearly resolved in each of the meshes that were tested.

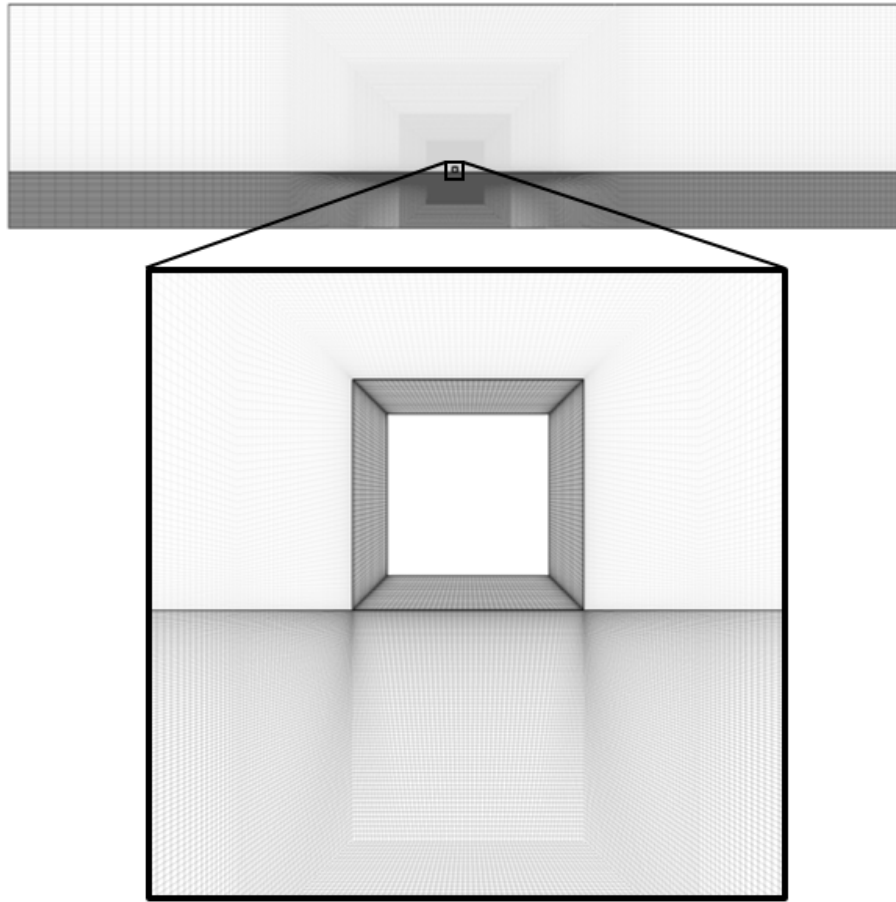


Figure A-3. The grid used in the steady-state simulations of Chapter 3.

Table A-3. Grid convergence study in Chapter 3.

| Case | No. of Elements | $L_{proximal}$ (mm) | GCI | L_{distal} (mm) | GCI |
|------|-----------------|---------------------|-----|-------------------|-----|
| 1 | 74,099 | 0.065 | - | 0.115 | - |
| 2 | 149,726 | 0.065 | 0% | 0.115 | 0% |
| 3 | 306,396 | 0.065 | 0% | 0.115 | 0% |

To test if the drug-transport behaviour was also well resolved, the AWAC value obtained with each mesh at the culmination of 24 hours of drug transport was also compared. These AWAC values were calculated using the same representative area of tissue used in Chapter 2, whilst convergence was again deemed to occur once $\leq 2\%$ change was observed between successive mesh refinements. These results are listed in Table A-4 and the convergence is

visualised in Figure A-4. These results were each obtained using a time-step size of $\Delta t = 30$ s, as this time-step produced the same AWAC values as when $\Delta t = 1$ s. As both the AWAC and the recirculation lengths were adequately resolved using the 149,726 element mesh, this mesh was subsequently used in all simulations in Chapter 3.

Table A-4. Mesh Independence of the AWAC Drug Transport Variable.

| Case | No. of Elements | AWAC | % Change |
|------|-----------------|-----------------------|----------|
| 1 | 74,099 | 1.88×10^{-5} | - |
| 2 | 149,726 | 1.92×10^{-5} | 2.0% |
| 3 | 306,396 | 1.94×10^{-5} | 1.0% |

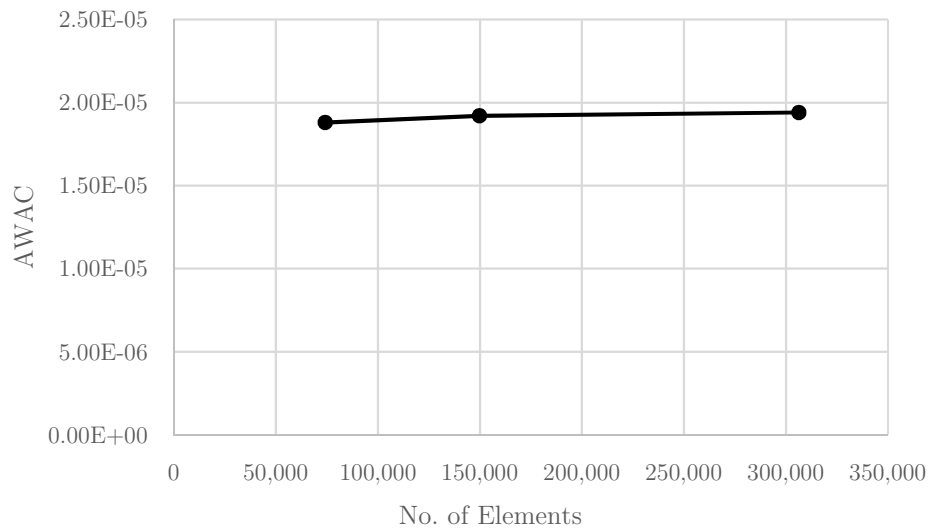


Figure A-4. Convergence of the AWAC variable with respect to the mesh size.

When the simulation time was reduced to 60 s instead of 24 hours, however, it was found that this time-step was insufficient to temporally resolve the drug transport. Instead, a time-step of $\Delta t = 0.1$ s was used for these shorter simulations in the cases where a steady flow was assumed. This time-step yielded the same AWAC as that obtained with a time-step of $\Delta t = 0.01$ s.

Grid Convergence in Chapter 4

The same meshing strategy that was used in Chapter 3 was reused in the transient simulations of Chapter 4. The mesh is once again fully structured and an o-grid was used to create regions of high mesh density near the stent strut. The final mesh contains 276,358 elements and may be seen in Figure A-5.

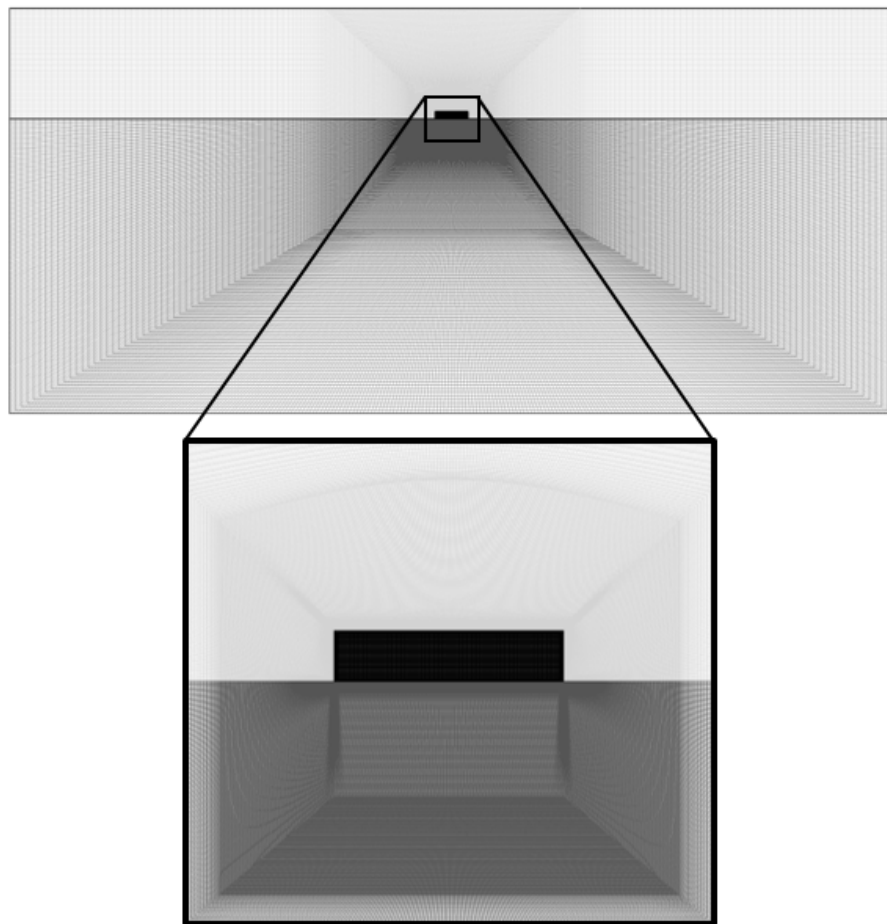


Figure A-5. The final mesh used in Chapter 4.

The flow was deemed to be adequately resolved once the grid convergence index (GCI) corresponding to the recirculation lengths proximal and distal to the

stent strut fell below 2%. As in the previous chapters, the flow was found to be clearly resolved in each of the meshes tested, as shown in Table A-5.

Table A-5. Grid convergence study in Chapter 4.

| Case | No. of Elements | $L_{proximal}$ (mm) | GCI | L_{distal} (mm) | GCI |
|------|-----------------|---------------------|-----|-------------------|-----|
| 1 | 139,832 | 0.048 | - | 0.178 | - |
| 2 | 276,358 | 0.048 | 0% | 0.178 | 0% |
| 3 | 566,023 | 0.048 | 0% | 0.178 | 0% |

The grid independence of the drug-transport behaviour was then assessed by calculating the AWAC within a representative area of arterial tissue for each mesh. The representative area that was used in this study was again defined as the area of a rectangle bounded by the upper and lower extents of the tissue and axial extents 3.5 strut widths either side of the strut. These AWAC values were obtained using the methodology described in Section 4.1.3 and with a time-step of $\Delta t = 30$ s. The final AWAC values were obtained at the conclusion of the 200 minute simulation time, which includes the 10 minutes before and after the 180 minute simulation in which no fluid flow occurs. As the AWAC that was produced with a diffusion coefficient of $D_{hydrogel} = 4.27 \times 10^{-11}$ m²/s was greater than that produced with a diffusion coefficient of $D_{hydrogel} = 2.53 \times 10^{-10}$ m²/s, only this smaller coefficient was used in the grid convergence study.

These grid convergence study results are listed in Table A-6 and the convergence of the AWAC variable is shown in Figure A-6. As in the previous chapters, grid convergence was defined to occur once $\leq 2\%$ change in AWAC was observed between two successive mesh refinements. As both the AWAC and the recirculation lengths were adequately resolved using a mesh containing 276,358 elements, this mesh was subsequently used in all simulations in Chapter 4.

Furthermore, as a time-step of $\Delta t = 30$ s was found to yield an identical AWAC to that obtained when $\Delta t = 1$ s, this larger time-step was utilised in both of the Chapter 4 simulations.

Table A-6. Mesh Independence of the AWAC Drug Transport Variable.

| Case | No. of Elements | AWAC | % Change |
|------|-----------------|-----------------------|----------|
| 1 | 139,832 | 7.02×10^{-5} | - |
| 2 | 276,358 | 7.14×10^{-5} | 1.7% |
| 3 | 566,023 | 7.18×10^{-5} | 0.6% |

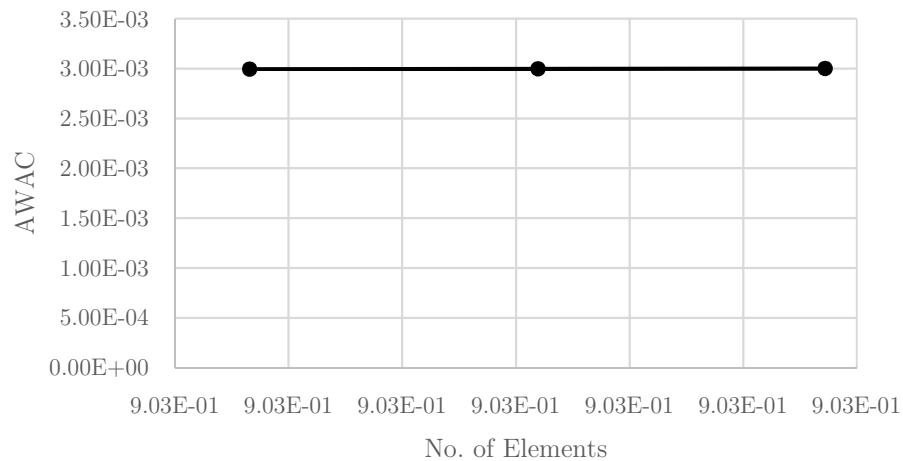


Figure A-6. Convergence of the AWAC variable in Chapter 4.

Grid Convergence in Chapter 5

The final grid used for the Model I geometry of Chapter 5 is shown in Figure A-7a. This mesh is fully structured and features 5,003,861 elements. The cross-sectional view of this mesh, shown in Figure A-7b, shows that an o-grid was once again used to ensure that the mesh elements are finest in the regions close to the stent strut. As in the previous meshes, the mesh density was also increased in the

regions close to the wall boundaries, to ensure that the boundary layer of the flowing blood is well-resolved.

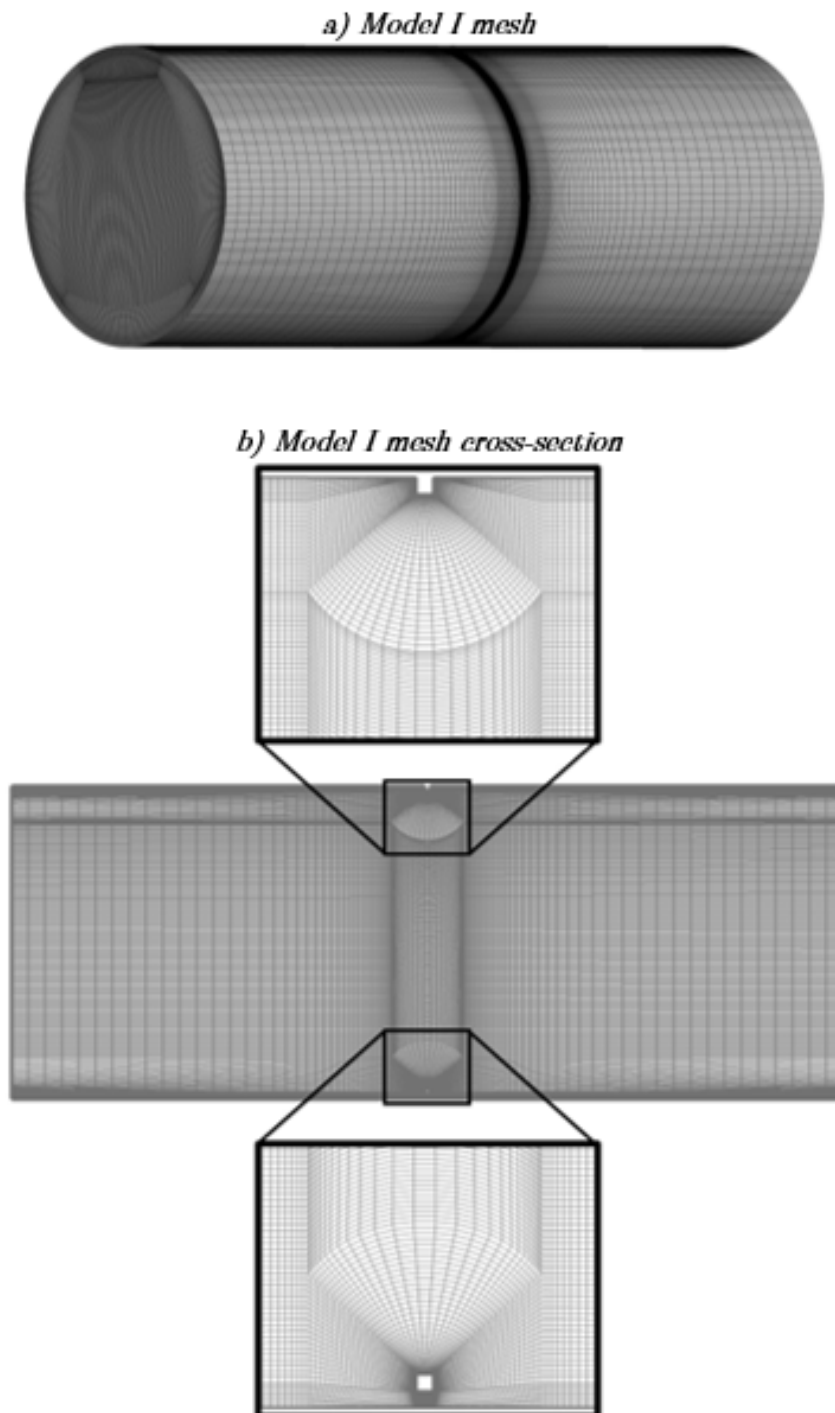


Figure A-7. Final mesh used in the Model I geometry of Chapter 5.

In order to ensure that the mesh is fully structured, a step had to be created in the strut ring geometry, as shown in Figure A-8. This was an important feature as it allowed the strut to transition from being in contact with the arterial wall to being malapposed without producing highly skewed elements. Both the well-apposed and malapposed sections of the strut can be seen in the cross-sectional view of Figure A-7b.

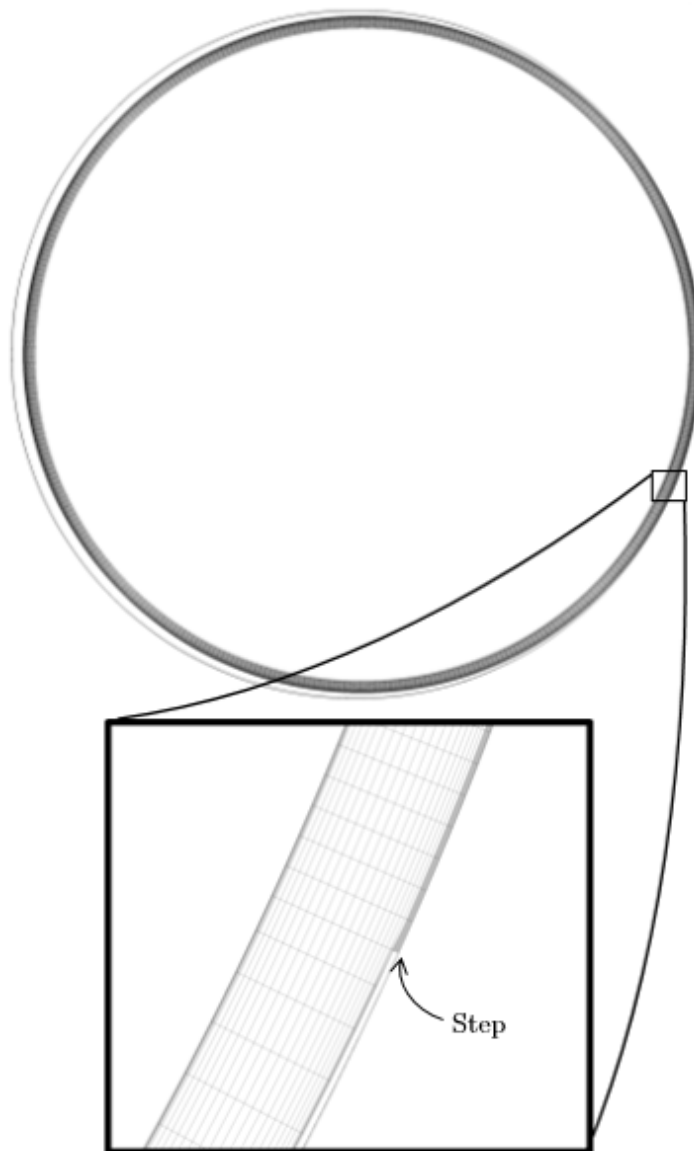


Figure A-8. A step in the strut geometry had to be created to ensure that the mesh was fully structured in the gap between the malapposed ring and the arterial wall.

The flow through the Model I geometry was deemed to be adequately resolved once the grid convergence index (GCI) corresponding to the area of coverage of the recirculating flow regions fell below 5%. As this three-dimensional geometry was only used to confirm whether the qualitative flow behaviour in two-dimensional malapposed strut geometries is accurate, a smaller GCI threshold was not deemed to be unnecessary. These grid convergence studies may be seen in Table A-7. As only the fluid flow was investigated with this model, no further grid convergence studies involving any drug transport variables were required.

Table A-7. Grid convergence study in Chapter 5 for the Model I geometry. The recirculation area is the area of coverage of the recirculation zones along the arterial wall.

| Case | No. of Elements | Recirculation area (mm ²) | GCI |
|------|-----------------|---------------------------------------|-----|
| 1 | 1,770,327 | 3.65 | - |
| 2 | 5,003,861 | 3.59 | 5% |

As grid convergence for the steady-state simulations of Chapter 2 was already obtained, a similar meshing strategy was utilised in the steady-state simulations obtained using the Model II geometries. An identical grid to that used in the tissue in the Chapter 2 mesh was intended to be used in each of the malapposed Model II geometries; however, it was determined that the case where $\delta = 10 \mu\text{m}$ yielded greater drug uptake than the well-apposed case. Hence, a new mesh was created for this geometry which featured finer elements downstream of the strut and which was coarser in other regions than in the well-apposed ($\delta = 0 \mu\text{m}$) geometry. The final mesh that was used for this geometry may be seen in Figure A-9.

The flow through this malapposed geometry was deemed to be adequately resolved once the grid convergence index (GCI) corresponding to the recirculation

lengths proximal and distal to the stent strut fell below 2%. As in the meshes used in the previous chapters, the flow was found to be clearly resolved in both of the meshes tested. The results of this grid convergence testing may be seen in Table A-8.

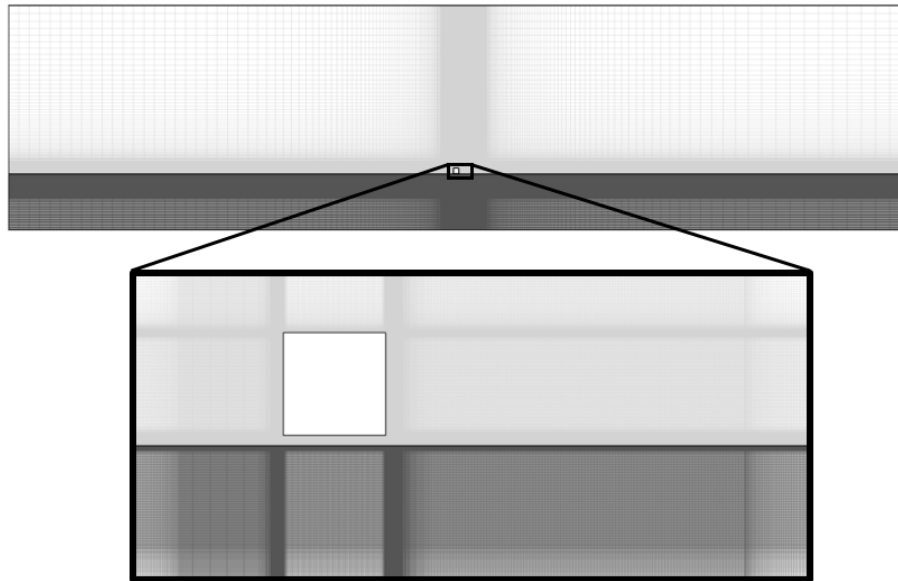


Figure A-9. Model II mesh for the case where $\delta = 10 \mu\text{m}$.

Table A-8. Grid convergence study in Chapter 5 for the Model II geometries.

| Case | No. of Elements | $L_{proximal}$ (mm) | GCI | L_{distal} (mm) | GCI |
|------|-----------------|---------------------|-----|-------------------|-----|
| 1 | 945,005 | 0.054 | - | 0.117 | - |
| 2 | 1,897,105 | 0.054 | 0% | 0.117 | 0% |

The grid convergence of the drug transport behaviour was then assessed by comparing the AWAC within the same representative area of arterial tissue that was used in the Chapter 2 grid convergence study. Mesh convergence was again deemed to occur once $\leq 2\%$ change was observed between two successive mesh refinements. These results are listed in Table A-9. As both the AWAC and

the recirculation lengths were adequately resolved using the 1,897,105 element mesh, it was this mesh that was used to simulate the Model II geometry in which $\delta = 10 \mu\text{m}$. The mesh used in the tissue of this geometry was subsequently kept the same for the remaining Model II meshes. The grid spacings in the lumen were also maintained for each of the remaining Model II meshes.

Table A-9. Mesh Independence of the AWAC Drug Transport Variable for the Model II geometry in which $\delta = 10 \mu\text{m}$.

| Case | No. of Elements | AWAC | % Change |
|------|-----------------|-------|----------|
| 1 | 945,005 | 0.121 | - |
| 2 | 1,897,105 | 0.124 | 2.0% |

As grid convergence for the transient simulations was already obtained using the mesh in Chapter 3, a similar meshing strategy was utilised to mesh the malapposed Model III geometries. Unlike Model II, the well-posed ($\delta = 0 \mu\text{m}$) geometry was found to yield the greatest drug uptake with this model. Hence, the mesh that was used in the tissue in Chapter 3 was simply reused for each of the malapposed Model III geometries. The geometry in which $\delta = 10 \mu\text{m}$ may be seen in Figure A-10.

A mesh convergence study was performed using this geometry to investigate whether the flow was adequately resolved with this mesh. The GCI obtained for the extent of the recirculation zones produced may be seen in Table A-10. Again, the flow was found to be clearly resolved in both meshes. The grid spacings in the lumen were subsequently maintained for each of the remaining Model III meshes. As no significant drug uptake was observed with these malapposed geometries, it was deemed unnecessary to perform further grid convergence studies to assess the mesh independence of the drug transport

behaviour. The final mesh sizes of each of the geometries in Chapter 5 are shown in Table A-11.

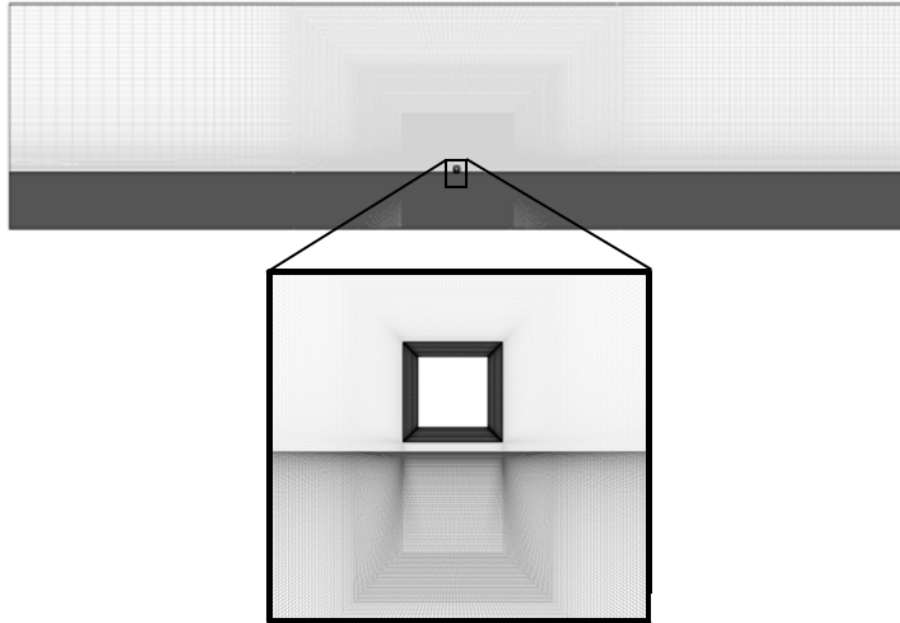


Figure A-10. Final mesh used in the Model III simulations of Chapter 5. This geometry possesses a malapposition distance of $10\ \mu\text{m}$.

Table A-10. Grid convergence study in Chapter 5 for the Model III geometry in which $\delta = 10\ \mu\text{m}$.

| Case | No. of Elements | $L_{proximal}$ (mm) | GCI | L_{distal} (mm) | GCI |
|------|-----------------|---------------------|-----|-------------------|-----|
| 1 | 166,206 | 0.054 | - | 0.117 | - |
| 2 | 334,105 | 0.054 | 0% | 0.117 | 0% |

Table A-11. Final mesh sizes.

| Model (Geometry) | No. of Elements |
|----------------------------|------------------------|
| I | 5,003,861 |
| II | |
| $\delta = 0 \mu\text{m}$ | 2,009,929 |
| $\delta = 10 \mu\text{m}$ | 1,897,105 |
| $\delta = 25 \mu\text{m}$ | 2,239,387 |
| $\delta = 50 \mu\text{m}$ | 2,335,819 |
| $\delta = 75 \mu\text{m}$ | 2,436,187 |
| $\delta = 100 \mu\text{m}$ | 2,534,587 |
| III | |
| $\delta = 0 \mu\text{m}$ | 149726 |
| $\delta = 10 \mu\text{m}$ | 166206 |
| $\delta = 25 \mu\text{m}$ | 179004 |
| $\delta = 50 \mu\text{m}$ | 193224 |
| $\delta = 75 \mu\text{m}$ | 200334 |
| $\delta = 100 \mu\text{m}$ | 207444 |

Grid Convergence in Chapter 6

The final grid used in the two-dimensional steady-state simulations of Chapter 6 may be seen in Figure A-11. As in previous chapters, the mesh densities were highest in the regions close to the stent strut and near the arterial wall. The mesh is fully structured and features no skewed elements.

The flow was deemed to be adequately resolved once the grid convergence index (GCI) corresponding to the recirculation lengths proximal and distal to the stent strut fell below 2%. This grid convergence study may be seen in Table A-12 for a non-magnetic strut. As the recirculation lengths obtained with the two meshes were found to deviate by less than 2%, the flow was assumed to be adequately resolved by a mesh containing 225,064 elements.

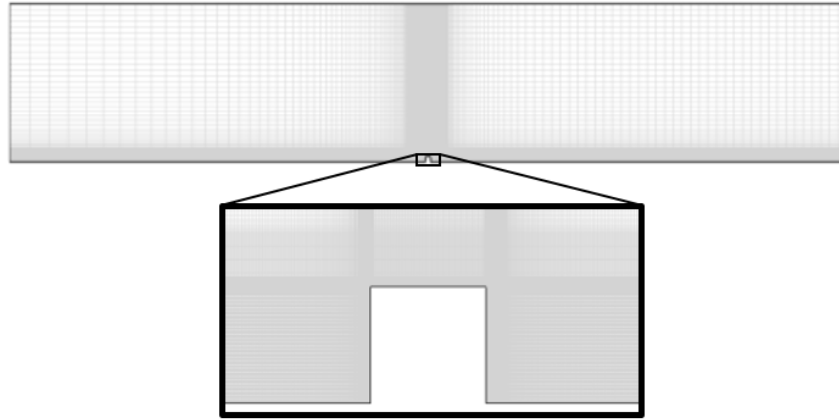


Figure A-11. The grid used in the steady-state simulations of Chapter 6.

Two further grid convergence studies were then performed to check that the impact of the magnetic field on the surrounding blood flow was also adequately resolved with this mesh. These studies were both performed using a magnetic strut with a peak magnetic flux density of 8T. Additionally, deoxygenated blood was used in both cases as its higher magnitude magnetic susceptibility allowed it to be more greatly affected by the magnetic strut than oxygenated blood. In both the Fore-Aft and Top-Bottom magnet configurations, the calculated recirculation lengths were found to be independent of the size of the grid, as shown in Table A-13. Hence, the impact of the magnetic field on the blood flow was found to be well resolved using a mesh containing 225,064 elements.

Table A-12. Chapter 6 grid convergence study for a non-magnetic stent strut.

| NON-MAGNETIC STRUT | | | | | |
|--------------------|-----------------|---------------------|-----|-------------------|-----|
| Case | No. of Elements | $L_{proximal}$ (mm) | GCI | L_{distal} (mm) | GCI |
| 1 | 113,897 | 0.065 | - | 0.115 | - |
| 2 | 225,064 | 0.065 | 0% | 0.115 | 0% |

Table A-13. Grid convergence study in Chapter 6 for a magnetic strut with a peak magnetic flux intensity of 8T and in deoxygenated blood.

| FORE-AFT CONFIGURATION | | | | | |
|--------------------------|-----------------|---------------------|-----|-------------------|-----|
| Case | No. of Elements | $L_{proximal}$ (mm) | GCI | L_{distal} (mm) | GCI |
| 1 | 113,897 | 0.065 | - | 0.112 | - |
| 2 | 225,064 | 0.065 | 0% | 0.112 | 0% |
| TOP-BOTTOM CONFIGURATION | | | | | |
| Case | No. of Elements | $L_{proximal}$ (mm) | GCI | L_{distal} (mm) | GCI |
| 1 | 113,897 | 0.064 | - | 0.115 | - |
| 2 | 225,064 | 0.064 | 0% | 0.115 | 0% |

Grid Convergence in Chapter 7

The last series of grid convergence studies were performed for the two- and three-dimensional geometries used in Chapter 7. For the two-dimensional geometries, grid convergence studies had already been performed using the square-profiled strut geometries in Chapter 3 and Chapter 5. Hence, only the well-apposed and malapposed semicircle-profiled struts required a grid convergence study in these initial two-dimensional simulations. In the three-dimensional simulations, mesh independence studies were performed for both strut profile geometries.

The final Geometry I and Geometry II grids obtained using the semicircle-profiled strut geometry may be seen in Figure A-12 and Figure A-13 respectively. For comparison, the final Geometry II grid in which the square-profiled strut geometry was used is also shown in Figure A-14. As in the grids used in Chapters 3 and 5, the grid densities in each geometry were greatest in the regions closest to

the struts and near the interface between the tissue and lumen. The final Geometry I meshes contained 149,726 and 109,792 elements for the Strut Profile I and Strut Profile II cases respectively. Similarly, the final Geometry II meshes contained 193,224 and 135,336 elements for the Strut Profile I and Strut Profile II cases respectively.

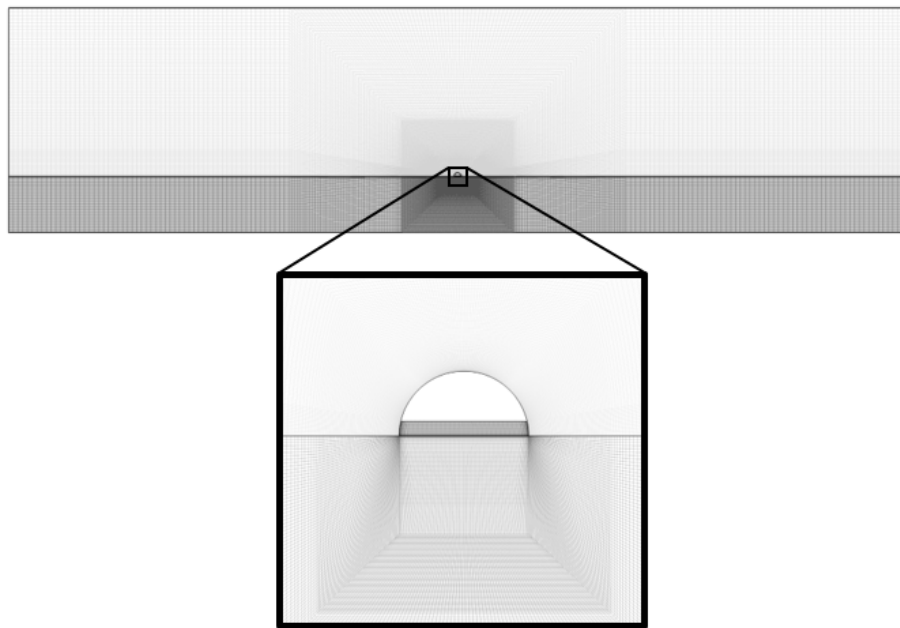


Figure A-12. Final Geometry I mesh for the case in which Strut Profile II was used.

Using Strut Profile II, the flow through Geometry I was deemed to be adequately resolved once the grid convergence index (GCI) corresponding to the recirculation lengths proximal and distal to the stent strut fell below 2%. The results of this grid convergence testing may be seen in Table A-14. As shown, the 109,792 element mesh was found to be suitable to use for the well-apposed semicircular strut geometry.

As in previous chapters, the convergence of the drug transport behaviour was assessed by comparing the AWAC values obtained with each mesh at the culmination of 24 hours of drug transport. For the well-apposed geometries, grid

convergence was again assumed to occur once $\leq 2\%$ change in the AWAC variable was noted between mesh refinements. Unlike the previous chapters, however, the average concentration was determined over the entire tissue domain as opposed to within a smaller representative area. The results of this mesh convergence study are listed in Table A-15 and were used to justify the implementation of the 109,792 element mesh shown in Figure A-12. As a time-step of $\Delta t = 30$ s was already found to be appropriate to use in conjunction with the square strut profile geometry in Chapters 3 and 5, the same time-step was utilised in these two-dimensional geometries.

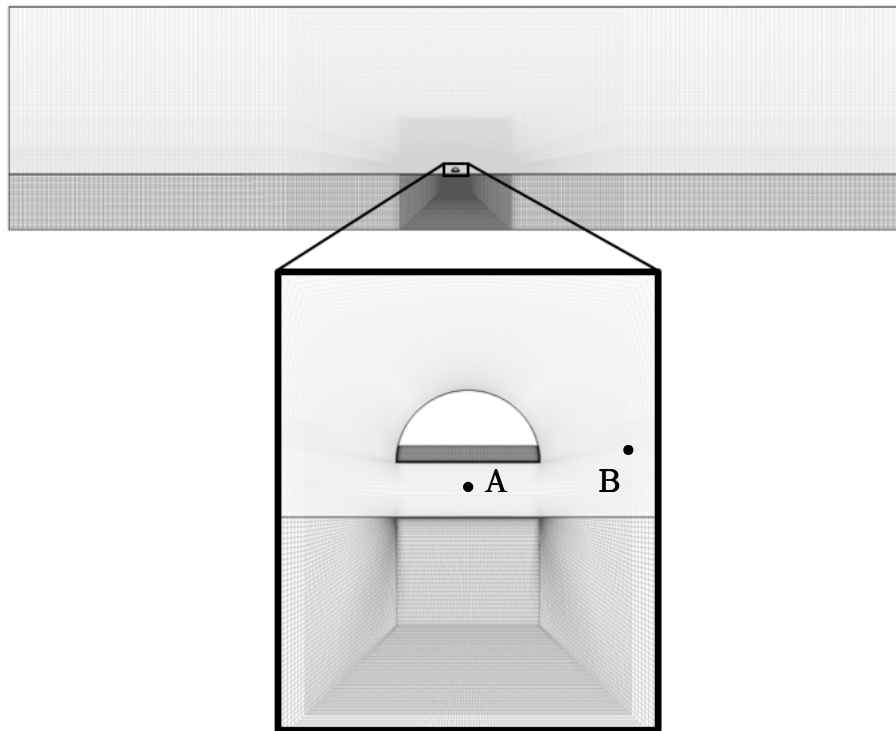


Figure A-13. Final Geometry II mesh for the case in which Strut Profile II was used. As no recirculation zones were produced with this geometry, the velocity at the points labelled A and B were instead measured in the grid convergence studies.

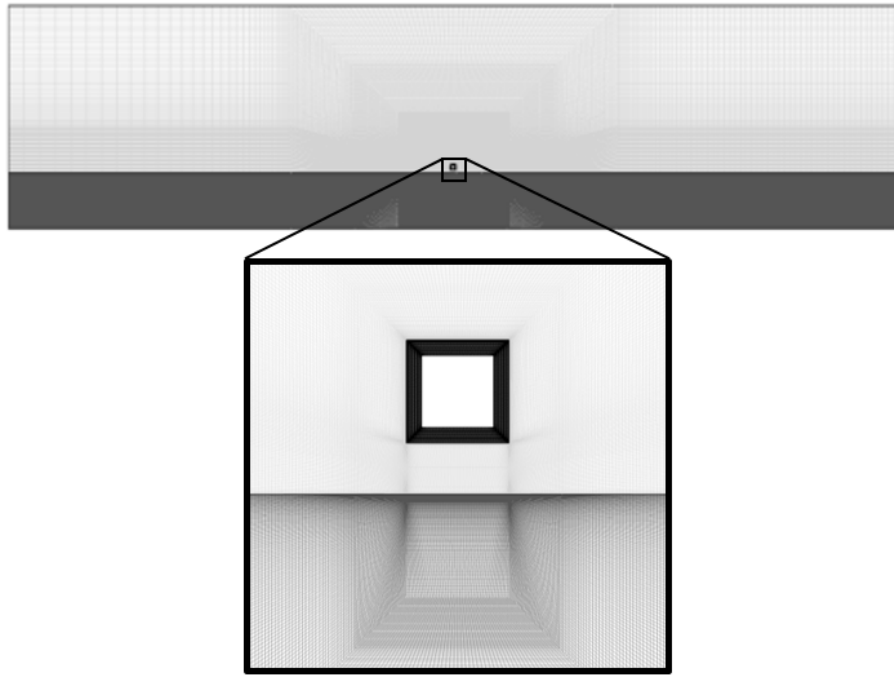


Figure A-14. Final Geometry II mesh for the case in which Strut Profile I was used.

Table A-14. Grid convergence study in Chapter 7 for the well-posed semicircular strut geometry.

| Case | No. of Elements | $L_{proximal}$ (mm) | GCI | L_{distal} (mm) | GCI |
|------|-----------------|---------------------|-----|-------------------|-----|
| 1 | 55,010 | 0.018 | 0% | 0.027 | - |
| 2 | 109,792 | 0.018 | 0% | 0.027 | 0% |

Table A-15. Mesh Independence of the AWAC Drug Transport Variable for the Model II geometry in which $\delta = 10 \mu\text{m}$.

| Case | No. of Elements | AWAC | % Change |
|------|-----------------|-----------------------|----------|
| 1 | 55,010 | 2.07×10^{-6} | - |
| 2 | 109,792 | 2.11×10^{-6} | 1.9% |

It should be noted that recirculation zones were absent in the malapposed semicircular strut profile geometry and thus could not be used to test whether grid convergence had been obtained. The grid convergence study for Geometry II featuring Strut Profile II was instead performed by measuring the velocity of blood at two points, labelled A and B in Figure A-13. As shown in Table A-16, a mesh with 135,336 elements was found to be suitable for simulating the flow of blood through an artery with a malapposed semicircular strut profile geometry. This mesh was identical in the tissue region to the mesh that used in the well-apposed semicircular strut, as may be seen through comparison of Figure A-12 and Figure A-13. However, as no significant drug uptake was observed with this geometry, no further studies were performed to investigate the mesh independence of the drug transport behaviour. As a result, a mesh with 135,336 elements was deemed to be suitable to use for the malapposed semicircle-profiled strut simulation of Chapter 7.

Table A-16. Grid convergence study in Chapter 7 for the malapposed semicircular strut geometry.

| Case | No. of Elements | Velocity at A (m/s) | GCI | Velocity at B (m/s) | GCI |
|------|-----------------|-----------------------|------|-----------------------|------|
| 1 | 55,010 | 2.00×10^{-3} | - | 3.21×10^{-3} | - |
| 2 | 109,792 | 2.01×10^{-3} | 1.5% | 3.19×10^{-3} | 1.8% |

Finally, the three dimensional meshes that were used may be seen in Figure A-15. Unlike the previous meshes, a fully structured mesh was not implemented due to the complexity of the three-dimensional stent strut geometries. Although hexahedral elements were utilised throughout most of the

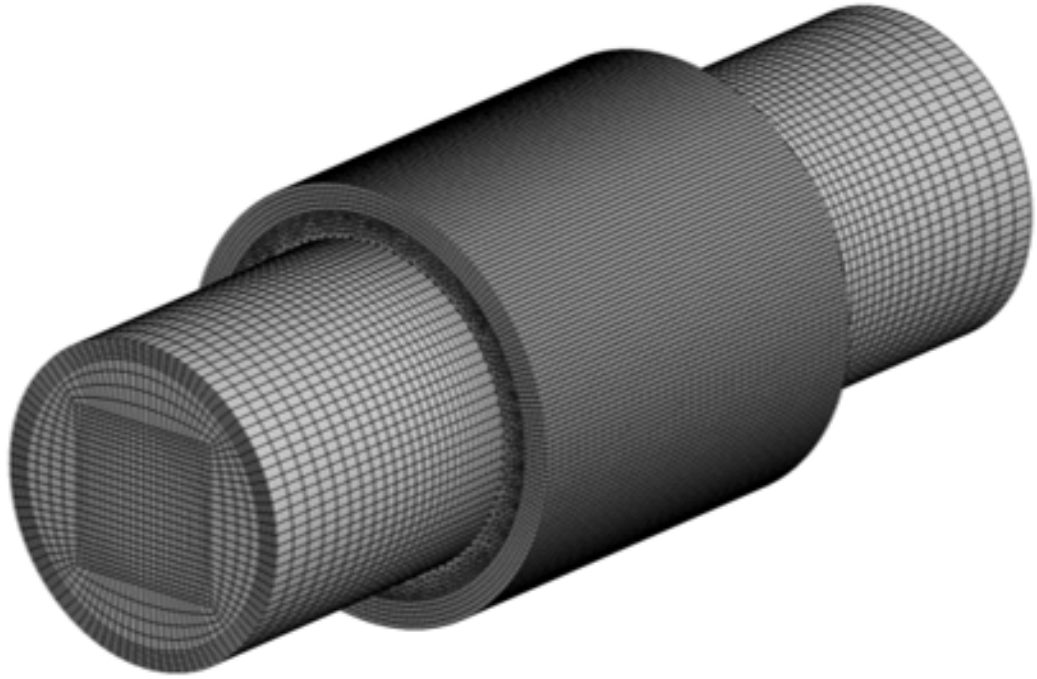
geometry, tetrahedral elements were used near the interface between the tissue and the lumen, as may be seen in Figure A-16 and Figure A-17. Prism layers were added in the lumen at the locations where it is in contact with the tissue and with the strut. This enabled the resolution of the thin boundary layers that occur along the no-slip boundaries that define the artery wall and the stent strut walls. Prism layers were also added within the stent coating to enable the resolution of the strong drug concentration gradients. The grid density in the tissue domain directly beneath the strut was also increased to further resolve the strong drug concentration gradients. The same grid densities and the same meshing strategy was used with both strut profile geometries to ensure that the meshes produced were as alike as possible. The same grid densities and the same meshing strategy was used with both strut profile geometries to ensure that the meshes produced were as alike as possible.

The flow through both geometries was deemed to be adequately resolved once $\leq 5\%$ change in the area of coverage of recirculating flow regions was observed between two successive mesh refinements. The results of this grid convergence testing may be seen in Table A-17. As shown, the 22,613,628 element mesh was found to be suitable to use for the case where Strut Profile I was used. Furthermore, a 20,481,254 mesh was found to be suitable to use for the case where Strut Profile II was used.

Finally, the drug transport behaviour of both geometries was deemed to be adequately resolved once $\leq 5\%$ change in the volume-weighted average concentration (VWAC) of drug in the tissue occurred between two successive mesh refinements. The VWAC values were obtained at the end of the 24 hour simulations in both geometries and the results of this grid convergence testing may be seen in Table A-18. A 22,613,628 element mesh was found to be suitable

to use for the case where Strut Profile I was used. Furthermore, a 20,481,254 mesh was found to be suitable to use for the case where Strut Profile II was used.

a) Strut Profile I



b) Strut Profile II

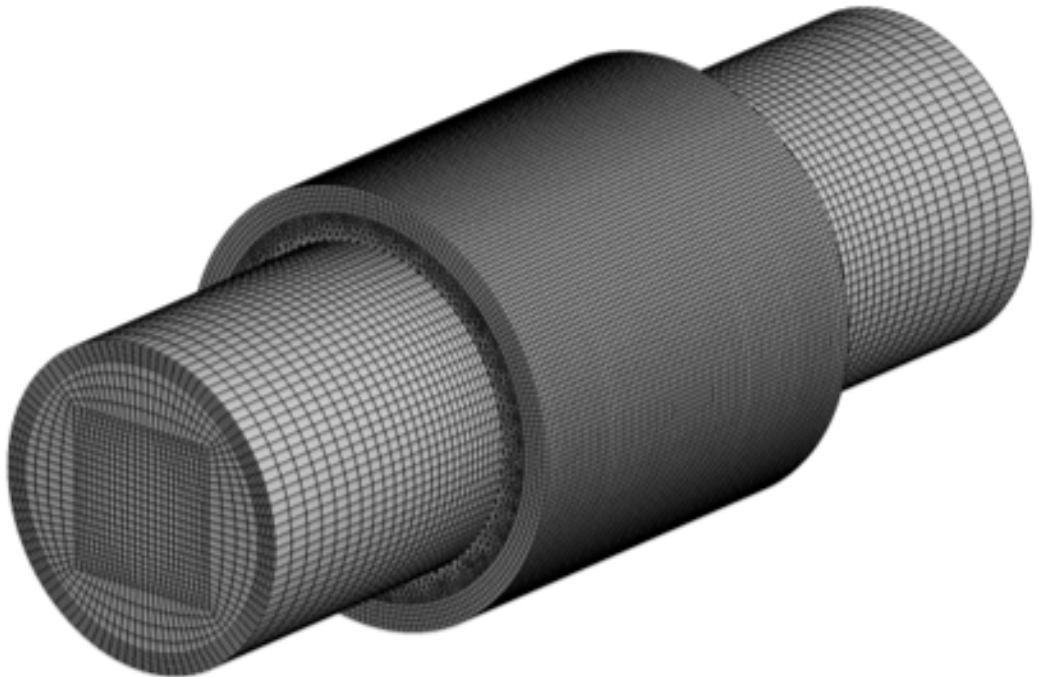


Figure A-15. The final meshes used in the three-dimensional simulations of Chapter 7.

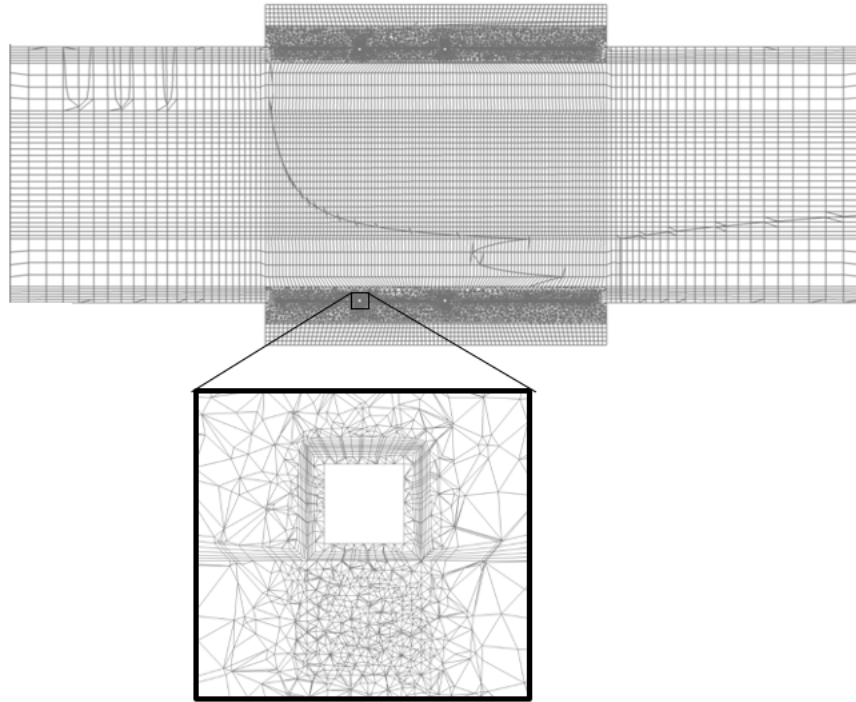


Figure A-16. Cross-section of the Geometry III mesh in which Strut Profile I was used.

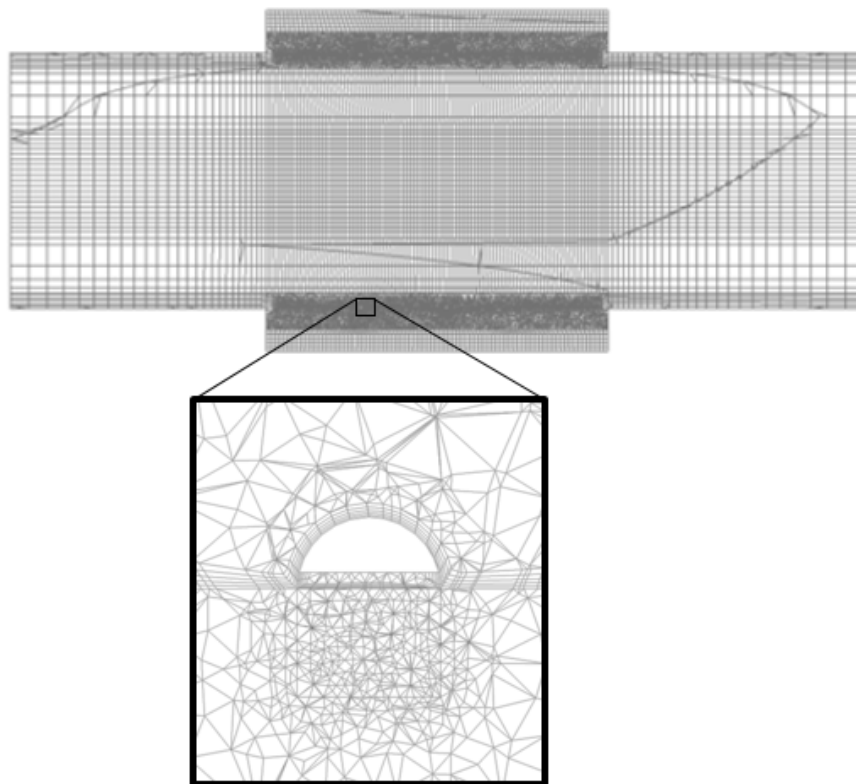


Figure A-17. Cross-section of the Geometry III mesh in which Strut Profile II was used.

Table A-17. Grid convergence of the flow in the Geometry III studies.

| Strut Profile I | | | |
|------------------|-----------------|--|----------|
| Case | No. of Elements | Total area of recirculation zones (mm ²) | % Change |
| 1 | 11,593,434 | 1.73 | - |
| 2 | 22,613,628 | 1.82 | 4.9% |
| Strut Profile II | | | |
| Case | No. of Elements | Total area of recirculation zones (mm ²) | % Change |
| 1 | 10,175,062 | 0.23 | - |
| 2 | 20,481,254 | 0.22 | 4.5% |

Table A-18. Grid convergence of the VWAC in the Geometry III studies

| Strut Profile I | | | |
|------------------|-----------------|-----------------------|----------|
| Case | No. of Elements | VWAC | % Change |
| 1 | 11,593,434 | 0.89 | - |
| 2 | 22,613,628 | 0.93 | 4.3% |
| Strut Profile II | | | |
| Case | No. of Elements | VWAC | % Change |
| 1 | 10,175,062 | 1.54×10^{-5} | - |
| 2 | 20,481,254 | 1.60×10^{-5} | 3.8% |

Appendix B

In-Vitro Experiment

Setup

Equipment

- PCO pixelfly CCD camera
- Nikon Eclipse TE2000 microscope with mercury arc-discharge lamp
- Acrylic flow rig with 4 × M1.2 screws and 16 × M3 screws
- Rhodamine B/PDMS strut
- PVA-MA hydrogel
- Computer with CamWare64 installed
- Razor blade
- Thermocouple
- Small, slotted screwdriver
- Timer
- Reservoir with at least 1 litre of glycerol-water

Method

1. Mount the PCO pixelfly CCD camera to the side of the Nikon Eclipse TE2000 microscope as shown in Figure B-1.



Figure B-1. The PCO pixelfly camera is mounted to the side of the microscope.

2. Fasten the microscope stage onto the microscope, as shown in Figure B-2.



Figure B-2. The microscope stage is fastened to the microscope.

3. Turn on the microscope and the mercury arc-discharge lamp. Then set up the microscope so that the 4× magnification lens and the green excitation filter are in use. Also ensure that the shutter is closed, as shown in Figure B-3.

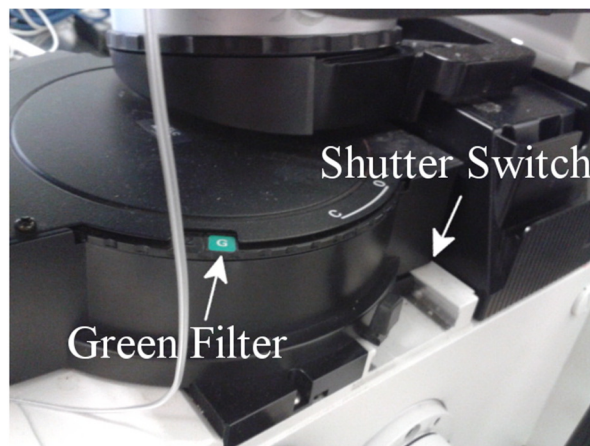


Figure B-3. The green filter is used but the shutter is closed for the moment.

4. Place the hydrogel into the recess within the acrylic test rig and clamp a Rhodamine B/PDMS strut on top of the hydrogel. Ensure that the strut is

placed at the centre of the hydrogel and that its orientation is perpendicular to the flow channel, as depicted in Figure B-4.



Figure B-4. The Rhodamine B/PDMS strut is clamped onto the hydrogel within the acrylic test rig.

5. Connect the acrylic test rig to the LongerPump BT600-2J peristaltic pump and immerse the inlet and outlet tubes within a reservoir of glycerol-water, as shown in Figure B-5.



Figure B-5. Pump, reservoir, flow rig, mercury lamp and microscope arrangement.

6. Commence pumping the glycerol-water solution through the flow rig whilst simultaneously commencing timing.

7. Connect the PCO pixelfly camera to a laptop or computer that supports the CamWare64 program. A green light will appear on the camera when it is properly connected and ready to capture images. Then double click on the icon depicted in Figure B-6.



Figure B-6. The CamWare64 icon.

8. Under the 'Camera Properties' menu, change the exposure of the camera to 400 ms, as shown in Figure B-7.

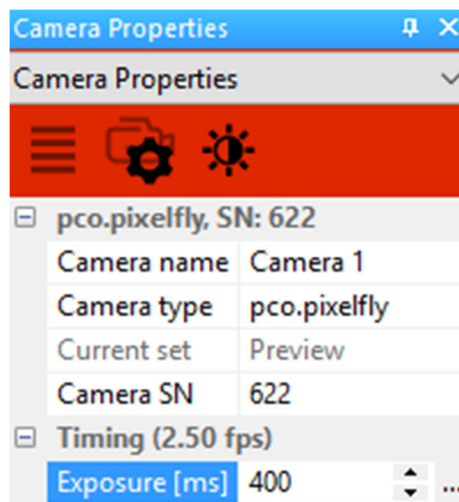


Figure B-7. A 400 ms exposure time was chosen for this study.

9. Under the 'Color Balance' menu, change the minimum and maximum values of the sliders on the histogram shown in Figure B-8 to 500 and 7000 respectively. Values below the minimum mark are set to 0 (i.e. black) whilst values above the maximum mark are set to a value of 255 (i.e. white). The values from the collected images that fall between these extremes are

assigned values between 0 and 255 according to the contrast and gamma settings.

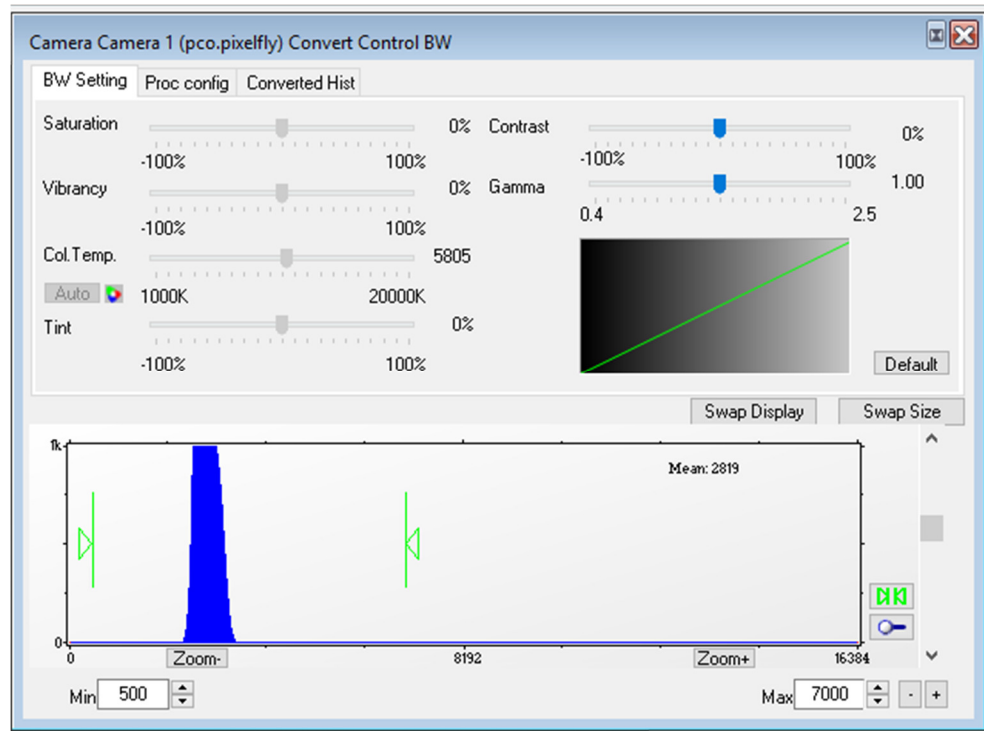


Figure B-8. The left and right hand sliders are adjusted to values of 500 and 7000 respectively.

10. Click on the 'Live Preview' button and open the shutter on the microscope. Green light should flood the hydrogel and strut, as shown in Figure B-9.

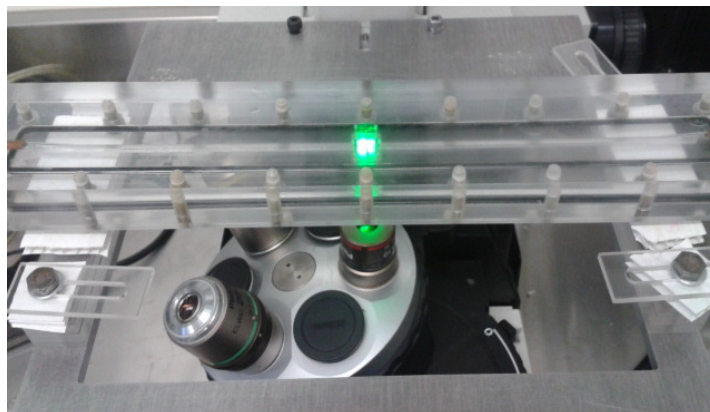


Figure B-9. The shutter is opened, allowing green light to flood the area of interest.

11. With the room darkened, adjust the coarse focus knob on the microscope until the strut and hydrogel come into focus. The image on the screen should look similar to that depicted in Figure B-10. Black cloth may need to be draped over the flow channel to mitigate exposure to external light.

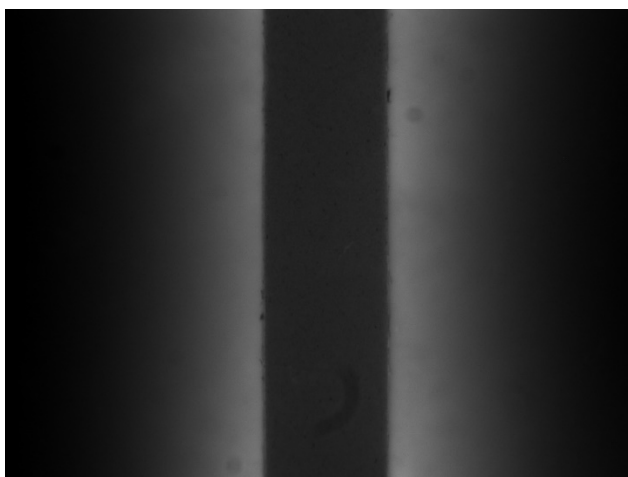


Figure B-10. Sample image collected from the PCO pixelfly camera.

12. Collect images at 30 minute intervals from the commencement of timing until three hours have elapsed. Ensure that the shutter is closed whilst images are not being taken to mitigate the risk of photobleaching. These images were used to create Figure 4-13. Also collect the temperature of the glycerol-water solution at the outlet pipe each time an image has been collected using a thermocouple.
13. After collecting the last of these images, evacuate the glycerol-water from the flow rig and take another image. These images of the strut and hydrogel sans glycerol-water were used to create Figure 4-12.
14. Remove the lid of the flow channel as well as the strut. A pink stripe should be present in the region where the strut had contacted the hydrogel, as depicted in Figure Figure B-11. The hydrogel can be removed by first

removing a small section of hydrogel downstream of the pink stripe using a slotted screwdriver. This section, depicted using grey stripes in Figure B-11, must be far away from the region where strut had contacted the hydrogel. Using the slotted screwdriver, the remaining hydrogel can be carefully lifted from the hydrogel recess.

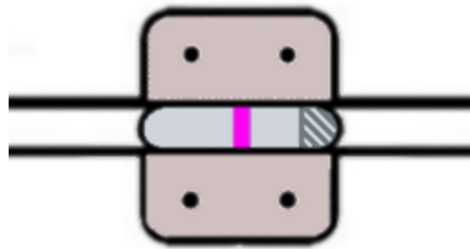


Figure B-11. The hydrogel was extracted by breaking off the striped section with a slotted screwdriver and lifting out the remaining hydrogel.

15. Slice the hydrogel in half along its longitudinal axis using a razor blade and place the two halves face down under the microscope to observe the cross-sectional distributions of Rhodamine B within the hydrogel. These distributions should look like the black and white images in Figure B-12 and it was these images that were used to create Figure 4-14. Remember when collecting these images that the flat end of the hydrogel is the side that was downstream of the strut during the experiment.

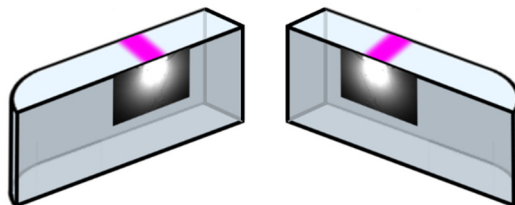


Figure B-12. Images of the cross-sectional distribution of Rhodamine B within the two halves of the hydrogel were collected at the end of the experiment.

Appendix C

Hydrogel Preparation

Equipment

- 1000 mg poly-vinyl alcohol (PVA, 16k Da, 98% hydrolysed) macromer with 7 methacrylate crosslinks
- 3750 μ L deionised water
- 250 μ L UV initiator solution (Irgacure 2959 1 wt.% in water)
- Adhesive tape
- Plastic centrifuge tube with lid
- Glycerol-water (40 wt.% glycerol and 60 wt.% deionised water) solution
- Specimen container
- Windscreen washer fluid (Rain-X)
- Hydrogel mould
- A small spatula or spoon
- 1000 μ L pipette and tips
- Four 75 mm \times 25 mm glass slides
- Electric balance
- Heat bath
- Vortex mixer
- UV lamp
- Detergent
- Cleaning tissues
- Tweezers

Method

1. Using an electronic balance and tweezers, transfer 1000 mg of the PVA-MA macromer into a centrifuge tube.

2. Add 3750 μL of deionised water to the solute using a 1000 μL pipette.
3. Mix the contents of the centrifuge tube using a vortex mixer, as shown in Figure C-1.



Figure C-1. A vortex mixer is used to mix the contents of the centrifuge tube.

4. Seal the lid of the tube using adhesive tape to ensure that no vapour escapes.
5. Place the tube into a heat bath at 80°C for approximately two hours and mix the solution intermittently using the vortex mixer. Check that the solution is clear and homogeneous, as shown in Figure C-2.

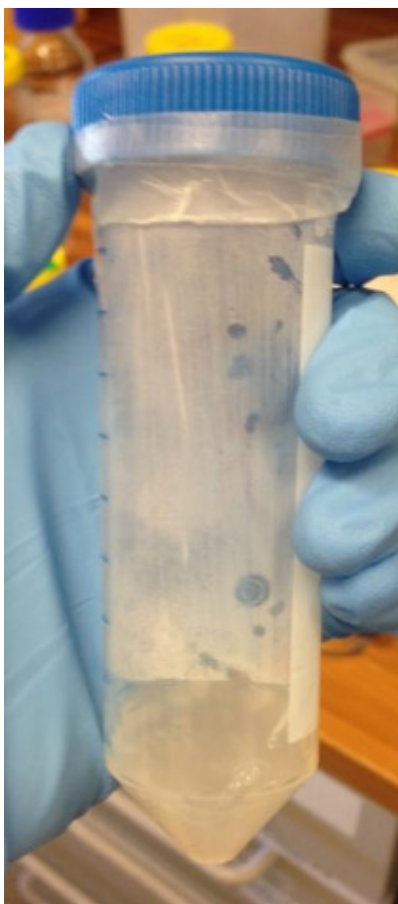


Figure C-2. The PVA-MA solution should turn clear when it is well-mixed.

6. Remove the centrifuge tube from the heat bath and cover it in aluminium foil in preparation for the addition of a UV initiator solution.
7. Add 250 μL of the UV initiator solution to the test-tube using a 1000 μL pipette. Ensure that the UV initiator solution is exposed to as little light as possible during this process.
8. Mix the solution further using the vortex mixer. Keep the speed of the mixer slow enough to ensure that bubbles do not form.
9. Coat the Perspex hydrogel mould and four 75 mm \times 25 mm glass slides with windscreen washer fluid and leave them to dry. This step allows the hydrogels to be more easily extracted from the moulds.

10. Two 75 mm × 25 mm glass slides are placed under the Perspex hydrogel mould and the solution is slowly transferred into the mould using a small spoon or spatula. It is important to ensure that no air bubbles are trapped in the mould and that the mould is slightly overfilled. It is also important to ensure that no solid pieces of PVA-MA enter the mould.
11. Slowly slide two further 75 mm × 25 mm glass slides along the top of the mould until the top of the mould is covered. This process can be seen in Figure C-3.

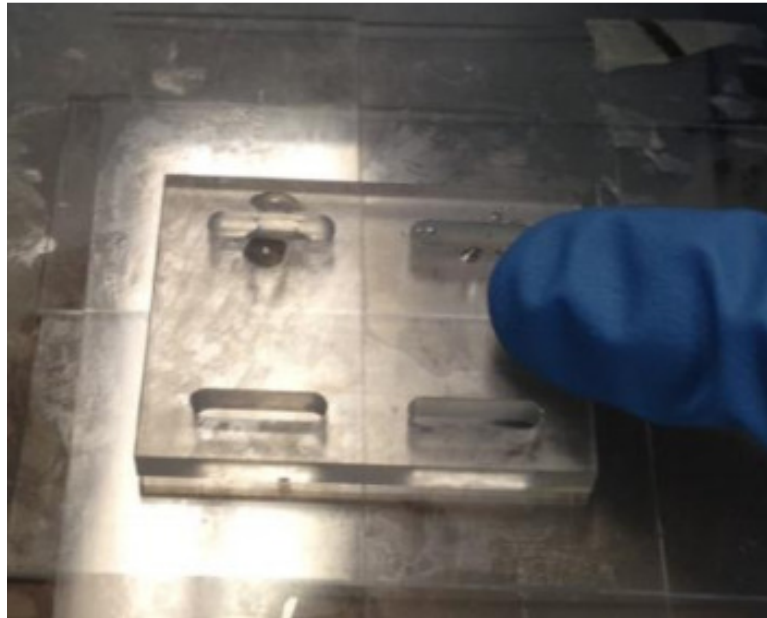


Figure C-3. Glass slides are used to retain the PVA-MA solution within the Perspex mould.

12. Adjust the height of a UV lamp to produce an irradiance of 0.03 W/m² at the location of the mould. This irradiance can be measured using a radiation meter. Radiate the solution for a period of 180 seconds to create the hydrogels. Note that the maximum time that can be set is 90 seconds, so the UV lamp must be activated twice. This process can be seen in Figure C-4.

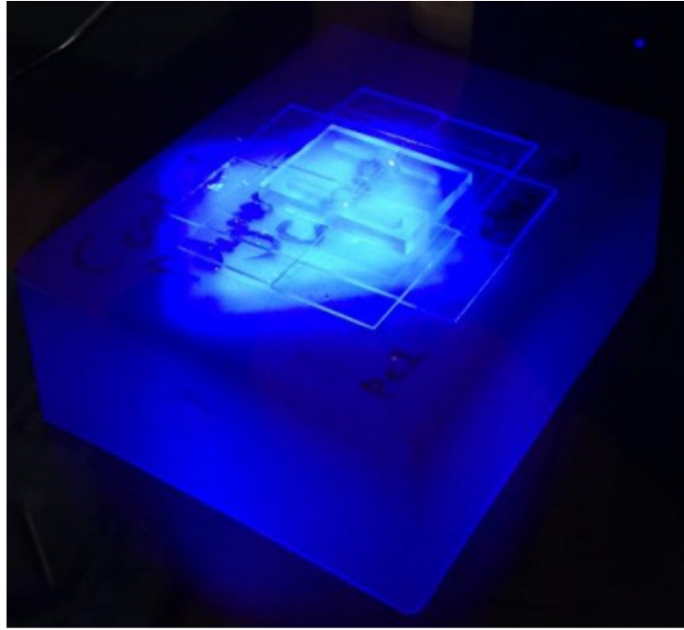


Figure C-4. The mould and its contents are placed under a UV lamp for 180 seconds to create the hydrogel.

13. Carefully remove the glass slides whilst wetting the mould with distilled water to reduce the chances of breaking the hydrogel.
14. Gently push the hydrogels out of the mould using a small spoon or spatula.
15. Place the completed hydrogels inside a specimen container filled with glycerol-water.
16. Repeat steps 9-15 until the PVA-MA solution is depleted.

Appendix D

Rhodamine B/PDMS

Strut Preparation

Equipment

- Rhodamine B powder
- Ethanol
- Sylgard 184 base
- Sylgard 184 curing agent
- Oven
- Vacuum chamber
- Fume hood
- Cleaning tissues
- Detergent
- Separate chemical disposal containers for PDMS, Rhodamine B and used gloves
- Aluminium foil
- Electric balance
- Disposable syringe
- Stir rod
- 48mm diameter Petri dish
- Beaker
- Disposable spoon
- Tweezers
- Cutting tool

Method

1. Preheat an oven to 65°C

2. Place a clean, dry, 48 mm petri dish on an electronic balance and zero the balance.
3. Add 0.02 g of Rhodamine B powder into the petri dish
4. Add 1.75 g of Sylgard 184 solution into the petri dish.
5. Stir the contents of the petri dish with a disposable spatula until the Rhodamine B is roughly evenly distributed.
6. With the disposable spatula still inside the petri dish, zero the electronic balance again.
7. Add approximately 0.1 g of ethanol into the petri dish and stir the contents with a disposable spatula until well mixed. The solution should change colour from dark green to dark purple. If there are still visible Rhodamine B particles, add more ethanol and continue stirring until well mixed.
8. Place the petri dish inside the oven and keep inside for 10 minutes. This ensures that any ethanol still within the mixture evaporates and is no longer part of the Rhodamine B/PDMS solution.
9. Place the petri dish back on the electronic balance. If the reading is positive, repeat step 8. If not, keep the petri dish on balance for an additional 5 minutes and observe the display to ensure that the reading does not decrease. If it does decrease, then repeat step 8 until the reading ceases to change with respect to time and until bubbles cease to appear within the mixture. At this point, it can be assumed that there is no longer any ethanol within the Rhodamine B/PDMS base mixture.
10. Zero the balance again and pour 0.25 g of PDMS curing agent to the petri dish.
11. Using the disposable spatula, stir the contents of the petri dish for 10 minutes.

12. Degas the solution within a vacuum chamber for an hour. Check that the solution is uniform and bubble free, as shown in Figure D-1.

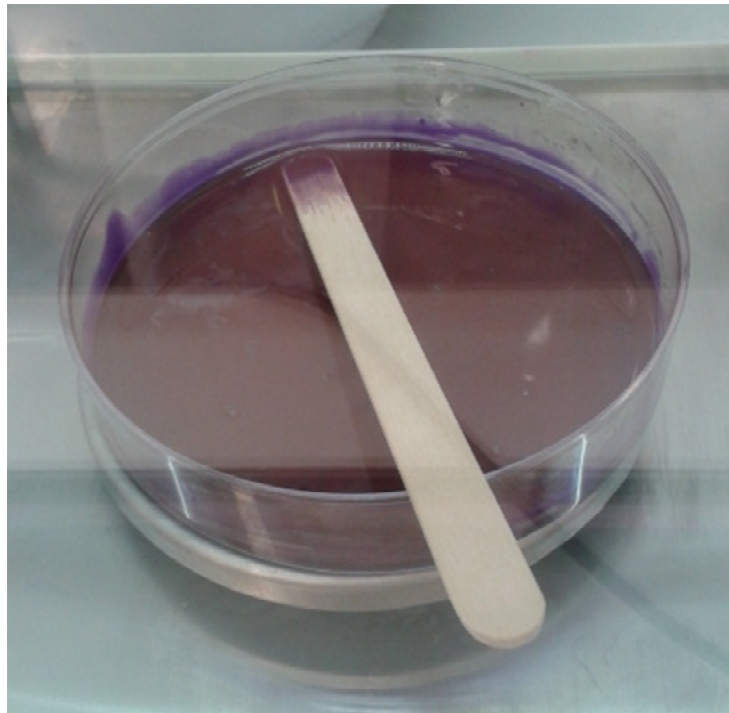


Figure D-1. The final Rhodamine B/PDMS solution

13. While the solution is being degassed, apply adhesive tape to the short edges of two microscope slides in the manner depicted in Figure D-2. This tape is 50 μm in thickness and acts as a spacer. Ensure that the tape lies flat against the slides and that there aren't any creases.



Figure D-2. Tape was applied to the short edges of two microscope slides.

14. Apply a small amount (~1 drop) of detergent onto both microscope slide, onto the faces on which the tape was applied. Spread the detergent evenly using tissues so that the glass surfaces are completely covered. This will prevent the Rhodamine B/PDMS films from sticking to the slides.
15. Pour a small amount of the Rhodamine B/PDMS solution onto the detergent-coated surface of one of the slides, as shown in Figure D-3.



Figure D-3. A small amount of Rhodamine B/PDMS was added to one of the slides.

16. Slowly press the detergent-coated surface of the other slide against this slide so that the taped edges align. Try to ensure that no Rhodamine B/PDMS solution touches the tape whilst the slides are being pressed against one another, as shown in Figure D-4.

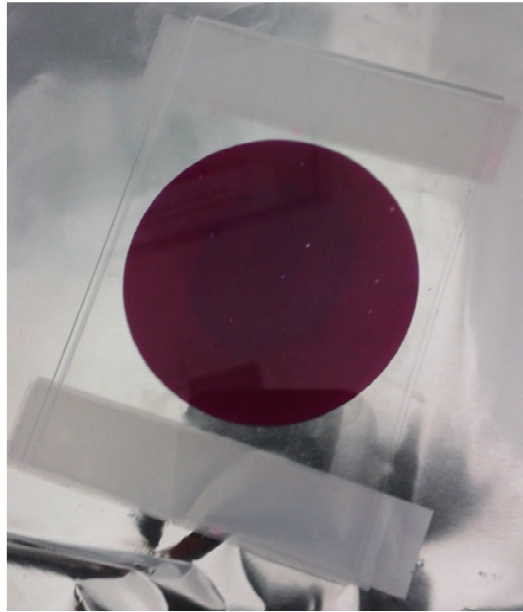


Figure D-4. The two glass slides were brought together to create a 0.1 mm thick film.

17. Using bull clips, clamp the taped sides of the slides against one another.
18. Repeat steps 13-17 if more struts are desired.
19. The clamped slides and their contents were kept within an oven at 65°C over 60 hours to cure. Note that much shorter curing times can probably be achieved.
20. Carefully remove the film from the slides using tweezers.
21. Place the film onto a placemat and then cut the film into thin strips by applying pressure against a cutting tool like the one depicted in Figure D-5 until it slices through the film. The cutting tool may also need to be dragged from side to side to ensure that it has sliced all the way through the film.



Figure D-5. The cutting tool was constructed by bolting together two pencil sharpener blades and a 0.5 mm thick washer. The washer used was used as a spacer and produced struts that were approximately 450 μm thick.

22. Arrange the strips within a petri dish and measure their width and thickness using a digital microscope. Only keep the struts that are within 5% of the desired width of 450 μm and the desired thickness of 100 μm . One of the finalised struts may be seen in Figure D-6.



Figure D-6. One of the finalised Rhodamine B/PDMS struts.

23. Place a lid on the petri dish and cover with aluminium foil to prevent overexposure to light. Store in a cool, dark place until the struts are needed.

Appendix E

Diffusion Studies

Equipment

- ~100 mL glycerol-water mixture (40 wt.% glycerol, 60 wt.% deionised water)
- ~100 mL Rhodamine B/glycerol-water mixture (4 mg/100 mL)
- 10 plastic cups
- 3 cell strainer membranes (Corning, 431751)
- 3 PVA-MA films (1 mm thick)
- 3 Rhodamine B/PDMS films (1 mm thick).
- A peristaltic pump
- A large beaker or flask
- Cleaning tissues
- Detergent
- Disposable spoons or spatulas
- A waste disposal container
- Aluminium foil
- 1000 μL pipette and tips
- 100 μL pipette and tips
- 82 black Eppendorf tubes
- Up to 3 pairs of side-by-side diffusion cells with magnetic bead stirrers
- A sequential timer device (e.g. <http://www.timeanddate.com/timer/>)
- Microplate reader (Infinite F200, Tecan Group Ltd)
- Electric balance
- Fumehood

Diffusion Study of Rhodamine B in Glycerol-Water

1. Label fifteen black Eppendorf tubes. The labels that were used, shown in Table E-1, were written so that the time, in minutes, at which the sample was collected were written alongside a letter representing the diffusion cell pair. For example, a sample collected at the 75th minute from the third pair of diffusion cells would be labelled as '75C'.

Table E-1. Labels used in this experiment.

| | | |
|-----|-----|-----|
| 3A | 3B | 3C |
| 12A | 12B | 12C |
| 27A | 27B | 27C |
| 48A | 48B | 48C |
| 75A | 75B | 75C |

2. Pour ~100 mL of the glycerol-water mixture into a plastic cup
3. Pour ~100 mL of the Rhodamine B/glycerol-water mixture into a plastic cup
4. Clean the Side-Bi-Side diffusion cells (PermeGear Inc.) and place a magnetic bead stirrer into each cell. Connect the peristaltic pump to the cells and a reservoir full of tap water at room temperature, as depicted in Figure E-1.



Figure E-1. Two pairs of diffusion cells were connected to a peristaltic pump and a reservoir of tap water.

5. Place a cell strainer membrane (Corning, 431751) between each pair of diffusion cells, as depicted in Figure 4-5.

6. Tighten the screws in the cells until the membrane is clamped between the clamping surfaces and the connections between the cells are watertight.
7. Cover the cells with aluminium foil to shield the Rhodamine B from light.
8. Using a 1000 μL pipette, fill each recipient cell with 3 mL of glycerol-water.
9. Set the times on a sequential timer to the following: 3 min, 12 min, 27 min, 48 min and 75 min.
10. Using a 1000 μL pipette, fill each donor cell with 3 mL of the Rhodamine B/ glycerol-water solution. Commence the sequential timer once the first of the donor cells has been filled.
11. Using a 100 μL pipette, remove 100 μL of solution from each recipient cell at the designated time-points and place the samples into their corresponding black Eppendorf tube. Ensure that the magnetic stirrers are turned on prior to collecting the samples so that the collected samples are well-mixed. Replenish each recipient cell with 100 μL of glycerol-water after collecting each sample so that 3 μL of fluid remains within the cell. With a 1000 μL pipette, dilute the collected sample with 900 μL of glycerol-water and place the tubes in a labelled plastic cup within a refrigerator to minimise evaporation.
12. After the final sample has been taken, wipe the diffusion cells clean using tissues and detergent (or preferably a solvent such as ethanol or isopropanol). Place all waste in an appropriately labelled waste disposal container.
13. Repeat the experiment if necessary to ensure that three trials are performed.

Diffusion Study of Rhodamine B in PVA-MA

1. Label thirty black Eppendorf tubes as shown in Table E-2. The same naming convention used in the previous diffusion study was used, although this time the experiment ran for five hours.

Table E-2. Labels used in this experiment.

| | | |
|------|------|------|
| 3A | 3B | 3C |
| 12A | 12B | 12C |
| 27A | 27B | 27C |
| 48A | 48B | 48C |
| 75A | 75B | 75C |
| 108A | 108B | 108C |
| 147A | 147B | 147C |
| 192A | 192B | 192C |
| 243A | 243B | 243C |
| 300A | 300B | 300C |

2. Pour ~100 mL of the glycerol-water mixture into a plastic cup
3. Pour ~100 mL of the Rhodamine B/glycerol-water mixture into a plastic cup
4. Clean the diffusion cells and place a magnetic bead stirrer into each cell. Connect the peristaltic pump to the cells and a reservoir full of tap water, as depicted in Figure D-1.
5. Place a PVA-MA hydrogel film between each pair of diffusion cells, in the manner depicted in Figure 4-5.
6. Tighten the screws in the cells until the film is clamped between the clamping surfaces and the connections between the cells are watertight.
7. Cover the cells with aluminium foil to shield the Rhodamine B from light.
8. Using a 1000 μ L pipette, fill each recipient cell with 3 mL of glycerol-water.

9. Set the times on a sequential timer to the following: 3 min, 12 min, 27 min, 48 min, 75 min, 108 min, 147 min, 192 min, 243 min and 300 min.
10. Using a 1000 μL pipette, fill each donor cell with 3 mL of the Rhodamine B-infused glycerol-water solution. Commence the sequential timer once the first of the donor cells has been filled.
11. Using a 100 μL pipette, remove 100 μL of solution from each recipient cell at the designated time-points and place the samples into their corresponding black Eppendorf tube. Ensure that the magnetic stirrers are turned on prior to collecting the samples so that the collected samples are well-mixed. Replenish each recipient cell with 100 μL of glycerol-water after collecting each sample so that 3 μL of fluid remains within the cell. With a 1000 μL pipette, dilute the collected sample with 900 μL of glycerol-water and place the tubes in a labelled plastic cup within a refrigerator to minimise evaporation.
12. After the final sample has been taken, wipe the diffusion cells clean using tissues and detergent (or preferably a solvent such as ethanol or isopropanol). Place all waste in an appropriately labelled waste disposal container.
13. Repeat the experiment if necessary to ensure that three trials are performed.

Diffusion Study of Rhodamine B in a Rhodamine B/ PDMS film

1. Label thirty black Eppendorf tubes as shown in Table E-3. The same naming convention used in the previous diffusion study was used, although this time the experiment ran for five hours.

Table E-3. Labels used in this experiment.

| | | |
|------|------|------|
| 3A | 3B | 3C |
| 12A | 12B | 12C |
| 27A | 27B | 27C |
| 48A | 48B | 48C |
| 75A | 75B | 75C |
| 108A | 108B | 108C |
| 147A | 147B | 147C |
| 192A | 192B | 192C |
| 243A | 243B | 243C |
| 300A | 300B | 300C |

2. Pour ~100 mL of the glycerol-water mixture into a plastic cup
3. Pour ~100 mL of the Rhodamine B/glycerol-water mixture into a plastic cup
4. Clean the diffusion cells and place a magnetic bead stirrer into each cell.
Connect the peristaltic pump to the cells and a reservoir full of tap water, as depicted in Figure E-1.
5. Place a PDMS/Rhodamine B film between each pair of diffusion cells, in the manner depicted in Figure 4-5.
6. Tighten the screws in the cells until the film is clamped between the clamping surfaces and the connections between the cells are watertight.
7. Cover the cells with aluminium foil to shield the Rhodamine B from light.
8. Set the times on a sequential timer to the following: 3 min, 12 min, 27 min, 48 min, 75 min, 108 min, 147 min, 192 min, 243 min and 300 min.
9. Using a 1000 μ L pipette, fill each cell with 3 mL of glycerol-water.
Commence the sequential timer once the first cell has been filled.

10. Using a 100 μL pipette, remove 100 μL of solution from each recipient cell at the designated time-points and place the samples into their corresponding black Eppendorf tube. Ensure that the magnetic stirrers are turned on prior to collecting the samples so that the collected samples are well-mixed. Replenish each recipient cell with 100 μL of glycerol-water after collecting each sample so that 3 μL of fluid remains within the cell. With a 1000 μL pipette, dilute the collected sample with 900 μL of glycerol-water and place the tubes in a labelled plastic cup within a refrigerator to minimise evaporation.
11. After the final sample has been taken, wipe the diffusion cells clean using tissues and detergent (or preferably a solvent such as ethanol or isopropanol). Place all waste in an appropriately labelled waste disposal container.
12. Repeat the experiment if necessary to ensure that three trials are performed.

Preparation of Standard Dilution Series

1. Label seven black Eppendorf tubes as follows: '100%', '50%', '20%', '10%', '5%', '2%' and '1%'.
2. Place a plastic cup on an electronic balance and zero the balance.
3. Inside a fumehood, use a disposable spoon or spatula to transfer a small amount of Rhodamine B powder into the plastic cup.
4. Measure the mass of the Rhodamine B powder within the cup by placing the cup back onto the balance.
5. Repeat steps 2-4 until the mass of the Rhodamine B powder within the bottle is approximately 4 mg. Record the exact value in a logbook.

6. Using a 100 mL measuring cylinder, add 25 mL of glycerol-water per mg of Rhodamine B powder to the cup (e.g. if 4 mg of Rhodamine B was measured, add 100 mL of glycerol-water).
7. Stir the contents of the cup with a disposable spoon or spatula until the glycerol-water and the Rhodamine B powder are fully mixed.
8. Using a 1000 μL pipette, remove 1000 μL of the solution and transfer it into the black Eppendorf tube labelled '100%'
9. Using a 1000 μL pipette, remove 500 μL of the solution and place into a black Eppendorf tube labelled '50%'. With a second 1000 μL pipette, dilute the collected sample with 500 μL of glycerol-water. Close the lid on the Eppendorf tube and shake it to ensure that its contents are mixed.
10. Using a 1000 μL pipette, remove 200 μL of the solution and place into a black Eppendorf tube labelled '20%'. With a second 1000 μL pipette, dilute the collected sample with 800 μL of glycerol-water. Close the lid on the Eppendorf tube and shake it to ensure that its contents are mixed.
11. Using a 100 μL pipette, remove 100 μL of the solution and place into a black Eppendorf tube labelled '10%'. With a 1000 μL pipette, dilute the collected sample with 900 μL of glycerol-water. Close the lid on the Eppendorf tube and shake it to ensure that its contents are mixed.
12. Using a 100 μL pipette, remove 50 μL of the solution and place into a black Eppendorf tube labelled '5%'. With a 1000 μL pipette, dilute the collected sample with 950 μL of glycerol-water. Close the lid on the Eppendorf tube and shake it to ensure that its contents are mixed.
13. Using a 100 μL pipette, remove 20 μL of the solution and place into a black Eppendorf tube labelled '2%'. With a second 1000 μL pipette, dilute the collected sample with 980 μL of glycerol-water. Close the lid on the Eppendorf tube and shake it to ensure that its contents are mixed.

14. Using a 100 μL pipette, remove 10 μL of the solution and place into a black Eppendorf tube labelled '1%'. With a second 1000 μL pipette, dilute the collected sample with 990 μL of glycerol-water. Close the lid on the Eppendorf tube and shake it to ensure that its contents are mixed.
15. Place the Eppendorf tubes in a labelled plastic cup within a refrigerator to minimise evaporation
16. Clean up any spilled Rhodamine B powder using tissues and detergent (or preferably a solvent such as ethanol or isopropanol). Place waste in the appropriate waste disposal bin.

Plate Readings

1. Pipette 100 μL of each of the standard solutions and each of the sample solutions into the plate reader wells and label the wells accordingly.
2. Insert these collected samples into the plate reader
3. Set the fluorescent excitation and emission wavelengths to 554 nm and 627 nm respectively and adjust the gain as required to differentiate the light intensities produced by the different solutions.